DOCTOR OF PHILOSOPHY

# Unearth: Revealing the Effects of Stellar Activity on Exoplanet Host Stars

Thompson, Andrew Patrick Gustave

*Award date:*
2019

*Awarding institution:*
Queen's University Belfast

# Unearth:
# Revealing the Effects of Stellar Activity on Exoplanet Host Stars

A thesis submitted for the degree of
Doctor of Philosophy

by

Andrew Patrick Gustave Thompson, MSci
(Queen's University Belfast, 2014)

Faculty of Engineering and Physical Sciences

School of Mathematics and Physics
Department of Physics and Astronomy
Queen's University Belfast
Belfast, Co. Antrim, Ireland

# Acknowledgements

Of utmost importance, I would like to thank my supervisor Dr Chris Watson for support and guidance over these last 3 and a bit years. But I must also thank him for being the bright and shining spotlight on my moments of stupidity. A story he will never let me live down (and so I write it here for prosperity) was during my attempts at developing my own Gaussian Process Regression code. Try as I might I couldn't get it to work, it just would not converge! Chris decided enough was enough, it was intervention time and we sat together going through the code line by line and trying to understand the subtle nuances of Bayesian statistics. After a few moments of intense decoding he saw it..."Andrew", he finally said, "are you...are you minimising the maximum likelihood? No wonder it won't work! You're trying to find the *least* likely solution to your problem!". Red-face, embarrassed and with the sound of hysterical laughter emanating from the floor where Chris had now collapsed in a heap, I quickly fixed the issue hoping to never hear of it again. Little did I know then that he would bring it up at every opportune moment and every conference we attended after that day. I've had many incidences like this since (lets not speak of the "HARPS fringing" incident) but this one stands out as a time when I was entirely lost, not knowing what to do and Chris was both able to help me figure it all out as well as having a good laugh along the way. What more can you ask for in a supervisor?

I'd like to thank Andrew McNeill, Tom Seccull, Rachel Booth, Matthew Hooton, and Stephen Durkan – PhD students who allowed me to vent my frustrations in their general direction – as well as the ARC department as a whole. I'd like to thank Ernst de Mooij (EdM) for useful discussion, insightful suggestions and interesting company during observing runs. EdM is also credited with providing us with the catch all term of Error dominated Measurements (EdMs) to help better explain problems in our data reduction. For example "I must have applied the RV correction wrong, the relative spectra are full of EdMs.". I hope the science community as a whole can make use of this term. I'd like to thank Heather Cegla for her useful discussions and friendship. She also introduced me to boxing, which helped me get though some tough weeks. A word of thanks to my piano teacher Cettina Musumarra, the pursuit of music over the last two years has been a welcomed break from the toils of data analysis.

And finally, I'd like to thank my close friends and family, in particular my Mother and Father, for their care and patience (especially over the last few months of thesis writing). There are too many to name here but know that I fully appreciate the support you have given me.

A. P. G. T.
June 2018, Belfast

# Abstract

With the push towards finding true Earth-analogs, instrumental radial velocity (RV) precision no longer presents a limiting factor. The effects of astrophysical noise, which can act to mask or mimic planetary RV motions, represents the fundamental barrier to achieving this goal. For inactive stars like the Sun, plage/faculae are thought to be the major contributors to this noise, but its effects have so far proven difficult to trace.

In this thesis, I investigate the effect activity has on stellar spectra, using HARPS data of the well observed K1 V star $\alpha$ Centauri B. I compare spectra from high- and low-activity periods (as traced by $\log R'_{HK}$) of $\alpha$ Cen B. I produce 'relative spectra' by dividing the high-activity spectra by a low-activity template, and find a forest of pseudo-emission features. The features show a strong correlation with $\log R'_{HK}$, modulation on the stellar rotation period, and a peak-to-peak RV variation of 300m $s^{-1}$, all of which suggest that the features are activity driven. The features also show two distinct morphologies that, when modelled, show evidence that the 'immaculate photosphere' during the more active phase is fundamentally different to the inactive case. This may be due to enhanced contributions of e.g. magnetic bright points and plage, which act as a source of additional line broadening. An extension of this work looked at HARPS-N Solar Telescope data, where similar 'relative spectra' were created for the Sun, making use of the unique Sun-as-a-star observing capability of the instrument. Here the relative spectra were compared not only to $\log R'_{HK}$ but to spot and faculae filling factors calculated using SDO images. Equivalent features to those found in $\alpha$ Cen B were found, further confirming that the features are activity driven. With the solar data, the features were found to more strongly correlated with changes in unassociated faculae than with spots. This suggests that the features seen in the relative spectra are driven by facular regions, and may provide a way of tracking plage/faculae on the surface of stars by measuring their influence directly from stellar spectra.

Finally, I constructed a tool called UnEarth that combines the techniques of wavelet analysis, GLS, and DCF to search for stellar rotation. This tool was specifically designed to be used with NGTS light-curves. I apply the tool to a number of interesting NGTS targets with the results from each target highlighted in the relevant sections. The combined methods were able to provide more robust detections of stellar rotation periods and a potential correlation between the likelihood of a flare event and the concentration of active regions on the stellar surface.

# Contents

**Acknowledgements** i

**Abstract** ii

**List of Tables** vi

**List of Figures** 1

**1 Introduction** 2

1.1 Introduction . . . 3
1.2 Detection Methods . . . 5
1.2.1 Direct Imaging . . . 6
1.2.2 Gravitational Microlensing . . . 8
1.2.3 The Transit Method . . . 12
1.2.4 The Radial Velocity or 'Doppler wobble' Method . . . 18
1.2.5 Other Methods . . . 20
1.3 Planet Formation and Migration . . . 22
1.3.1 Core Accretion . . . 22
1.3.2 Disk Instability . . . 23
1.3.3 Planet Evolution and Migration . . . 24
1.4 The Rossiter-McLaughlin Effect . . . 28
1.5 Structure of the Thesis . . . 29

**2 Astrophysical Noise Sources and Removal Methods** 31

2.1 Introduction . . . 32
2.2 Formation of Spectral lines . . . 33
2.2.1 Types of Absorption . . . 35
2.2.2 Broadening of Spectral Lines . . . 36
2.3 Astrophysical Noise (Non-activity related) . . . 38
2.3.1 Granulation . . . 39
2.3.2 Oscillations . . . 40
2.4 Astrophysical Noise (Activity related) . . . 40

2.4.1 Stellar Dynamo . . . 40
2.4.2 Spots . . . 42
2.4.3 Plage and Faculae . . . 44
2.5 Mitigation of Stellar noise . . . 47
2.5.1 Avoid Active Stars . . . 48
2.5.2 Cross-Correlation Function (CCF) analysis . . . 51
2.5.3 Optimal Observing Strategies . . . 52
2.5.4 Periodogram Searches . . . 54
2.5.5 Modelling Stellar Activity using Photometry . . . 57
2.5.6 Harmonic Decomposition and Fourier Component Analysis . . 60
2.5.7 Detrending by Local RV Trends . . . 62
2.5.8 Gaussian Process Regression . . . 63
2.5.9 Correlations with Chromospheric Activity . . . 64
2.6 Conclusion . . . 66

**3 Probing the Spectral Impact of Stellar Activity 67**
3.1 Introduction . . . 68
3.1.1 The Alpha Centauri System . . . 68
3.1.2 Activity on Alpha Centauri B . . . 69
3.2 Data and Data Processing . . . 71
3.3 Analysis . . . 76
3.3.1 Tellurics . . . 80
3.3.2 Systematics . . . 81
3.4 Explanation for the Pseudo-Emission Feature Morphologies . . . 83
3.4.1 Extension of the Simple Model using VALD . . . 94
3.4.2 Model limitations . . . 96
3.5 Measuring Equivalent Widths . . . 98
3.6 RV Variation of Pseudo-emission Features . . . 99
3.7 Links to Spectral Line Properties . . . 102
3.7.1 TiO Bandheads . . . 102
3.7.2 Landé Factor and Excitation Potential . . . 103
3.8 Conclusions . . . 105

**4 Activity on the Sun 109**
4.1 Introduction . . . 110
4.2 Data and Data Reduction . . . 111
4.2.1 Data Processing . . . 113
4.2.2 Investigation and Removal of the Ripple Pattern . . . 114
4.3 Feature Search . . . 119

4.3.1 Trailed Spectra of Features . . . 126
4.4 Discussion . . . 128
4.5 Conclusion and Future Work . . . 131

**5 Stellar Rotation with NGTS** **134**
5.1 Introduction . . . 135
5.1.1 The Next Generation Transit Survey (NGTS) . . . 135
5.2 Stellar Rotation Detection Techniques . . . 138
5.2.1 Generalised Lomb-Scargle Periodogram . . . 138
5.2.2 Discrete Correlation Function . . . 138
5.2.3 Wavelet Analysis . . . 140
5.3 Combined Approach to Period Searching . . . 142
5.3.1 NGTS-1b – A hot Jupiter around an M-dwarf . . . 146
5.3.2 NGTS-2b – An inflated hot Jupiter Orbiting an F-Star . . . 148
5.3.3 NGTS-4b – An Ultra-short Period hot Jupiter . . . 152
5.3.4 A Rare Equal-mass eclipsing M-dwarf Binary . . . 156
5.4 Conclusions . . . 160

**6 Conclusions and Future Work** **163**
6.1 Conclusions . . . 164
6.1.1 Relative Spectra of $\alpha$ Cen B . . . 164
6.1.2 Sun-as-a-star Analysis with the HARPS-N Solar Telescope . . . 166
6.1.3 Periodicity in NGTS Light-curves . . . 167
6.2 Future Work . . . 169
6.2.1 Extended Analysis of $\alpha$ Cen B . . . 169
6.2.2 Atlas of Tailored CCF masks . . . 170
6.2.3 Line Formation Models . . . 172
6.2.4 The HARPS-N Solar Telescope and Semi-empirical Model . . . 173
6.2.5 Data from Solar Telescopes . . . 173
6.2.6 UnEarth Code Distribution . . . 175

**A Appendix** **176**
A.1 Morphology line list . . . 177

# List of Tables


2.1 Planet radial velocity estimates . . . . . 34

3.1 VALD line strengths of Ti II 4443.81 Å and V I 4444.21 Å . . . . . 95

4.1 Pearson's r correlation of relative features (2016 interval) . . . . . 120
4.2 Pearson's r correlation of unassociated plage region . . . . . 123
4.3 Pearson's r correlation of relative features (2017 period) . . . . . 126

5.1 Mass and radius estimates for the M-dwarf binary . . . . . 160

A.1 Eye-balled line morphologies . . . . . 177

# List of Figures


1.1 Mass vs period of known planets . . . 6
1.2 Direct Imaging of the HR8799 System . . . 9
1.3 Light-curve of OGLE-2006-BLG-109 . . . 11
1.4 Schematic of Exoplanet Transit event . . . 13
1.5 Cumulitive Histogram of planet discoveries . . . 15
1.6 Photot of NGTS facility . . . 16
1.7 Field of View of TESS . . . 17
1.8 Schematic of RV eccentricity . . . 19
1.9 Schematic of the Linblad resonances . . . 26
1.10 Schematic of the Rossiter McLaughlin Effect . . . 29

2.1 RV variation due to activity on the Sun . . . 33
2.2 Schematic of Solar Oscillations . . . 41
2.3 Solar Dynamo Schematic . . . 43
2.4 Image of a Sun spot . . . 44
2.5 Schematic of the formation of spectral line emission bump . . . 45
2.6 Image of Solar faculae . . . 47
2.7 Measurement of Ca II H & K . . . 49
2.8 CFF Bisector Schematic . . . 51
2.9 Example of the BLS periodogram . . . 55
2.10 Harmonic decomposition of GJ 674 . . . 61
2.11 Gaussian Process Regression model of CoRoT 7 . . . 65

3.1 $\log R'_{HK}$ variation of $\alpha$ Cen B . . . 70
3.2 Example HARPS spectrum of $\alpha$ Cen B . . . 74
3.3 Division vs Subtraction of the Relative spectra . . . 75
3.4 Relative spectra of $\alpha$ Cen B . . . 77
3.5 Example of the broad features seen in the relative spectra . . . 78
3.6 Example of the narrow pseudo-emission features seen in the relative spectra . . . 79
3.7 Relative spectrum from Basri et al. (1989) . . . 80

3.8 Relative Features compared to telluric effects . . . . . 82
3.9 Example of the morphologies seen in the relative spectra . . . . . 84
3.10 Simplistic model of Activity . . . . . 84
3.11 Relative features from simple spot model – Baseline . . . . . 87
3.12 Relative features from simple spot model – Active Region × 2 . . . . . 88
3.13 Relative features from simple spot model – 10% Broader Active Region 89
3.14 Relative features from simple spot model – 50% Broader Active Region 90
3.15 Relative features from simple spot model – Best Fit . . . . . 91
3.16 Four line component model of Cegla et al. (2013) . . . . . 92
3.17 Four component model of Beeck et al. (2015) . . . . . 93
3.18 Convective flow velocity schematic . . . . . 94
3.19 Relative features from simple spot model – Addition of VALD . . . . . 97
3.20 Fitting Psuedo-Equivalent Width . . . . . 99
3.21 Psuedo-Equivalent Width Correlations . . . . . 100
3.22 RV measurement of Relative Features . . . . . 101
3.23 Histogram of relative feature vs. Landé factor . . . . . 104
3.24 Histogram of relative feature vs. Excitation Potential . . . . . 105
3.25 Histogram of relative feature vs. Excitation Potential, per element . . . 106

4.1 $\log R'_{HK}$ measurements of the Sun . . . . . 112
4.2 GLS periodogram of solar spectrum Echelle Orders . . . . . 116
4.3 Ripple Removal Process . . . . . 118
4.4 Relative spectrum of the Sun versus $\alpha$ Cen B . . . . . 120
4.5 Equivalent Width of relative features on the Sun (2016 interval) . . . . . 122
4.6 HMI Solar images (2016 period) . . . . . 123
4.7 Example of 4501Å pseudo-absorption dip . . . . . 124
4.8 Equivalent Width of relative features on the Sun (2017 interval) . . . . . 125
4.9 Trailed relative spectrum of 4375Å relative feature (2016 interval) . . . 127
4.10 Trailed relative spectrum of 4375Å relative feature (2016 interval) . . . 128
4.11 Trailed spectrum of 4375Å and 4501Å relative features (2017 interval) . 128
4.12 Trailed spectrum of 4501Å relative feature (2017 interval) vs SDO images 130

5.1 Image of NGTS facility . . . . . 136
5.2 Discovery Space of NGTS . . . . . 137
5.3 DCF of Kepler 78 . . . . . 139
5.4 Example of Morlet Wavelet . . . . . 141
5.5 UnEarth Output on NGTS flare star . . . . . 145
5.6 Phase Folded NGTS flare star light-curve . . . . . 146
5.7 UnEarth Output of NGTS 1 . . . . . 147

5.8 UnEarth Output of NGTS-2 . . . 150
5.9 Median GLS periodogram of NGTS-2 . . . 151
5.10 UnEarth Output of NGTS-4 . . . 153
5.11 Phase-folded NGTS-4 light-curve . . . 155
5.12 UnEarth Output of M-dwarf Binary . . . 158
5.13 Phase Folded light-curve of M dwarf binary . . . 159
5.14 Mass-radius plot of M-dwarf binaries . . . 159

6.1 Schematic of Tailored CCF . . . 171
6.2 Relative Solar spectra from DST . . . 174

# *Chapter 1*

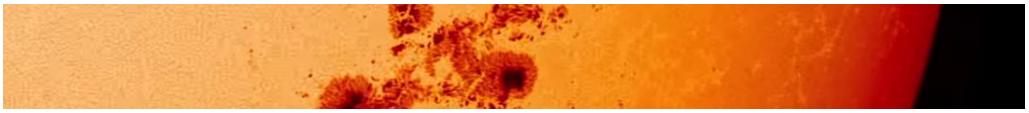

# Introduction

*"Moreover,*
*there is an infinite number of worlds,*
*some like this world,*
*others unlike it."*

- Epicurus (341 - 270 BC), Letter to Herus

## 1.1 Introduction

The term planet is so ubiquitously used that a formal definition seems almost unnecessary but, as our understanding of the planetary systems outside our own Solar system grows, the exact definition of "a planet" becomes something very difficult to distill into a single statement. Consider the planets of the Solar system, here a planet may be defined as a large body that orbits the Sun. With the huge array of objects known to exist in the Solar system (from asteroids to gas giants) this loose definition of a planet is not adequate. A definition is needed that includes all the classically defined planets of the Solar System but not other bodies like natural satellites and comets. The International Astronomical Union (IAU) sought to clarify this and in 2006 came up with the following definition of a planet (Perryman 2011). An object is considered a planet if it meets three criteria:

1. The object must orbit the Sun,
2. It must be massive enough so that it collapses under self gravity and assumes hydrostatic equilibrium,
3. It must clear its neighbourhood of planetesimal.

This definition, although met by some with contention, is mostly accepted for defining planets in the Solar system.

Exoplanets (or extra-solar planets) are planets that orbit around stars (or stellar remnants) other than the Sun, even on generalising this definition for all stars and not just the Sun the lack of detailed knowledge of these systems means that most of these points cannot be verified. Additionally, the variety of exoplanet orbital configurations found to date do not agree well with what is seen in the Solar system, and hence this argues against using the Solar system model to shape our understanding of planet formation and migration theory. A number of other definitions of a planet have been considered to better conform to the exoplanetary systems seen. The first defines an upper mass limit for planets and, in doing so, separate planets from stars. This leads to the IAU working definition of a planet as being an object whose mass is below the limit for burning (or fusion) of deuterium (approximately $13M_J$ assuming a solar metallicity) that orbits a star or stellar remnant; objects above this mass (but below the mass for hydrogen fusion), are considered brown dwarfs – or 'failed stars' (Perryman 2011).

Udry (2010) investigated the mass distribution of stellar companions up to $25M_J$ and found no characteristic features that would justify a cut at $13M_J$. Additionally, Chabrier et al. (2014) argues that deuterium burning plays no role in the formation of the giant

planets or brown dwarfs. Schneider et al. (2011) arbitrarily set the maximum mass of a planet to $25 M_J$ for the *Exoplanet Encyclopaedia* (http://exoplanet.eu/) arguing that this gave a more open approach to comparing giant planets and brown dwarfs. Finally, Hatzes & Rauer (2015) considered the mass-density distribution of a range of objects and found three regions based on observed inflections in mass-density. The authors termed objects with $M < 0.3 M_J$ as "Low Mass Planets"; objects with $0.3 M_J < M < 60 M_J$ as "Giant Gaseous Planets"; and $M > 60 M_J$ as "Stellar Objects".

Soter (2006) argued for a different definition based on the formation mechanism rather than defining an upper or lower mass limit. The author suggests that planets should be defined as the end product of secondary accretion in a disk around a primary star (where primary accretion is the formation of the host star). Hatzes & Rauer (2015), however, argues caution against such an approach, citing incompleteness in the theories that these mechanisms rely on. Hatzes & Rauer (2015) also argues that a different formation mechanism is no reason to differentiate between objects, making comparisons between different star forming processes all leading to the same end product – a main-sequence star. The exact definition of a planet is still very much an open question that can only be settled once we have a more complete picture of the variety of exoplanet systems.

The first planets to be discovered were found around the pulsar PSR B1258 + 12 (Wolszczan & Frail 1992). These $M \sin i \simeq 2.8\ M_\oplus$ and $3.4\ M_\oplus$ objects were discovered by measuring the variations in the arrival times of the pulses of PSR B1258 + 12, concluding that 2 (or possibly 3) planetary mass bodies were responsible for it. Pulsars are the highly magnetised remnant from a supernova explosion, and their name comes from the pulses generated by the misalignment of their spin and magnetic axis. Pulsars emit beams of electromagnetic radiation along their magnetic poles that appear to pulse as the stellar remnant rotates. It was around one of these exotic objects that the first planets were found and pushed the understanding of the formation of planet systems beyond what can be seen in the Solar system.

These exotic systems represent a small number of the exoplanets discovered, making up just 29 of the 3737[1] planets discovered to date. Most planets are found around more conventional main sequence FGK dwarf stars. The first of these planets to be discovered was 51 Peg b (Mayor & Queloz 1995). This planet orbits a G5 V star (not dissimilar to the Sun) with a minimum mass of $0.47 M_J$ and an orbital period of 4.2293 days. This places the Jupiter-mass planet extremely close to its host star, with a semi-major axis of just 0.05 AU. These 'hot Jupiters' are highly irradiated, often bloated gas

[1]The Extrasolar Planets Encyclopaedia: http://exoplanet.eu/

giants that orbit very close to their host star (typically with orbital periods of $\leq 10$ days) and make up a large proportion of the first planets to be found. More recently (especially with space missions like Kepler) the Hot Jupiters make up a smaller, but well studied, segment of the total planet population found to date. The short periods and large masses of these planets make them easier to detect than smaller, more Earth-like, worlds. They represent a departure from the Solar System model, which expects rocky terrestrial planets in the inner-portion of the planetary system (closest to the host star), and large gas and ice giants at larger orbital radii beyond the 'snow line' of the star (the distances from a star at which ices can condense).

This arrangement of massive, close-in planets is unexpected but part of this could be due to the methods used to find planets. Observational biases in these methods show a preference for finding these types of planets, which may go part of the way to explain why solar system-like planetary systems are not seen. A survey by Wright et al. (2004), sampling 1200 FGKM stars, showed that 6-7% of stars have planets with masses $> 0.5 M_J$ and orbital separations of $< 5$ AU. Petigura et al. (2013) looked at the 42,000 stars observed by the Kepler mission and found that $11 \pm 4\%$ of solar-like stars had an Earth-sized planetary companion and further constrained this to $\sim 5\%$ having Earth-sized planets on orbits of between 200-400 days (i.e. Earth-analog). These results support the claim made by Cassan et al. (2012) who, in a statistical microlensing study, showed occurrence rates for super-Earth (5-10 $M_\oplus$) planets at over 60% and concluded that planets are the rule rather than the exception. This is a striking result given that just over two decades earlier not a single planet outside the Solar system had been found.

Results to date have shown that planetary system configurations can look very different to what is seen in the Solar system. The exact definition of a planet seems to be further away now that our understanding of the variety of systems grows. It may be that the Solar system represents an uncommon arrangement of planets, but what is more likely is that the methods used to discover exoplanets have detection biases that preferentially find systems that are different from the Solar system. In Section 1.2 the main detection methods are discussed, which highlights the bias towards discovering larger, close in planets.

## 1.2 Detection Methods

There are a number of different techniques used to detect and characterise exoplanets. Each probe their own part of parameter space, with overlap between some techniques. In this section the main planet hunting methods used will be discussed, highlighting their strengths and weaknesses as well as how, by using some techniques together, the

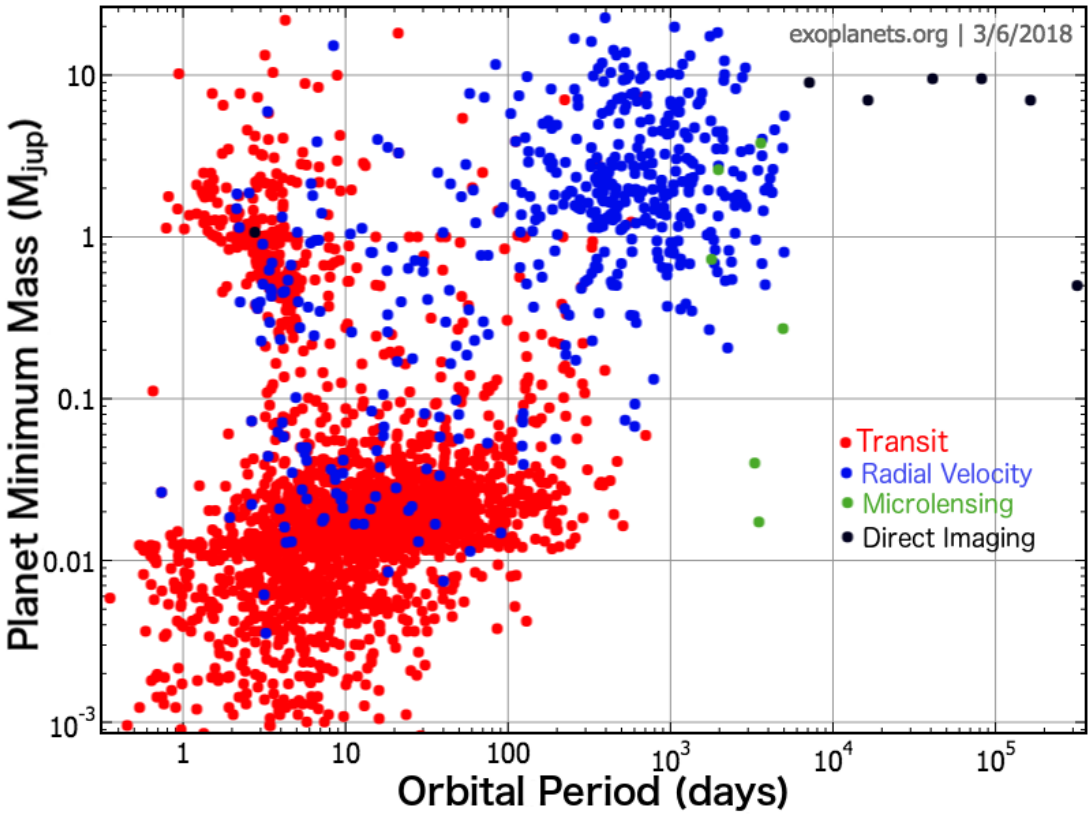


**Figure 1.1**: A beakdown of all planet found by the four main exoplanet detection methods: transits, radial velocity, gravitational microlensing and direct imaging. The most densely populated part of parameter space is that of the short period planets – due to the observational biases of the two most successful techniques (transits and radial velocity). Figure generated using exoplanets.org.

information gained can be more than the sum of its parts. Figure 1.1 shows the masses and orbital periods of currently known planets, and is broken down into the four main detection methods, highlighting the current selection biases of each technique (this is discussed more in the following sections). Note the preference for short period planets, which is due to the detection bias inherent to the two detection methods that have found the majority of planets: the transit method (see Section 1.2.3) and the radial velocity method (see Section 1.2.4).

### 1.2.1 Direct Imaging

Direct imaging is the only technique that directly detects the presence of a planet around a star, all other techniques exploit indirect methods – relying on dynamical, photometric, or spectroscopic effects to infer the existence of an unseen planet. This makes direct imaging unique as it is the only method that allows a glimpse of some of the major components that make up the system, giving first hand evidence of planets hidden in the light of their host star.

The detection of these planets relies on measuring the thermal radiation intrinsic to the planet itself (in the infrared), theoretically it is also possible to measure light reflected from the parent star. The method is complicated by a number of technical issues – resulting in the first directly imaged planet being confirmed over a decade after the first exoplanets were discovered (2M 1207-39 b, Chauvin et al. 2004). The two main obstacles to overcome when performing direct imaging is the contrast between the star and the planet, and their on sky angular separation. The contrast is the ratio of the planet to stellar flux, $f_p/f_\star$, and depends on a number of parameters from stellar luminosity and spectral type to planet parameters, like orbital semi-major axis, radius, mass and atmospheric contribution to the observation wavelength. The angular separation is guided by the angular resolution of the telescope being used, with larger telescopes having a better angular resolution that enables objects with smaller separations to be resolved. In the case of diffraction limited optics, the angular resolution $\theta$ is given by,

$$\theta = 1.22\,\frac{\lambda}{D}\ \text{radians} \equiv 251643.3\,\frac{\lambda}{\mathrm{D}}\ \text{arcsec} \tag{1.1}$$

where $\lambda$ is the observing wavelength and $D$ is the diameter of the telescope light-collecting area. For a 4-m class telescope, observing in the visible, this amounts to an angular resolution of 30 milliarcsecs (mas).

As an example, consider the Jupiter-Sun system viewed at a distance of 10 parsecs (pc). The system has an orbital semi-major axis of ∼5 AU resulting in an angular separation of 500 mas (this reduces to ∼100 mas for the Earth-Sun system observed at the same 10 pc) and would have a contrast of $f_\oplus/f_\odot = 10^{-10}$ in the visible. Current instrumentation is sensitive to contrasts down to $10^{-10}$ in the visible and $10^{-5}$ in the infrared (Bozza et al. 2016), making Jupiter just on the cusp of observability. Direct imaging is then sensitive to younger massive planets on wider orbits. The wider orbits help to reduce the resolution requirements and younger planets have higher levels of thermal radiation leading to self-illumination (due to ongoing contraction of the planet or possible accretion) reducing the contrast between the planet and the host star (Bozza et al. 2016).

The glare of the star is another issue, the light from the planet can be encompassed by the light from the star. This glare is complicated by instrumental imperfections leading to the formation of a speckle pattern. The issue is further exacerbated for ground based instruments as atmospheric turbulence leads to a separate speckle noise pattern that interacts with that of the speckle pattern from the instrumental imperfections. Additionally, ground based observations are not diffraction limited. Atmospheric turbulence has a profound effect on the angular resolution, reducing it to 1 arcsec or worse

depending on conditions. A number of techniques and technologies have been employed to help overcome these effects: coronagraphs are used to block out the light of the host star and reveal faint objects inside the stellar glare; and adaptive optics (AO) systems use deformable mirrors that can counter act the effects of the Earth's atmosphere allowing ground based telescopes to push back towards their diffraction limit. Additionally, techniques like spectral differential imaging (SDI, Marois et al. 2003) and angular differential imaging (ADI, Marois et al. 2006) are used to help reduced the speckle pattern and reveal signals of planets lost in the noise of the system. A total of 93 planets have so far been discovered using direct imaging (in combination with the techniques and technologies mentioned).

One of the most interesting systems detected by direct imaging is HR 8799, which was one of the first directly imaged systems and initially showed three planets (Marois et al. 2008) with a fourth being found 2 years later (Marois et al. 2010, see Figure 1.2). Oppenheimer et al. (2013) performed spectroscopic measurements of the planets directly and noted that, spectroscopically, the worlds are very different from other astrophysical objects (showing slight similarities to low mass L and T-dwarf stars and Saturn, but are not directly comparable) and tentatively identify the presence of molecular gases. This opens up a new era of measuring the properties of exoplanet atmospheres directly, which was not possible before.

This result demonstrates the power of direct imaging. Although the technique is limited by effects from astrophysical (star-planet contrast), physical (diffraction limits) and engineering (efforts to counteract atmospheric effects) barriers, it has the power to probe parts of parameter space not available to other methods. The ability to 'see' and measure the physical properties of an exoplanet directly is unique to direct imaging, making the technique an invaluable source of direct evidence of planets and an important tool within the field.

### 1.2.2 Gravitational Microlensing

From general relativity, matter causes a warping of spacetime that can alter the path of electromagnetic radiation. If two stars are in near perfect alignment relative to the observer, the foreground star acts as a lens and magnifies the light from the background (source) star. This is known as gravitational lensing and in the specific case where the background source and the lens are not resolvable it is termed gravitational microlensing. If a planet orbits the lensing object then it can produce a secondary magnification of the light (with the system acting as a binary, rather than a single lens). This is the fundamental principle that underlines the use of gravitational microlensing for exoplanet

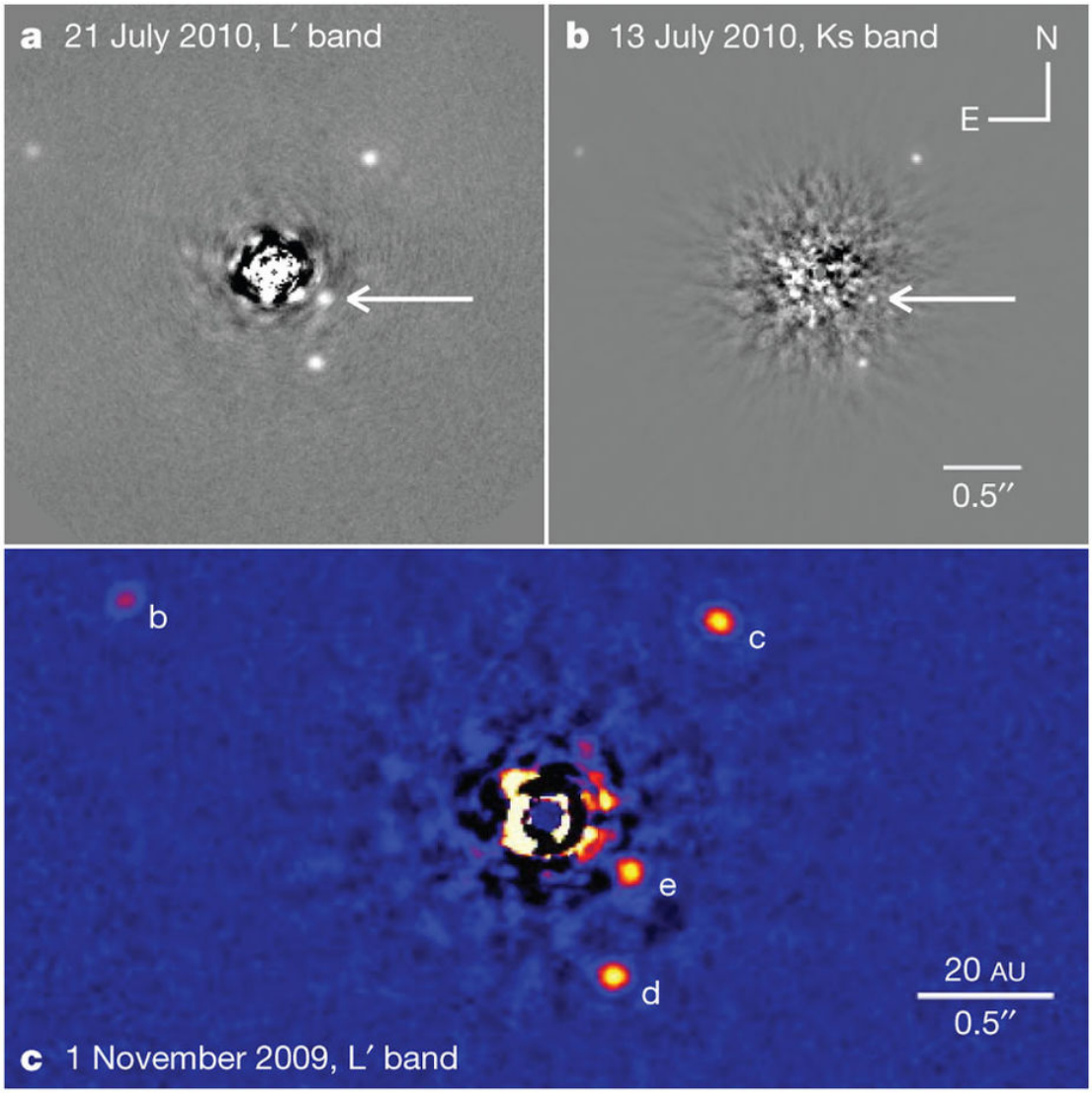


**Figure 1.2**: Image of the 4 planet system HR7899 using the direct imaging tecnhique. Panel *c* shows the system imaged ~8 months after images *a* and *b* were taken. The position of the planets have changed slightly between the two epochs – allowing their orbits to be better constrained. Figure taken from Marois et al. (2010).

detection. The smaller mass of the planet produces a microlensing event that is shorter than the main event, lasting just a few hours (3-5 hours in the case of an Earth mass object – see, for example, the peak marked "4" in Figure 1.3), compared to the main event that can last for days (or weeks).

Two of the most important quantities that are retrieved from microlensing events are the duration of the perturbation (giving the mass ratio of the planet and its parent star $q = M_p/M_\star$) and the magnitude of the perturbation. The mass ratio, $q$, is straightforward to find from the duration of the perturbation, which is given by:

$$t_{E,p} = \frac{q^{1/2}}{t_E}, \tag{1.2}$$

where $t_{E,p}$ defines the duration of the deviation caused by the planet; and $t_E$ is the total time of the lensing magnification (the Einstein radius crossing time), this is defined as:

$$t_E = \frac{\theta_E}{\mu_{LS}}, \tag{1.3}$$

where $\theta_E$ is the angular Einstein radius and $\mu_{LS}$ is the proper motion of the source relative to the lens (Gaudi 2010). The magnitude of the perturbation, together with the duration of the perturbation[2], can also provide quantities like the projected separation of the star-planet system (this mathematical derivation is less straightforward and not within the context of this thesis so will not be given here, the interested reader is referred to Gaudi (2010); Perryman (2011); Bozza et al. (2016)).

Microlensing does not directly measure the flux of the host star or the exoplanet but rather it measures the gravitational effect of the system. This lack of dependance on the parameters of the planetary systems allows microlensing to detect planets in a wide range of configurations (as described in more detail later).

Microlensing has found the most distant planet, OGLE-2005-BLG-390L b, at a distance of 8.5 kpc and having a mass of ~5 $M_\oplus$ (Beaulieu et al. 2006). Additionally, microlensing can find free-floating planets (i.e. planets that do not orbit a host star) and planets far beyond the snowline (defined as the distance from the host star that ice can form, Gaudi 2012). To date 67 exoplanets have been discovered through microlensing including 2 multi-planet systems OGLE-06-109L b, c (Gaudi et al. 2008) and OGLE-2012-BLG-0026L b,c (Han et al. 2013). The microlensing event of the OGLE-06-109L system is shown in Figure 1.3 highlighting the complex light-curve that can result from a three body lens.

Gravitational microlensing surveys designed to search for evidence of dark matter, including OGLE (Optical Gravitational Lensing Experiment), EROS (Expeŕience pour la Recherche d'Objets Sombres'), and the MACHO (MAssive Compact Halo Objects) are also used to search for exoplanets. These surveys target the galactic bulge, as the large number of stars helps increase the chances of seeing a (rare) microlensing event. This region of space is usually avoided by surveys that utilise other detection techniques as the density of the field increases the number of false positive detections. This is

[2]This is not the duration of the perturbation defined above as $t_{E,p}$ but the time during the microlensing event when the secondary microlensing of the planet occurs.

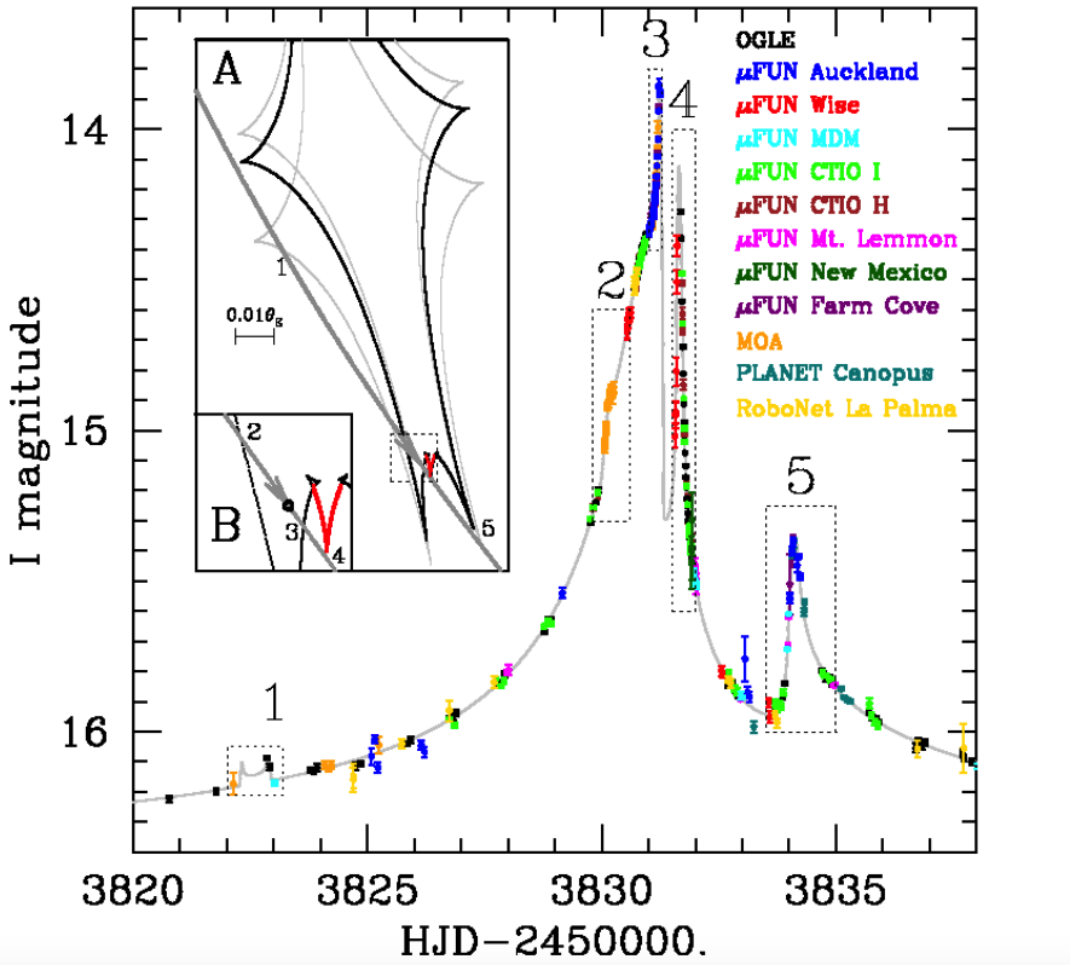


**Figure 1.3**: Lightcure of the ~ 20 day microlensing event due to the ~0.71 and ~0.27 $M_J$ planets orbiting OGLE-2006-BLG-109, with data from a number of surveys highlighted in various colours. The shape of the caustic is shown in insert A in black with the gray line showing the path of the background source. Insert B shows a close up of the caustic crossing that is thought to be due to the second planet OGLE-06-109L c in red. Figure taken from Gaudi et al. (2008).

another advantage of microlensing, being able to target parts of the night sky not open to other techniques. New space missions such as the NASA led WFIRST (Wide Field InfraRed Survey Telescope) and ESA's Euclid hope to push the observational limits down to $\geq 0.1 M_\oplus$ and separations of $a \leq 0.5$AU as well as providing robust discoveries of Earth-mass free-floating planets (Bennett & Rhie 2002).

Microlensing has the ability to probe parts of the planet discovery parameter space that are not open to any other techniques, looking at planetary systems furthest from the Solar system, or detecting 'cold Earths' (i.e. small planets far from their host star). It provides important results both for statistical studies of planets and setting constraints on planet formation models (see Section 1.3 for more detail on planet formation models). For example, its ability to detect far-flung planetary systems potentially allows for

a Galactic census to be conducted. This could allow for planet formation as a function of metallicity (for example) in different regions of the galaxy to be probed. The advantages of microlensing, however, are countered by some major setbacks. Microlensing events are stochastic in nature, so any planets discovered by this method cannot be followed up. Additionally, most lens stars are too faint to be observed outside of the event and so additional measurements are not possible. Finally, these events are also extremely rare, even in the crowded fields of the galactic bulge, where most microlensing surveys are focused, the probability that a star is appreciably lensed at any given time is of the order of $10^{-6}$. This value represents all microlensing events, not just the events with a star-planet lens, making the probability of these events even smaller.

### 1.2.3 The Transit Method

The transit method is both the easiest to understand and the most successful of exoplanet detection techniques. The presence of a planet can be inferred by taking precise photometric measurements of a star. If a planet passes between the observer and the star, it will occult some of the light from its host star, producing a dip in the measured flux. This dip in flux is then used to infer the existence of a planet orbiting the star. The morphology of the dip is dependent on a number of factors including the ratio of the radius of the star and planet to the orbital separation of the two objects. This is shown schematically in Figure 1.4, the numbers 1 through to 4 indicate the ingress (1 and 2) and egress (3 and 4) of the planetary transit. From the schematic a second effect of transiting planets can also be seen. As the planet moves around its orbit more of the 'day side' of the planet can be seen. The additional reflected light from the planet can contribute to the overall luminosity of the star resulting in the total system appearing brighter. As the planet moves behind the host star a secondary eclipse can be observed as at this time only light from the star is seen. This effect is much smaller than the main transit event.

Of interest is to calculate the probability of a transit occurring. For randomly orientated orbits the probability of a transit is given by,

$$\Pr\left(\cos i < \frac{R_\star + R_p}{a}\right) = \frac{1}{2}\int_{-(R_\star+R_p)/a}^{(R_\star+R_p)/a} = \frac{R_\star + R_p}{a} \tag{1.4}$$

where $R_\star$ and $R_p$ are the stellar and planet radius, respectively, $a$ is the semi-major axis of the orbit, and $i$ is the inclination angle of the planet's orbit. In this case, the probability includes grazing transit geometries. For most cases it can be assumed that $R_\star >> R_p$ so the equation reduces to

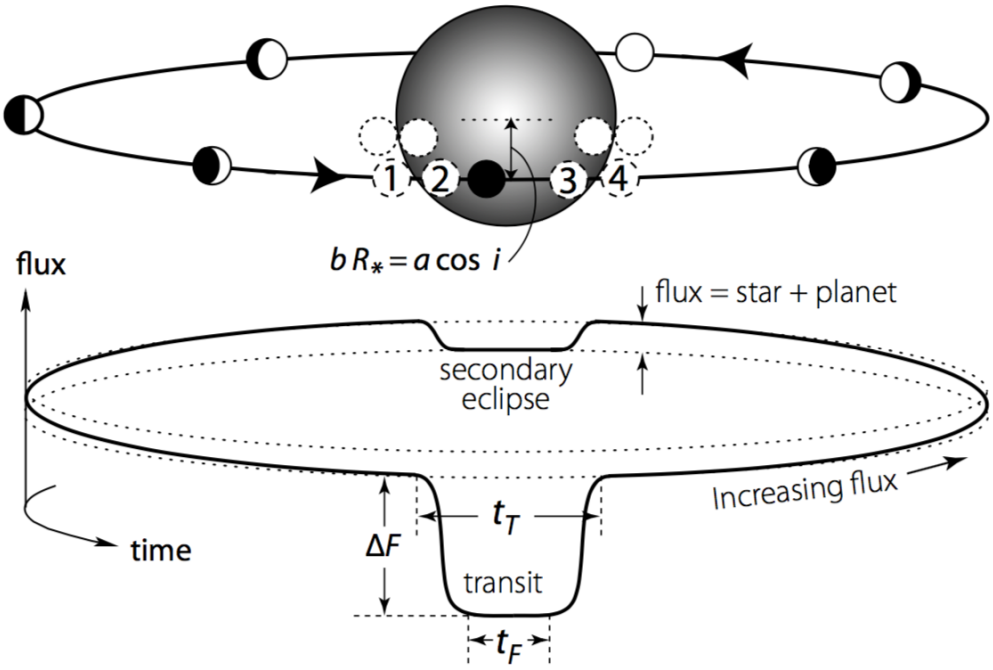


**Figure 1.4**: Representation of the the main features of a transiting planet with the top showing a schematic of the planet star system and the bottom giving a representive lightcurve – the main transit event is labeled as 1 through 4. A number of planet parameters are shown, indicating the impact parameter $b$, transit time $t_T$, full transt depth time $t_F$ and flux change $\Delta F$. Additional out of transit effects also are seen, where the amount of flux increases as more of the star lit side of the the planet is seen. This results in a smaller secondary eclipse as the planet moves behind the star and only starlight remains. Image taken from Perryman (2011).

$$\Pr\left(\cos i < \frac{R_\star}{a}\right) \cong \frac{R_\star}{a} = \left(\frac{R_\star}{R_\odot}\right)\left(\frac{R_\odot}{1au}\right)\left(\frac{1au}{a}\right) \tag{1.5}$$

with $R_\odot$ as the radius of the Sun. Substituting in the appropriate value for $R_\odot$ the equation reduces to

$$\Pr\left(\cos i < \frac{R_\star}{a}\right) = 0.0046\left(\frac{R_\star}{R_\odot}\right)\left(\frac{1au}{a}\right) \tag{1.6}$$

Thus, for an Earth-like planet the probability of observing a transit is only 0.46%, with this further reducing to 0.09% for Jupiter at 5.2 AU. The probability of seeing a transit is affected by the ratio of radius of the star and planet, where a larger planet radius increases the probability. The orbital separation is the other factor, with the probability of seeing a transit increasing as the orbital separation decreases. Equation 1.6 suggests that the transit method would target larger stars as this increases the probability, how-

ever, this equation does not take into consideration the depth of the transit. The depth of a transit can also be easily calculated where the observed decrease in flux, $\Delta F$, is proportional to the square of the ratio of the radii of the star, $R_\star$, and planet, $R_p$,

$$\Delta F = \left(\frac{R_p}{R_\star}\right)^2 \tag{1.7}$$

For the Jupiter-Sun system this corresponds to a depth of 1% and for the Earth-Sun system this is ~0.01%. Modern ground-based wide field transit surveys have an achievable photometric precision of ~ 0.1%. To find an Earth-sized planet from the ground (assuming a transit depth of 0.1%) would require the star to be ~0.03 $M_\odot$ (i.e. an M-dwarf). From this new constraint the transit method is then most sensitive to larger planets in close orbits around smaller stars. The transit gives the radius ratio of the star-planet system, and the orbital period can also be readily obtained by measuring the time between multiple transits. The orbital inclination of the system is already constrained by the nature of a transit but non edge-on orbits (i.e. inclination $\neq 90°$) are still possible due to the planet crossing the star at different latitudes. This is know as the impact factor, $b$, and is given by

$$b = \left(\frac{a\cos i}{R_\star}\right)\left(\frac{1-e^2}{1+e\sin\omega}\right) \tag{1.8}$$

where $\omega$ and $e$ are the argument of periastron and eccentricity, respectively. The impact factor can be seen in Figure 1.4 as the offset of the planet from the centre line of the star.

The first detection of a transiting exoplanet was HD209458 b found in 1999 (Charbonneau et al. 2000). Since then, the number of planets discovered by this method has grown massively and in 2014 it overtook RVs as the most successful detection technique, making up almost 75% of the 3737 planets discovered to date (over 2700 planets). This large number is mostly due to the space-based telescope Kepler, aided by the high photometric precision of the instrument. This is highlighted in Figure 1.5 where the two jumps in total number of detections at 2014 and 2016 can be attributed to planets detected by Kepler.

Measuring a transit-like dip in the light from a star cannot alone confirm a suspected candidate as being a bone-fide planet. There exists a number of other sources that can produce similar transit shaped light-curves. These false-positives include grazing eclipsing binaries, background eclipsing binaries, as well as brown dwarfs and main

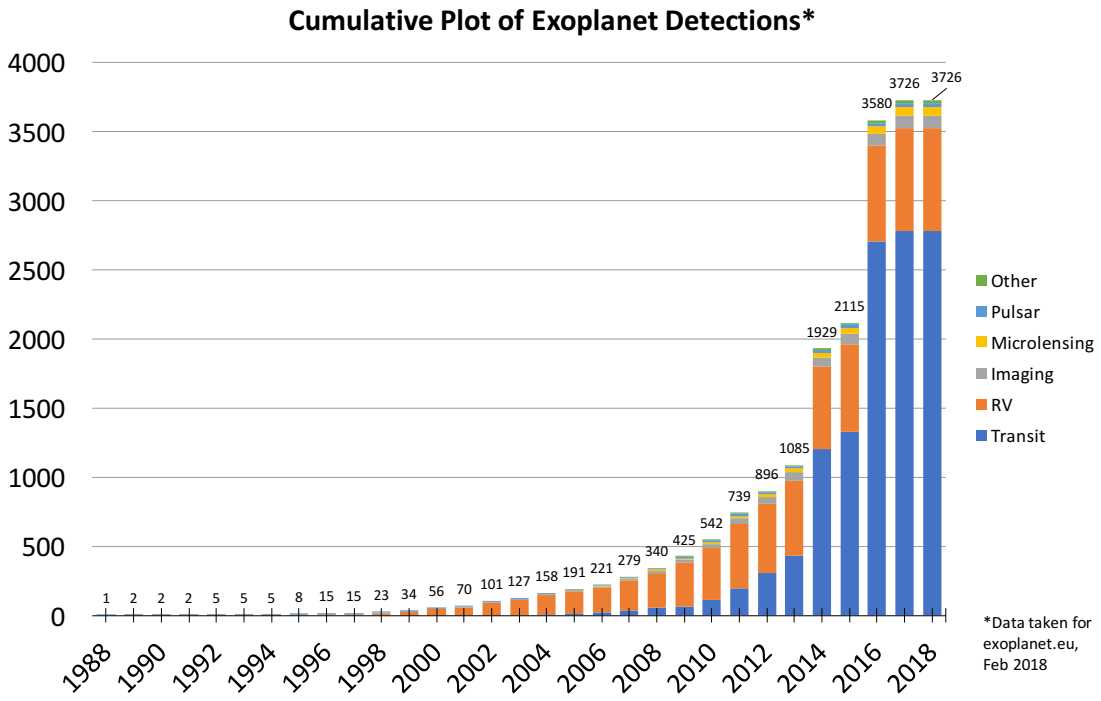


**Figure 1.5**: Cumulitive histogram of exoplanet discoveries broken down by year and detection method, above each bar is the total number of planets detected. Most methods show a steady increase in total planets detected with the expection being the transit method, which shows two large jumps due to data coming from the Kepler mission. Generated using data from exoplanet.eu.

sequence stars transiting red giant stars. Only by measuring the density of the eclipsing body can a candidate be confirmed as a real planet. For this reason, where possible, transit candidates are followed-up with radial velocity (RV) measurements (see Section 1.2.4) to obtain a planetary mass estimate. Transit information is beneficial to RV measurements since the orbital inclination degeneracy associated with RV measurements is removed when combined with transit observations allowing for the true mass of the planet to be measured and an estimate of the planet density. This allows the bulk density of the planet to be ascertained, which in turn places constraints on the planetary composition.

Not all transiting exoplanet candidates can be followed-up by RV measurements, this is either due to the low mass of the planet not producing a sizeable RV variation, or the host star being unsuitable for precise spectroscopic measurements (e.g. the host star is too faint or a fast rotator, or exhibits high levels of stellar activity – see Chapter 2). Planet candidates in this position can be vetted using statistical means, where a series of false positive scenarios are applied to the data through a process known as probabilistic validation. This relies on the principle of proving that all other astrophysical false positives have a negligible likelihood to cause the transit signal, leaving a planet as

**Figure 1.6**: Four of the 12 telescopes of the ground-based survey NGTS (Next Generation Transit Survey), aiming to fill in the gap in masses of planets by targeting the regime of Super-Earth up to Neptune-sized planets (10 - 30 $M_{\oplus}$). Image credit: ESO/ G. Lambert.

the only reasonable source (Borucki et al. 2012; Díaz et al. 2014; Morton et al. 2016). Planets that pass this vetting are referred to as *validated* and make up the bulk of the planets detected by the Kepler space telescope.

The relative ease of measuring transits compared to other methods has made small ground based telescopes a viable option for detecting them. The most successful of these is the Wide Angle Search for Planets (WASP), and its upgraded version SuperWASP. The telescope utilises off-the-shelf commercial camera components to perform wide field surveys of the sky and was able to detect over 170 planets. WASP is not unique, other small wide field surveys that have had good success include HAT (Hungarian-made Automated Telescope) and KELT (Kilodegree Extremely Little Telescope).

The success of these small telescopes have led the way for more dedicated instruments such as NGTS (Next Generation Transit Survey), the spiritual successor to the WASP project. Where WASP had 8 cameras on a single mount, NGTS has 12 robotised telescopes on individual mounts, with more sensitive detectors (see Figure 1.6). NGTS is specifically aiming for the discovery of smaller Super-Earth and Neptune sized planets orbiting relative bright ($V < 15$) stars (allowing for easier RV follow-up). Where most previous ground-based surveys aimed for large hot Jupiters and space-based mis-

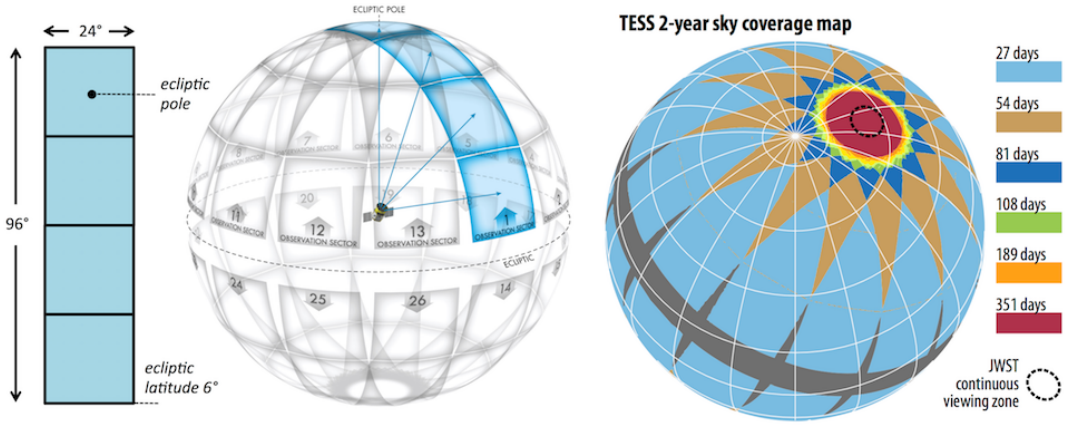


**Figure 1.7**: The field of view of TESS, with 4 cameras the telescope will images strips of the sky, with most parts of the sky getting a minimum of 27 days of cover. Image credit: NASA.

sions targeting smaller Earth-sized, rocky worlds, NGTS aims to fill in the gap and target the planets in-between these two regimes. As of writing one planet has been published (Bayliss et al. 2018), with simulations suggesting that approximately 231 Neptune- and 39 super-Earth-sized planets are expected over a four year baseline for the survey (Wheatley et al. 2013). More detail on NGTS will be given in Chapter 5.

The transit method is currently the top exoplanet detection technique, this is mostly due to the success of the Kepler mission (Borucki et al. 2010) in finding planets. Kepler has now moved into a new mode called K2 (owing to the loss of two of the four reaction wheels of the telescope), where it is still performing transit photometry but at a reduced precision. Other space missions include the recently launched TESS (Transiting Exoplanet Survey Satellite), which will survey the whole sky for transiting planets. TESS targets will be observed for a minimum of 27 days up to a maximum of 351 days (see Figure 1.7). In addition, the European led PLATO (PLAnetary Transit and Oscillations of stars) mission has the specific goal of finding Earth analog worlds around bright stars, allowing for RV follow-up, and is expected to launch in 2026. The consensus seems to be that transit photometry, by itself, is not enough to verify a planet candidate and that measuring the density of these candidates (through follow-up RV measurements) is necessary to claim the object as a planet. The relative observational expense of RV spectroscopy means that by using the two methods together (i.e. RV surveys primarily being used to follow-up 'good' transiting planet candidates), planet parameters can be more accurately measured, putting the more observationally expensive RV measurements to better use.

### 1.2.4 The Radial Velocity or 'Doppler wobble' Method

The Radial Velocity (RV) technique is a highly successful method for finding planets. The method is credited with finding 51 Peg b, the first exoplanet found around a main sequence star (Mayor & Queloz 1995) and is responsible for discovering over 700 planets since. The methods relies on the fact that in a gravitationally bound system (like a star-planet system) all bodies orbit a common barycentre of the system. If a planet exists around the star, its presence can be inferred by measuring the reflex motion of the star as it orbits around the barycentre. This motion causes a blue- and red-shifting of the light from the star as it moves towards and away from the observer, respectively. By measuring this 'wobble' around the barycentre (also referred to as a 'Doppler wobble') the existence of a planet can be inferred and a number of planet parameters can be defined – these parameters are complementary to those generated by transit detections of planets and so the two techniques are used together where possible (see Section 1.2.3).

The radial velocity of the star $v$ can be measured by making use of the Doppler equation,

$$v = c\left(\frac{\lambda - \lambda_0}{\lambda_0}\right) \tag{1.9}$$

where $c$ is the speed of light; $\lambda$ is the observed wavelength of the line and $\lambda_0$ is the expected position for the unshifted line (or its rest wavelength). The RV motion due to a planet is usually small, ranging from several 100 m s$^{-1}$ in the case of hot Jupiters down to a few $\sim$1 m s$^{-1}$ for super-Earth sized planets and $\sim$10 cm s$^{-1}$ for an Earth-analog. Instruments used for RV studies, like HARPS (the High Accuracy Radial velocity Planet Searcher), must be highly stabilised to be able to measure the Doppler wobble effect due to a planet. HARPS is one of the best instruments for RV studies but even with its high spectral resolution (resolving power $R = 115,000$) it still has an instrumental resolution of $\sim 2.4$km s$^{-1}$. To measure the RV Doppler wobble of the system, the stellar spectra are cross-correlated with a template spectrum line mask that closely resembles the star. The template has no radial velocity component (i.e. all lines lie at their correct rest wavelength, $\lambda_0$). By cross-correlating the star with this template a cross-correlation function (CCF) is generated with the offset of the peak of the CCF (in velocity-space) indicating the RV shift of the star. This process essentially sums the RV effect from thousands of spectral lines and can push the RV precision to $\sim$1 m s$^{-1}$ levels. Effects from the star itself in the form of activity can add noise to the measured RVs or produce signals that can mimic the variation induced by a planet (see chapter 2). These effects must be accounted for before the RV motion of a planet can be isolated.

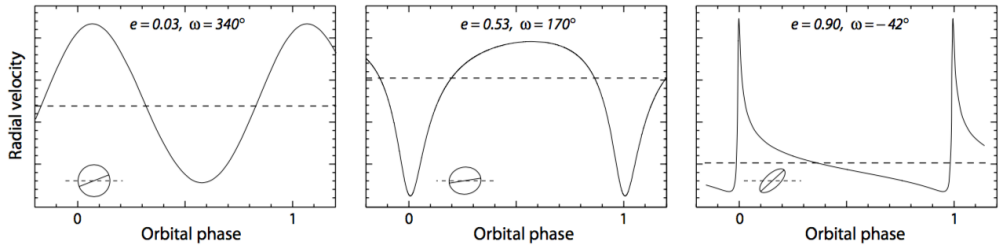


**Figure 1.8**: Radial velocity curve for the three planetary systems: HD 73256, HD 142022, and HD 4113 (going from left to right). These schematics show the dependency of each on eccentricity and argument of pericentre for the systems and the difficulties in finding more eccentric systems. The dashed line shows the systemic velocity and the ellipses at lower left show the geometric view of the system. Image: Perryman (2011)

Once an RV variation due to a planet signal has been identified, the mass of the planet can be measured. This information is encoded in the semi-amplitude $K_S$ of the RV signal given by the equation,

$$K_S = \left(\frac{2\pi G}{P}\right)^{\frac{1}{3}} \frac{M_p \sin i}{\left(M_\star + M_p\right)^{2/3}} (1-e)^{-1/2} \tag{1.10}$$

where $G$ is the gravitational constant, $P$ is the orbital period of the planet, $i$ is the inclination of the orbit, $e$ is the eccentricity of the orbit, and $M_\star$ and $M_p$ are the masses of the star and planet, respectively.

If the mass of the star is known (usually estimated from spectral analysis), then the minimum mass of the planet can be determined. Equation 1.10 shows that $K_S$ is proportional to the mass of the planet and inversely proportional to the orbital period, making the technique more sensitive to detecting hot Jupiters (like the transit method). The equation also shows that the planet mass is not given directly but rather a minimum mass is returned, with the mass dependent on the inclination of the planet's orbit. This can be greatly constrained using the transit method, and this is one of the reasons why the two methods are so closely aligned. For a circular orbit ($e = 0$) the RV motion is sinusoidal and easy to determine, for more eccentric orbits the shape of the RV motion can be radically different. Figure 1.8 shows example schematics of three planets with different eccentricities and arguments of pericentre. The low eccentricity planet has a RV that is easy to measure while the planet showing $e = 0.9$ has very few times during its orbital phase when an appreciable RV variation can be detected, which affects planet detectability of these highly eccentric planets.

The current flagship instrument for the study of exoplanets is HARPS – and its northern hemisphere twin HARPS-N. These instruments boast a long term RV precision of ∼0.5 m $s^{-1}$, allowing easy detection of hot Jupiters as well as pushing down to the regime of the (Super-)Earth-sized planets. The Earth analog (i.e. an Earth-sized planet orbiting at 1 AU around a Solar-like star) produces an RV variation of just ∼10 cm $s^{-1}$, placing it out of reach of current instrumentation. RV surveys preferentially aim for lower mass K dwarf stars where the RV variation of an Earth-sized planet will be larger. ESPRESSO (the Echelle SPectrograph for Rocky Exoplanet and Stable Spectroscopic Observations), is the next generation of high precision instruments and is aiming to detect RV variations at the ∼10 cm $s^{-1}$level. Seeing first light at the end of 2017, the instrument will take advantage of the larger light gathering area of the VLTs and will soon become the workhorse instrument for finding, and characterising, rocky, terrestrial worlds (Pepe et al. 2014).

HIRES is a proposed future instrument on the E-ELT (one of the next generation of large telescopes), aiming for a RV precision of just 1 cm $s^{-1}$. Both ESPRESSO and HIRES should be able to, technically, readily detect the signal of an Earth-sized planet but, even in the era of HARPS and HARPS-N, instrumental precision is no longer the limiting factor. Activity on the host star can act to mask or mimic planetary signals making the understanding of the surface of exoplanet host stars a vital component of any search for small planets (see Chapter 2 for more details of stellar activity and its effect on RV measurements).

### 1.2.5 Other Methods

A number of other methods are also used to detect planets, these methods have had less success and so will only be mentioned in passing. This is by no means an exhaustive list of all other detection methods but only serves to highlight a number of other techniques that can be applied.

#### 1.2.5.1 Timing

The first discovered exoplanets were found around the pulsar PSR B1258 + 12 (Wolszczan1992), where the presence of a planet caused a variation in the arrival time of the pulses. The existence of the planetary companion to the system led to a perturbation of the pulsars' position, causing a variation in the pulse arrival times. Eclipsing binary stars may also be probed for planets in a similar way. The existence of a planet around the binary could perturb the eclipse times, with variations in eclipse times used to indicate the presence of an unseen companion. One system to be measured in this way

is the post common-envelope binary NN Ser, where the difference in mid-eclipse time was shown to be due to two massive planets (6.9$M_J$ and 2.2$M_J$, respectively, Beuermann et al. 2010). The lack of planets found in this way is mostly due to the high mass of planet needed to produce a measurable variation, to date no planets have been found (using this method) around two main sequence FGK dwarf stars.

Another problem is the Applegate mechanism (Applegate 1992), whereby activity cycles on one (or more) of the stellar binary components causes the stellar quadrupole moment to change. Essentially, magnetic energy is converted to rotational energy (and vice versa) causing the shape of the star to change. In turn, this changes the tidal pull on the stellar companions, and leads to long-term quasi-periodic changes in the binary orbital period. This can then be mistaken for light travel time variations caused by an orbiting planet.

Planets found in stable orbits are very predictable, with the period of a transit being a constant. If, however, a second (non-transiting) planet orbits the star, the unseen planet can tug on the transiting planet and present an additional force acting on the orbit of the planet. By taking precise measurements of the times of a transit the existence of the unseen planet can be inferred by the variation in the transit times. Kepler-46c is one example of a planet discovered by this method, the use of Transit Timing Variations (TTVs) is a primary validation method for Kepler candidates in multi-planet systems. The large TTVs seen by the planet Kepler-46b ($\sim 6$ $M_J$) was modelled by a 0.37 $M_J$ perturber on a 5:3 resonance (Nesvorný et al. 2012). The TRAPPIST-1 system also made use of TTVs to constrain mass estimates (Gillon et al. 2017).

Finally, for planets with orbiting moons (so called exomoons), the presence of the moon around the planet can cause variations in the transit duration of a planet (Kipping 2009). These Transit Duration Variations (TDVs) are another way in which the timing of a transit can be precisely measured to probe deeper into the system.

#### 1.2.5.2 Astrometry

Astrometry is one of the oldest tools for astrophysical measurements. The technique measures the position of stars as they move across the sky and assigns a magnitude to the signal, the presence of a planet around that star will alter its motion (as both bodies orbit around the barycentre of the system). If a circular orbit is assumed, the astrometric signature, $\alpha$, is given by:

$$\alpha = \frac{M_p}{M_\star + M_p}\, a \simeq \frac{M_P}{M_\star}\, a \equiv \left(\frac{M_P}{M_\star}\right)\left(\frac{a}{1\mathrm{AU}}\right)\left(\frac{d}{1\mathrm{pc}}\right)^{-1} \mathrm{arcsec} \tag{1.11}$$

where $M_\star$ and $M_p$ are, as before, the star and planet masses, respectively, $a$ is the semi-major axis and $d$ is the distance of the system. The equation reduces to the form on the right under the assumption that $M_p \ll M_\star$. This makes astrometry more sensitive to planets on longer orbital periods but not as wide as planets found by direct imaging. The technique then becomes a useful bridge between the short period transiting and RV planet, and the long period imaged planets and is able to give information on the orbital period as well as the planet mass and orbital inclination.

To date, only one planet has been found using this method, the 1.5 $M_J$ HD 176051 b (Muterspaugh et al. 2010). The lack of planets is mostly due to instrument sensitivity limiting the detectability. The astrometric precision of ground based telescopes is of the order of milli-arcseconds (mas), in contrast the astrometric signature of the Jupiter-Sun system observed at a distance of 10 pc is only 500 $\mu$as, with the value dropping to 10 $\mu$as for Jupiter at a 1 AU orbit. It is hoped that the improved astrometry measurements from GAIA, having an astrometric precision of 20 $\mu$as, will be able to add to the number of planet detected astrometrically. Estimates put the total number of planet detections via GAIA astrometry at $21000 \pm 6000$ for the 5 year mission (Perryman et al. 2014). With the first data release from GAIA in 2016 and a second data release slated for 2018 it's just a matter of time before more planets are discovered by this method, potentially making astrometry a very successful planet finding technique.

## 1.3 Planet Formation and Migration

The detection of different exoplanet systems is aimed at exploring different planetary configurations in order to constrain planetary formation and evolution theories. Initial models of planet formation and migration used the Solar system as the prototypical star system, with small, rocky worlds interior to gaseous, giant planets. The variety of planetary systems now found, ranging from hot Jupiters on extremely short orbital periods (like the 1.09 day period of WASP-12b; Hebb et al. 2009) to planets on highly inclined orbits (e.g. WASP-121b in a polar orbit around it host star (Delrez et al. 2016), or the ultra short period Kepler 78b (Pepe et al. 2013) have forced a re-evaluation of the theories being used. The two main theories of planet formation are core accretion and disk instability, which are outlined below.

### 1.3.1 Core Accretion

Core accretion is a bottom-up scenario, where small grains clump together to form larger and larger bodies. It can be separated into two key stages. In the first stage, small dust grains left in the disk from star formation clump together to form km sized

planetesimals. In the second stage, these planetesimals are large enough to gravitationally influence their surroundings, with collisions leading to accretion of material (in the case of a dynamically cold scenario) in a runaway growth phase. This phase eventually slows as the growing bodies begin to perturb the planetesimal in their immediate vicinity, causing some to move towards other growing bodies rather than being accreted. At the end of this phase, a number of protoplanets exist that all grow at comparable rates. Simulations starting with a system of protoplanets and planetesimal (with similar mass contained in both the protoplanets and planetesimal) are able to form a plausible analog to the Solar system terrestrial planets (Chambers & Wetherill 1998; Raymond et al. 2009).

Beyond the snowline (the distance from a star where ices can start to form) growth rates are faster and planetary cores can readily reach masses in excess of $1M_{\oplus}$. Growth in this case is limited by a finite supply of planetesimal, with a preference for larger mass bodies at greater orbital radii. Once the mass of the planetary core is of the order of a few $M_{\oplus}$ it can bind a hydrostatic gas envelope, forming an ice giant planet. Above some critical mass, in the range of 5-$20M_{\oplus}$, disk gas can accrete more rapidly on the planetary core and form a gas giant planet. How the later stages of core accretion works depends on the mechanism for cooling the gas envelope (convection and radiative diffusion), this is dependent on the opacity of the envelope, which is poorly constrained (Rafikov 2006; Piso et al. 2015).

In addition to being able to model the interior rocky planets of the Solar system, core accretion has been able to successfully predict the core masses of Jupiter and Saturn and the heavy metal content of their envelopes (Alibert et al. 2005). Core accretion also predicts that a greater surface density of planetesimal leads to a faster core growth and an increased chance of reaching runaway prior to disk dispersal, which has been found to be consistent with the observed correlation between massive planet frequency and host star metallicity (Fischer & Valenti 2005). Most observed exoplanets have properties consistent with what would be expected from core accretion models.

### 1.3.2 Disk Instability

The alternative to the bottom-up scenario of core accretion is the top-down, gravitational disk instability model. The model is based on the premise that the gas disk, during part of its evolution, becomes gravitationally unstable, perturbing the disk. This perturbation causes clumping, which can grow to form the seed points of planet formation. The important parameter that controls the conditions for disk instability is called the Toomre parameter, $Q$

$$Q = \frac{c_s \Omega}{\pi G \Sigma} \tag{1.12}$$

where $G$ is the gravitational constant, $c_s$ is the speed of sound in the disk, $\Omega$ and $\Sigma$ are the angular velocity and the local surface density of the disk, respectively. A value of $Q > 1$ indicates that the disk is stable, and $Q \sim 1$ is the critical value that results in the (marginal) instability required for the disk instability scenario to occur. In a disk at 10 AU around a Solar mass star and a sound speed of $c_s \approx 0.5$ km s$^{-1}$ the surface density required for Q=1 is $\Sigma \sim 10^4$g cm$^2$. Even as an order of magnitude estimate, this is a factor of two greater than the predicted minimum mass solar nebula at the same distance, suggesting that the mechanism operates, if at all, preferentially at early epochs when the disk mass is still high.

Simulations by Boss (1997) seeded a disk with a bar-like density distribution and found that, while inner regions of the disk remained stable ($Q \gg 1$), the disk became unstable ($Q \sim 1$) at around 7.5 AU. The initial bar-like density distribution winds up into a two-armed spiral, where self-gravity overtakes thermal pressure forming two giant gaseous protoplanets, with masses of $1 - 8$M$_\mathrm{J}$.

Disk instability predicts large planets on wide orbits, which are the type of planetary systems found by direct imaging. HR8799, for example (see Figure 1.2), is a system where the wide orbiting planets hint that disk instability may have played a role in its formation (Dodson-Robinson et al. 2009). Most planets discovered, however, can be explained using the core accretion scenario but this does not rule out disk instability as a formation mechanism. Detection biases means that most exoplanets so far discovered orbit close to their host star, where disk instability would not be an effective means of planet formation. Core accretion is also not able to predict the close orbits of the hot Jupiters, indicating that some mechanism for migration is needed to explain these close in systems.

### 1.3.3 Planet Evolution and Migration

Both core accretion and disk instability fail to predict short period giant planets like the ones that make up the bulk of the detected exoplanets to date. Large gas and ice giant planets are thought to form beyond the snowline, where enough material exists that can be accreted to form these massive planets. Migration, the movement of planets from where they initially formed, is the mechanism used to explain these planets. Large Jupiter sized objects form further out and migrate in, either through interaction with the protoplanetary disk or other massive bodies (i.e. planet-planet or planet-star interactions). Migration theory can be broken into two main classes, which I now outline.

#### 1.3.3.1 Disk Interactions

Planets that form within a protoplanetary disk can further interact gravitationally with the disk giving rise to resonances. The (orbital) rotational frequency of a planet, $\Omega_p$, can be given by the Keplerian frequency

$$\Omega_p = \sqrt{\frac{GM_\star}{a^3}} \tag{1.13}$$

where $M_\star$ is the mass of the star and $a$ is the semi-major axis of the planet. This gives rise to two types of resonances, the first is the corotation resonance, which is a resonance that is found at the same orbital radius as the planet i.e.:

$$\Omega = \Omega_p \tag{1.14}$$

The second are the Lindblad resonances, which are found interior and exterior to the planet's orbital radius and, assuming a keplerian disk, are found at radii, $r_L$, given by:

$$r_L = a\left(\frac{m}{m \pm 1}\right)^{-\frac{2}{3}} \tag{1.15}$$

where $m$ is an integer. Thus a circular Keplerian disk has a single corotation resonance and a series of Lindblad resonances on either side of the planet that pile-up as they get close to the planet's orbital radius (see Figure 1.9). The combination of these resonances leads to a torque that in general causes inward migration (though outward migration is also possible given the correct initial conditions). This inward migration can be classified into one of two types.

**Type I migration:** Type I migration is thought to dominate for low mass planets that cannot clear out a gap in the protoplanetary disk. The planet's gravity causes spiral waves that exert a torque on the planet, with the inner spiral waves pushing the planet outward and the outer spiral waves pushing the planet inward. The balance of the forces in general favours the outer spiral waves, causing the planet to migrate inwards. The timescale for migration is rapid, with numerical calculations typically finding that migration occurs on timescales of $\sim 10^5$ yr, with larger planets migrating more rapidly (Tanaka et al. 2002).

This rapid migration presents a problem for planet formation theory, since the

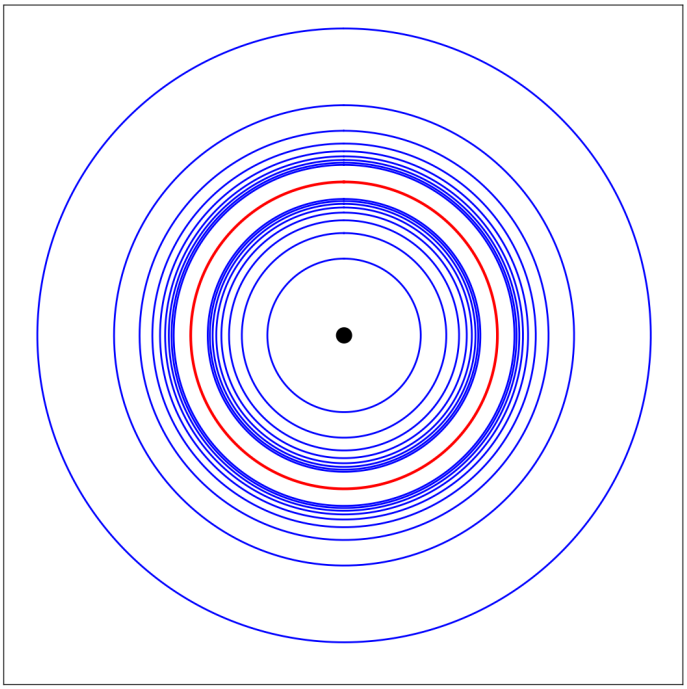

**Figure 1.9**: Schematic of the Lindblad resonances. The red line is the planet orbital radius, with the blue lines representing the Lindblad resonances. These can be seen to pile-up as they get closer to the planet. These resonances lead to a torque that can cause the planet to migrate.

timescale of migration is much shorter than the lifetime of the disk. This would suggest that migration during the early phase of protoplanetary formation would lead to the loss of developing planetary cores into the star. However, modelling of disks with turbulence has shown that, for small planets, the effectiveness of Type I migration at moving planets inward can be reduced, with the turbulence exerting random torques on the planet (Nelson & Papaloizou 2004; Uribe et al. 2011).

**Type II migration:** Where Type I is characterised by a planet embedded in the gas disk, Type II is the case where the massive planet is able to clear a gap in the disk. There are two requirements for a gap to open. First, the Hill sphere (the region in space where the gravity of the planet dominates) must be larger than the thickness of the gas disk. In terms of the planet-to-star ratio, $q = M_p/M_\star$, this can be written as:

$$q \geq \left(\frac{H}{a}\right)^3 \tag{1.16}$$

where $H$ is the thickness of the disk and $a$ is the semi-major axis of the planet. For typical protoplanetary disks, this implies that mass-ratios greater than $q \geq 10^{-4} - 10^{-3}$

are required to open a gap in the disk.

The second requirement for producing a gap is that the torque from the planet must exceed the viscous torque from the disk (otherwise any gap cleared would be replenished by the viscosity of the disk). This condition is found to have a similar value $q \geq 10^{-4}$. A Jupiter mass planet would easily be able to open a gap in the disk, while a Saturn mass planet is close to the boundary for gap-opening (for mass-ratios involving a Solar mass star).

Once the planet has grown massive enough to open a gap, torques from the gas resonance diminishes (representing a shift from Type I to Type II migration) and the planet evolves on the same timescale as the viscous time scale of the protoplanetary disk.

#### 1.3.3.2 Planet-Star or Planet-Planet Interactions

While most hot Jupiter exhibit relatively low eccentricity orbits, there are some planets with small semi-major axes and high eccentricities (Kane et al. 2012; Xie et al. 2016). One mechanism that can give rise to such high eccentricity systems involves the tidal influence of a third body in the system. The third body can excite periodic oscillations in both the eccentricity and inclination of the planet's orbit, shrinking the orbit via tidal dissipation. This mechanism is known as the Kozai effect (Kozai 1962; Lidov 1962).

For the mechanism to be effective the orbital separation of the planet and the host star must be significantly smaller than the orbit of the third interacting body – usually a star in a wide binary with the host star. The orbit of the binary must initially be inclined by at least $I = 39.2°$ relative to the planetary orbit. Under these conditions the binary can perturb the planetary orbit even when the perturbing body is at large distances ( $>$ 1000 AU) from the planet. The Kozai effect can lead to an exchange of angular momentum with the companion's orbit, resulting in large cyclic variations of the eccentricity and orbital inclination of the planet. The Kozai integral $L_K$ given by:

$$L_K = (1 - e^2)^{1/2} \cos I \tag{1.17}$$

is conserved during the process, which means that a maximum in eccentricity, $e$, occurs at a minimum in inclination, $I$, and vice versa. On its own, the Kozai effect is not able to modify the planet's semi-major axis, but it can induce large eccentricity variations that will bring the planet close to its host star. As a result, the tidal forces from the host star increase significantly during periods of close approach. Angular momentum is then

transferred from the planetary orbit to the star, driving inward migration of the planet that will then eventually have its orbit circularised at a new smaller semi-major axis. When the planet moves sufficiently close to its host star, forces from tidal interactions compensate for the Kozai effect and suppress any further eccentricity excitation. Tidal evolution then stops when the planet's orbit becomes circularised at this new, smaller, semi-major axis – resulting in a hot Jupiter.

Planet-planet scattering is another effect that can produce close in planets, where close encounters of giant planets results in angular momentum exchange between the two orbits. This may result in one planet losing angular momentum and moving to a shorter orbit. Both planet-planet scattering and the Kozai effect are expected to produce hot Jupiters in a range of orbital inclinations. These mis-aligned orbits can be measured by exploiting an effect known as the Rossiter-McLaughlin effect.

## 1.4 The Rossiter-McLaughlin Effect

The Rossiter-McLaughlin (RM) effect (Rossiter 1924; McLaughlin 1925) is a spectroscopic effect seen during transit. The effect is a Doppler shift, independent of the Doppler wobble of the planet (see Section 1.2.4) but due to the occultation of part of the rotating stellar surface. The rotating surface of a star can be broken into two halves, one that is rotating toward the observer (blueshifted) and one rotating away from the observer (redshifted) this causes the well known rotational broadening of spectral lines on the surface of star, with faster rotating stars having lines that are more broadened. When a planet passes in front of its host star it occults part of the surface causing a shift in the balance of the blue- and redshifted hemispheres of the star. For a planet in a prograde orbit, this would mean that the planet first eclipses the blueshifted hemisphere – resulting in a net redshift in the RV measurements – then, at some later time, eclipses the redshifted hemisphere – resulting in a net blueshift in the RVs.

The RV component of the light blocked by the planet as it traverses the stellar disc depends on the star's inclination, and the instantaneous position of the planet (in projection) on the star's disc. If the star's spin axis and the planet's orbital axis are aligned, the RV waveform is antisymmetric about the time of mid-transit, with the expected maximum amplitude occurring slightly after ingress and slightly before egress. For a non-zero impact parameter, $b$, this symmetry is broken and the resulting asymmetry depends on the angle between the stellar spin and the orbital angular momentum vector. A schematic example of the RM effect is shown in Figure 1.10, note that the RM effect is also sensitive to the direction of the orbit, with retrograde orbits showing a feature of the same magnitude but of opposite sign.

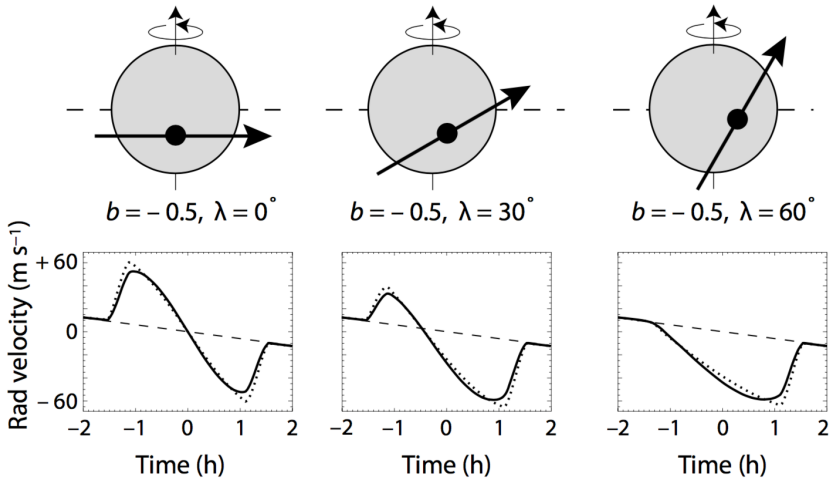


**Figure 1.10**: Three different RM profiles, dependent on the sky-projected spin-orbit alignment. The top panels show a schematic of the planetary orbit and stellar spin orientations, with the respective impact parameter, $b$, and sky-projected misalignment angle $\lambda$ indicated. The bottom panels show the expected RV variation due to the mis-alignment. The dotted line is the case for no limb-darkening of the star, with the solid line representing a stellar disc with a linear limb darkening law. Image credit: Perryman (2011).

The first planet reported to have a misaligned orbit was XO-3b (Hébrard et al. 2008), with an initial measurement of the spin-orbit alignment angle as $70° \pm 15°$ (this was later revised down to $37.3° \pm 3.0°$; Hirano et al. 2011). Since then a number of other planets have been found to have mis-aligned orbits, with some showing retrograde rotation and others having a polar orbit. Currently there are 92 known planets with published measurements of the RM effect[3].

Current evidence suggests a preference for mis-alignment of planet around hot stars, while cooler stars (with an effective temperature $T_{eff} < 6250K$) show planets that are preferentially aligned (e.g. Winn et al. 2010; Albrecht et al. 2012). The presence of a convective outer layer on these stars could be an explanation for this result. Tidal interactions between the hot Jupiter and convective outer layer may cause the star to realign itself with the planetary orbital momentum vector. Higher mass stars lack a convective outer envelope, and hence cannot realign themselves.

## 1.5 Structure of the Thesis

In this thesis I present a study of the effects of stellar activity on the spectroscopic and photometric measurements of exoplanets. The thesis will concentrate on analysing spectra from the HARPS instrument to investigate the effects that activity can have on

[3]catalogue: http://www.astro.keele.ac.uk/jkt/tepcat/tepcat.html

the spectral lines of exoplanet host star. Additionally, photometric variability due to stellar activity is investigated for data from the wide field survey NGTS. In this chapter I have outlined the background as to what defines a planet, the techniques used to detect and study them, and the theories of planet formation and migration.

In Chapter 2, I will give a more detailed account of what is meant by stellar activity, with a breakdown of the various types of activity. I will also highlight some of the methods that are used by the community to mitigate the effects of activity and push down the radial velocity precision to the regime of Earth-like planets. Chapter 3 is a detailed analysis of the effects of activity on the spectra for $\alpha$ Centauri B, with Chapter 4 being an analogous analysis but for the Sun (using data from the HARPS-N Solar telescope). Chapter 5 will detail methods I employ to determine the rotation period of exoplanet host stars from photometry, with a number of NGTS targets being analysed for detectable rotation periods. Finally, in Chapter 6 I will summarise the main conclusions of my work and highlight the various directions of future work.

*Chapter 2*

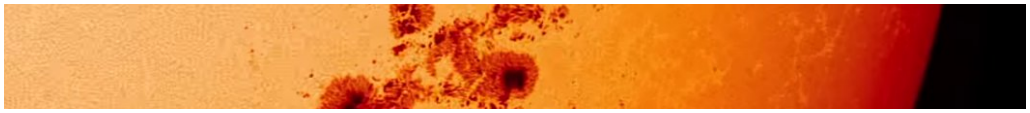

# Astrophysical Noise Sources and Removal Methods

## 2.1 Introduction

Chapter 1 showed that there are detection biases in the various exoplanet detection techniques that are dependent on the method of detection or the instrument used. Even if these limitations did not exist, features inherent to the star itself can add noise that affect the detectability of exoplanets. The outer layers of main sequence FGK stars can exhibit features (e.g. spots and faculae) caused by the interaction of these layers with the magnetic field, or by the convective motions of material in these layers (e.g. granulation). Understanding how these features manifest themselves on stars other than the Sun can help gain a better insight into the surface properties and evolution of stars. However, within the field of exoplanets, this activity is considered a source of noise that must be removed to reveal the worlds that lie beneath.

In this thesis the terms stellar activity, astrophysical noise and stellar jitter will be used interchangeably but in essence all refer to signals inherent to the host star that can mask or mimic the signal of an exoplanet. Stellar activity can affect each detection method differently but this thesis will concentrate on mitigation of astrophysical noise in RV measurements. With the push towards identifying true Earth analogs (i.e. a planet of Earth mass, on an Earth-like orbit, around a Sun-like star), the RV method is seen as the best tool suited to identify these worlds. Understanding and removing stellar activity from RV measurement is essential both for current and next generation planet detecting echelle spectrographs. As an example, Figure 2.1 shows the comparative strengths of the RV measurements of the Sun, measured during the approach to its cycle activity minimum (data from the HARPS-N Solar telescope), and the RV variations induced by the Earth during the same period.

A number of proposed planet detections have, on deeper analysis, been shown to be due to stellar activity. For example HD 166435, HD 219542 B, TW Hya, BD +20 1790 and $\alpha$ Cen B, all have RV variation initially attributed to a planet but have later been found to be either a result of activity or a spurious signal added by the techniques used to help mitigate the activity signal (Queloz et al. 2001; Desidera et al. 2004; Huélamo et al. 2008; Figueira et al. 2010; Rajpaul et al. 2016a). Although certain stellar activity features can mimic planetary signals, it is more likely to obscure the RV variation due to planets. The RV motion of a low mass planet can be completely dwarfed by the effects of stellar activity (Meunier et al. 2010), with the effect made worse for planets with orbital periods close to the rotation period of the star (e.g. Boisse et al. 2011). Table 2.1 lists a range of planet masses and orbital separations, giving a sense of scale for various 'standard' exoplanets. These values have been calculated assuming the planet is in a circular orbit around a $1M_{\odot}$ star. Comparing these values to typical stellar jitter

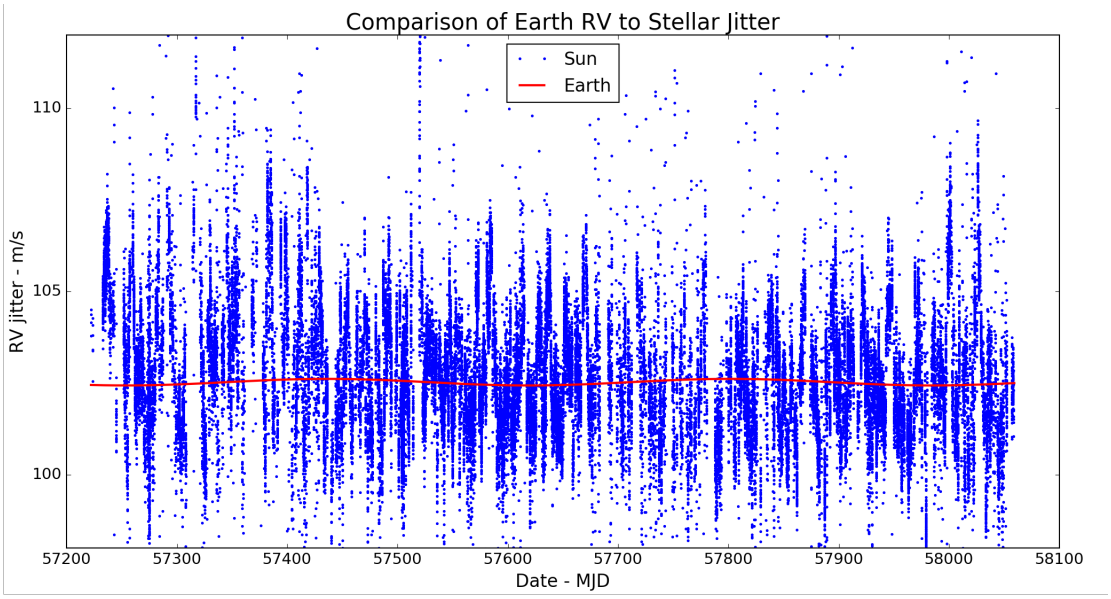


**Figure 2.1**: Comparison of the RV variation due to solar activity (shown as blue points) compared to the RV variation induced by the Earth (red line). This solar RV data was taken from the HARPS-N Solar telescope, with Earth RV variations calculated using the JPL HORIZONS system. Note this data was taken on approach to the minimum in the solar cycle, with relatively few active regions recorded during this period.

variations, which can be of the order of a few 100 m $s^{-1}$ for a highly active star to $\sim$ 1 m $s^{-1}$ for quiet stars, shows the impact that activity can have on exoplanet detections.

As instrumental precision increases, stellar activity becomes the limiting factor in finding these worlds. A common saying by the community is 'know thy star, know thy planet' as so much of what is known about a planet relies on accurate measurements of the properties of the host star. For this reason the understanding and removal of the effects of activity has become critical with the push towards Earth analogs. In this Chapter I will highlight the main features of stellar activity and the techniques employed by the community to mitigate their effects.

## 2.2 Formation of Spectral lines

Prior to any discussion on the effects that activity has to spectral lines it is instructive to first lay out the basics of how spectral lines are formed in a star. At its most basic, as photons escape from the inner layers of a star they pass through a medium that is affected by absorption, emission, and scattering processes. The total sum of all of these events (at a specific wavelength) as the radiation propagates through the medium then determines the specific intensity of the photon field as it leaves the medium. These interaction are described by the equations of radiative transfer. A full radiative transfer

| Planet | Separation (AU) | RV semi-amplitude ($ms^{-1}$) |
|---|---|---|
| Jupiter (1 $M_J$) | 1.0 | 28.4 |
| Jupiter(1 $M_J$) | 0.1 | 89.8 |
| Neptune ($\sim$ 17 $M_\oplus$) | 1.0 | 1.5 |
| Neptune ($\sim$ 17 $M_\oplus$) | 0.1 | 4.8 |
| Super-Earth (10 $M_\oplus$) | 1.0 | 0.9 |
| Super-Earth (10 $M_\oplus$) | 0.1 | 2.8 |
| Earth (1 $M_\oplus$) | 1.0 | 0.09 |
| Earth (1 $M_\oplus$) | 0.1 | 0.3 |

**Table 2.1**: The expected RV variation of various 'standard' planets at two distances from their host star (a $1M_\odot$ star) The typical signals of stellar activity can be of the order of $1 - 100$m $s^{-1}$, which would mask the smaller planets.

approach is beyond the scope of this thesis (with several books written on the matter e.g. Mihalas 1978; Gray 2008, for detailed derivations and discussion) but the principles that it lays down are fundamental to aid in the understanding of the formation of spectral absorption lines and in interpreting changes found to the shape or strength of these lines.

As a start consider an intensity of light $I_\lambda$ moving through an absorbing gas of small thickness $ds$. The change in the specific intensity $dI_\lambda$ can be written mathematically as

$$dI_\lambda = -\kappa_\lambda \rho I_\lambda ds \tag{2.1}$$

where $\rho$ is the density of the gas, and $\kappa_\lambda$ is the absorption coefficient. This $\kappa_\lambda$ can also be thought of as an opacity term and together with the density also defines the inverse of the mean free path that a photon can travel. We can also define a quantity called the optical depth $\tau_\lambda$ where

$$\tau_\lambda = \int_0^s \kappa_\lambda \rho ds \tag{2.2}$$

This can be defined such that the surface of the star is at $s = 0$. The optical depth can be thought of as the number of mean free paths that the photon needs to travel from its position in the stellar interior to the surface. Integrating over Equation 2.2 and using the definition of Equation 2.1 gives

$$I_\lambda = I_{\lambda,0}\, e^{-\tau_\lambda} \tag{2.3}$$

this is the simple extinction law and is the simplest example of the radiative transfer equation and its solution. From it we can define a gas as optically thick if $\tau_\lambda \gg 1$ and optically thin if $\tau_\lambda \ll 1$. Note that although this equation looks simple it is really dependent on a good determination of $\tau_\lambda$, which in itself can be a complex function taking into account changes in temperature, pressure, density and chemical composition through the column of gas considered. A more full treatment of the gas including the effects of emission within the gas results in

$$\cos\theta \frac{dI_\lambda}{d\tau_\lambda} = I_\lambda - S_\lambda \tag{2.4}$$

where $S_\lambda$ defines the source function, which is the ratio of emission to absorption events and better reveals the true complexities of radiative transfer. The $\cos\theta$ on the left side of the equation takes into account the geometry of the system (i.e. the case where the observer is no longer placed normal to the defined coordinates of the system). Equation 2.3, however, can still be instructive in understanding the formation of absorption lines in a star but with the knowledge now that any real system will be more complex than that considered here.

### 2.2.1 Types of Absorption

The absorption coefficient, then, is made up from a number of physical processes these are highlighted below.

**Bound-bound absorption** This is the case of a photon being absorbed by an atom and causing an electron to move between energy states. It is the source of absorption (or emission) lines at discrete wavelengths with the spectrum.

**Bound-free absorption** The case of photo-ionisation, where the electron is disassociated from its parent atom. This occurs as long as the absorbed photon has energy greater than the ionisation potential of the electron, any excess energy is taken by the escaping electron as kinetic energy adding to the heating of the gas. Here we can say that some of the energy of the photon is put into ionisation while the rest of the energy is thermalised. This type of absorption occurs over a range of wavelength (owing to the range of energy excess that the electron may have after the photon is absorbed) and changes the global shape, or continuum level, of the stellar spectrum. This is determined by temperature alone (and under the assumption of local thermodynamic equilibrium it is the Planck function) making bound-free interactions a source of continuum opacity.

**Free-free absorption** Free-free absorption occurs when a electron come in close contact with an atom, if a photon is absorbed during this interaction the electron (and ion) speed up and the energy of the photon is again thermalised, which also makes these interaction a source of continuum opacity. The opposite is the familiar case of bremsstrahlung (or "breaking radiation") where the interaction of an electron with the electric field of an ion causes it to decelerated and emit a photon.

**Electron scattering** This is the scattering of photons by free electrons. This cross section of this scattering process is independent of wavelength so also adds to the continuum opacity. This process relays on a high density of free electrons only having a significant effect when the gas is almost fully ionised i.e. it is only an effective source of absorption for the hottest stars.

### 2.2.2 Broadening of Spectral Lines

From this, the basics of spectral absorption line formation can be seen. The line in question is formed when an atom/ion (e.g. Hydrogen) has an electron that moves from a lower energy level to a higher by absorbing an incident photon. However from the discussion so far it is clear that only a single discrete wavelength of light is absorbed but from real spectra we see that lines have a characteristic width to them, which suggest that other physics are at play in line formation. These are know as line broadening effects and below I explore the major elements involved.

**Nature broadening** From the Heisenberg Uncertainty Principle, each atomic energy levels does not have a discrete energy but instead shows a spread in energy $\Delta E$, which is related to the time, $\Delta t$, the electron spends in the energy level by $\Delta E = \hbar/\Delta t$ (where $\hbar$ is the reduced Planck constant). The shape of spectral lines from this uncertainty can be solved by invoking the analogous mechanical system of a damped driven harmonic oscillator. Solving this leads to a Lorentz profile for the natural line broadening, which takes the form

$$L(x) = \frac{1}{\pi} \frac{Y}{(x - x_0)^2 + Y^2} \tag{2.5}$$

where $Y$ is a scaling parameter that dictates the height and width of the function. In the case of natural broadening this would be related to the number of electron entering and leaving an atomic state, which is called the damping constant. $\frac{1}{\pi}$ is a normalisation factor and $x_0$ defines is the centre of the peak, for absorption lines this can be either

the frequency or wavelength (given the correct constants are added to the normalisation factor). Of importance for Lorentz profiles is the longer wings formed compared to Gaussian profiles because of the inverse square relation. Natural broadening is very small but it is independent of wavelength and can have a larger impact in the other layers of the stellar atmosphere where densities are low.

**Pressure broadening** In the dense atmosphere of stars the atoms and ions can interact, either directly by collisions or indirectly by the electric field of the ion (the Stark effect) to perturb the electronic energy levels. As this is dependent on the distance of particles it is related to the pressure of the atmosphere and is termed Pressure broadening. Full Pressure broadening is a complex undertaking but as a simple example take collisional de-excitation. Here the lifetime an electron spends in an atomic energy level is shorten by collisions, this implies an increase in the energy spread of that state as $\Delta E = \hbar/\Delta t$ still needs to be satisfied. This is just one simple example with other effects such as linear and quadratic Stark, Van der Waals or resonance effects also needing to be considered for a more full approach to the effects of pressure broadening. Pressure broadening, like natural broadening, produces a Lorentz profile and, since this depends on the density of the gas, spectral lines in dwarf stars tend to be wider than those of giant stars.

**Thermal broadening** The atoms of the stellar atmosphere are not at rest but instead show random motions that depend on the temperature of the gas. This motion follows a standard Maxwellian distribution of velocities, which takes the form of a Gaussian. Thermal broadening is then caused by the movement of the atoms, with atoms moving toward the observer absorbing blueshifted photons, while those atoms moving away will absorb redshifted photons. This thermal broadening follows a Gaussian profile (like the Maxwellian distribution that underlies it) and is dependent on the temperature of the gas.

**Turbulent broadening** Where Thermal broadening is the movement of individual atoms, Turbulent broadening is the bulk movement of material (for example granulations – see Section 2.3.1). This motion can depend on the location on the stellar disk and the broadening of the spectral lines can be approximated by a Gaussian profile.

These four effects can be brought together into one function to define a spectral line shape. This is a Voigt profile, which is the convolution of a Lorentz profile and Gaussian profile. The Lorentz defines the effects of natural and pressure broadening and affects the wings on the line more, while the Gaussian represents the Doppler broadening from

thermal and turbulent effects and has a greater effect at the line core. With this we are now equipped to look at how a spectral absorption line forms.

Stellar absorption lines are the result of the light intensity at a specific wavelength being reduced by the effects of bound-bound absorption. At or close to the central wavelength the optical depth is larger, this means that the cores of spectral lines come from the upper regions of the stellar atmosphere as mean free path of photons is short and only photons close to the surface are not absorbed or scattered away. Moving away from this central wavelength, the effects of Doppler broadening of the line become more pronounced and the mean free path of photons becomes larger. This is because there are fewer atoms at this velocity compared to the mean velocity of the gas and in effect decreases optical depth as the density of particles is lower. As a result the mean free path of the photons is longer and we see deeper into the atmosphere of the star. As we move even further from the central wavelength the wings of the line take on a inverse square relation owing to the Lorentz profile shape of pressure (and natural) broadening to the spectral line. Another feature sometimes seen in spectral lines is core re-emission (see for example the Ca II H & K lines in Figure 2.7), this is due to an increase in the source function (a measure of the ratio of emission to absorption events) compared to the layers slightly deeper (in the case of the Ca II H & K this means that the source function in the chromosphere is higher than that of the photosphere).

This is of course a very simple understanding of the physics involved in calculating the spectral line, for example in we didn't consider the effects of stellar rotation or Zeeman splitting and the hyperfine structure in broadening of the spectral line. In addition, this discussion of the fundamentals of radiative transfer tried, where possible, to avoid the maths of the problem (which are both extensive and complex) and concentrated more on the concepts involved. In the next sections of this chapter I look at the various types of activity and how they can alter the shape of spectral lines. It is hoped that the above gives a good sense of what is involved in the creation of a spectral line, which will help in understanding some of the results shown in this thesis.

## 2.3 Astrophysical Noise (Non-activity related)

There are various type of activity that can be seen to affect the methods used to detect exoplanets, these can be broadly broken into magnetic and non-magnetic features. Here I will discuss the major non-magnetic related jitter terms, namely granulation and stellar oscillations, highlighting the effect each has on the RV measurements of exoplanets. This type of astrophysical noise exists even when no magnetic-field related activity is present on the star, and can act to add random variations to the measurements, hiding planets beneath the noise.

### 2.3.1 Granulation

Due to the convective nature of the outer layers of main sequence FGK (and M) stars, even with no magnetic active regions (discussed later in Sections 2.4.2 and 2.4.3) on the surface of a star, there still exists an intrinsic RV jitter. This is due to surface magneto-convective motions known as granulation. Consider a bubble of plasma in the convective zone, if this is hotter than the surrounding material it will rise. As it rises it will expand due to buoyancy forces and keep rising until it reaches the stellar surface. Once at the surface the bubble of plasma will be able to lose some heat by radiating photons away. The temperature can drop low enough to cause hydrogen ions to re-combine with the electrons to become neutral, releasing ionisation energy as photons. This causes the region to become over-dense and so the bubble sinks back down. The upwards moving regions are known as granules and the downward moving regions are called intergranular lanes. Granulation has a corrugated nature, with the granules forming high plateaus, while the intergranular lanes form lower down in the 'valley' of the corrugation. Examples of granulation are visible in both Figure 2.4 and 2.6, forming the background structure in the images (the solar surface is covered by approximately $10^6$ granules).

For the Sun, typical granules have a diameter of 1 Mm, and have a lifetime of $5-10$ minutes. This scales with the height of the convective zone with a larger convection layer producing larger, longer lived, granules. The granules on the Sun have a typical vertical upward velocity of $2-4$ km s$^{-1}$, while the intergranular lanes (which make up a smaller portion of the solar surface) have a higher downward velocity. This is due to conservation of mass and the geometry of the granulation, where the large slowly upward moving material of the granules must flow more quickly through the smaller intergranular lanes. This geometry also dictates the overall RV jitter due to granulation, with the contribution from granules dominating over that of intergranular lanes. The result is a net blueshift of the surface of the Sun, often referred to as convective blueshift.

Convective blueshift is dynamic, it changes as different granules evolve on the stellar surface producing varying RV signals. Unlike spots and plage, which rotate across the visible stellar hemisphere and can be confused with a planet, granulation is seen across the entire surface and adds noise to the RV measurements. Although the individual convective motions velocity can be of the order of $2-4$km s$^{-1}$, averaging the effects of the upward rising granules and down flowing intergranular lanes over the $\sim 10^6$ granules of the solar surface mostly cancels out the RV shifts. However, there still remains an RV jitter that is of the order of $\sim$1 m s$^{-1}$(Schrijver & Zwaan 2000). Comparing this to the RV signal of Earth (0.09 m s$^{-1}$) it is easy to see that even in a

star without any active regions, granulation, if not corrected for, makes it impossible to find low mass planets.

### 2.3.2 Oscillations

The turbulent motion of the convective layers in a star can generate acoustic waves that interfere with one another resulting in resonant modes being established. This can cause the star to expand and contract as the acoustic waves move towards and away from the stellar surface, generating stellar oscillations. The dominant restoring force that can produce stellar oscillations is pressure (Broomhall et al. 2009, and references therein). So called p-modes can cause a Doppler shifting of the light from a star as different portions expand and contract causing blue- and red-shifting of the light (see Figure 2.2). Other than the Sun, stars are point sources so the effects of oscillations averages across the stellar disk, resulting in only low degree p-modes showing any effect and higher degree modes cancelling out. The RV variation from oscillations can range from $0.1 - 4$ m s$^{-1}$ depending on spectral type and evolutionary state (Schrijver & Zwaan 2000) – for solar-type stars this is reduced to $0.1$ – $0.5$ m s$^{-1}$ (Mayor et al. 2003).

Timescales for these oscillations are of the order of minutes up to half an hour, and in the Sun p-modes are responsible for the well-known '5-minute' oscillation. The timescales of stellar oscillations are far shorter than the expected period of an exoplanet but oscillations, like granulation, add noise to measurements, making it more difficult to detect small mass planets. Most stars will show some level of stellar oscillations, making understanding and removal of its effect as important as granulation.

## 2.4 Astrophysical Noise (Activity related)

The magnetic field that can exist in stars acts to further impede the detection of planets: the interaction of the magnetic field with the outer convective layer of stars can produce surface inhomogeneities that can show variations similar to the signals expected from a planet. Here I will give a brief outline of the stellar dynamo before discussing the two main manifestations of magnetic activity: spots and plage.

### 2.4.1 Stellar Dynamo

Starspots and plage/faculae are both manifestations of the magnetic activity of a host star and are a by-product by a magnetohydrodynamical stellar dynamo i.e. the interac-

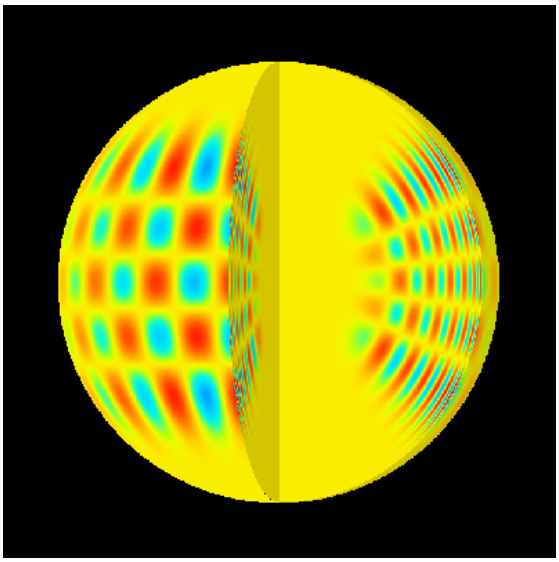

**Figure 2.2**: Illustration of the pressure (or p) modes present in stellar oscillations. The colours represent the movement of different portions of the stellar surface with the blue sections expanding outward (blueshifted) and the red sections contracting inward (redshifted). Image credit: http://soi.stanford.edu/results/heliowhat.html.

tion of the plasma of the star with its magnetic field. Even in the case of the Sun the exact mechanism for the production of this magnetic field is not known, but the most accepted theory is the $\alpha\Omega$ (or flux transport) dynamo (Choudhuri 2007).

The process relies on differential rotation between a radiative core and a convective outer envelope, and thus is only valid for low mass stars. The initial formation of the magnetic field of a star is believed to result from the magnetic field that existed during the initial star formation. Low mass stars, however, do not rotate as solid bodies but show differential rotation on their surface (e.g. the angular velocity at the equator of the Sun is ~20% faster than at the poles). Magnetic field lines within the plasma are 'frozen' in place, a mechanism known as flux freezing, and causes the field lines to move with the plasma. Because of this flux freezing the differential rotation causes a stretching and winding of the magnetic field lines of the star, changing the poloidal field into a toroidal field (i.e. from a north-south direction to the direction of rotation of the star). The strongest toroidal fields are generated in regions with the strongest differential rotation, this region is known as the tachocline and is the interface between the bottom of the convective zone and the radiative interior.

From numerical modelling of the interaction of magnetic field with convection in plasma it has been shown that, rather than causing a uniform distribution of field lines within the plasma, two regions form (Choudhuri 2007). One where convection dominates and magnetic field lines are excluded, and one with a concentrated bundle of field lines, known as a flux tube. The flux tubes align with the toroidal field and have a mag-

netic buoyancy, causing them to rise to the surface. If the flux tubes break the surface of the star they may produce 2 spots, each having the opposite magnetic polarity – these are known as bipolar spots. The toroidal field is then transformed back into a poloidal field but the exact process for this is still an open question.

One approach to understanding this process considers the effect of the hot rising convective cells that rotate as they rise, due to the Coriolis force. This twists the toroidal flux tubes, frozen in the plasma, and creates loops in the poloidal plane. Many of these small scale cyclonic turbulent motions form throughout the convective zone, which diffuse the small scale loops into a poloidal field (Parker 1993; Choudhuri 2007). This solution assumes that the toroidal magnetic field lines can be twisted by the convective motions but magnetic tension would resist such a movement. Additionally, the mechanism would not be able to twist a toroidal field as strong as the one generated at the tachocline ($\sim 10^5$G) back into a poloidal field (Choudhuri 2007). The more likely scenario makes use of the Babcock-Leighton mechanism (Babcock 1961; Leighton 1969), where the bipolar spots (produced by the buoyant magnetic flux tubes breaking the surface) have a tilt defined by Joy's law – with one spot located closer to the stellar equator than the other. This results in each spot diffusing its polarity at different latitudes on the stellar surface, giving rise to the formation of a poloidal field at the surface. The field lines then migrate towards the poles by meridional circulation after which they flow to the tachocline as a poloidal field and restart the cycle. This sets up the cycle of the solar dynamo with poloidal fields being twisted into toroidal fields by differential rotation and the toroidal field being changed back into poloidal fields either by Coriolis force effects or the Babcock-Leighton mechanism. Figure 2.3 schematically shows the main processes involved in both processes.

### 2.4.2 Spots

The stellar dynamo requires bipolar spots in order to effectively change the field direction. The generation of these spots is due to the interaction of the magnetic field with the outer convective layer of the Sun. As mentioned earlier, flux tubes are concentrations of magnetic field lines, the magnetic tension in these lines acts to suppress convection, which in turn leads to reduced heat transport. Flux tubes also have a magnetic buoyancy that cause parts to rise to the surface, while other parts stay anchored to the bottom of the convective zone. This leads to a 'horseshoe' shape to the flux tube as it penetrates the surface and, in turn, produces the bipolar spots (see (h) of Figure 2.3). Spots have a central dark region known as the umbra, which is surrounded by a filament-like structure called the penumbra. Spots are darker due to the reduced heat transport in the

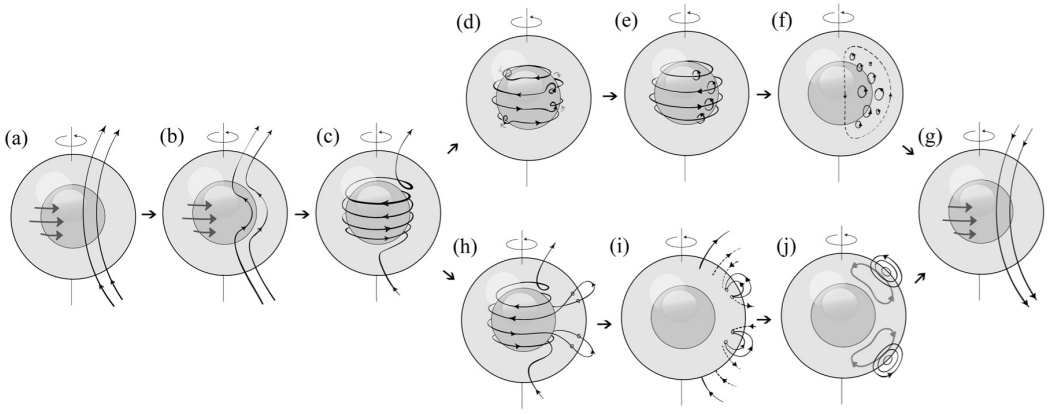


**Figure 2.3**: Schematic of the main processes of what is thought to be the solar dynamo. (a) the initial poloidal field. (b) and (c) generation of the toroidal field by differential rotation. (d) and (e) cyclonic turbulence generated by the Coriolis effect forming magnetic field loops in the poloidal plane. (f) diffusion of poloidal loops into a large scale poloidal field and the restoration of the poloidal field (g). (h) is the beginning of the Babcock-Leighton mechanism with buoyant magnetic field lines rising to the surface forming tilted bipolar spots. (i) diffusion of the magnetic field at the surface, with the resulting poloidal flux being advected by meridional circulation to the poles (j), resulting in the restoration of the poloidal field (g). Image credit: Sanchez et al. (2013).

flux tubes making the spots cooler than the surrounding photosphere (typically ~2000 K for the Sun). Figure 2.4 shows an example of a sunspot. The whole spot also sits slightly lower on the surface due to the magnetic pressure in the spot lowering the gas pressure as well as the temperature, this is known as the Wilson depression. The size and lifespan of a spot is tied to the strength of the magnetic field, with stronger fields resulting in longer lasting spots but typical lifetimes are of the order of hours to weeks (in the case of Sun) with most spots lasting a stellar rotation (Bradshaw & Hartigan 2014).

Spots exist on the surface of stars with convective outer envelopes and as such (nearly) co-rotate with the stellar surface. As spots are cooler and darker than the surrounding photosphere their presence reduces the overall luminosity of the star resulting in a variation in the photometric brightness of the star as the spot rotates in and out of view. The presence of spots impact on the accuracy of transit measurements, where out-of-transit spots can affect the transit depth by lowering the stellar luminosity, while in-transit spots can produce emission bumps also affecting the precision of transit measurements. With spectroscopic measurements, spots causes an 'emission bump' in the spectral lines. The position of the bump within the line relates to the position of the spot on the stellar surface, moving from the blue- to the red-wing of the line as the spot moves across the stellar surface. For rapidly rotating stars the emission bump of the

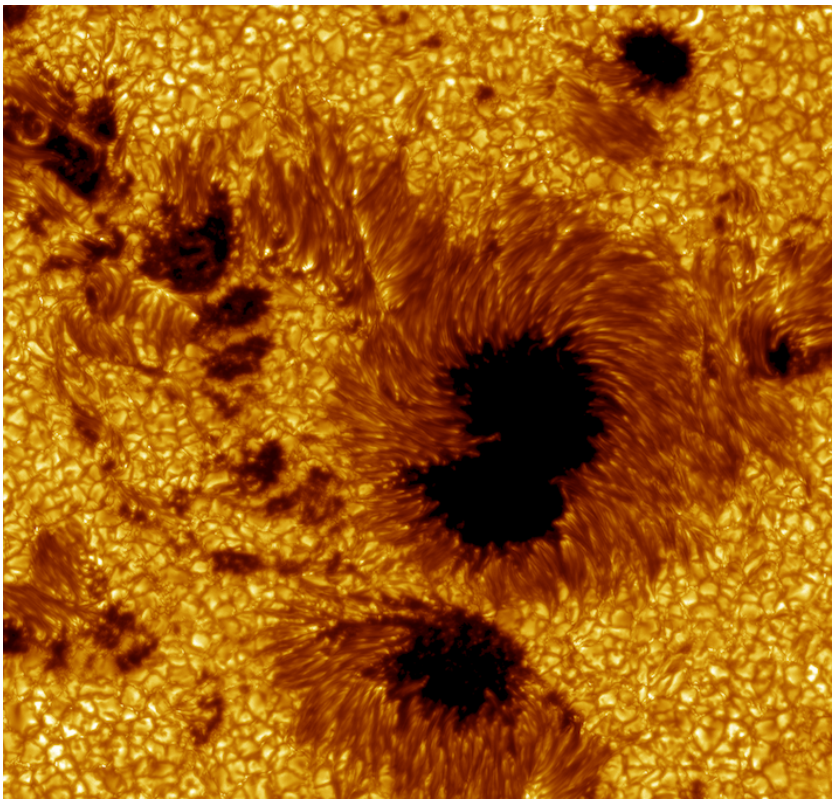

**Figure 2.4**: Example of a bipolar sunspot. The false colour image shows the dark area at the centre, known as the umbra, and the surrounding filament-like structure of the penumbra. This particular sunspot is approximately 10 Mm in diameter. Image Credit: Göran Scharmer/SST.

spot can be observed and used to map the stellar surface in a technique called Doppler imaging (Vogt & Penrod 1983, – see Figure 2.5). For slow and moderate rotating stars (the kind targeted for planet hunting) these emission bumps are not resolved and instead result in an asymmetry of the line profile. When the stellar spectrum is cross-correlated (see Section 2.5.2) the movement of the spot as the star rotates changes the asymmetry of the line profile, affecting the position of the line centre, which could be mistaken for the RV motion of a planet. Spots, then, can mimic the RV effects of a planet, and can induce an RV shift of a few m $s^{-1}$ up to $\sim$ 100 m $s^{-1}$depending on stellar activity levels. Compared to the RV shifts for the planets outlined in Table 2.1 this can completely obscure the signals of a planet, adding to the need to understand and remove this source of astrophysical noise.

### 2.4.3 Plage and Faculae

Another manifestation of magnetic activity is bright regions that can appear on the surface layers of a star. These bright regions are given different names depending on the

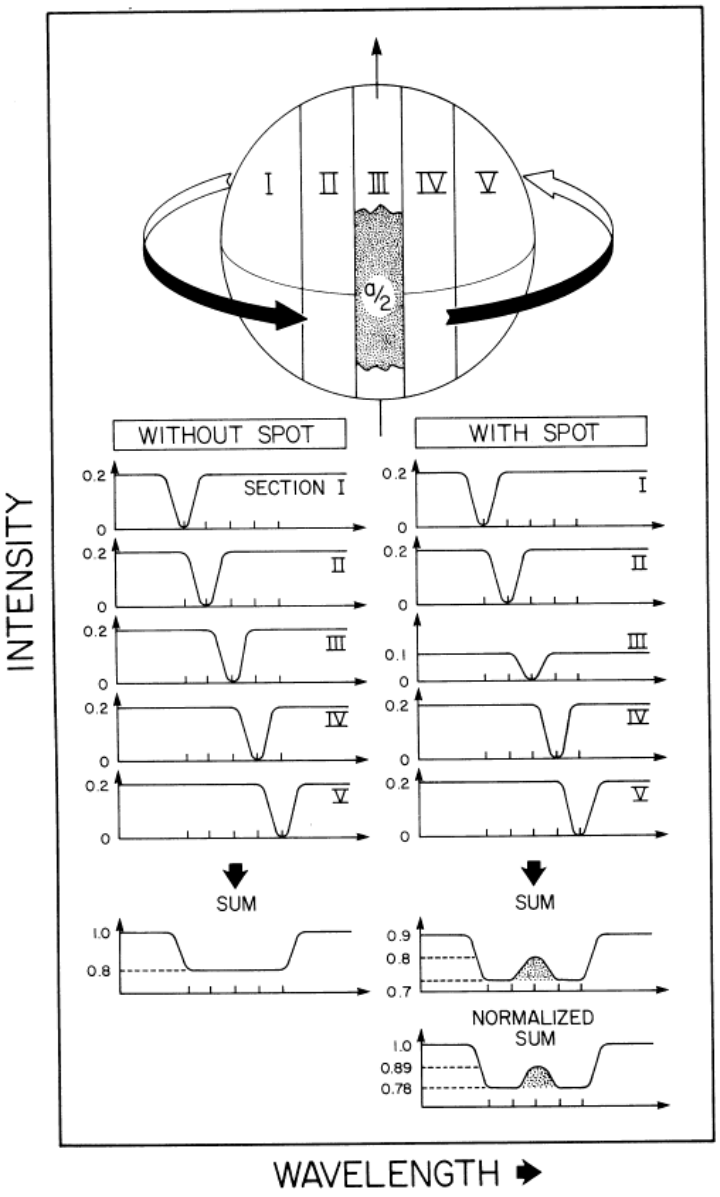


**Figure 2.5**: A schematic of the formation of an emission bump in a spectral line due to the presence of a spot. The star is split into equal sized strips, with a line profile in each strip. Summing these contributions together generates the disk integrated line profile shape. Strip III has a spot covering half of its surface area resulting in a smaller line profile of this strip, and leading to an emission bump when summed together. Image credit: Vogt & Penrod (1983).

layer of the stellar atmosphere being studied. On the photosphere these regions are known as faculae, and on the chromosphere they are called plage. Plage and faculae are spatially associated but, as the magnetic flux tubes diverge as they ascend through the outer layers, this leads to plage having a larger spatial scale than faculae. The two terms, however, are often used synonymously. While starspots appear darker than the photosphere due to reduced heat transport, faculae/plage are brighter. Both activity features are a product of the magnetic flux tubes, but in the case of faculae/plage the field strength inside the flux tube is not high enough to suppress convection. The increased magnetic field, however, does lower the opacity at the surface allowing for a view deeper into the photosphere where it is hotter and therefore brighter. Recent theoretical and observational evidence has shown that faculae are part of the granular wall, which is corrugated in nature (see section 2.3.1). This corrugated structure results in an increase in the effective contribution of faculae as it moves from disk centre to the limb, in an effect known as limb brightening.

As both spots and faculae originate from the same magnetic feature (flux tubes) they can often be found together on the solar surface, with faculae/plage sometime preceding the appearance of spot. Spots, then, are usually associated with faculae/plage but faculae/plage does not need to be associated with spots (due to the reduced magnetic field requirements of faculae/plage). The weaker magnetic field strength needed to produce faculae/plage mean they are longer lived and more abundant across the stellar disk than spots. In fact, even though faculae/plage have a lower contrast than spots, their larger abundance means that during solar maximum (when solar activity is highest) the total solar irradiance increases due to the greater contribution of faculae/plage. For other solar type stars a similar case is seen, with increased magnetic activity also producing an increase in brightness (Kostik & Khomenko 2012). This is the case for quiet stars; with more active stars the higher magnetic field leads to more spots so the star becomes spot dominated with faculae/plage having little contribution (Lockwood et al. 2007). An example of faculae is shown in Figure 2.6, where they are the bright regions seen on the granular walls. The faculae also highlight the corrugated nature of granulation, showing the intergranular lanes forming valleys between the granules.

The low contrast of faculae/plage means that they are not usually observed in photometry. However, the higher magnetic field found in faculae (compared to the surrounding photosphere) acts to suppress the upward convective motions of the granules, which, in turn, attenuates the normal convective blueshift of the regions resulting in an observed spectroscopic signal. This suppression of convective blueshift produces an RV shift of similar strength to that seen with spots. As plage is brighter than the surrounding photosphere the RV variation it produces may be thought of as an opposite

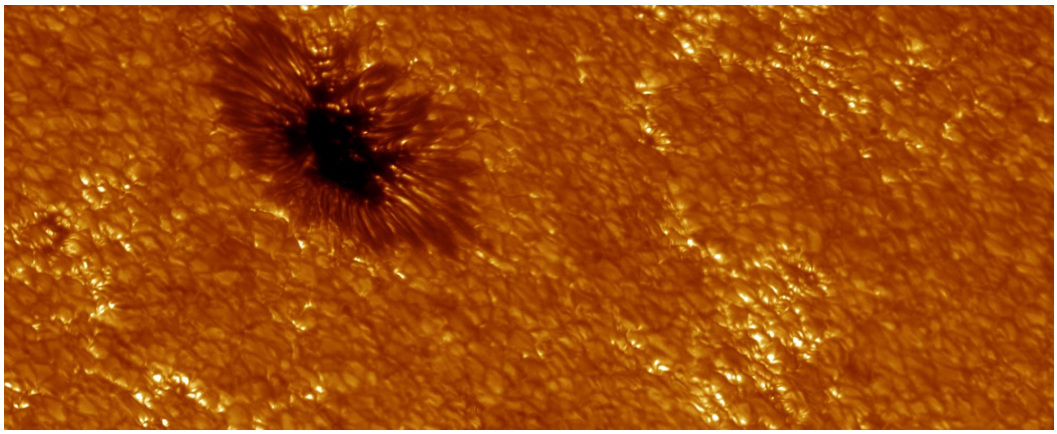

**Figure 2.6**: Example of faculae. In this case, the bright faculae can be seen both closely associated with a spot and further away. This image was taken close to the solar limb, the faculae also highlight the corrugated nature of granulation, with the faculae being part of the granular wall. Image credit: Dan Kiselman, ISP.

effect to that of spots and should cancel the effects of spots. However, as plage is longer lasting, has a larger extent, and does not need to be spatially associated with spots this is not the case. Meunier et al. (2010) found, for the solar case, that the combined RV shift from both spots and plage was still 44 cm $s^{-1}$(almost equalling the individual effects of 48 cm $s^{-1}$ and 44 cm $s^{-1}$ for spots and faculae/plage, respectively). This would still mask the RV shifts from small mass planets. In the case of low activity stars, the effects of plage are the dominant source of RV jitter, as the activity increases this switches to spots being the dominant source (Radick et al. 1990; Hall et al. 2009; Lockwood et al. 2007; Shapiro et al. 2016).

The RV data shown in Figure 2.1 is for the Sun from June 2015 to December 2017, during a minimum in its 11 year magnetic cycle. A considerable amount of variability in the RV measurements is due to the suppression of the convective blueshift (as is clear by the rotational modulation of the variations), finding Earth-analogs even around stars this quiet is impossible if the RV effect of plage is ignored.

## 2.5 Mitigation of Stellar noise

The above section highlights some of the features that can exist on the surface of stars. Understanding the extent of these features on stars other than the Sun can help reveal information about the physical properties of stars. Within the field of exoplanets, however, stellar activity is considered a source of astrophysical noise that needs to be understood so that it can be removed in order to unveil any planets hidden beneath. In this section I outline the most commonly used stellar jitter mitigation strategies and techniques.

### 2.5.1 Avoid Active Stars

The easiest way to limit the effects of activity is to preferentially target stars with low levels of activity. A range of methods exist that can indicate the level of activity of a star, and these can be used to gauge the difficulty in performing planet retrieval, or determining if an exoplanet candidate is worth investing more observational time on. At its most basic, knowing just the rotation period of the star allows for an estimation of the activity level based on an empirical relationship that exists between the two. When stars form, the angular momentum within the collapsing cloud dictates the rotation period of the star. For stars with a convective outer envelope and a magnetic field the interaction between the two causes an effect known as magnetic braking, which causes the star to lose angular momentum and spin down over time. As the spin rate of the star decreases, the level of magnetic activity also decreases due to the two properties being linked through the interaction between the magnetic field and the convection at the tachocline (see Section 2.4.2). Skumanich (1972) first investigated this and established an age-rotation-activity relation, called the Skumanich law,

$$\Omega_e \propto t^{-\frac{1}{2}} \tag{2.6}$$

where $\Omega_e$ is the angular velocity at the equator and $t$ is the age of the star. Simply knowing the rotation (or age) of a star allows for a rough estimate of its activity level. Stellar activity can also be gauged from photometric data, where variations due to active regions on the surface of the star allow for a rotational period to be measured. When choosing candidates from transiting surveys for RV follow-up (which is more observationally expensive), avoiding host stars with high levels of photometric variability helps optimise planet confirmation rates. Radial velocity surveys can preferentially target low $v \sin i$ stars (which implies a low rotation rate) to further aid in avoiding the more active stars. These low $v \sin i$ stars have the additional benefit of narrower spectral lines making for sharper CCFs and hence higher precision RV measurements.

The activity of a star can also be measured spectroscopically. A number of spectral lines are magnetically sensitive and can be used to indicate the level of activity – the most well known are the Ca II H & K lines. The core of the Ca II H & K lines show a re-emission that correlates with the chromospheric activity of a star and can be used as a proxy for spot and plage activity. The measurement of these line cores was first performed by Wilson (1968) using the facilities at the Mt Wilson observatory, looking for variation in long term stellar activity similar to the 11-year cycle of the Sun. Later, the measurement of these line cores were standardised as the S-index (Duncan et al. 1991). The S-index requires the definition of four bandpass filters, two for the Ca II H

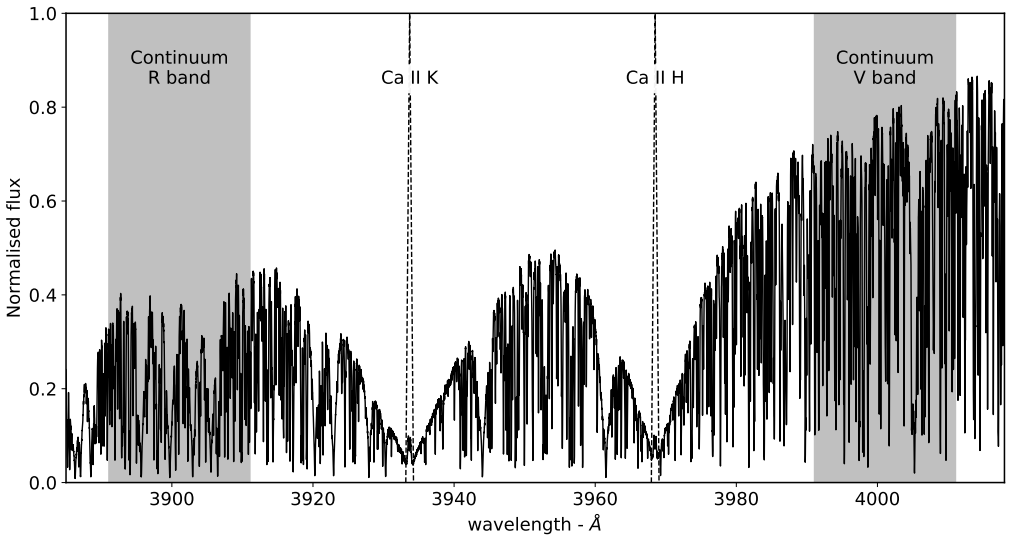


**Figure 2.7**: A spectrum highlighting the various passbands used to measure the Ca II H & K emission cores for $\log R'_{HK}$. In total for bands are used: two triangular passbands for the H and K lines (with a FWHM of 1.09Å) and two broad continuum passbands (of width 20Å) used to normalise the strength of the emission core to that of the spectrum. Note from a line formation perspective the large width these lines indicating that they are dominated by pressure broadening (the Lorentz profile giving a inverse square relation to the line wings) compared to the other sharper spectral lines in the range, which are most likely dominated by Doppler broadening. The re-emission core also indicates an increase in the source function at higher layers of the stellar atmosphere.

& K line cores and two more for reference continuum levels. For the Ca II H & K line cores, the bands are centred at 3933.7 Å (K) and 3968.5Å (H) and have a triangular shape, with a FWHM of 1.09Å. The two continuum passbands are centred at 3901.070 Å (V) and 4001.070 Å (R) and are 20 Å wide. The S-index is then defined as:

$$S = \alpha \frac{H+K}{R+V} \tag{2.7}$$

where $H, K, R$ and $V$ are the summed flux in each passband, and $\alpha$ is a calibration constant fixed at either 2.4 or 2.3 (Duncan et al. 1991). It is standard practice to correct all S-index measurements to the expected value if measured using the Mt Wilson spectrophotometer. The Mt Wilson spectrophotometer uses a rapidly rotating slit that allows for 8 times the exposure at the H and K passbands compared to the R and V passbands. For conventional spectrographs (like HARPS), an extra factor of 8 is applied to correct to the Mt Wilson scale. Thus the S-index is defined as:

$$S = 8\alpha \frac{H+K}{R+V} \tag{2.8}$$

Additional modifications can be applied to further correct for any offsets between the Mt Wilson scale and the other instrument being calibrated. This is done by selecting a number of well observed reference stars and comparing the S-index measures. For the HARPS instrument, for example, a simple linear fit is all that is needed to correct the HARPS S-index to the Mt Wilson (Lovis et al. 2011).

The S-index provides a measure of the Ca II line cores normalised to the local continuum level. The core of the Ca II H & K line contains both photospheric and chromospheric contributions, but it is the chromospheric component that is of interest as it is directly related to the amount of chromospheric heating through magnetic fields. Additionally, the chromospheric component needs to be normalised to the bolometric luminosity of the star to allow for comparisons between different stars to be made. This has led to the well known $\log R'_{HK}$ quantity (Noyes et al. 1984) and is given by:

$$R'_{HK} = C_{cf}(B-V) \times S - R_{phot}(B-V) \tag{2.9}$$

where $C_{cf}(B-V)$ is a conversion factor that corrects for varying flux in the continuum passbands as a function of colour $(B-V)$ and normalises it to the bolometric luminosity, and $R_{phot}$ is the photometric contribution in the Ca II H & K line cores. Stars with a $\log R'_{HK}$ of $< -4.8$ are considered inactive and stars with a $\log R'_{HK}$ of $> -4.6$ are considered active. The Sun, for example, has a mean $\log R'_{HK} = -4.9427 \pm 0.0072$ (Egeland et al. 2017)[1].

By avoiding active stars and targeting quiet stars, the distribution of planet parameters around these more active stars will be ignored, which could affect theories of planet formation and evolution. Additionally, the activity level of a star is not a constant. The Sun exhibits a change in activity level over an 11-year period. Analysis of other stars have shown similar long term changes to their activity level (Lovis et al. 2011). A star selected as being quiet at first can begin to show increased levels of activity over a large enough time range. A specific example of this is $\alpha$ Cen B (Dumusque et al. 2012), where the increasing stellar activity coupled to the observational window function ultimately led to the spurious RV detection of an Earth (minimum-) mass planet. The opposite is also true, where a star rejected as being too active can show a decrease in its activity, allowing for easier RV measurements.

On a final point, although the avoidance of active stars can help deal with spots and plage it cannot help beat down the noise from granulation or stellar oscillations.

[1] value calculated by: https://sites.google.com/site/mamajeksstarnotes/basic-astronomical-data-for-the-sun based on S-index measurements of (Egeland et al. 2017)

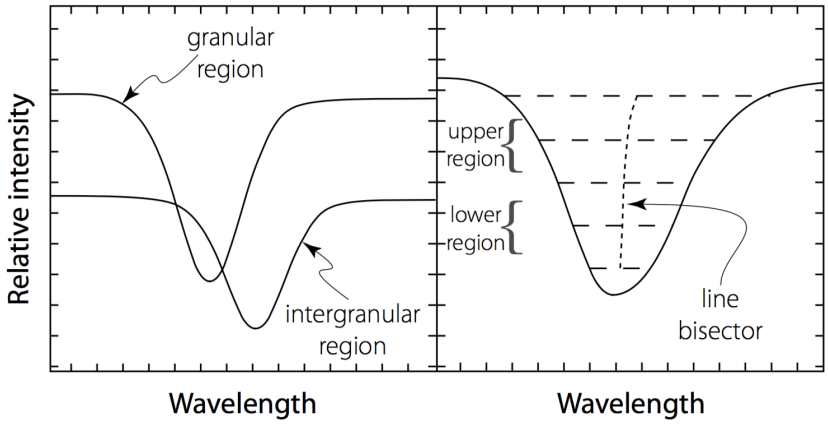


**Figure 2.8**: Schematic of the effect that convection has on the stellar line profile shape. *Left*: the individual components that make up the line profile with the blueshifted granules and redshifted intergranular lanes. *Right*: The resulting line profile (when the components are summed together) produces an asymmetric line shape that can be measured by considering the line mid-point as a function of line depth – the line bisector. Note the slight curve to the line bisector, this is a characteristic 'C'-shape caused by granulation Figure taken from Perryman (2011).

These astrophysical noise sources remain unchanged by changes in the activity level and would still produce an RV jitter. Even the most quiet stars generate stellar activity RV variations that are larger than the Doppler wobble signal of an Earth-analog (see Figure2.1). This forces a deeper understanding of stellar activity and the development of strategies for its removal (the subject of this thesis).

### 2.5.2 Cross-Correlation Function (CCF) analysis

The cross-correlation function (CCF) is a measure of the similarity of two time series, and within the field of exoplanets it is used to measure the RV variations by comparing the spectrum of a Doppler shifted star against a zero RV shifted template or line mask. A number of other useful attributes of the CCF can be used in stellar activity measurements. One of the most popular is to analyse the line bisector. This measures the degree of asymmetry in the shape of individual line profiles but can also be applied to a CCF. The existence of a planet around a star causes the centre of the CCF to shift, and it is this shift that is used to measure the RV variation of a planet. Activity, on the other hand, does not shift the CCF profile, but instead the presence of spots, faculae/plage and granulation affect the shape of the line profile. The shape change caused by varying activity is captured by changes in the CCF line bisector, which is invariant to wholesale Doppler shifts caused by planets.

Granulation (see section 2.3.1) on the surface of cool stars imprints a characteristic 'C'-shape line bisector. The granules alone have a blueshifted line profile component, while the intergranular lanes have a redshifted line profile component. The result of combining together these components into a disk-integrated spectral line produces an asymmetric line profile shape, with the granules causing a blueward shift of the line core, and the intergranular lanes, which contribute weakly, causing a redward shift to the upper region of the line wings (see Figure 2.8). The asymmetry in the CCFs are small and so require high spectral resolution to measure the feature (typically R $> 100\,000$). Spots and plage introduce their own bisector variations. Their contribution depends on their position on the stellar surface, with active regions closer to the stellar limb producing the largest shifts. The effects of spots and plage then add to the bisector variations already induced by granulation.

There is no agreed method for measuring the line bisector, with different authors taking slightly different approaches to the measurement. One such measure is the bisector inversion slope (BIS), which measures the inverse slope of the line connecting the top and bottom portions of the line bisector. The top is defined as the first $10-40\%$ of the line depth and the bottom as $60-90\%$ of the depth (Queloz et al. 2001) – this is also the standard bisector analysis performed by the HARPS instrument. Another example is the bisector curvature, which defines three sections of the line profile (at $20-30\%$, $40-55\%$, and $75-100\%$ of the line depth) and measures the difference between the mean velocities in each of these regions (Dall et al. 2006). However, irrespective of the measurement used, all methods are still tracking the activity induced asymmetry of the line profile.

A strong correlation between the line bisector and RV variations indicates that at least some of the RV shifts are induced by stellar activity (Queloz et al. 2001; Hatzes 2002; Desort et al. 2007). Fitting and removing this correlation can reveal planets lost in the astrophysical noise or improve the accuracy of known planet parameters (e.g. Melo et al. 2007; Boisse et al. 2009). But no correlation does not in itself indicate that no activity is present on the surface of the star. If multiple active regions are present on the surface it is possible for them to create bisector variations that cancel each other out. Desort et al. (2007) additionally showed that the correlation between bisector variations induced by activity and RVs begins to break down for slowly rotating stars.

### 2.5.3 Optimal Observing Strategies

All of the activity features mentioned in Section 2.1 have a characteristic timescale. For granulation and oscillations the characteristic timescales are dependent on the spectral type of the star, and for spots and plage that exist on the surface of the star this is

linked to the stellar rotation period. With knowledge of these timescales an observational strategy can be developed that attempts to average out the effects of these various astrophysical noise sources.

Dumusque et al. (2011b,c) developed a strategy for reducing stellar jitter for a Sun-like star. The authors found that by taking three 10 minute exposures, each separated by 2 hours, over 10 consecutive days for each month the star was visible they were able to reduce the effects of stellar oscillation and granulations. Additionally, the authors found that, for a solar rotation period, taking 10 observations over a month with each observation separated by 3 days they were able to adequately sample the rotation period, helping reduce the effect of spots by averaging out their contribution. This strategy changes depending on the spectral type and evolution of the star. The authors note that for shorter rotational periods, the measuring frequency can be increased but for longer period stars the frequency of observations should not be decreased as this would reduce the sampling of short period planets.

As well as being a good planet discovery technique, the RV method is being used more and more for follow-up of planet candidates found through the transit method. Information gleaned from transit surveys can then be useful for optimising the Doppler wobble follow up observing strategy. If the planet period is notably different from the stellar rotation period then an observing strategy can be developed that maximises the RV variations due to the (known) planet companion and minimises the RV shifts due to activity. Pepe et al. (2013) used this strategy to observe Kepler-78b, the known transiting planet had a measured orbital period of 8.5 h while the stellar rotation period was 12.6 days. The star was seen as moderately active with an average $\log R'_{HK}$ of -4.52 over the observations. By observing twice per night at the times when the planet RV semi-amplitude was greatest (at quadrature) the observing time was minimised, while maximising the RV information gained about the planet (i.e. the semi-amplitude of the RV signal). The authors were then able to separate the signals of the star from that of the planet, with stellar contributions determined as the sum of the two nightly measurements and planetary motions as the differences. It should be noted that this was only possible due to the short orbital period of the planet relative to the stellar rotation period. This meant that covering ~half of the planet's orbit can be done in,

$$S_{rot} \sim \frac{\Delta t_{\frac{1}{2}}}{P_{rot}} \times 360^{\circ} \tag{2.10}$$

where $\Delta t_{\frac{1}{2}}$ is half the orbital period of the planet, $P_{rot}$ is the stellar rotation period and $S_{rot}$ is the stellar rotation fraction (in degrees). For Kepler 78b observing consecutive quadratures of the planet's orbit can be done in the time that the star rotates by just

$S_{rot} \sim 3.6°$. This essentially 'freezes' the stellar activity variation, since both the evolution of spots and their rotational modulation will be small over this time. This strategy cannot be done on longer period planets but for the so-called ultra-short period planets, with orbital periods of < 1 day (like Kepler-78b, or WASP-19b, Hellier et al. 2009) this can be an effective means of reducing the effects of stellar activity.

### 2.5.4 Periodogram Searches

An important set of tools for detecting exoplanets are periodogram algorithms. These algorithms search data for periodic signals, which can imply the existence of a planet as well as detecting the signs of stellar activity. For transit searches the box-fitting least squares (BLS) is most useful, while for RV variations a Generalised Lomb Scargle (GLS) is the preferred choice of periodogram. Both rely on a similar principle of fitting a repeating pattern to a dataset and measuring the quality of the fit.

For a typical transiting planet, the main transit event occupies less than 5% of the total orbital period. The resulting light-curve, though periodic, is extremely non-sinusoidal. The BLS was constructed with the specific purpose of detecting transit signals by fitting a box shape of different sizes and depths and measuring the Signal Residue (SR) for any given trial period (Kovács et al. 2002). An example of the BLS is shown in Figure 2.9 and demonstrates the power of the algorithm for retrieving signals in data.

Outside of transits, most other signals can be assumed to be sinusoidal in nature, these include RV variations for low eccentricity planets, stellar activity due to spots or plage, and rotational periods of stars. For these types of signals the Generalised Lomb-Scargle (GLS) is used. The Lomb-Scargle (LS) periodogram (Scargle 1982) is a widely used tool for frequency analysis but suffered from a number of short falls for use within the field of exoplanets. The LS periodogram does not take into account measurement errors, it assumes that the mean of the data and the mean of the fitted sine wave are the same, and also requires a uniform data sampling. Zechmeister & Kürster (2009) formulated a revised version of the LS periodogram and 'generalise' it for use with real data. Following the formulation laid out by Zechmeister & Kürster (2009), with a time series of data defined as $(t_i, y_i)$, the GLS is defined as $p(\omega)$ (power as a function of frequency $\omega$) and given by

$$\mathrm{GLS} \equiv \mathrm{p}(\omega) = \frac{1}{\mathrm{YY} \cdot \mathrm{D}} \left[ \mathrm{SS} \cdot \mathrm{YC}^2 + \mathrm{CC} \cdot \mathrm{YS}^2 - 2\mathrm{CS} \cdot \mathrm{YC} \cdot \mathrm{YS} \right] \tag{2.11}$$

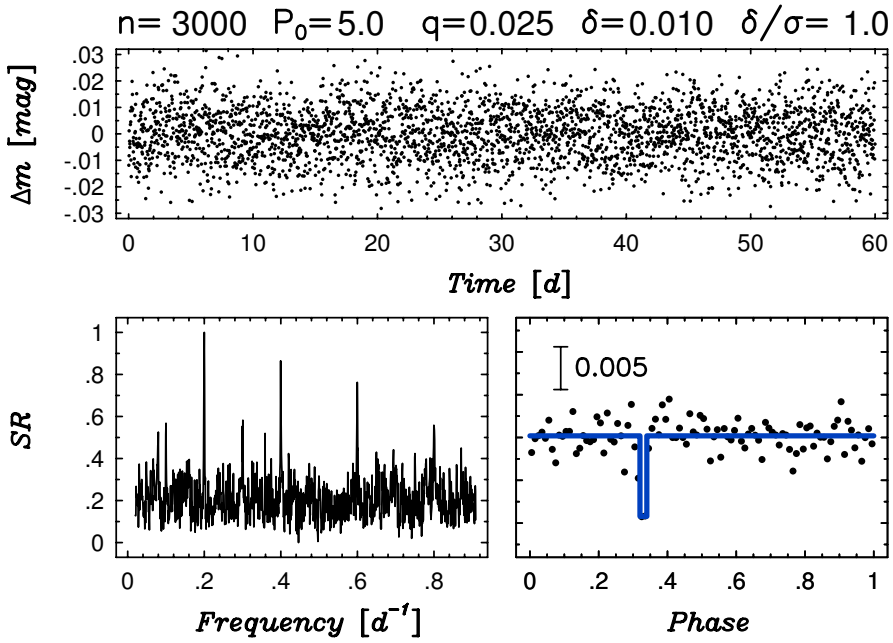


**Figure 2.9**: Example of the power of the BLS periodogram to find signals in noisy data. *Top* is synthetic data with a transit signal of period $P_0 = 5$ days, a signal-to-noise, $\sigma/\delta = 1.0$, and a transit depth, $q = 0.025$. *Bottom left* is the BLS frequency spectrum showing a strong peak in SR at 0.2 days$^{-1}$ (i.e. 5 days) and the *bottom right* is the data phase-folded on this peak period from the BLS. Figure taken from Kovács et al. (2002).

with:

$$D(\omega) = CC \cdot SS - CS^2 \tag{2.12}$$

The values $Y$, $S$ and $C$ are abbreviations for the following summations:

$$Y = \sum w_i y_i \tag{2.13}$$

$$C = \sum w_i \cos \omega t_i \tag{2.14}$$

$$S = \sum w_i \sin \omega t_i \tag{2.15}$$

$$
\begin{aligned}
YY &= \widehat{YY} - Y \cdot Y & \widehat{YY} &= \sum w_i y_i^2 \\
YC(\omega) &= \widehat{YC} - Y \cdot C & \widehat{YC} &= \sum w_i y_i \cos\omega t_i \\
YS(\omega) &= \widehat{YS} - Y \cdot S & \widehat{YS} &= \sum w_i y_i \sin\omega t_i \\
CC(\omega) &= \widehat{CC} - C \cdot C & \widehat{CC} &= \sum w_i y_i \cos^2\omega t_i \\
SS(\omega) &= \widehat{SS} - S \cdot S & \widehat{SS} &= \sum w_i y_i \sin^2\omega t_i \\
CS(\omega) &= \widehat{CS} - C \cdot S & \widehat{CS} &= \sum w_i y_i \sin\omega t_i \cos\omega t_i
\end{aligned}
\tag{2.16}
$$

where $w_i$ are the normalised weights defined as:

$$
w_i = \frac{1}{W}\frac{1}{\sigma_i^2} \qquad\qquad W = \sum \frac{1}{\sigma_i^2}
\tag{2.17}
$$

The above formulae completely define the GLS for a given frequency $\omega$ and can then be applied over a frequency range of interest to look for signals. Real data has additional effects, such as uneven data sampling, and uncertainties that can add spurious signals to the periodogram. An example that affects all of astronomy is spurious signals caused by ground based observations. As observing can only occur at night, the gaps in the data from the lack of observations during the day can create a window function that gives rise to the well-known one-day alias of ground based observations. In addition to the base frequency, harmonic frequencies can exist in the data (i.e. if a period $P$ exists in the data, periods $P/2, P/3, ...$ and $2P, 3P, ...$ can also exist), as well as other signals possibly due to other astrophysical or instrumental effects.

An important part of periodic analysis is distinguishing which periods are real and which are due to windowing of the data or an alias effect. The False Alarm Probability (FAP) measures the 'believability' of a signal by setting a limit based on some lower confidence interval. Any peak falling below this limit is viewed as not a real signal. The FAP can be approximated by

$$
FAP \approx 1 - (1 - e^{-z})^{N_i}
\tag{2.18}
$$

where $z$ is the maximum peak in the periodogram and $N_i$ is the number of independent

frequencies, which can be estimated as the number of peaks in the periodogram. This method does require the time series to be evenly spaced so is not practical given the nature of real astronomical data. A more robust approach is to use a boot-strapping process (Efron 1992) where the time values of the dataset are kept the same while the other measured values (flux, RV or other measurements being analysed for periodicity) are randomly re-arranged and the periodogram re-run. This rearranging of the data and running the periodogram is done many times and the FAP is calculated by measuring the spread in periodogram power at each frequency and defining a cut on the power of periodogram at each frequency below which no signal is believed (for example, > 99% of the points). This approach more accurately take into account the non-uniformity of real data sampling but is much more computationally expensive to calculate.

As mentioned, the RV and transit method can take advantage of periodogram algorithms to identify planets, but periodograms can also be a useful tool for identifying stellar activity. Hatzes et al. (2010) calculated periodograms for four quantities: RVs, CCF line bisector, S-index, and CCF FWHM. All four quantities are affected by activity but only the RVs are affected by the presence of a planetary companion. Comparing the peaks in the frequency spectrum of the bisector, Ca II, and FWHM periodograms to those of the RV periodogram allows for signals from activity and planets to be distinguished, with peaks that only appear in the RV periodogram being identified as due to a planetary companion. Hatzes et al. (2010) used periodogram searches to better estimate the parameters of the planets around CoRoT-7 and, by isolating the stellar activity, was able to identify a potential third planet in the system (this is still to be confirmed). This technique was also used, in conjunction with other techniques, in a study of the ultra-short period (8.5h) planet Kepler-78b (Pepe et al. 2013). By analysing the same four quantities, Pepe et al. (2013) was able to confirm that the prominent 4.2 day and 10 day periods seen in the RV periodogram were due to activity.

### 2.5.5 Modelling Stellar Activity using Photometry

As stars rotate, spots, which exist on the surface, will traverse the visible stellar hemisphere. From the point of view of the observer, spots will then move in and out of view with the rotation period of the star and can cause a change in the apparent brightness of the star. Modelling this photometric variability can be a useful tool for removing activity within RV measurements. Aigrain et al. (2012) developed a technique that uses variations seen in photometry as a basis for modelling the RV activity of a star. The technique (called the FF′) only aims to provide a first order estimate of the RV variation caused by stellar jitter and so limits itself to the effects of spots and magnetic regions associated with spots.

Aigrain et al. (2012) defines two RV contributions due to activity: the spots, which are tied to the stellar rotation, $\Delta RV_{rot}$, and the inhibition of convective blueshift in the magnetic region surrounding the spot, $\Delta RV_c$. The RV signature of a spot can be expressed as:

$$\Delta RV_{rot}\,(t) = -F(t)\dot{F}(t)\frac{R_\star}{f} \tag{2.19}$$

where $F(t)$ is the relative drop in flux due to a spot on the surface, $\dot{F}(t)$ is its first time derivative, $R_\star$ is the radius of the star and $f$ is the relative drop in flux for a spot at disk centre. Both $F(t)$ and $\dot{F}(t)$ can be estimated from the light curve, as:

$$F(t) = 1 - \frac{\Psi(t)}{\Psi_0} \qquad \text{and} \qquad \dot{F}(t) = -\frac{\dot{\Psi}(t)}{\Psi_0} \tag{2.20}$$

where $\Psi(t)$ is the observed flux, $\dot{\Psi}(t)$ is its first time derivative and $\Psi_0$ is the flux in the absence of spots. The RV signature for spots is then:

$$\Delta RV_{rot}\,(t) = \frac{\dot{\Psi}(t)}{\Psi_0}\left[1 - \frac{\Psi(t)}{\Psi_0}\right]\frac{R_\star}{f} \tag{2.21}$$

The convective blueshift effect can be treated in a similar way, and defined as:

$$\Delta RV_c\,(t) = F^2(t)\frac{\delta V_c \kappa}{f} \tag{2.22}$$

$$\Rightarrow \Delta RV_c\,(t) = \left[1 - \frac{\Psi(t)}{\Psi_0}\right]^2 \frac{\delta V_c \kappa}{f} \tag{2.23}$$

where $\delta V_c$ is the difference between the convective blueshift in the unspotted photosphere and that within the magnetised areas, and $\kappa$ is the ratio of this area to that of the spot area.

Aigrain et al. (2012) tested their spot model (which they termed the FF′ method) on both the Sun and HD 189733 and compared their results to the more sophisticated (and much more computationally intensive) maximum entropy (ME) model of Lanza et al. (2011). The models by Lanza et al. (2011) more fully captures the effects of stellar activity, including effects from starspots, faculae, inhibition of convection around active regions, limb darkening, and micro/macro-turbulence. For the active star HD

189733 Aigrain et al. (2012) found their much simpler model was able to reproduce RV variations modelled as well as ME, with the two models giving essentially identical fits. For the analysis of the Sun, the data was spit into two periods: one of high and one of low activity with the FF′ method being separately applied to each period. The FF′ model fitted the high activity solar data better than the low activity solar data but the authors point out that this could be due to plage dominating the RV variation at lower activity.

Another approach to modelling the activity takes a more numerical approach, where the surface of a star is modelled with various active regions and the expected photometric variability measured. The SOAP (Spot Oscillation And Planet) code does just this: it simulates the effects of spots and plages on the surface of a rotating star by considering flux contrast effects (Boisse et al. 2012). Dumusque et al. (2014) presented an upgraded version of the code (SOAP 2.0) that estimates the activity-induced variations seen in photometry and spectroscopy, including effects from convective blueshift and its suppression within active regions. Dumusque et al. (2014) showed that for a spot dominated star, the RV jitter due to activity is dominated by the temperature contrast of spots combined with stellar rotation. For plage dominated stars the inhibition of convective blueshift due to the active regions takes over as the dominant factor. The SOAP 2.0 code can be thought of as a numerical equivalent approach to the FF′ method but, where the FF′ method only models spots and associated plage, the SOAP 2.0 model can consider a isolated rotating plage region instead. This makes the SOAP 2.0 code more useful for low activity stars where plage is the dominate source of astrophysical noise.

Oshagh et al. (2017) compared the two methods by taking simultaneous HARPS spectroscopic measurements and high-precision photometry (from the K2 space telescope) of 9 stars. The authors concluded that for active stars, both methods worked equally well at reducing the RV jitter due to activity (with the SOAP 2.0 modelling a single spot region). At low activity levels, however, the SOAP 2.0 code, modelling a single plage region, was able to provide more accurate predictions than the FF′ method. Oshagh et al. (2017) additionally found that the FF′ method systematically under-predicted the amplitude of the RV jitter over the range of activity levels tested, which became significant at low-activity levels. Low-activity stars are known to be plage dominant (Radick et al. 1990; Hall et al. 2009; Lockwood et al. 2007; Shapiro et al. 2016), with the FF′ method only treating the effects of spots directly and the contribution from plage being inferred from its association to spots, it is not unexpected that it would have difficulties predicting activity changes in these low activity cases especially for plage regions unassociated with spots.

The simplicity and ease of implementation of the FF′ method has allowed it to be adopted for use, especially in cases where the activity level is high or more exact modelling of the stellar jitter is not required. Dai et al. (2017), for example, analysed the star EPIC 228732031 and found that the strongest peak in the RV periodogram was at 3-days. By using the FF′ method the authors were able to attribute the signal to stellar activity – this could have otherwise been viewed as a second planet in the system.

It should be noted that any technique that relies on photometric changes to model RV variability due to activity will only be useful when the contrast between the activity and the immaculate photosphere is large enough to produce measurable photometric changes. The techniques can also be insensitive to certain spot configurations, where the presence of multiple spot groups on the visible hemisphere of the star can lessen (or cancel out) the effect active regions have on photometry. As an extreme example, two spots, at the same latitude but separated by 180° would show little photometric variability as when one spot moves on to the visible surface the other spot moves off. Additionally, if the observing cadence is not high enough to capture the evolution of the activity (especially for more rapidly rotating stars) such techniques will become ineffective.

### 2.5.6 Harmonic Decomposition and Fourier Component Analysis

An effective way of disentangling the signals of stellar activity from those of a planet is to make use of the periodic nature of the active regions. As active regions exist on the surface of stars, they are inherently linked to the stellar rotation period. By removing signals corresponding to the rotation period of the star, stellar activity signals will also be removed. This is the goal of harmonic decomposition, where the rotation period of the star is identified, usually via the Lomb-Scargle periodogram (see Section 2.5.4), as well as its harmonics and fitted out with a series of sinusoids. The removal of the rotation period $P_{rot}$ removes an active region rotating on the surface, while its harmonics $P_{rot}/2, P_{rot}/3, ...$, can represent higher order situations where multiple spot groups exist that are equally spaced over the surface of the star. These harmonics can also help when the signal of activity diverges from a perfect sine curve (Queloz et al. 2009).

Once the rotation period and its harmonics are fitted with a sinusoid, it can be subtracted from the RV variations of the host star, and the residuals searched for a Keplerian planet signal. Boisse et al. (2011) found that by just removing the rotation period and its first two harmonics (i.e. $P_{rot}, P_{rot}/2$, and $P_{rot}/3$) enabled the removal of up to 90% of the astrophysical noise in their RV data. Applying the technique to the planetary system GJ 674 the authors were able to recover the planetary RVs (see Figure 2.10). The technique is anchored on the accurate measurement of the the stellar

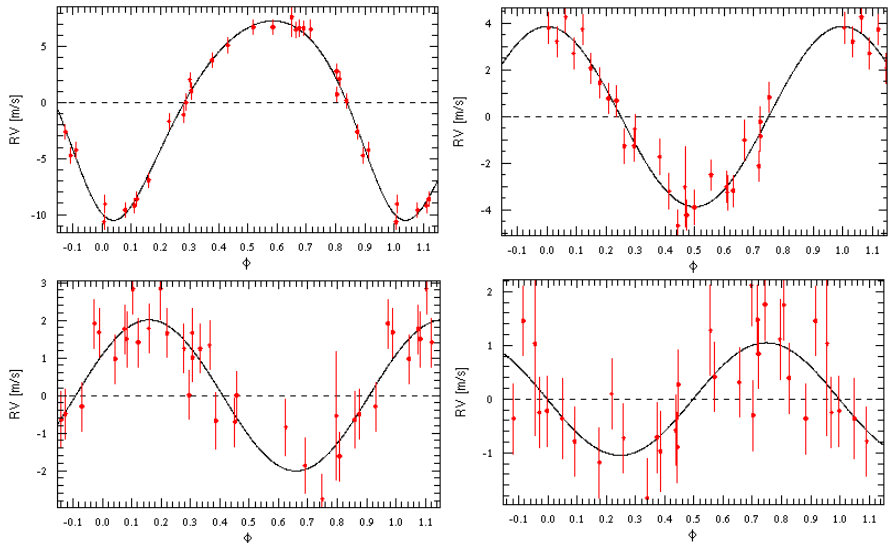


**Figure 2.10**: Harmoic decomposition applied to the GJ 674 system. *Top right* shows the RV measurements for the system in red with the model used to fit it as a black line. The model consisted of one Keplerian for the planet and three sinusoids for the activity – $P_{rot}$ and its first two harmonics. *Top left* shows the Keplerian planet model and the *bottom left* and *bottom right* show the first and second harmonics, respectively. Figure taken from Boisse et al. (2011).

rotation period, if this is not known then the technique cannot be applied.

A more general form of harmonic decomposition is Fourier component analysis (also known as pre-whitening). For this method a Fourier transform is applied to the data (which produces equivalent data to the periodogram used for harmonic decomposition). The highest peaks in the frequency spectrum of the Fourier transform are identified and removed from the data (this is done by fitting sine waves of the identified frequencies). With harmonic decomposition the frequencies removed correspond to the rotation period of the star. With Fourier component analysis the strongest frequency is fitted out using a sine wave. The process is repeated on the residuals of the data until the noise floor is reached. This allows for the removal of spurious signals not on the rotation period of the star and, where harmonic decomposition can only be run over a few rotation periods, Fourier component analysis can be applied to much 8longer datasets (Hatzes 2013).

Both harmonic decomposition and Fourier component analysis have been used to find planets, Dumusque et al. (2012) used harmonic decomposition to search for planets around $\alpha$ Cen B, while both techniques have been applied to the CoRoT-7 system. Queloz et al. (2009) used Fourier component analysis to identify all the strong periodic signals in the data, and were able to determine that all but two signals, at 0.85 and 3.69 days, belonged to the stellar rotation period. The signal at 0.85 days was confirmed as

the transiting planet CoRoT-7b. The signal at 3.69 days was analysed using harmonic decomposition acting as a high pass filter. This harmonically filtered data was found to contain a strong periodic signal that could then be attributed to a second planet in the system, with a mass of $8.4 \pm 0.9 M_{\oplus}$.

There are a number of drawbacks to these techniques. For harmonic decomposition, planetary signals close to the rotation period of the star will also be filtered out by the removal of stellar rotation period, while stellar activity not on the rotation period of the star will not be removed at all (Queloz et al. 2009; Boisse et al. 2011). For Fourier component analysis, aliases in the frequency spectrum make it difficult to know which peak is from the true frequency (Queloz et al. 2009), while not removing enough Fourier components for pre-whitening can lead to a discrepancy between the true activity variations and the fit removed.

### 2.5.7 Detrending by Local RV Trends

A technique aimed at reducing the impact of long-term RV variability uses detrending based on nightly averaged RV measurements. By calculating the mean RV offset per night and subtracting these from the corresponding individual RV measurements, RV variations on long-term timescales can be removed (Hatzes et al. 2011). The evolutionary and rotational timescales for stellar activity are such that, for a single night, the activity level can be assumed to be constant. By removing an average RV shift on a night-by-night basis any residual RV shifts may be attributed to a planetary companion. Additionally, the technique (also called 'cut-and-shut') is able to remove long-term instrumental effects that could hinder planet detection. However, as the detrending removes long-term variation it cannot be used for planets on longer orbital periods as these will also be removed in the detrending. This is most apparent for planets with orbital periods close to the stellar rotational period.

A more flexible approach would instead be to take the data and split it into small enough segments that any long-term underlying trend can be fit with a simple function. This helps account for the evolution of activity, which may not be periodic in nature (e.g. the migration of active regions to higher latitudes would change the RV contribution from that active region). The time span of each data segment is defined such that it is shorter than the stellar rotation period (to capture rotationally modulated activity) and longer than the planet orbit (so prior knowledge of the planet is needed). Over this time span the RV variation due to activity should only change slowly so can be fit with a low order polynomial. This local trend filtering was used to analyse $\alpha$ Cen B and provide evidence that the RV signal attributed to a planet may be due to the treatment of activity as a coherent source.

### 2.5.8 Gaussian Process Regression

A recent trend within the field is to move to a Bayesian framework to help deal with the effects of activity. Gaussian process (GP) regression is a flexible framework that models $n$ data points in a non-parametric way. Where parametric models have a finite set of parameters that make future predictions independent of the data, nonparametric models grow in information as the amount of data increases, allowing for a more flexible approach to modelling. GP regression allows for the modelling of complex stochastic processes by parameterising the covariance between pairs of data points, rather than writing an expression for the data themselves. In classical (frequentist) statistics we ask: what is the *probability* that a measurement has a given value under an assumed model. In Bayesian statistics, the question becomes: what is the *likelihood* the model is correct given the data measured.

A GP is determined by two components. The first is a mean function that incorporates deterministic components of the model. In the field of exoplanet RV measurements, this can be in the form of Keplerian fits to model a number of planets, or sine waves to account for rotationally modulated activity like spots. The second component is a covariance function, this accounts for the more stochastic nature of the data and defines how each pair of data points correlates with one another. This forms a $n \times n$ covariance matrix $\mathbf{K}$ that contains information about the uncorrelated (white) and correlated (red) noise within the system including stellar activity.

Haywood et al. (2014) used GPs as part of their analysis of CoRoT-7. The authors determined the elements of the covariance matrix using a quasi-periodic kernel function, $k$, of the form:

$$k(t,t') = \eta_1^2 \exp\left( -\frac{(t-t')^2}{2\eta_2^2} - \frac{2\sin^2\left(\frac{\pi(t-t')}{\eta_3}\right)}{\eta_4^2} \right) \tag{2.24}$$

where $t$ and $t'$ are two points in the time series and the terms $\eta_i$ are the hyperparameters of the GP. $\eta_1$ is the amplitude of the GP, $\eta_2$ is the timescale for growth and decay of the kernel, $\eta_3$ is a recurrence timescale and $\eta_4$ is a smoothing parameter. The kernel function can be seen as the combination of a periodic function and an exponential decay function and so represents evolving active regions coming in and out of view. Using this kernel function Haywood et al. (2014) was able to apply the FF′ method (see Section 2.5.5) to account for the activity of the star. The authors added a second GP of the same quasi-periodic form to model the RV activity not captured by the FF′ method (e.g. the influence of faculae). The hyperparameters in this second GP used the same values as those defining $\eta_2$, $\eta_3$, and $\eta_4$ for the first GP used to model the photometric

variations, with only the amplitude of the GP, $\eta_1$, being a free hyperparameter. Finally, a number of Keplerian orbits were added to model the effects of planets around the star. The model was fitted by maximising a likelihood function using a Markov Chain Monte Carlo (MCMC) method. The MCMC is the preferred choice for GP regression as it allows for acceptance of worse fits via the Metropolis-Hastings algorithm (Metropolis et al. 1953) to stop the chain from being trapped in local maxima and better explore parameter space (a necessity given the number of free parameters). The final model for this approach is shown in Figure 2.11.

Rajpaul et al. (2015) developed a similar framework specifically to model RV variation when photometric data is not available. The authors jointly modelled the BIS and $\log R'_{HK}$ activity indicators alongside the activity-induced RVs with the motivation that all can be modelled using a single underlying GP. Using this framework, Rajpaul et al. (2015) were able to both disentangle the activity and planet of the Gl 15 A system and show that the RV variation seen in $\alpha$ Cen B can be explained by activity alone.

While GPs are able to account for activity, they have a number of drawbacks. GPs are computationally intensive to compute, with a computational complexity that scales with $O(N^3)$. GPs then prefer smaller datasets to remain computationally feasible (typically $n \lesssim 1000$, Gibson 2014). Also of importance is the choice of kernel function, while a poor choice will still be able to produce a fit it will converge more slowly and given the computational efficiency this is worth considering. Finally, interpretation of the parameterisation of a GP is not straightforward, and how each of the hyperparameters relate to real quantities may not be intuitive given that the nature of underlying activity signals is not understood.

### 2.5.9 Correlations with Chromospheric Activity

Finally, in more recent years, owing to the increased precision of instruments, a correlation has been found between long-term RV variations and chromospheric activity (as indicated by $\log R'_{HK}$). Simply subtracting this correlation the RV variability can be significantly reduced (Lovis et al. 2011; Dumusque et al. 2011a; Meunier & Lagrange 2013). Lovis et al. (2011) and Meunier & Lagrange (2013) also applied a sinusoidal fit to the chromospheric activity measurements, which additionally reduced RV variability. Meunier & Lagrange (2013) also looked at using a linear fit rather than a sinusoidal and found this to be more appropriate during periods of low activity.

Dumusque et al. (2011a) was able to successfully apply this technique to remove the long-term RV variability of 5 planetary systems for a range of planet masses (~

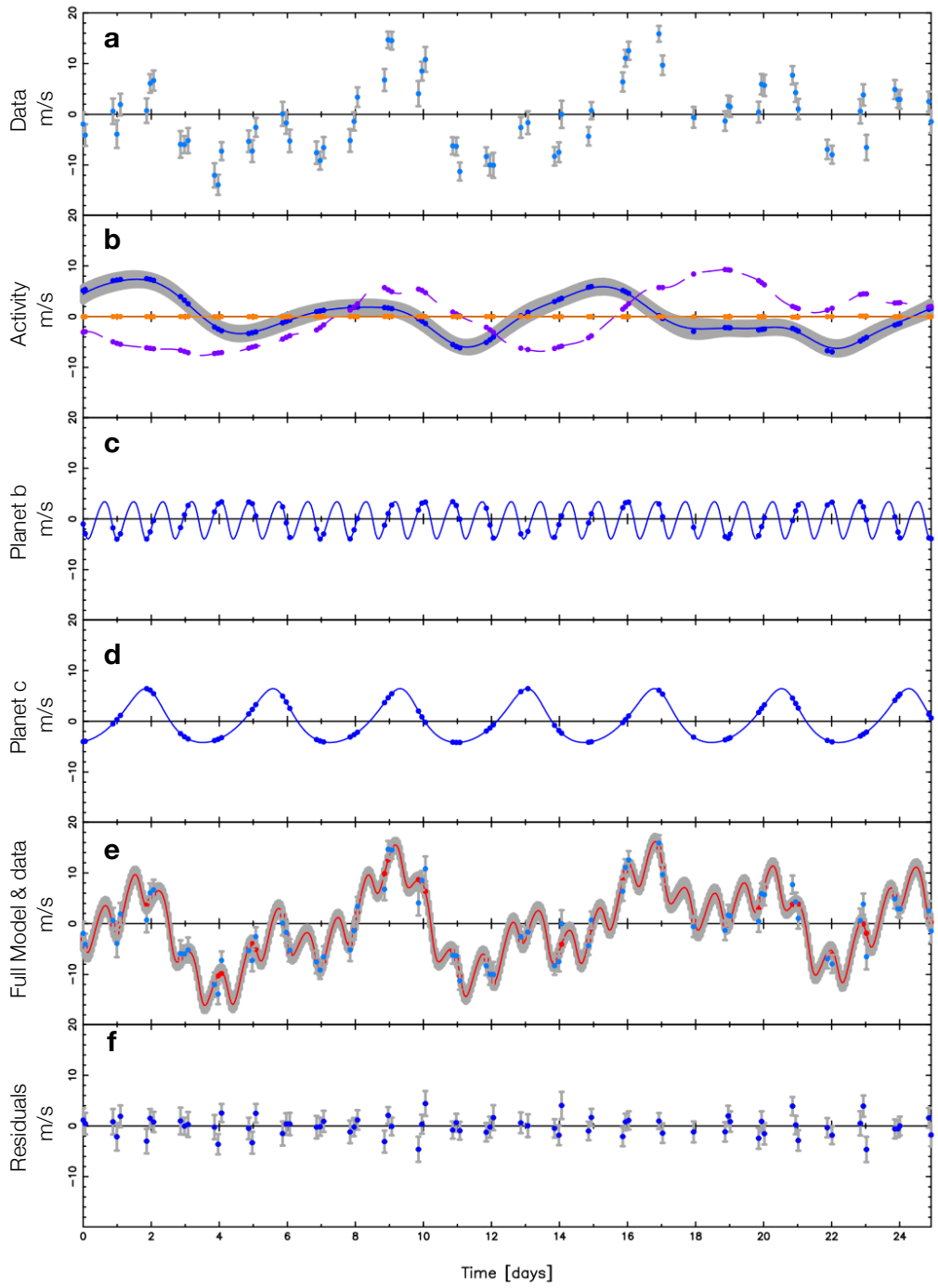


**Figure 2.11**: The gaussian process (GP) regression model for the CoRoT-7 system. *a:* the raw RV measurements of the star. *b:* The fit for the activity, with the orange being the RV contribution from rotation and purple being the RV contribution from the suppression of convective blueshift (both these are calculated using the FF' method). The blue line is the GP model for the additional activity variation not picked up by the FF' method. Panels *c* and *d* are the Keplerian models for the two planets of the system. *e:* the full model overlaid on top of the raw RVs and *f* is the residuals after its removal. Image credit Haywood et al. (2014).

$0.2-2M_J$) and orbital separations ($0.9-5$ AU). Lovis et al. (2011) found that for well-sampled targets with more than 3 years of observations (44 of 304 sampled) there was a clear trend between RV-$\log R'_{HK}$ correlation slope and the effective temperature of the star, with hotter stars having a steeper total RV-$\log R'_{HK}$ correlation slope. This suggests that long-term activity trends may affect the RV observations of a large number of stars, with a higher impact on quieter stars and stars with a higher effective temperature.

## 2.6 Conclusion

This chapter highlighted some of the common techniques and methods used by the community to mitigate the effects of stellar activity and RV jitter from exoplanet detection methods. Many of these techniques are un-informed, looking at the correlation of a signal with stellar rotation or inferring that the activity is stationary over a small time range and has a more limited impact. A better understanding of the physical effects that activity imprints on the spectra of a star would lead to more informed models and, potentially, a better stellar activity removal technique. In the next 2 chapters I try to probe this by studying the activity changes of $\alpha$ Cen B and the Sun. The goal for the analysis is to directly detect the manifestations of stellar activity in the stellar spectra of quiet stars. This may then open up the possibility of better stellar variability correction, essential in our long-term quest to confirm Earth-analog planets.

*Chapter 3*

# Probing the Spectral Impact of Stellar Activity

## 3.1 Introduction

The contents of the following chapter have been published in the Monthly Notices of the Royal Astronomical Society: Letters, Volume 468, Issue 1, p.L16-L20 as the letter entitled "The Changing Face of $\alpha$ Centauri B: Probing Plage and Stellar Activity in K Dwarfs" (Thompson et al. 2017), and modified here to fit within the framework and context of this thesis. This chapter discusses the work done by Thompson et al. (2017) in greater depth than was permissible in the letter as well as providing a slightly extended analysis of possible activity correlations.

### 3.1.1 The Alpha Centauri System

The stars of the Alpha Centauri system are the closest to our own Solar System, this hierarchical triple-star system has an average distance of only $\sim$ 1.3 parsecs. The two main stars of the system ($\alpha$ Cen A, G2 V and $\alpha$ Cen B, K1 V) are not separable by the naked eye, making the light from the combined stars one of the brightest in the southern hemisphere. A third wide companion, referred to as either $\alpha$ Cen C or Proxima Centauri, was discovered in 1915 (Innes 1915). The stars of this system have been the subject of many studies, most pertinently this includes long term RV programs to detect orbiting planets.

Anglada-Escudé et al. (2016) reported the recent discovery of a planetary companion to the star Proxima Cen using a range of RV measurements (including HARPS). The detection of a 1.12 $M_\oplus$ minimum mass planet on a $\sim$ 11.2 day period is much easier around this low mass (0.12 $M_\odot$) star as it produces a larger RV variation (having a semi-amplitude of $\sim$ 1.4 m/s) compared to a similar massed planet around a main sequence FGK star. This is the only confirmed planet within the system and also represents the closest planet to those of our own solar system. Currently, no planets have been found around $\alpha$ Cen A or $\alpha$ Cen B.

The orbital plane of $\alpha$ Cen A and $\alpha$ Cen B is only 11 degrees from edge on, resulting in periods of low projected separation. The next periastron passage of $\alpha$ Cen AB is 2035 giving a projected separation of less than 2 arcseconds. A secondary minimum was reached in 2017 when the minimum separation of the two star was $\sim$ 2 arcseconds. This has put a hiatus on observations of $\alpha$ Cen A and $\alpha$ Cen B as separations less than 5 arcseconds are avoided due to cross-contamination between both sources, making robust RV measurements difficult. Zhao et al. (2018) used the currently available data from a number of instruments to put limits on the planet detectability. Looking specifically at the classically defined habitable zone of each star, they place detection thresholds at about $M \sin i$ of $53 M_\oplus$ for $\alpha$ Cen A, $8.4 M_\oplus$ for $\alpha$ Cen B, and $0.47 M_\oplus$ for

Proxima Centauri.

The system is of great interest to the exoplanet community, while no planets have been found around the A or B components of the Alpha Centauri system this does not rule out the existence of planets around these stars. The extensive RV measurements from the system (especially $\alpha$ Cen B) makes it an excellent candidate for in-depth analysis of the stellar activity of K-dwarfs, and the impact such activity may have directly on the stellar spectra themselves.

### 3.1.2 Activity on Alpha Centauri B

$\alpha$ Cen B is a relatively inactive K1 V star. This low-activity, combined with a mass of $0.937 M_{\odot}$ (Torres et al. 2010), makes $\alpha$ Cen B a prime target for RV planet searches. $\alpha$ Cen B was the target of many RV planet searches using the HARPS (High Accuracy Radial velocity Planet Searcher) instrument. Spectra for the star span approximately 4 years (from 28$^{\text{th}}$ February 2008 to the 13$^{\text{th}}$ July 2011), with initial observations in 2008 showing a $\log R'_{HK}$ of $-5.0$. The low-activity level reduces the effects of stellar activity contributions to the RV noise, further improving the possible detectability of planets.

Dumusque et al. (2012), here after in this chapter referred to as D12, reported the discovery of a planet around $\alpha$ Cen B. They performed an in-depth study of the star using data from over four years of HARPS observations. Analysis of the star presented a challenge as the close binary companion ($\alpha$ Cen A) caused both an RV motion as well as producing occasional light contamination during periods of poor seeing. In the end, a model with 23 free parameters was fit to account for the effects of stellar activity (e.g. the long-term activity signal and rotationally modulated activity effects) and the binary companion. From this work they claimed to detect an Earth mass planet (1.11 $M_{\oplus}$) around $\alpha$ Cen B with an orbit period of $3.2357 \pm 0.0008$ days. At the time, this represented one of the lowest (minimum) mass exoplanets discovered around a main sequence dwarf star, having an RV variation of 0.5m s$^{-1}$as well as being the closest exoplanet to our own Solar System. The discovery sparked interest in determining the viability of the signal, with some arguing that the modelling approach was incorrect (e.g. Hatzes 2012, 2013). The legitimacy of the planet detection was resolved by Rajpaul et al. (2016b) who showed that the signal attributed to the orbital motion of a planet was, in fact, due to data sampling – where a window function in the time series was the source of the signal. Though no planets were found around the star, the large amount of high quality spectra is ideal for a study of stellar activity – the focus of my work.

The results of D12 also show quite nicely the long term $\log R'_{HK}$ of the $\alpha$ Cen B over

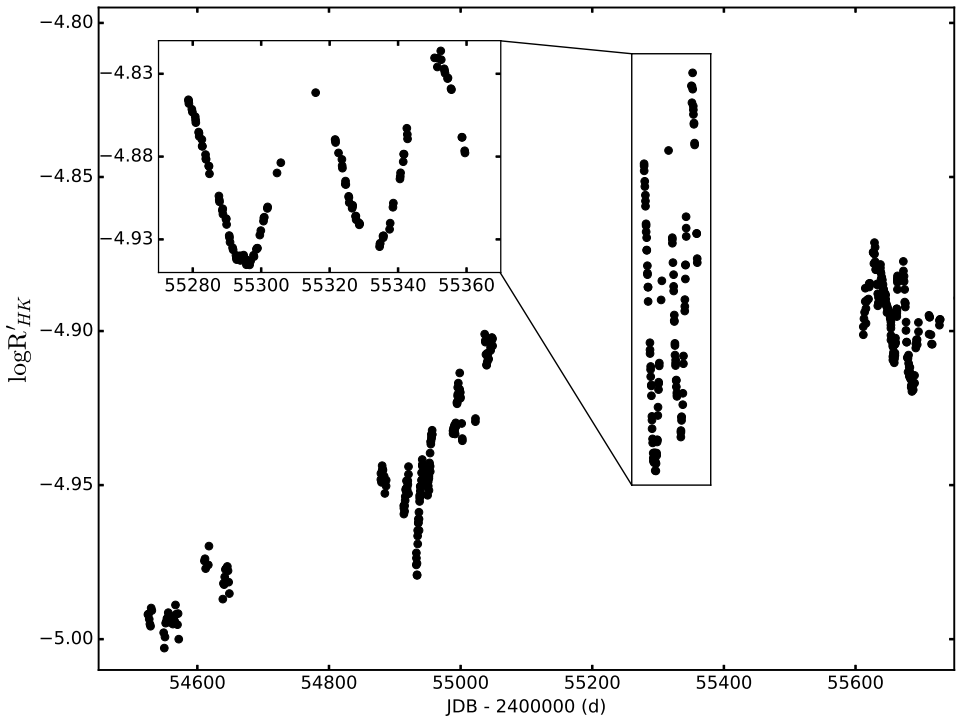


**Figure 3.1**: $\log R'_{HK}$ values for the data used in D12 showing a clear long term activity cycle variation. The insert highlights a well sampled time where an obvious periodicity in $\log R'_{HK}$ can be seen. This is due to active regions on the photosphere of the star rotating in and out of view. Image taken from Dumusque et al. (2012).

the ∼4 years of observations of the system. In Figure 3.1 the activity of the star can clearly be seen to change. On the longer timescales of years, there is a slow ramping of the activity level, this is akin to the ∼ 11-year solar cycle, where the Sun goes through a period of low- and high-activity (the period is technically 22-years as the magnetic polarity switches once per 11 years). On shorter timescales the star shows a change in activity that coincides with the stellar rotation period. During a particularly well observed period, a clear periodicity can be seen in the $\log R'_{HK}$ value of the star, which is modulated on the stellar rotation period of 41 days (highlighted insert of Figure 3.1).

Rather than looking for planets around the star, the observed change in activity level provided a platform to study the effects that active regions have on the spectra of the star itself. The changing activity level and large amount of high signal-to-noise HARPS data available for $\alpha$ Cen B made it a unique and well-suited testbed to perform such an analysis. In this chapter I will discuss, in detail, the results of an analysis of the effects of activity on the spectra of $\alpha$ Cen B.

## 3.2 Data and Data Processing

This analysis made use of data from the High Accuracy Radial velocity Planet Searcher (HARPS). HARPS is a highly stabilised, high resolution (R=115,000) echelle spectrograph on the ESO 3.6 metre telescope. It is designed with the purpose of providing high precision radial velocity (RV) measurements for the detection of exoplanets. With a long-term precision of $\sim 1\text{m s}^{-1}$ it is able to easily detect hot Jupiters-massed planets around low mass stars as well as pushing down to Neptune and super-Earth massed planets. To achieve this high precision HARPS uses two optical fibres, one to observe the target and the second used as a simultaneous reference making use of a Thorium Argon (ThAr) lamp to perform the calibration (Lovis et al. 2006). More recently HARPS has upgraded to a Laser Frequency Comb (LFC) to further improve its calibration (Lo Curto et al. 2012). The success of the HARPS instrument has inspired the development of a twin instrument on the Telescopio Nazionale Galileo (TNG) for northern Hemisphere observations (called HARPS-N, Cosentino et al. 2012) and a potential third instrument (HARPS3) on the Isaac Newton Telescope (INT) as part of a 10 year RV measurement programme to discover Earth-like planets (Thompson et al. 2016).

For the following analysis, the same HARPS data as used by D12 were selected. This was partly due to the obvious activity change present within the data, which is essential for this analysis, but also due to the complexities in RV correcting the data. As $\alpha$ Cen B is part of a binary, the RV effects from the binary interaction in combination with other stellar effects (contamination from $\alpha$ Cen A and barycentric motion of the Earth) must be corrected. This is a non-trivial process, and the data from D12 has RV measurements that properly account for these effects. In total, the data consisted of 9693 spectra that spanned approximately 3.5 years (from February 2008 to July 2011). This work focused mostly on the time range of $23^{rd}$ March 2010 to $12^{th}$ June 2010 – here after the March-June 2010 period. Not only is this a well sampled period in the data but within this range a very clear periodicity can be seen in the $\log R'_{HK}$ value of the star. This change in activity shows a periodicity of $\sim 41$ days, corresponding to the rotation period of $\alpha$ Cen B, and must then be caused by active regions on the stellar surface rotating in and out of view (see insert in Figure 3.1). Data were retrieved using the ESO archive, giving access to the fully pipeline reduced 1D spectra.

The reduction of raw echelle spectral data is an involved process, here I will give a brief overview of HARPS pipeline. This pipeline uses the same methods discribed in Baranne et al. (1996) where more information on the procedure can be found. Firstly, raw images go through the standard treatment of bad pixel correction, offset and bias subtraction. The positions of the echelle orders are then determined by fitting a gaussian at several locations along the order and measuring the peak. A polynomial is fit to the

peaks and defines the location of the order. During this process the blaze function and flat-field spectrum are also computed. An optimal extraction algorithm is then used to extract each of the orders as well as removing cosmic rays. The spectrum is then flat-field corrected using a flat-field spectrum defined earlier, which divides each order by an equivalent flat field order. The blaze function is also applied here. The spectrum is then wavelength calibrated using a Thorium Argon lamp (or more recently a laser comb) as a calibrator. Finally, the spectral orders are merged together and re-binned onto a constant wavelength grid of 0.01Å.

To test the effects that activity could have on the stellar spectra, the spectra from the March-June 2010 period (which show a higher activity level as traced by $\log R'_{HK}$) were compared to spectra from the star's most inactive phase. For this, the night of $28^{th}$ February 2008 was identified as having one of the lowest levels of activity from the whole data set and the spectra from that night were used to define a low-activity 'template'.

For the analysis, 'relative' spectra were created by dividing each of the spectra during the more active March-June 2010 period by the defined low-activity template spectrum. Before dividing the spectra, the data were processed with the main objective of normalising the continuum level of each spectrum to that of the low-activity template as well as moving all spectra to a common wavelength grid using a linear interpolation. As multiple spectra were available per night, these were stacked into nightly averages, which greatly improves the signal-to-noise. Given the relatively long rotation period of $\alpha$ Cen B any variability due to activity changes are on timescales larger than a single day and so stacking per night would not compromise the results.

For the creation of the low-activity template each spectrum during the night of the $28^{th}$ February 2008 was visually inspected for any obvious defects that could have resulted from data reduction issues or instrument systematics. No spectra from this night showed any of these effects and so all were used for the template. The signal-to-noise ratio of each spectrum was taken from the FITS header file (this signal-to-noise value is calculated as part of the standard HARPS data reduction pipeline), with the highest SNR taken as a reference spectrum for the continuum normalisation. Each individual spectrum was interpolated, using a linear interpolation, onto the wavelength grid of the reference spectrum. For this work with the high resolution HARPS instrument, the small wavelength shifts between spectra were such that a linear interpolation was felt to be sufficient, (especially given the signals seen – see Section 3.3) but if applying similar techniques to data from other, lower resolution instruments a more robust interpolation (e.g. cubic spline) may be required. Each interpolated spectrum was divided by the reference spectrum to produce residual spectra and a 4th order polynomial was fitted

to the resulting residuals over the spectral range of 4300 - 5300 Å. This polynomial fit was then applied to each of the interpolated spectra to normalise the continuum. A total of 10 spectra (with an average SNR of 363.47) from the night of $28^{th}$ February 2008 were vetted by eye before interpolating and continuum normalising in this way to produce the master low-activity template.

For all the other spectra from the March-June 2010 period (i.e. the spectra used in this analysis) a similar approach was used to process the data, with a number of small caveats. First, the master low-activity template defined above was used to set the wavelength grid that all other spectra were interpolated onto, as well as the continuum normalisation. Second, this period covers a total of 48 nights with 2475 spectra taken, rather than vetting spectra by eye a more robust method of defining a cutoff to remove suspect spectra was used. The root-mean-square of each residual spectrum (defined by dividing each spectrum by the master low-activity template) was measured over the wavelength range of $5050 - 5300$Å. Spectra with root-mean-square values greater than 1% were rejected. This represented the removal of spectra that were affected by echelle order mis-match or, on occasion, wrongly labelled $\alpha$ Cen B spectra, where erroneous observations of $\alpha$ Cen A took place. Finally, once all spectra were processed they were stacked into nightly averages, with the root-mean-square (RMS) defined for the cutoff also being used here as a weighting factor in the averaging. Formally, the nightly stacked spectrum $S$ can be written as,

$$S = \frac{\sum_{n=0}^{N} s_n w_n}{\sum_{n=0}^{N} w_n} \tag{3.1}$$

where $s_n$ is the individual spectrum (from $n = 0$ to $N$), and $w_n$ are the weights taken as $\frac{1}{RMS^2}$.

In all cases the data were restricted to a 1000 angstrom range of 4300 - 5300 Å. This excludes a significant portion of the spectral coverage of HARPS but was chosen as the signal-to-noise was highest in this part of the spectrum, as the signal-to-noise drops sharply at shorter wavelengths (see Figure 3.2). Redwards of 5300 Å the number of detectable telluric lines also increases, which limits the ability to determine the nature of any signals detected as well as causing issues for the polynomial fitting performed as part of the data processing. Finally, the detector of the HARPS instrument consists of a mosaic of 2 CCDs (altogether 4k×4k) with a gap in wavelength coverage just after 5300 Å, this gap could alter the polynomial fit so excluding this gap was a necessary

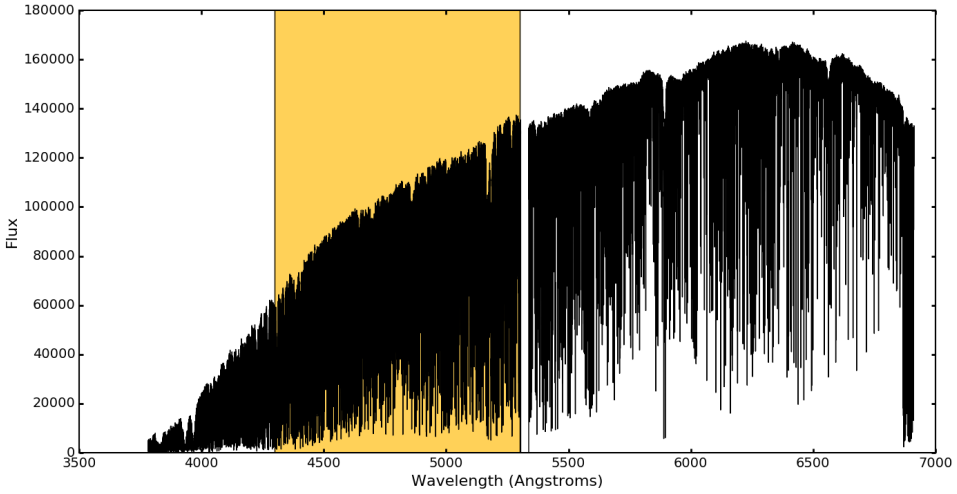


**Figure 3.2**: An example of a HARPS spectum of $\alpha$ Cen B. The area highlighted in orange was the wavelength range selected for the analysis. The gap in the data is due to a physical gap between the CCDs.

additional constraint.

Thus the final dataset consisted of a master low-activity template and 48 higher activity nightly stacked spectra covering a spectral range of 4300 - 5300 Å, all of which were stacked after being continuum normalised and interpolated onto a common wavelength grid – that of the master low-activity template. Using these stacked spectra 'relative' spectra were produced by dividing each nightly stack by the master low-activity template. As the only difference between the 48 spectra of the March-June 2010 period and the master low-activity template is the activity, as traced by $\log R'_{HK}$, these relative spectra highlight any difference between the high and low-activity states of $\alpha$ Cen B.

An alternative to dividing the spectra by a template would be to subtract one from the other. This would be the appropriate approach if we were trying to extract a component from the spectra. For example, in the case of a spectroscopic binary star system, one could subtract a model of one of the component stars to produce a spectrum of just the other star.

The use of division for the production of the relative spectra raises the question of whether this or subtraction is the more appropriate method. The reduction of the data was done again but this time subtracting a continuum normalised and interpolated spectrum from the master low-activity template. Figure 3.3 shows the results of this test, with the division case also showed as a comparison. The subtraction causes the residuals to be dominated by the noise within the continuum levels of the spectrum. This can be understood by considering the count level at two extreme parts of the spectrum. At

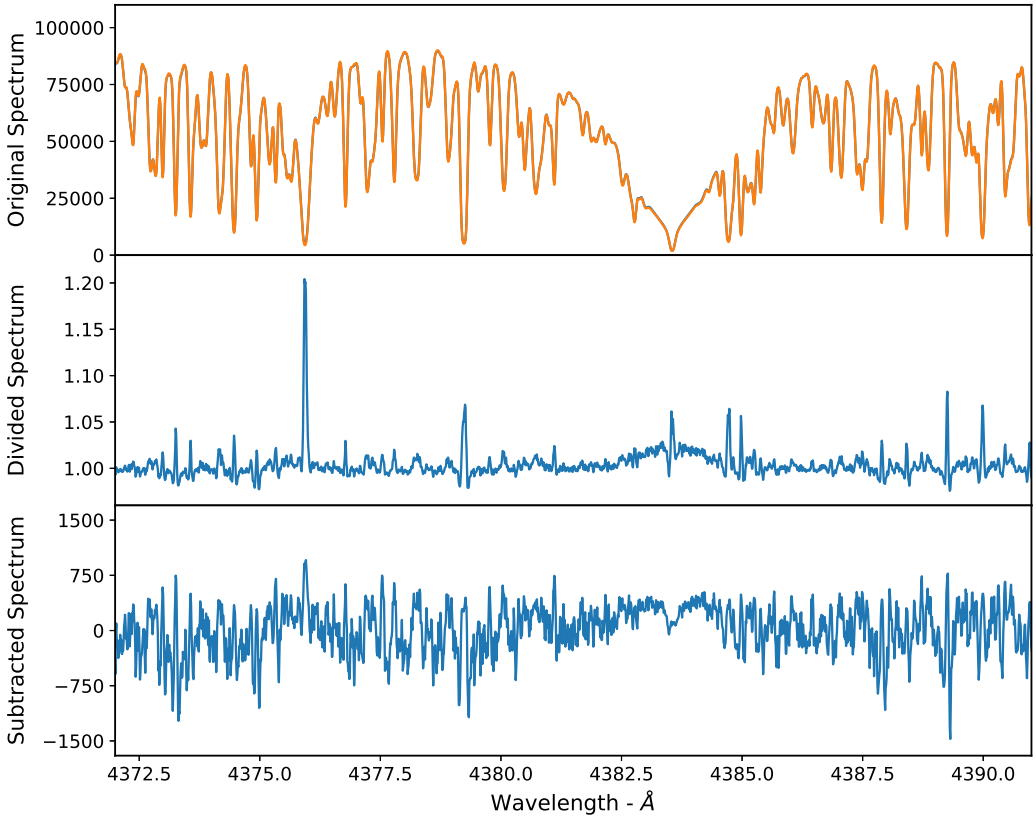


**Figure 3.3**: Comparison of the effects of dividing the spectrum by a template (*middle panel*) versus subtracting the spectrum from the template (*bottom panel*). The *top panel* shows the unaltered spectrum for comparison. Here it can be seen that the effects of changes to the continuum are dominating the relative spectra for the case of subtraction and the features of note become lost in this noise. Dividing on the other hand, highlights changes in the line cores (which are more counts limited) and it is here where activity may be expected to have an effect.

the continuum level the counts are large, showing values of close the 90000, a change of $\sim$ 320 counts (the standard deviation of the range shown) is of the order of a $\sim 0.3\%$ change here. At the line cores some of the deepest lines the counts are $\sim$4000, a similar change here represents a change of $\sim 10\%$. Thus in the subtracted spectrum it is difficult to determine whether the various seen represent a significant change to the central portion of the spectral lines, while for the divided spectrum these are highlighted. All of the features found are both small in size and lay in (or close to) the core of the spectral lines where the counts can be quite low. By dividing, the effects of the continuum can be reduced and changes seen in the line cores can be better measured.

## 3.3 Analysis

A visual inspection of the March-June 2010 relative spectra was performed. A representative region (4340 – 4480 Å) is shown in Figure 3.4 and highlights the range of features observed in the relative spectra (to help with observing the changes in the relative features only 16 of the 48 spectra available are shown in Fig. 3.4, these 16 are evenly spaced over the period to cover the entire range of $\log R'_{HK}$). Each relative spectrum has been colour coded with respect to its value of $\log R'_{HK}$ with an equivalently coloured plot of $\log R'_{HK}$ versus time shown at the top right of Fig. 3.4.

A number of broad features are seen in the relative spectra. Some examples of these can be seen in Figure 3.4 at 4383 Å and 4404 Å, and in Figure 3.5. These two lines are isolated to make viewing the change in their strength more clear. These features correspond to Fe I species that are used as spectral type indicators due to their temperature sensitivity (Giridhar 2010). Thus the broad peak of the Fe I features may indicate a change in effective temperature of the star. As these lines are known to be photospheric in origin this temperature change may indicate the presence of cooler active regions (i.e. spots) on the surface of $\alpha$ Cen B.

In contrast, numerous sharp 'pseudo-emission' peaks can also be seen, the most prominent in Figure 3.4 occur at 4375 Å, 4427 Å and 4462 Å (Figure 3.6, again, shows a zoom in of these lines making the changes in their strength easier to see by eye, $\log R'_{HK}$ is shown for comparison). Worth noting is that most of the "scatter" seen in Figure 3.4 is not the noise level of the relative spectra but is in fact due to many closely separated individual narrow 'pseudo-emission' peaks. Measuring the RMS of some of the feature free regions of the relative spectra shows values of $\sim 0.3\%$ level. These narrow features can be large, with the Fe I 4375 Å line, for example, showing a maximum peak at the $\sim 20\%$ level, which suggests a significant line change between the high-activity spectrum compared to the master low-activity template. The results shown here are similar to the findings of Basri et al. (1989), where a similar approach of generating relative spectra is used to produce pseudo-emission features from lines known to be photospheric in origin. Basri et al. (1989) used a sample of 29 stars ranging from G8 - K5, after grouping the stars into comparable classes a low-activity 'standard' for each class was chosen by selecting the star that showed the lowest activity level (as measured by $\log R'_{HK}$) in that class. The authors produced relative spectra and also found features, which they tentatively attribute to activity (see Figure 3.7). However, the result of this analysis of $\alpha$ Cen B differs from that of Basri et al. (1989), they constructed relative spectra using *different* stars to represent high- and low- activity cases. This meant that their results were somewhat inconclusive, as the authors could

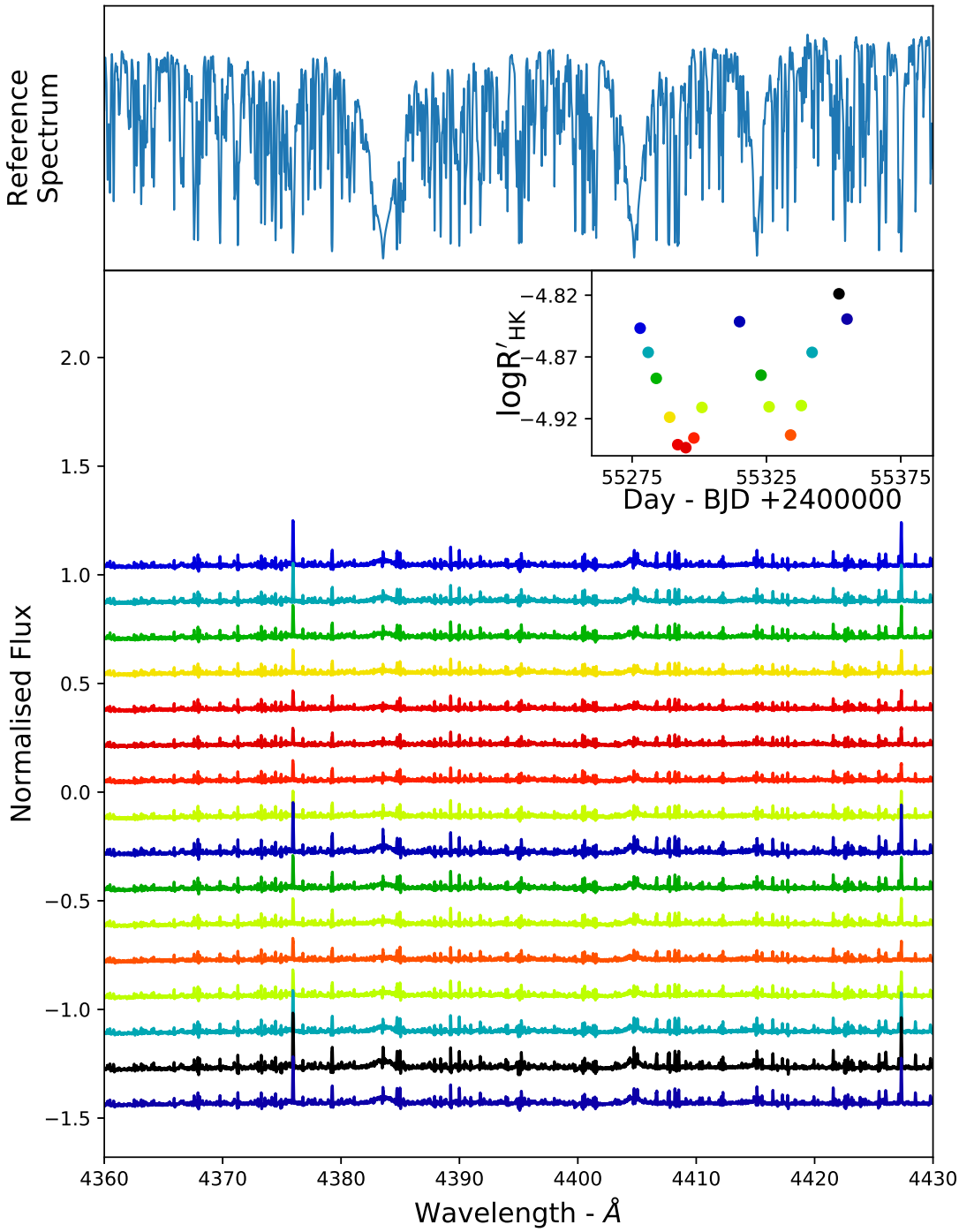


**Figure 3.4**: A selection of relative spectra from the March-June 2010 period – generated by dividing high-activity spectra by the master low-activity template – for ease of viewing only 16 of the 48 weighted spectra available for this period are shown. The broad features seen at 4383 Å and 4404 Å correspond to temperature sensitive Fe I lines. A large number of narrow 'pseudo-emission' peaks can also be seen with the feature at 4375 Å showing an excursion of $\sim 20\%$. The colour of the relative spectra corresponds to the activity as seen in the $\log R'_{HK}$ (see insert at the top right). Note the change in the strength of all these features clearly correlates with the rotation cycle of the star being weaker at lower values of $\log R'_{HK}$ and stronger at higher values. An example spectrum over the same range is shown on top for comparison.

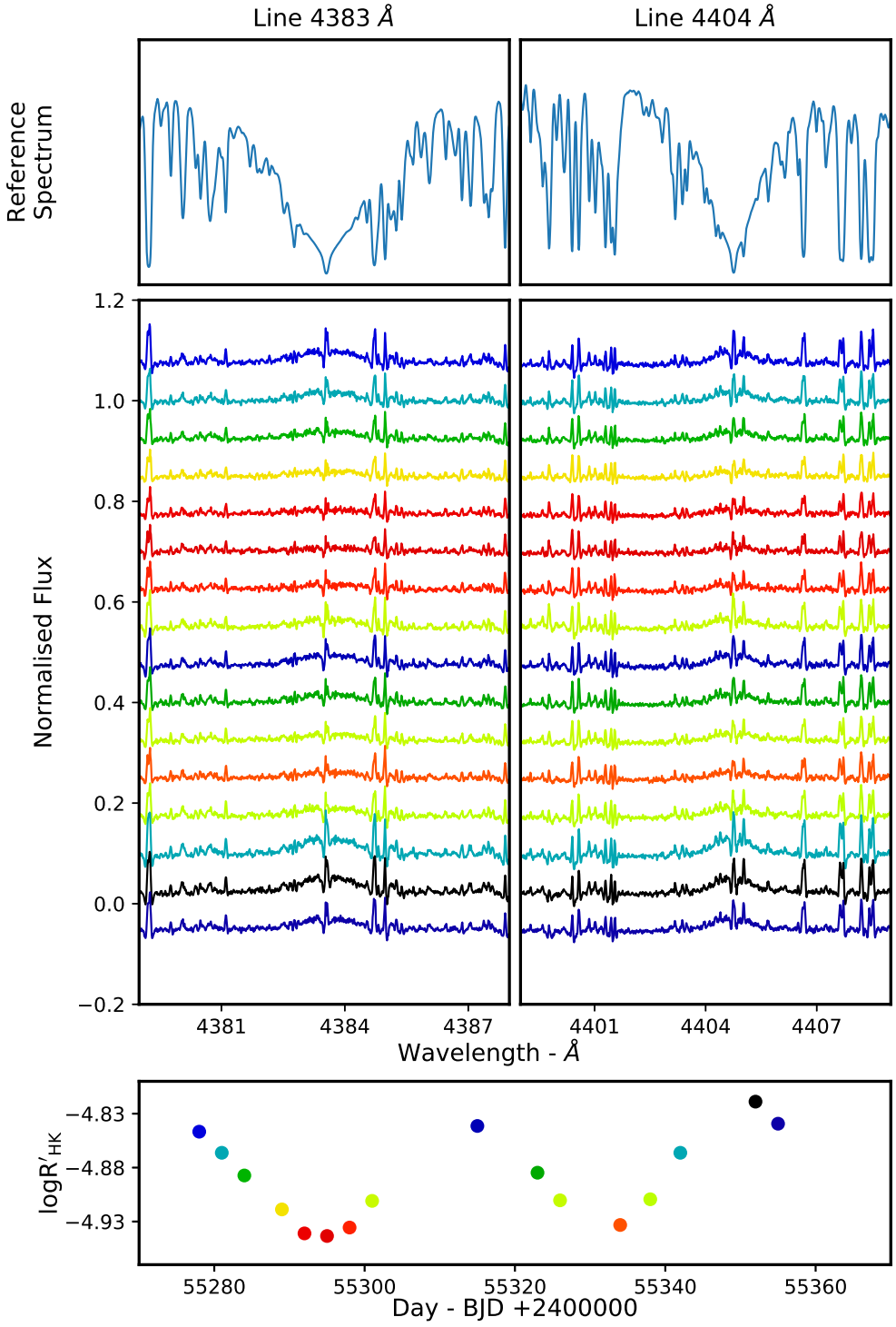


**Figure 3.5**: *Top:* The broad features of 4383 Å (left panel) and 4404 Å(right panel) seen in the relative spectra from the March-June 2010 period are isolated to make the changes in their strength more clear. The plot at the top of each panel correspond to the earliest observation, with time moving forward with each plot. As with figure 3.4 only 16 of the 48 relative spectra are shown – again for clarity. *Bottom:* $\log R'_{HK}$ values for the relative spectra shown, the colour of the relative spectra corresponds to the activity level. Example spectra over the same range are shown on top for comparison.

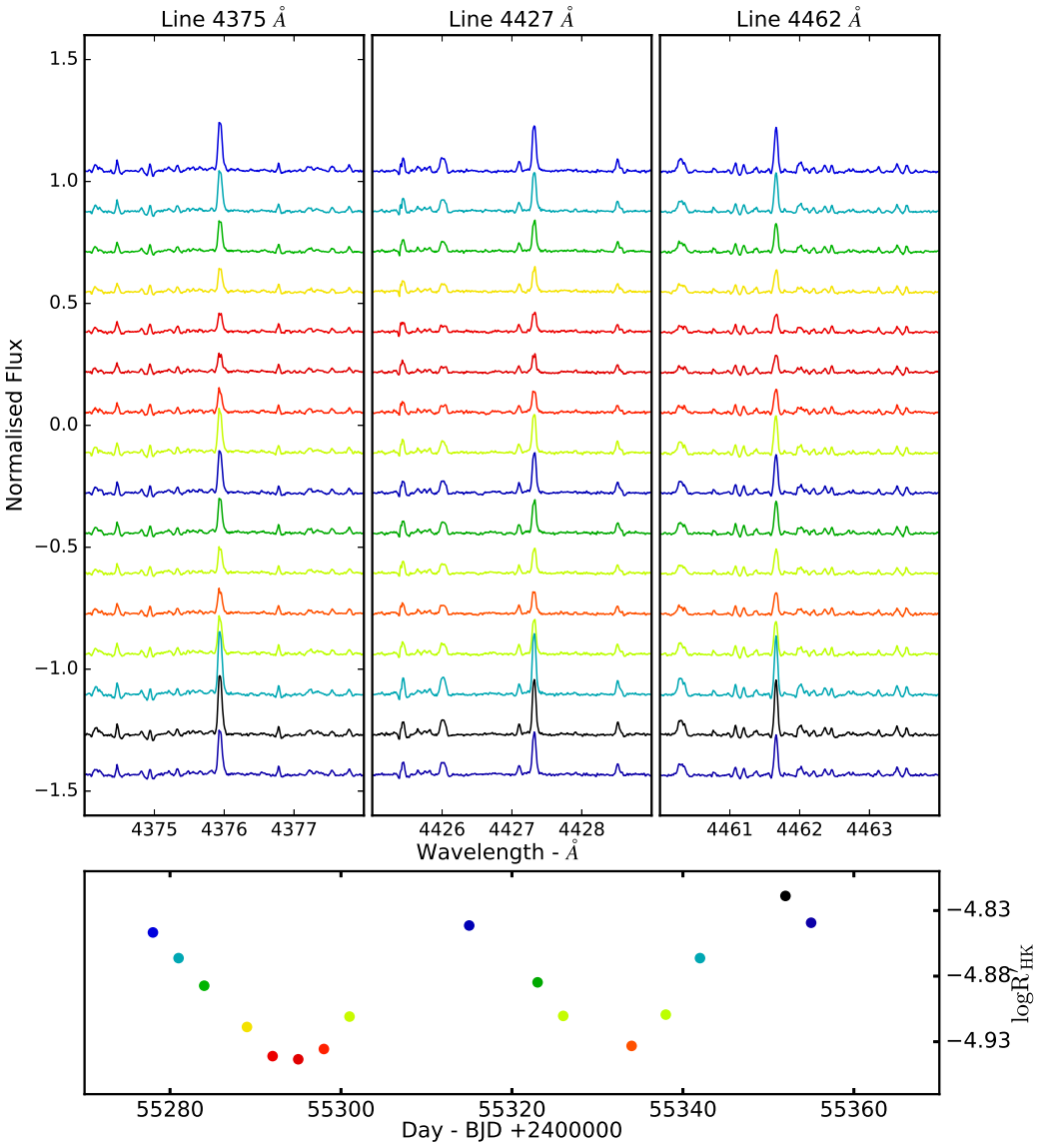


**Figure 3.6**: *Top:* The narrow features of 4375 Å, (left panel) 4427 Å (middle panel) and 4462 Å (right panel) seen in the relative spectra from the March-June 2010 period in a similar way to figure 3.5. *Bottom:* $\log R'_{HK}$ values for the relative spectra shown, the colour of the relative spectra corresponds to the activity level.

not be certain that the features they saw were activity driven, or caused by differences in the metallicities, age, $v \sin i$, temperature, surface gravity etc. between the active and inactive stars – a point raised by Basri et al. (1989) in their analysis.

Morphologically similar results to those reported by Basri et al. (1989) are seen here

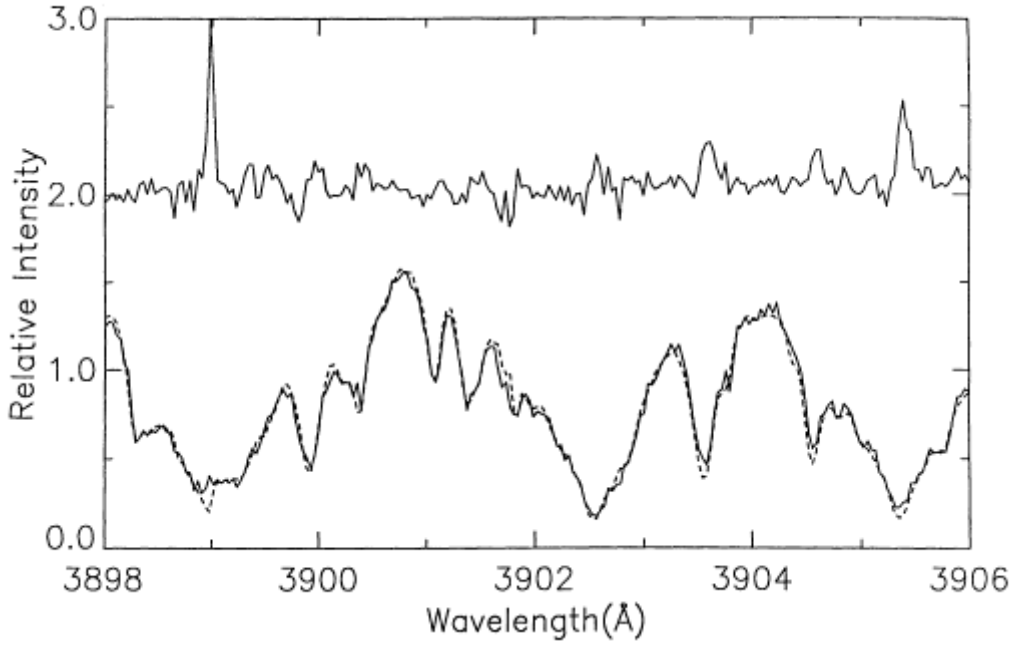


**Figure 3.7**: Relative spectra as generated by Basri et al. (1989), The lower plot shows spectra for the active star 36 Oph (solid line) and the inactive 'standard', taken as the average of two star (HR 6301 and HD 175541 spectra – dashed line). The upper plot shows the results of dividing the active star by the low activity standard, a clear pseudo-emission feature is seen at ~ 3898.5Å.

(but without the confusion generated by using different stellar types in the analysis). This work confirms that the bulk of the features reported by Basri et al. (1989) were indeed likely to have been activity driven. The strength of the features are also seen to change, this change is modulated on the stellar rotation period of $\alpha$ Cen B, which added further evidence to this conclusion. However, although unlikely, a number of other effects could also be responsible for the change in the lines. These are explored in the next two subsections.

### 3.3.1 Tellurics

Tellurics (or telluric contamination) are the effect of the Earth's atmosphere, where molecules in the atmosphere produce absorption lines. This means that for ground based observations any spectrum is really a combination of the object being observed ($\alpha$ Cen B in this case) with atmospheric absorption lines imprinted on top. For the HARPS instrument, tellurics are only seen to have a measurable effect on the spectrum beyond ~ 5500Å. As the pseudo emission features highlighted are over 1000 Å bluer than this (one of the reasons for selecting the wavelength range of 4300 - 5300 Å), tellurics would not be a reasonable explanation of the features.

Furthermore, as part of the standard HARPS data reduction pipeline, all spectra are radial velocity corrected to the barycentre of the Solar System. This correction includes perturbations from the rotational motion of the Earth, the influences of the moon, and the orbit of the Earth around the Sun. This is a necessary step in providing the most accurate RV measurement of a star. Telluric lines originate from the atmosphere of the Earth and as such will be shifted systematically compared to the stellar lines. When the relative spectra are created, all telluric lines produce features that look distinctly different from reported (see Figure 3.8).

As an example, consider the lines Fe I 6301 Å Fe I 6302 Å lines. These strong lines are used extensively by the Solar physics community to measure magnetic activity on the Sun (Martínez González et al. 2006), which would make them an excellent candidate for measuring stellar activity on other stars. However, these lines were not used in this analysis due to the strong O II telluric lines that are know to surround them. In the particular case shown in Figure 3.8 the tellurics produce a feature that closely resemble a inverse P-Cygni-like profile with a pseudo absorption trough to one side of the main peak. This is due to the mis-alignment of the telluric lines when the spectra are corrected to the barycentre of the Solar System and is the same for all tellurics. By comparing these telluric profiles to the Fe I lines, which produce a clear pseudo-emission peak, the two effects are clearly and easily distinguishable from one another.

### 3.3.2 Systematics

All spectrographs suffer to one degree or another from systematic effects due to optical imperfections and other instrumental effects. While HARPS is specifically designed to be a highly stabilised spectrograph it is still important to consider whether the observed pseudo-emission features could have arisen through instrumental effects. Here it is demonstrated that the features reported have characteristics that puts their nature at odds with that of a systematic effect and thus must be related to the star itself.

First, the changing strength of the features are modulated on the rotation period of the star, this is clear even by eye (a more rigorous treatment is given in section 3.5). It would be extremely difficult for an instrumental systematic to produce a feature that is modulated on a known astrophysical periodicity i.e. we can think of no reason for systematics to be modulated on the rotation period of the star.

Second, an additional effect is seen in the narrow pseudo-emission features, where two distinct morphologies are observed. This difference in feature shape could potentially be attributed to instrumental systematics, possibly due to some wavelength-

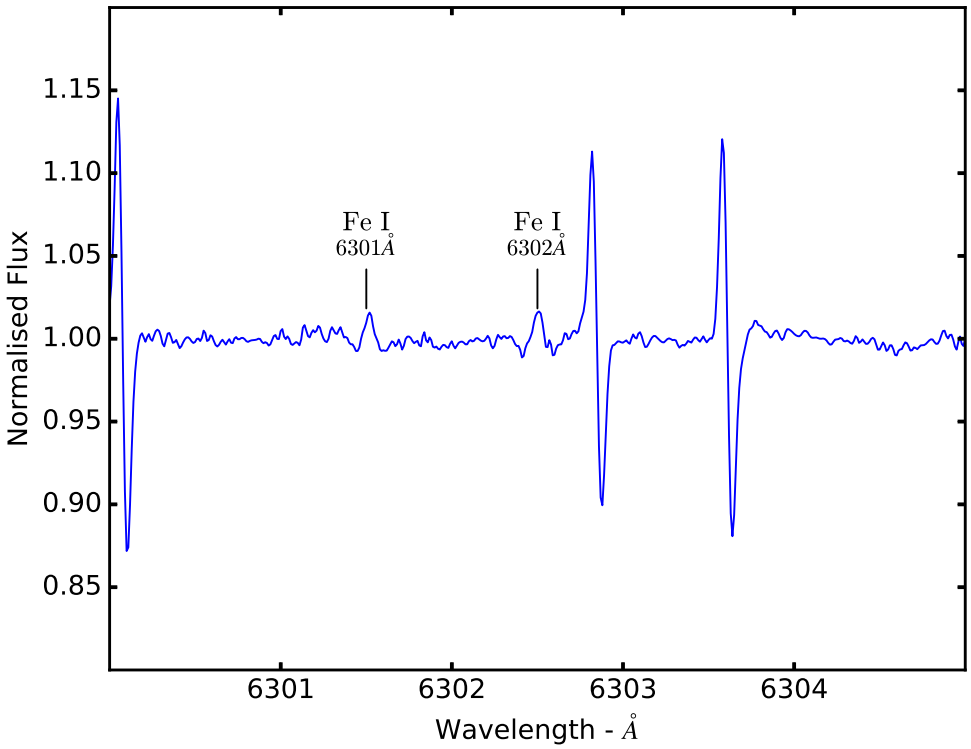


**Figure 3.8**: Comparison of the features produced by telluric effects to that of activity related features. The tellurics give an inverse P-Cygni-like profile due to the differential RV motion when correcting to the barycentre of the Solar System. The lines Fe I 6301 Å and Fe I 6302 Å, which are known to be good magnetic activity indicators, show a different pseudo-emission like feature. This also helps demonstrate why this part of the spectrum was avoided when producing the relative spectra.

dependency. Two example pseudo-emission features are shown in Figure 3.9, where the two lines are separated by less than one angstrom yet show very different morphologies. The HARPS instrument is, by design, an ultra-stable spectrograph, with instrumental stability an essential criteria for precise RV measurements. The different feature behaviours reported are over such a short wavelength range that, if this was due to instrumental stability, this would be outside the operational specification of HARPS. The morphologies of the narrow pseudo-emission features are therefore line-dependent (i.e. a product of the changing characteristics of the star) and not wavelength-dependent (which could be a sign of instrumental effects).

Third, there are numerous examples of similar strength lines that are closely positioned in wavelength, yet some show clear features in the relative spectra while other neighbouring lines exhibit no feature. This further supports the case of the features being line-dependent. For these reasons, it is highly improbable that the features are due to some unaccounted for systematics. A highly unlikely set of circumstances would be

needed to produce the features seen by anything other than a source located on the star $\alpha$ Cen B.

On a final note, the features could also be due to the chose of low-activity template being used. To test this, the night during the March-June 2010 period showing the lowest value of $\log R'_{HK}$ was instead used as the low activity template. The procedure of continuum matching and interpolating was performed again using this nightly stacked spectrum. The features were found in this case as well, with their strength weakened due to the higher activity of this low-activity template relative to the original low-activity template.

## 3.4 Explanation for the Pseudo-Emission Feature Morphologies

The features seen in the relative spectra can be categorised into different groups. One consists of broad features that contain the temperature sensitive lines alluded to by Giridhar (2010), and the other contains the narrow features – with most strong lines showing narrow features making these features a lot more abundant. These narrow features can be further subdivided into two distinctly different morphologies, with one group having a clear pseudo-emission peak near the line centre whilst the other shows a pseudo-absorption trough either side of the main 'emission' peak. This difference is thought to be a function of some changing properties of $\alpha$ Cen B and is most likely driven by activity given their modulation on the stellar rotation period during the highly active phase.

To further investigate the different morphologies a deliberately simplistic model was constructed to try and recreate these differences. For this modelling, two closely spaced features, the Ti II 4443.81 Å and V I 4444.21 Å lines, were chosen. They represent the two different morphologies (i.e. one showing an absorption trough and the other not), and are separated by $< 1$Å, which minimises the effect that wavelength changes could have (see Figure 3.8). The model considered the effect that an active region could have on the shape of a line profile. To investigate this, a disk was defined with a diameter of 1024 pixels. Geometric and limb darkening effects were added to the disk to better represent a stellar surface. The quadratic limb darkening law was used as defined by Kopal (1950)

$$\frac{I_\mu}{I_0} = 1 - c_1(1-\mu) - c_2(1-\mu)^2 \tag{3.2}$$

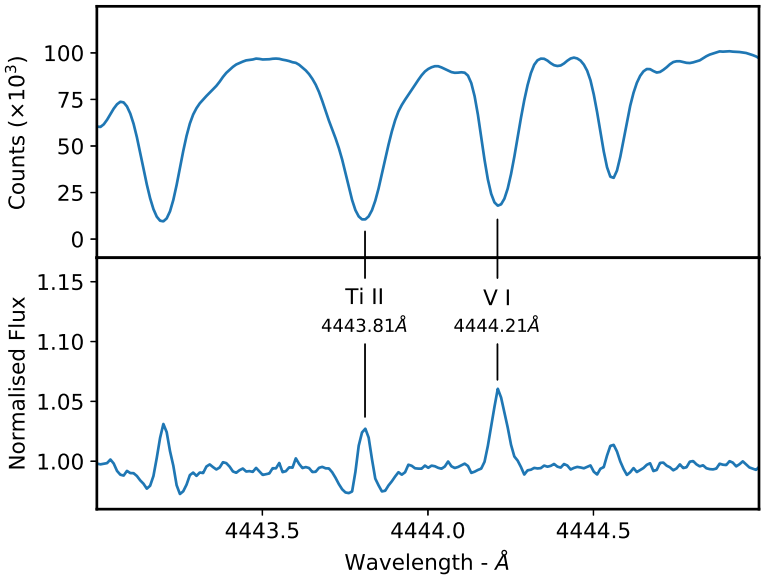


**Figure 3.9**: This highlights two lines (Ti II 4443.81 Å andV I 4444.21 Å) whose relative features show different moroplogies, as seen in the relative spectra. The *top panel* shows the two lines in the original spectrum while the *bottom panel* shows the features they produce in the relative spectrum. These are the features used as observed comparisons in the modelling active regions. These two lines are closely separated limiting any wavelength dependent effect and aiding in the modelling.

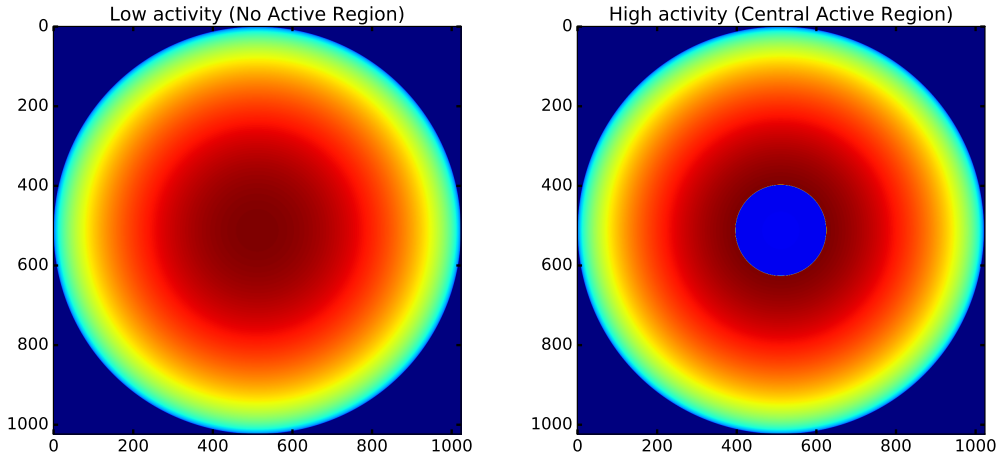


**Figure 3.10**: Example of the model used to investigate the relative features. The *left* plot represents the low-activity case with no active region (i.e. an immaculate photosphere) while the *right* plot is the high-activity model with an active region at disk centre. The colour represents the limb-darkening coefficient of that pixel. To create the model pseudo-emission feature, a Gaussian was generated for each pixel taking into account the relative stellar parameters (e.g. limb darkening, line depth, continuum level) and averaged over the whole disk. A line profile shape was generated for the high- and low-activity models and a relative line profile shape was then created by dividing the low-activity by the high.

where $\frac{I_\mu}{I_0}$ is the ratio of the intensity at a given location on the disk $\mu$, with $\mu = \cos\gamma$ where $\gamma$ is the angle between the normal and the line of sight of the observer; and $c_1$ and $c_2$ are the two limb darkening coefficients. For this work, the coefficients were taken from Claret (2000) for the stellar parameters of $\alpha$ Cen B– i.e. 0.72 and 0.1 for $c_1$ and $c_2$, respectively. Solid body rotation was assumed for the star, with a $v \sin i$ = 1.1km s$^{-1}$ (matching that of $\alpha$ Cen B – Maldonado et al. 2010)

Within each pixel of the stellar disk the absorption line profile was calculated as a Gaussian, taking into account the rotation and limb darkening effects , and then summed together to produce a disk integrated line-profile shape. This represents the immaculate photosphere of the star. To calculate the line profile for an active star, a circular spot was defined at the centre of the disk to simulate an active region. The continuum level for the active region was chosen such that it represents two spot temperates: a "cool" spot – having a temperature difference $\Delta T \approx 1400K$ compared to the surrounding immaculate photosphere (set to $5214K$, Dumusque et al. 2012) – and a "warm" spot – having a $\Delta T \approx 800K$. At the wavelength defined ($\sim$ 4444Å), this corresponds to the active regions having a continuum level of 10% and 30% that of the surrounding immaculate photosphere, respectively. The size of the active region was set to cover 5% of the disk (see Figure 3.10).

For both the immaculate and active star models, the parameters defining the Gaussian line-profile shape were varied in order to explore the cause of the features seen in the relative spectra. The intrinsic line width was set to 7.5 km s$^{-1}$(the approximate observed widths of the two lines chosen to fit). The depth of the line in the immaculate photosphere model was set to 0.9 (or 90% the depth of the continuum) – again, similar to the observed lines. For the active region, a range of line depths were considered. The values of 0 (i.e. no line in the active region), 0.5, 0.75, 0.99 (i.e. the line is almost saturated) were chosen to cover a full range of possible depths within the active region. Thus the line profile, $L$, for the disk can be modelled by summing together Gaussian line-profile shapes for each pixel from $n = 0$ to $n = Npix$ on the stellar disk. Formally, this can be written as,

$$L = \sum_{n=0}^{Npix} S_n \Big( 1 - D_n \exp\Big( \sigma_n \big(v_{grid} - v_n\big)^2 \Big) \Big) \tag{3.3}$$

where $S_n$ is the limb-darkening effect, $D_n$ is the depth of the line, $\sigma_n$ is the width of the

line and $v_n$ is the radial velocity component all evaluated at pixel $n$. Finally, $v_{grid}$ is a grid going from $-25$ to 25 km s$^{-1}$ over which the summed line profile was computed (in velocity space). Two model line profiles were created, one representing high-activity state and the other representing a low-activity state. The model 'relative' line profiles were created by dividing the high- by the low-activity states for the range of model parameters described, mimicking how the data was treated for $\alpha$ Cen B.

These parameters define the 'baseline' model, the results from which can be seen in Figure 3.11. In this case a clear pseudo-emission peak can be seen in most cases (with the extreme case of a lower contrast spot generating a deeper line giving a pseudo-absorption feature instead). This is evidence that dark spots (or more likely a spot group) could be the cause of the feature seen in V I 4444.21 Å (see Figure 3.11). The active region continuum level and line depth show a correlation, whereby the effect of increasing one can be counteracted by changing the other. An example can be seen for a model feature generated by assuming a line depth of 0 inside the active region (continuum level at 10% that of the immaculate photosphere), this looks very similar to a relative feature generated assuming a line depth of 0.5 inside the active region and the continuum level at 30% the immaculate photosphere (panels *a* and *f* in Figure 3.11).

This spot contrast may be a viable explanation for the pseudo-emission peaks seen in V I 4444.21 Å but cannot reproduce the obvious absorption troughs seen in Ti II 4443.81 Å. Only panel *d* in Figure 3.11 shows any hint of absorption but the strength and width of the feature in this case is far weaker than what is observed and, in fact, would be lost in the noise in the case of real data. This motivated the exploration of other parameters with the hope of generating something that may replicate the pseudo-absorption trough morphology. As a first attempt to better fit the pseudo-absorption trough, the size of the active region was increase so that it covered 10% of the visible disk, results of this iteration of the model are shown in Figure 3.12.

With a larger active region, the model shows broadly similar results to those of the baseline model (only having the effect of increasing the amplitude of the effects already seen in Figure 3.11, again panel *d* shows a small amount of absorption but this is still far weaker than the observed feature). This model still cannot recreate the Ti II 4443.81 Å feature, further increasing the size of the spot may produce a feature with the correct depth but it still is not able to produce the width seen in the relative feature. This spot coverage also reaches far beyond what is accepted for a star like $\alpha$ Cen B. It is possible to measure the spot coverage of close binary stars using Roche tomography. This is a process similar to Doppler imaging, where the presence of dark regions (spots) on the surface of a star can lead to pseudo-emission bumps in spectral

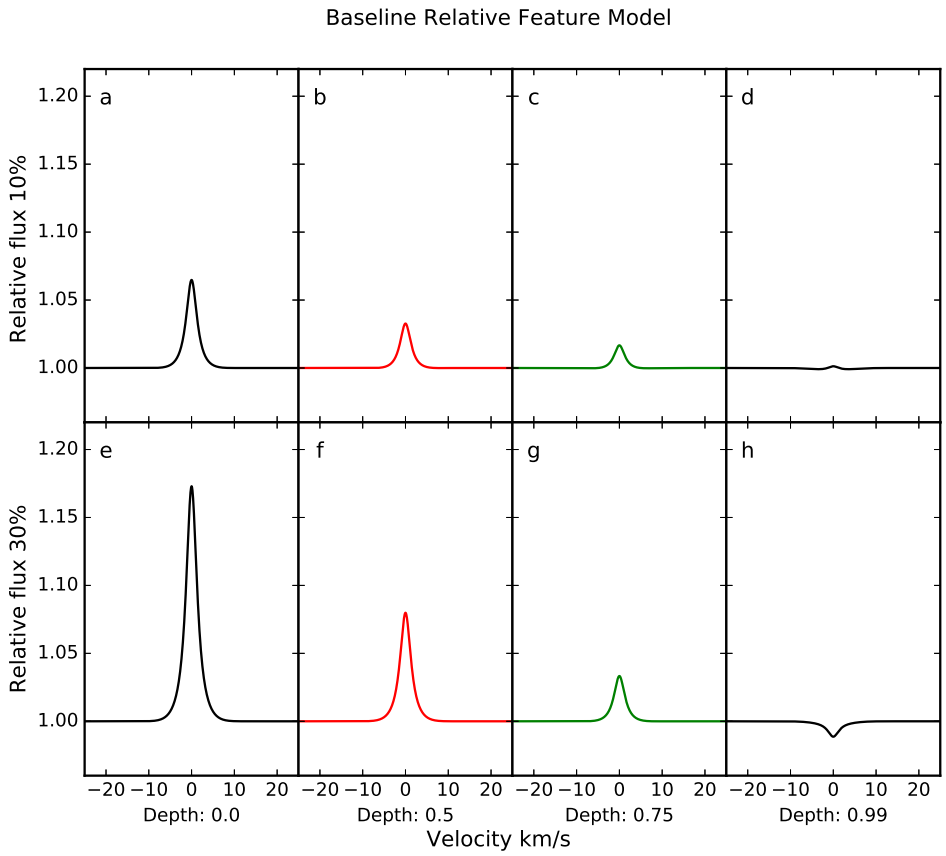


**Figure 3.11**: Baseline model for evaluating the nature of the features observed in the relative spectra. The top row shows the case with the continuum level in the active region set to 10% that of the immaculate photosphere, while the bottom row shows the case where it was set to 30% continuum. Each column then shows the different depth for the line in the active region, going from left to right they show lines that are 0.0, 0.5, 0.75, 0.99 the total depth, respectively.

lines (Vogt & Penrod 1983, see Figure 2.5). As the spots move across the surface of the star the pseudo-emission bumps move from the blue to the red-wing of the line, providing information about the stellar rotation at the latitude where the spot is. Roche tomography of cataclysmic variables (CVs) have shown main-sequence donor stars having spot coverages at the $\sim 20\%$ level (Watson et al. 2006, 2007). These fast rotating systems are very different to the quiet, isolated $\alpha$ Cen B but demonstrate the required levels of activity needed to produce high spot coverages. $\alpha$ Cen B is a slow rotator, like the Sun, and given the activity-rotation-age relation (Skumanich 1972), it can be expected to show similar levels of activity. Even at Solar maximum, a spot covering 1% of the solar surface is rare. Given the similarly long stellar rotation period of $\alpha$ Cen B it is highly unlikely to have a spot coverage this high. Thus using a spot coverage of 10% (or even further to match the features) cannot be a reasonable explanation for the observed features.

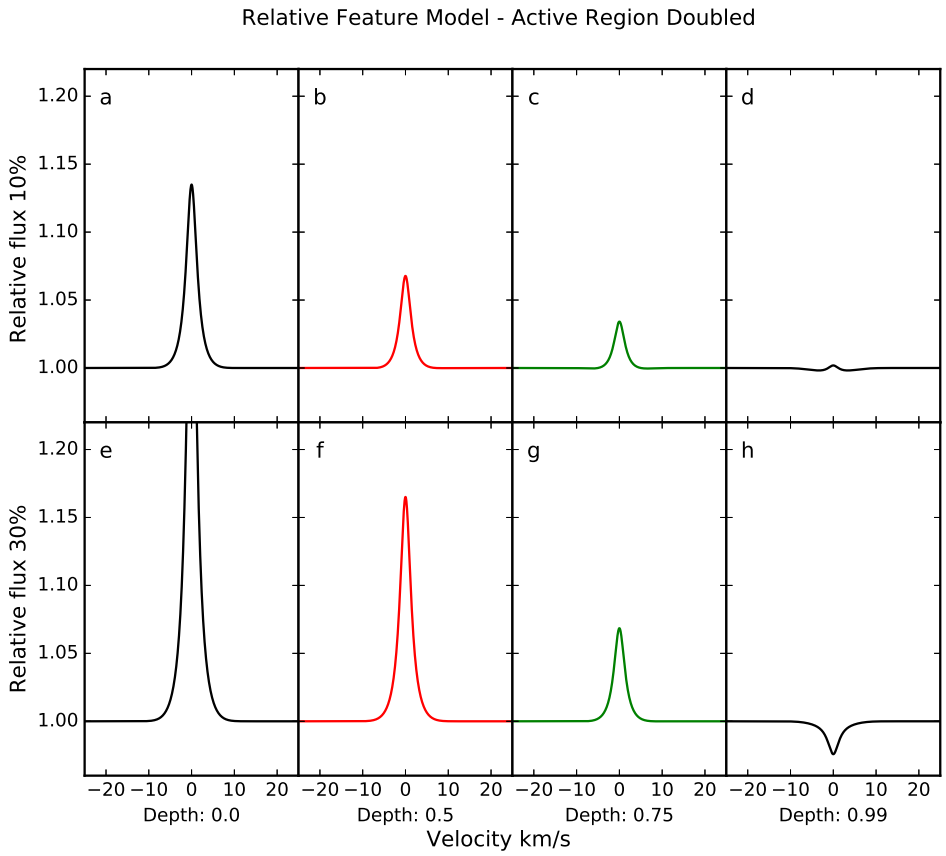


**Figure 3.12**: Same as Fig 3.11 but in this case takes active region has been doubled in size so that it covers 10% of the visible disk.

As increasing the spot coverage is not sufficient to reproduce the pseudo-absorption trough feature, the effect of changing the width of the line within the active region was considered. The width was set to 8.25km $s^{-1}$, which represented a 10% increase in the width of the line from the baseline value of 7.5 km $s^{-1}$. As active regions are a result of magnetic activity an increase in the field strength within the features may cause unresolved Zeeman splitting of the line (see red line of Figure 3.16), and it may be expected that lines within active regions could be broader than the surrounding photosphere. The addition of broader lines showed little appreciable impact on the shape or size of the model residual features (see Figure 3.13). In the models where the line depth in the active region is $\geq 0.75$ the continuum normalised line depth (i.e. panels *c*, *d*, and *g* in Figure 3.13) there are hints of an absorption trough, but again this fails to fit the width and depth of the relative feature seen. Again for this case, a low contrast active region with a deeper line produces an absorption trough.

The width of the line within the spot was further increased to 11.25 km $s^{-1}$, representing a line broadening of 50% than the immaculate photosphere. The pseudo-absorption trough becomes more clear in this case but is still not able to reach the depth

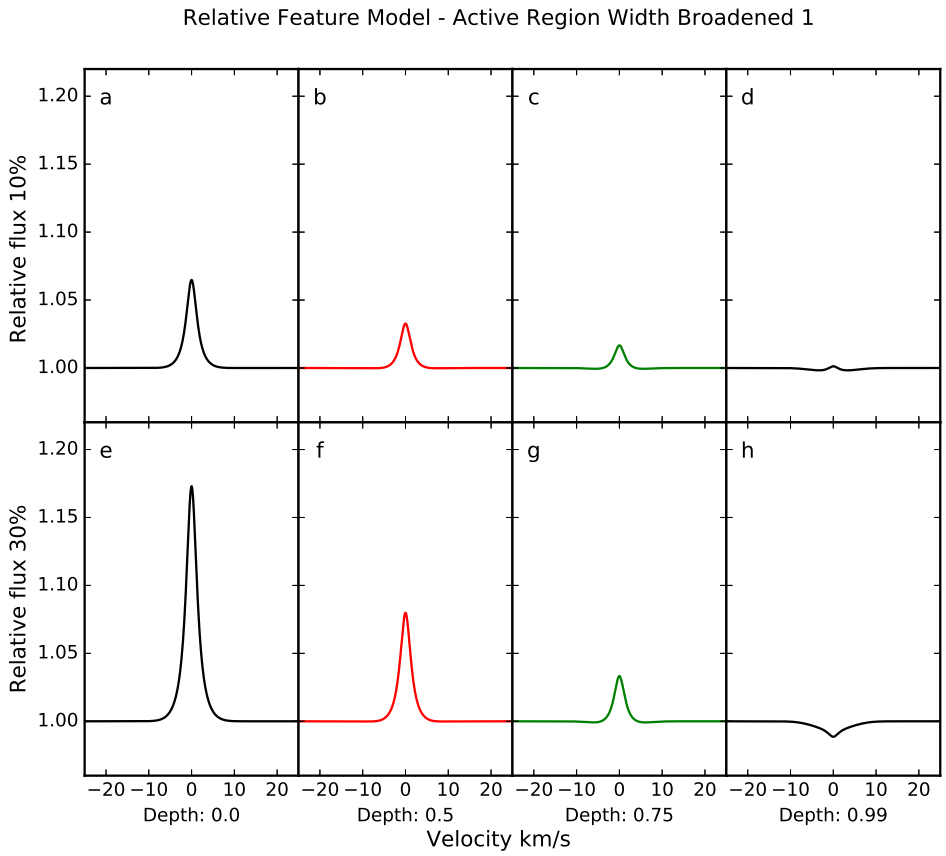


**Figure 3.13**: Same as Fig 3.11 but here the line within the active region is increased by 10% representing broadening due to increased magnetic contributions.

seen in Ti II 4443.81 Å (see Figure 3.14). Further broadening of the line within the active region may be able to better reproduce the feature observed but a broadening of 50% already represents an unphysical change to the line width. A small amount of broadening may be expected due to the increased magnetic field strength inside the active region causing unresolved Zeeman splitting of the line. However, Zeeman splitting would not be able to broaden the line by the amount needed to see the trough feature without also seeing the effects of Zeeman splitting in the spectral lines of $\alpha$ Cen B, which is not the case.

The final case looks at broadening the line outside the active region by a small amount i.e. making the line-profile shape in the immaculate photosphere of the active case broader than that of the inactive case. The line-profile shape was broadened by 2.5% compared to the low-activity template, while a line broadening of 10% was applied to the line-profile shape inside the active region. The rest of the parameters were kept the same as the baseline case. Again, the model relative feature was generated by dividing the (broadened) line-profile shape of the active by the inactive template. Figure 3.15 shows the outcome of this model. In this case a clear pseudo-absorption

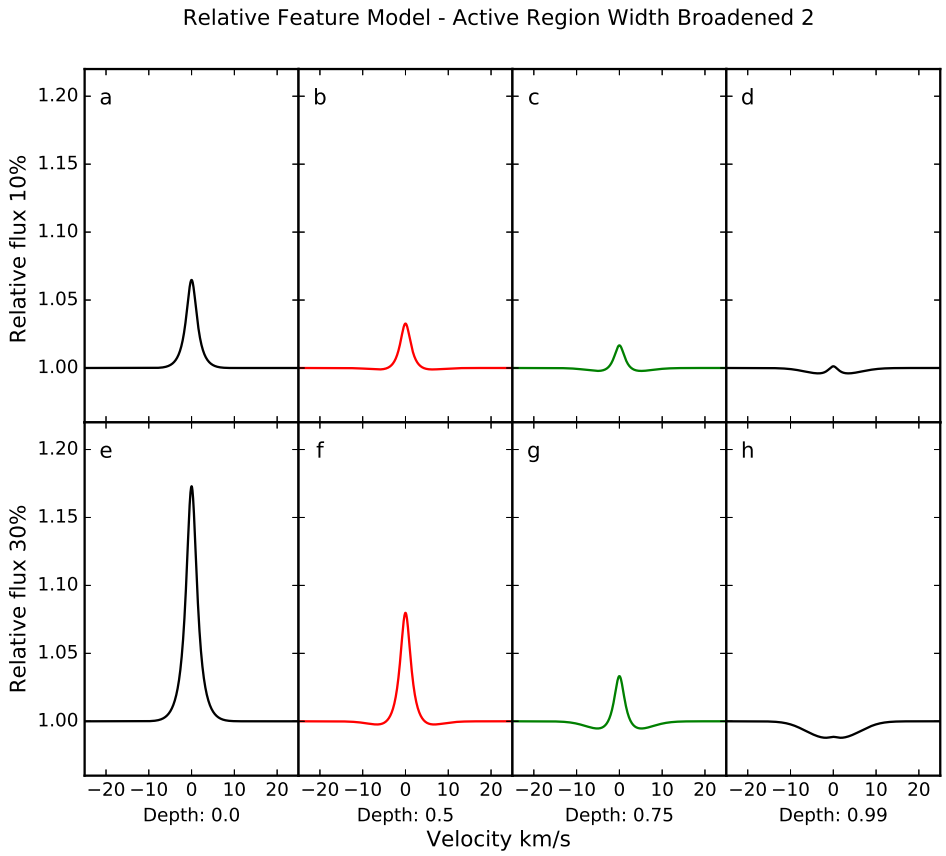


**Figure 3.14**: Same as Fig 3.11, however here the width of the line within the active region is increased by 50% relative to the immaculate photosphere, the pseudo-absorption troughs are more obvious but this represents an unphysical solution to explaining the features.

trough can be seen in the relative feature, this is a much better qualitative match to all the previous models.

This suggests that activity driven changes to the line-profile originating from the, so-called, immaculate photosphere best explains the observations. The work by Cegla et al. (2013) lends evidence that may explain these changes. Cegla et al. (2013) looked at the effect of activity on the line-profile shape, breaking down photospheric granulation into four components using a three-dimensional magnetohydrodynamic simulation. One of these components arises due to Magnetic Bright Points (MBPs). MBPs are small, bright, highly magnetic (typically of the order of 1kG) regions on the surface of the star that are thought to be the foot points of magnetic flux tubes in the darker intergranular lanes. The brightness of these MBPs is due to the reduced pressure within the flux tube allowing for a view of a deeper hotter region of the photosphere (Choudhuri 2007).

In the Sun, these MBPs are ubiquitous across the solar surface with the number of

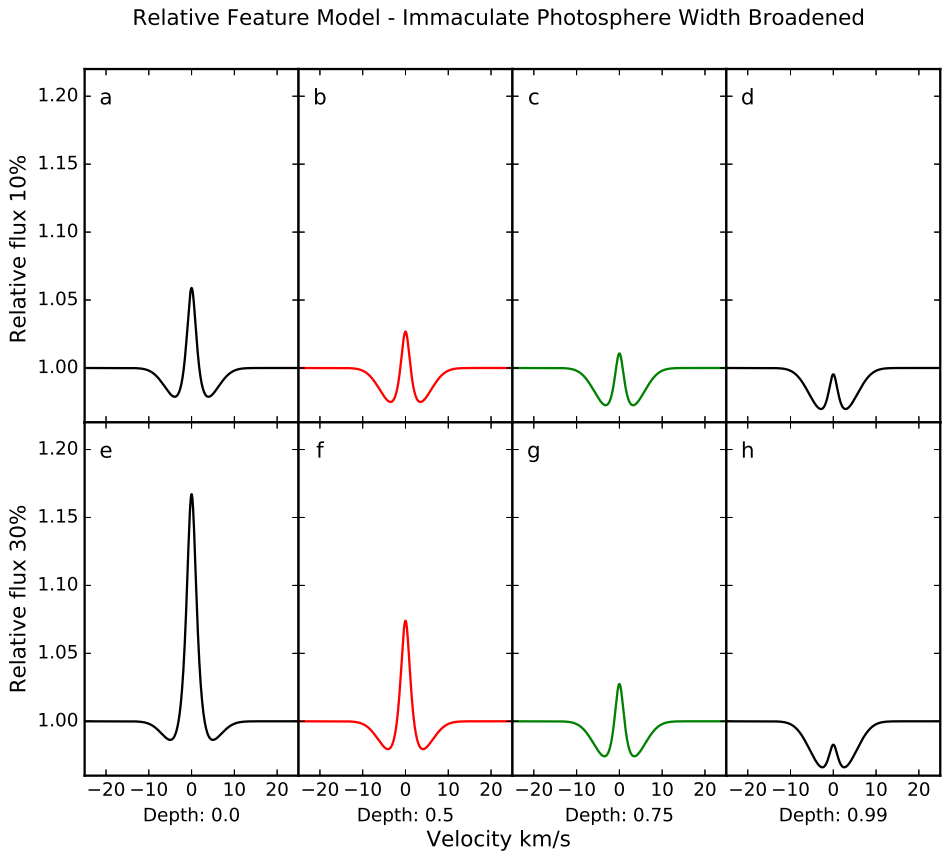


**Figure 3.15**: Same as Fig 3.11 for a broadening of 2.5% for the line width in the photosphere surrounding the active region with MBPs used to justify this change. The pseudo-absorption troughs so prominent in the relative spectra are now clearly seen.

such points being strongly linked to its magnetic activity. In the case of $\alpha$ Cen B, the higher activity March-June 2010 period would be expected to generate more MBPs on the surface (and thus a larger contribution) compared to the low-activity period. The models of Cegla et al. (2013) show a broadened Zeeman splitting of the line contribution from the MBPs that, when summed together with the other components of the model (granules, magnetic and non-magnetic lanes), has the effect of broadening the line profile (see Figure 3.16 – more detail available in Cegla et al. 2013). At disk centre, the MBPs show a red shifted component only, the effects of which are lessened when moving towards the limb. This would mean that the addition of MBPs could only explain the redward pseudo-absorption trough and not account for the full feature seen for Ti II 4443.81 Å. However, Cegla et al. (2013) focused on a model for a Sun-like star while $\alpha$ Cen B is a K1V star and may exhibit differences based on its later spectral type.

A study by Beeck et al. (2015) performed a similar analysis to Cegla et al. (2013) looking at the influence of magnetic activity on the shape of spectral line profiles using radiative magnetohydrodynamic simulations for a range of main-sequence stars (from

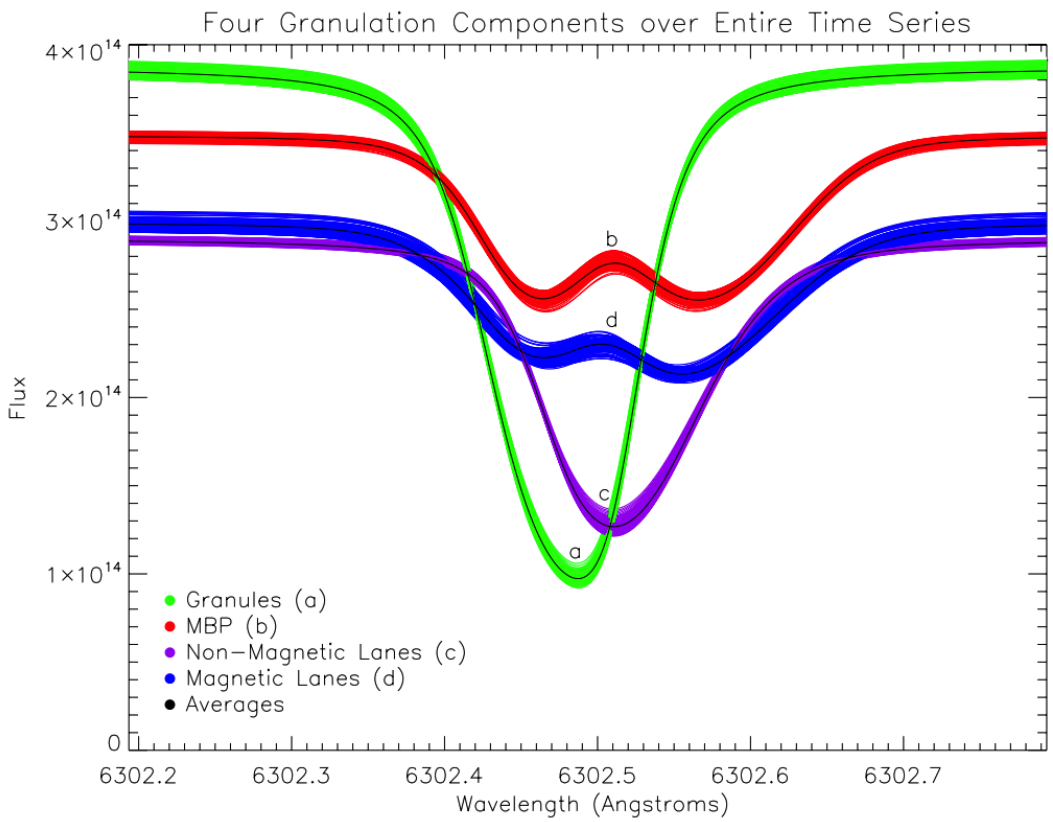


**Figure 3.16**: Four line component model of Cegla et al. (2013), with the different components coloured as labelled. The Magnetic Bright Points (MBPs), red lines, show a slight red shifted broader, Zeeman split, line width. Summing this with the other components would result in a slight broadening of the line profile, suggesting that during higher activity periods (when MBPs are more numerous) a broadening of the spectral lines could be expected.

F to early M). Where Cegla et al. (2013) looks at the interaction of known features on the Solar surface (such as MBPs and granules) and their contributions to the line profile, Beeck et al. (2015) breaks the various contributions into differing magnetic field strength (see Figure 3.17). Their simulations show that for a hotter F type star the line profile contribution belonging to areas having a magnetic field strength of 750 - 2000G (the expected field strength range for an MBP) has the same redward shifted effect as seen by Cegla et al. (2013). However, when moving to the cooler spectral type of a K1V the asymmetry in the line profile contributions almost entirely disappears (see Figure 3.17). This may be due to the different sizes of the convective envelopes in each case. For higher mass stars the smaller convective envelope size leads to a large difference between the upflows and the downflows and so exhibits a larger convective blueshift, with small 'jet'-like granular velocities and larger, slower moving intergranular lanes. For K stars this velocity difference is smaller, granules and intergranular lanes have sizes that are more similar (Figure 3.18, taken from Dravins 1990, shows a

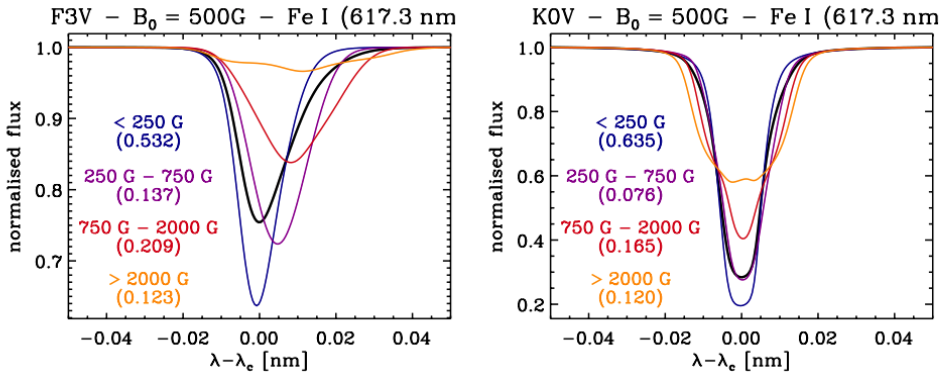


**Figure 3.17**: Four component model of Beeck et al. (2015) for a range of spectral types. The line in red is assumed to be MBPs as it covers the same range of magnetic field strengths expected for the feature. The F3 V model (right) shows that the MBP component is red-shifted similar to that reported by Cegla et al. (2013). The K0 V (left) shows all components lined up around the line centre, supporting the argument that MBPs could be responsible for the pseudo-absorption trough seen in $\alpha$ Cen B (a K1 V star).

schematic of this) so the convective blueshift component is smaller. As $\alpha$ Cen B is a later K1 V type star this supports the interpretation that the pseudo-absorption troughs seen in the relative spectra could be caused by an increased numbers of MBPs during the star's more active phase.

The results from the simple modelling show that the pseudo-emission feature V I 4444.21 Å can be reproduced by invoking the use of a darkened active region (i.e. a spot) on the surface of the star. A mixture of continuum contrast effects and change in line strength (due to temperature differences) is able to readily reproduce the feature seen. The feature with the pseudo-absorption trough, Ti II 4443.81 Å, is more complex and here it has been argued that, as well as an active region (a necessity to facilitate the modulation in the feature strength with rotation period), during its high-activity phase the star $\alpha$ Cen B possibly contains an increased number of MBPs on its photosphere.

The results of the relative spectra show that the spectrum of $\alpha$ Cen B looks distinctly different during its high-activity phase compared to quiescence. The modelling of the pseudo-emission feature morphology shows that not only is it the existence of active regions on the surface of $\alpha$ Cen B that make the spectrum look different but the 'immaculate' photosphere (i.e. the part of the photosphere thought not to be influenced by activity) is not the same during the star's more active phase. The existence of MBPs could be one explanation for this difference, as they could cause a broadening of the line-profile shape. Plage exists in a similar environment to MBPs (i.e. in the intergranular lanes regions that show higher levels of activity), its low contrast make it difficult

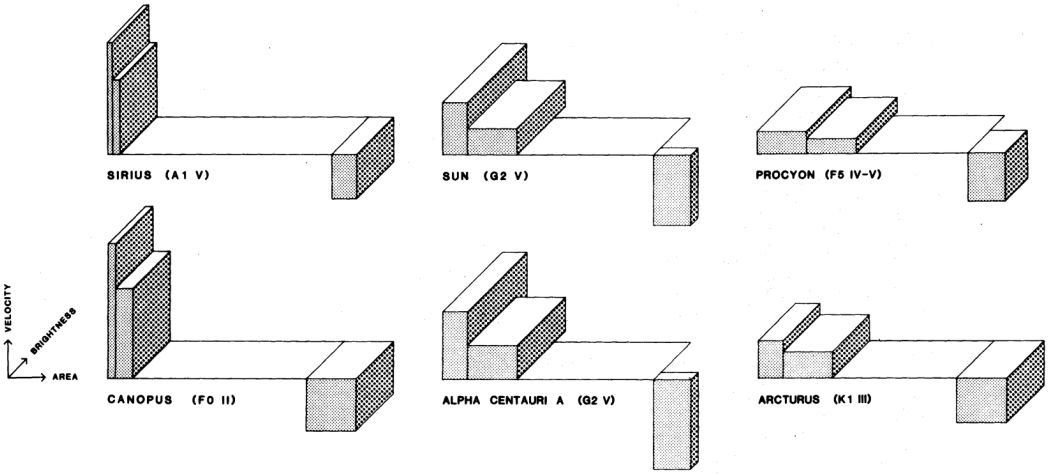


**Figure 3.18**: Schematic showing the filling factors, brightness, and velocities of surface features (due to convection) on stars of different stellar types, the contribution of each is indicated by the dimensions of the blocks (see lower left). In each schematic, four components of granulation are represented by these blocks, these are (going from left to right), granular centres, granules, neutral areas, and intergranular lanes. Note that earlier type stars show 'jet'-like granular velocities and hence large convective blueshifts, while later type stars show granules and intergranular lanes having velocities that are of similar magnitude, making the convective blueshift of these stars much smaller. Image taken from Dravins (1990).

to detect, and subsequently remove. The large extent of plages can have a large RV impact on the spectrum of a star, however, none of the RV jitter mitigation techniques highlighted in Chapter 2 are able to properly account for it. The pseudo-emission features may be influenced by changes in the plage filling factor. The broadening of the immaculate photosphere needed to explain the pseudo-absorption troughs could also be explained by plage regions being more homogeneously distributed across the stellar disk.

### 3.4.1 Extension of the Simple Model using VALD

The results up until this point have been concerned with reproducing the features seen in the relative spectra without real concern for the expected change in strength to the lines in question given the active region temperatures used in the model. To further investigate this the line models of VALD (Vienna Atomic Line Database, Ryabchikova et al. 2015) were used to more completely model these line strength changes. Using the known stellar parameters of $\alpha$ Cen B three synthetic line depth models were extracted, one at the temperature of the star (5214 K, Dumusque et al. 2012) and the other two at the reduced temperatures of 3414 K and 4414 K, representing the active region having a continuum level 10% and 30% that of the immaculate photosphere, respectively. Ta-

| Temperature (K) | VALD Line Strengths | |
|---|---|---|
| | Ti II (4443.81 Å) | V I (4444.21 Å) |
| 5214 | 0.917 | 0.800 |
| 4414 | 0.912 | 0.930 |
| 3414 | 0.842 | 0.952 |
| 5414 | 0.905 | 0.690 |

**Table 3.1**: Breakdown of the continuum normalised line strength taken from VALD of the two lines used for the modelling of line morphologies given various temperatures representative of $\alpha$ Cen B photospheric temperatures and two spot temperatures of $\Delta T = -1400$ K and $\Delta T = -800$ K. A third case of $\Delta T = +200$ K, representing a plage regions is also shown.

ble 3.1 details the various continuum normalised line strengths given the temperatures assumed. All other model parameters use the values that gave the best fit prior to the VALD result i.e. active region set to cover 5% the visible disk; broadening of the line width inside the active region by 10% (broadening of the surrounding photosphere by 2.5% to reproduce the pseudo-absorption trough case); and active region continuum levels were set to 10% and 30% that of the surrounding photosphere.

At first inspection the line strengths of Ti II 4443.81 Å andV I 4444.21 Å lines were assumed to have the same strength in the immaculate photosphere (a continuum normalised line strength of 0.9). The results from VALD show that the line strengths are slightly different (see Table 3.1). The model was rerun using these different line depths but no obvious change in the modelled relative features were observed. This modification only changes the models in small details, changing the strength of the relative features. This different still was not able to explain the pseudo-absorption troughs, so the interpretation given in the previous section (that a change in the immaculate photosphere is needed to produce the features) is still valid.

In fitting these parameters, it was found that assuming a cooler spot was not able to alter the line strengths in a way that could convincingly reproduce the features seen in the relative spectra (see right panels of Figure 3.19). The pseudo-absorption trough of Ti II 4443.81 Å is reproduced using the newly defined line strengths – supporting the case of a change in the immaculate photosphere of the star (e.g. MBPs and plage) being the source of this morphological features – but fails to reproduce the V I 4444.21 Å pseudo-emission peak, with the warmer spot temperature of 800 K producing an absorption feature (see green dotted line in the lower right panel of Figure 3.19). Instead of a spot, plage is considered for the active region. These regions are hotter than the surrounding photosphere and can be larger in extent than spots. A temperature

of +200 K was chosen for the active region and the VALD models rerun at this new effective temperature, the resulting continuum normalised line strengths are included in Table 3.1.

The active region modelling was subsequently rerun at the new line strengths and assuming a 200 K hotter active region (resulting in a ~ 16% increase in the continuum level within the active region). The pseudo-absorption trough of Ti II 4443.81 Å is again reproduced with a similar strength as before and the peak seen in V I 4444.21 Å is now readily observed (see blue dashed line in the right panels of Figure 3.19). Figure 3.19 shows the "best fits" for the two modelling approaches (with the middle panels showing the non-VALD driven results and the right panels showing the VALD driven approach) as well as the two lines being fitted.

To summarise, the best fit model found that in order to reproduce the pseudo-absorption trough seen in the Ti II 4443.81 Å relative feature the immaculate photosphere of the high activity model needed to be broadened. This was justified as being due to an increased amount of MBPs and plage on the surface during a star's more active phase. Extension of the modelling using continuum normalised line depths from VALD, showed that a cooler spot region was not able to produce the pseudo-emission feature of the V I 4444.21 Å line and, instead, a hotter plage region was needed to properly model for the feature. The VALD driven approach also required a broadening of the immaculate photosphere to model the Ti II 4443.81 Å relative feature.

### 3.4.2 Model limitations

In Figure 3.19 the models show good agreement to the observed relative features given the simple nature of their construction. The model, however, does not take into account many real aspects of activity that would additionally affect the shape of the feature. As an example, the model assumes a single active region at the centre of the stellar disk, when, in reality, the most likely cause of the activity change seen in the $\log R'_{HK}$ is a number of active regions scattered across the stellar disk. Groups containing spots would also contain plage (as they are both caused by increased magnetic activity they are likely to be spatially associated), while unassociated plage regions would also exist. This leads to a more complex picture of a combination of spot and plage that may or may not be spatially associated. The limb angle projection effect also needs to be considered, where effects such as Wilson depression in spots, or the corrugated nature of granulation causing limb brightening of plage would impact the spectrum. The model also assumes solid body rotation, which is known not to be the case for stars. The Sun, for example, shows a differential rotation rate, with a period of ~ 24.5 days at the

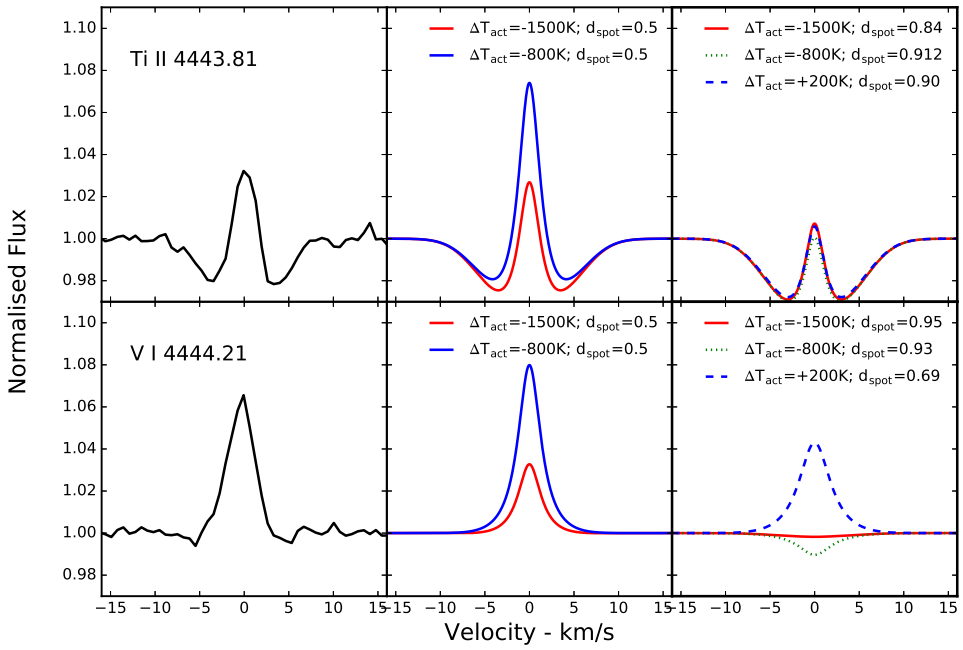


**Figure 3.19**: *Left panels:* Two examples of narrow pseudo-emission profiles in the observed relative spectra from closely spaced (~0.4 Å) and approximately equal strength lines. Both of these profiles show distinctly different morphologies, with the Ti II 4443.8 Å line (Top) displaying a clear pseudo-absorption trough. *middle panels:* Results for a simple model with a 5% spot feature at disk centre, having a continuum contrast corresponding to a ΔT of ~1400K and ~800K. The line absorption in the spot is ~50% weaker than the immaculate photosphere. For the top panel it is assumed that the immaculate line profile in the active spectrum is broadened by 2.5% relative to the inactive immaculate photosphere case – this results in the observed absorption trough. In the bottom panel, the line-widths in the active and inactive immaculate spectra are identical. *Right panels:* Models using the normalised line depth from VALD of the given temperature differences. An additional model of ΔT= +200K is also shown, which is a proxy for plage rather than a spotted region.

equator as compared to ~ 38 days at the pole. How this affects the line shape for active regions moving at these different velocities (due to different latitudes), would need to be considered.

The intention of the model was never to determine the size, distribution and type of active regions that could exist on the surface of $\alpha$ Cen B but was rather to perform a basic test of the hypothesis that activity could be responsible for the features seen in the relative spectra. The model presented demonstrates that activity (whether it is spot, plage, MBPs, or a combination of all three) can cause the features seen in the relative spectra and points to the conclusion that the 'immaculate' photosphere of $\alpha$ Cen B is different during its high-activity phase compared to its low-activity phase.

## 3.5 Measuring Equivalent Widths

The features shown in Figure 3.4 show a change in strength that appears to vary with the activity (as measured by $\log R'_{HK}$). To better quantify this change a number of features were selected and their strength measured. To do this a Gaussian was independently fit to each of the lines used and the area under the Gaussian taken as a measure of the strength of the feature. This 'pseudo-equivalent width' measure was performed for all relative spectra in the March-June 2010 period. Errors on the pseudo-equivalent width were taken as the standard error $\sigma_{\bar{x}}$ defined as

$$\sigma_{\bar{x}} = \frac{\sigma}{N} \tag{3.4}$$

where $\sigma$ is the standard deviation of the difference between the values and the fitted Gaussian and $N$ is the number of observations.

For this analysis three lines were chosen, those of Fe I 4375 Å , Fe I 4404 Å , and Fe I 4383 Å . These lines are all close to one another (limiting any wavelength dependent effects that could exist) and show a range of morphologies, with the Fe I 4383 Å and Fe I 4404 Å features both being broad features while the Fe I 4375 Å feature is narrow. No features showing a pseudo-absorption trough were selected as their shape is non-Gaussian in nature. Finally, all selected features are Fe I species, which are known to be photospheric in nature. This means that tracking changes in these lines can be more directly linked to changes on the photosphere of $\alpha$ Cen B and support the argument that the changes are activity related.

Extra processing was necessary on the broad features as the centre of the features exhibited what appears to be a narrow pseudo emission feature. This, however, leads to a non-Gaussian shape to the feature and so needed to be removed before fitting – this was done for both broad features. Additionally, Fe I 4383 Å also shows a number of narrow pseudo-emission features on its red wing, these were also removed before fitting (Figure 3.20 shows one such example).

In Figure 3.21 the pseudo-equivalent width of the three features are plotted for the March-June 2010 period. As mentioned previously, this period is characterised by a large change in the $\log R'_{HK}$ values that show a periodicity due to active regions on the surface of the star rotating in and out of view. In Figure 3.21 a clear periodic modulation of the strength of the pseudo-equivalent widths can also be seen, with a periodicity similar to that of the stellar rotation period (left plots of Figure 3.21). This alone suggests that the features reported are, in fact, due to changes on the surface of the

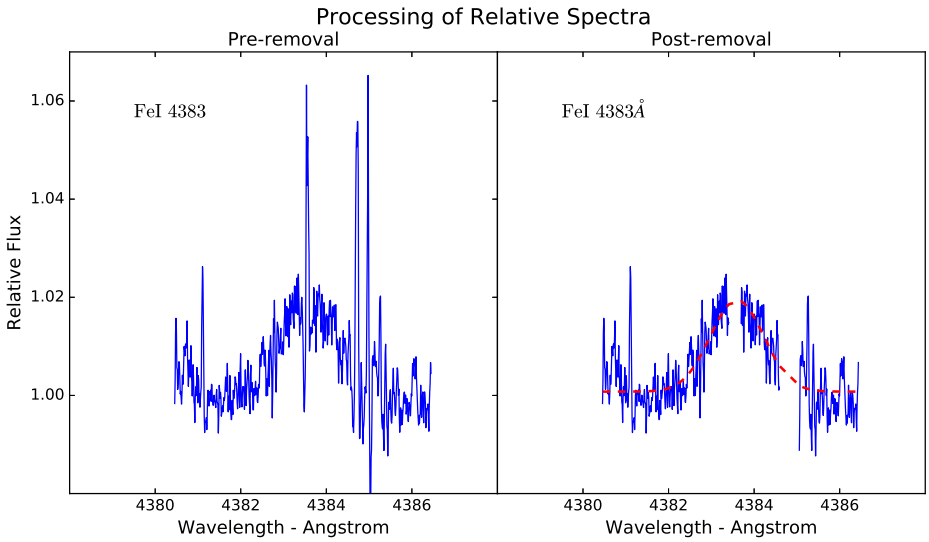


**Figure 3.20**: Example of pre- and post-snipping of the line Fe I 4383 Å to aid in the fitting of a Gaussian for pseudo-equivalent width measurements. The red dotted line shows an example Gaussian fit.

star $\alpha$ Cen B. This result is further strengthened when correlating the pseudo-equivalent widths with $\log R'_{HK}$(right plots of Figure 3.21). A strong positive correlation can be seen, and a Pearson's r statistic run on these correlations returns values of 0.97, 0.96, and 0.99 for the lines Fe I 4383 Å , Fe I 4404 Å , and Fe I 4375 Å , respectively.

This result more rigorously demonstrates how the changes observed in figure 3.4 mimic the rotational variation seen in the value of $\log R'_{HK}$. Combined with the modelling of the morphologies it is clear that the features seen in the relative spectra are a result of activity on the surface of the star.

## 3.6 RV Variation of Pseudo-emission Features

If the features are activity driven it would be expected that as active regions traverse the visible hemisphere of the star the peak of the features would shift and exhibit an RV motion. To test this, each relative spectrum was cross-correlated against a template to measure the RV variation. This template was created by taking one relative spectrum during the March-June 2010 period ($23^{rd}$ March 2010 was selected, it is the first night of that period and also contains relatively strong features) and fitting Gaussians to the strongest features. All features within the range $4300-5300$Å (the range over which the data was processed) whose relative strength was greater than 5% of the baseline of the residuals were selected. A Gaussian was independently fit to each of the features and combined into a model relative spectrum, and used for the cross-correlation.

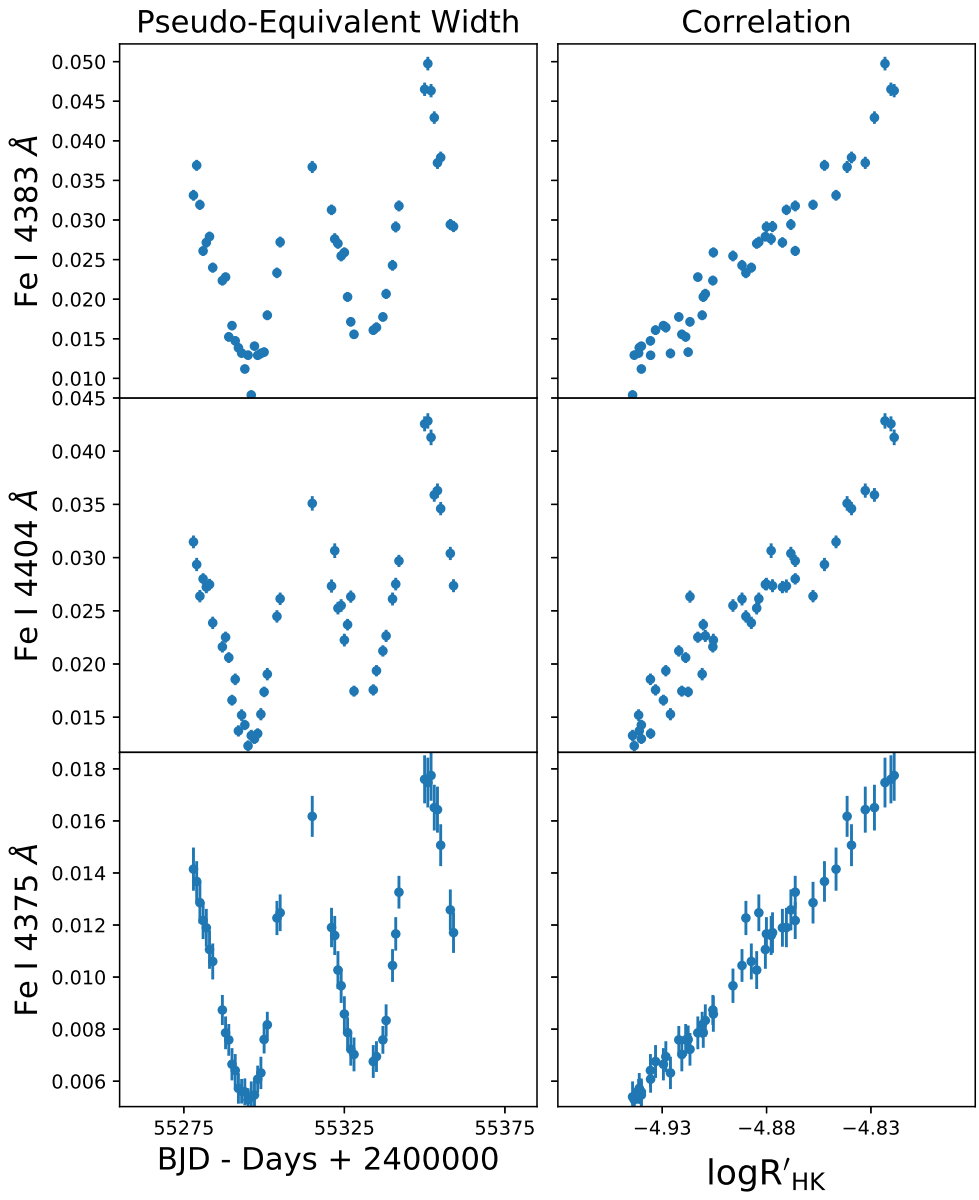


**Figure 3.21**: *Left:* The pseudo-equivalent width of the three features Fe I 4383 Å , Fe I 4404 Å , and Fe I 4375 Å seen in the relative spectra. The strength of the pseudo-equivalent width is plotted against day for the March-June 2010 period and shows a clear periodic modulation. *Right:* Correlation between $\log R'_{HK}$ and strength of the pseudo-equivalent over the same period. The error bars shown are standard error estimates.

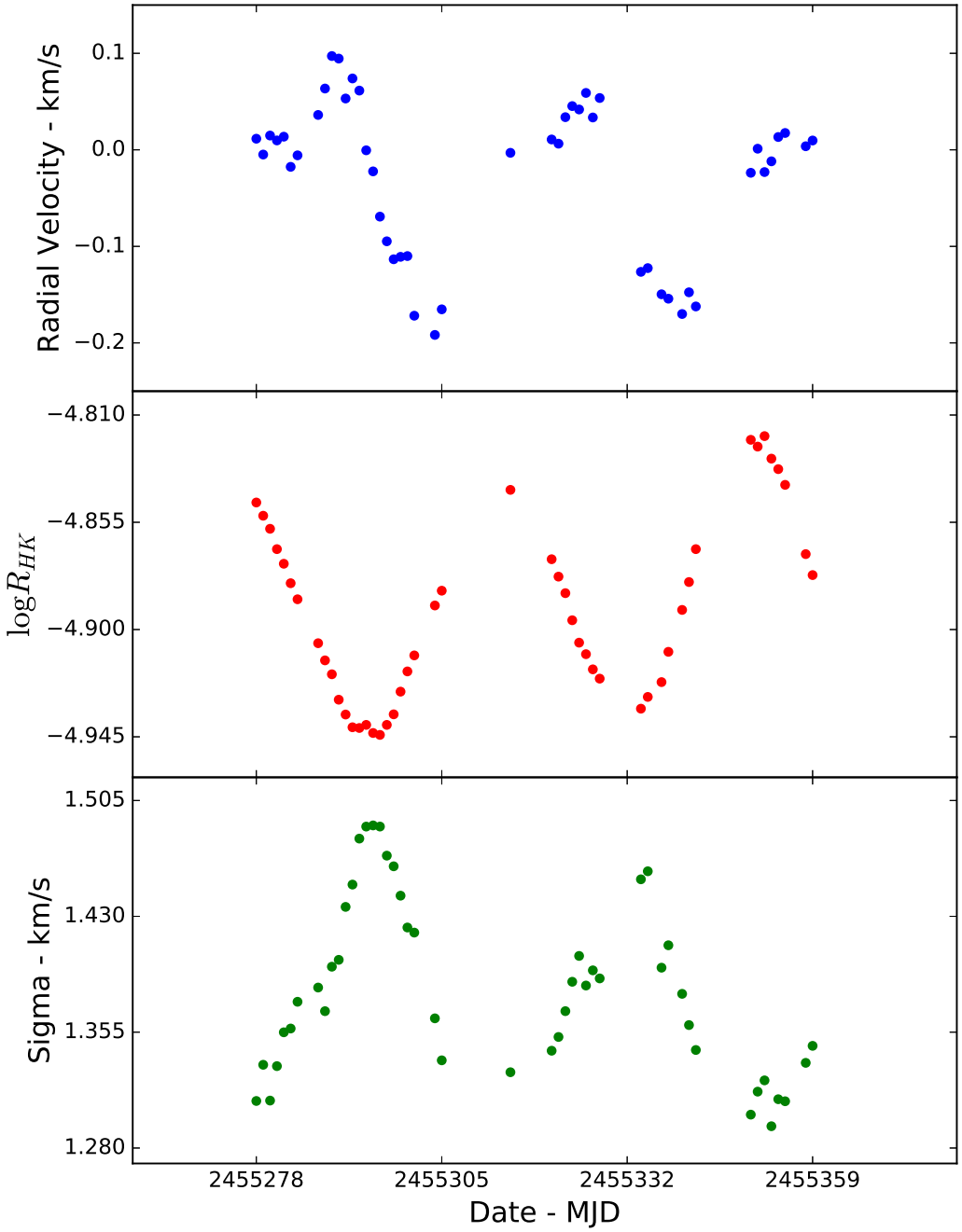


**Figure 3.22**: *Top:* The radial velocity measurements, as defined by the peak of the cross correlation function, for the narrow features in the relative spectra. *Middle:* The $\log R'_{HK}$ as taken from D12. *Bottom:* The width of the cross correlation function. Both Top and Bottom plots show, with varying degrees of phase lag, the same period variation seen in $\log R'_{HK}$.

The model template was cross-correlated with each of the relative spectra during the March-June 2010 period and the peak of the cross-correlation function (CCF) measured. From this, a radial velocity was measured, which shows a peak-to-peak variation of $\sim$ 300 m/s (top panel of Figure 3.22). Comparing to the $\log R'_{HK}$ (middle panel of Figure 3.22), the RV motion of the pseudo-emission peaks shows a phase offset of approximately 90 degrees. This offset can be explained by considering a rotating active region on the surface of the star. At disc centre, $\log R'_{HK}$ is at maximum as the active region has maximum visibility, however the RV of the active region will be at 0 km s$^{-1}$ (relative to the systemic velocity of the system). As the feature rotates out of view towards the stellar limb, foreshortening will decrease $\log R'_{HK}$ , and the feature will become progressively red-shifted. Conversely, the opposite trend occurs as the feature rotates back into view, leading to a blue-shifting of the feature. This is akin to the motion of apparent emission bumps due to spots through stellar line-profiles, typically associated with more rapidly rotating stars suitable for Doppler imaging (Collier Cameron & Donati 2002; Vogt & Penrod 1983).

The width of the CCFs are shown on the bottom panel of Figure 3.22). These are anti-correlated with $\log R'_{HK}$, with the CCFs broadest when $\log R'_{HK}$ is lowest. This suggests that active regions are more homogeneously distributed across the stellar surface during times when the main active region has rotated out of direct view. The narrow CCF widths at high $\log R'_{HK}$ then lend support for the presence of a localised highly active region (and hence spanning a limited range in stellar surface velocities). Of course, this is likely to be a simplistic picture as it is probable that several active regions are present. The effects of plage and MBPs would also need to be considered as they are shown to be the likely cause of the pseudo-emission features (see Section 3.4). The motions of these MBPs or the plage may be different to spots so may need to be considered separately in a cross-correlation analysis. As such, a more in depth analysis of the effects of plage on relative peak morphology, and spots on the temperature sensitivity of the broad relative peaks of the Fe I species, is needed to better constrain the effects reported here.

## 3.7 Links to Spectral Line Properties

### 3.7.1 TiO Bandheads

This work was initially motivated by the success of measuring star spot filling factors by modelling molecular bands originating in spots, as developed by Neff et al. (1995); O'Neal & Neff (1997). This technique uses the ratio of the TiO band heads at 7055 Å and 8860 Å to determine the spot coverage and temperature. If the effective temperature of a star is high enough TiO will only form in the cooler starspots. As an example,

the bandhead at 8860 Å only forms in dwarf stars with an effective temperature of $\leq 3500$ K. The two bandheads have different temperature sensitivity and it is this difference that can be used to estimate the spot filling factor and temperature by combining various standard spectra with cooler M dwarf spectra (simulating the spot spectrum). Although the spectral range of HARPS does not extend up the these two TiO bandheads other band heads exist at $\sim$ 6500 Å. No previous analysis has been performed on this bandhead mostly due to its weaker nature. Using the relative spectra, no obvious change or features were observed at the expected position of the $\sim$ 6500 Å TiO bandhead suggesting that the weakened state of the bandhead makes it unsuitable for such an analysis or the temperature response of this bandhead is different from the ones used by Neff et al. (1995). Alternatively, the spot filling factor is too low to create significant TiO to allow for detection. This latter interpretation would support the conclusion that plage/MBPs, and not spots, are driving the differences in the spectral lines.

### 3.7.2 Landé Factor and Excitation Potential

The narrow pseudo emission feature morphologies may have links to the properties of the line they form from. The VALD line list includes information on line properties such as Landé factor – which is a measure of the magnetic sensitivity of a line – and excitation potential. These properties may correlate with the different morphologies seen.

The features in the relative spectra were categorised based on morphology, with features separated into those with a pseudo-absorption trough surrounding the peak and those without. This was a by-eye examination, the line list of VALD was used to determine the line centre, and all lines having a VALD strength $\geq 0.5$ (a total of 1300 lines) being evaluated in this way. The weaker strength of some of the features made it impossible to determine, by eye, if the pseudo-absorption trough was real or noise. These ambiguous cases were excluded, resulting in a final count of 950 features being positively identified, plus a further 37 where no feature was observed (full list available in Appendix A.1).

Histograms for both Landé g factor and excitation potential are plotted in Figures 3.23 and 3.24, respectively, where features showing a pseudo-absorption trough are labeled as ‘trough’ and those without are labeled ‘peak’.

In the case of Landé g factor, both feature morphologies appear to come from the same underlying distribution. In Section 3.4, MBPs were suggested as the cause of the pseudo-absorption trough, which have higher magnetic field strengths than active

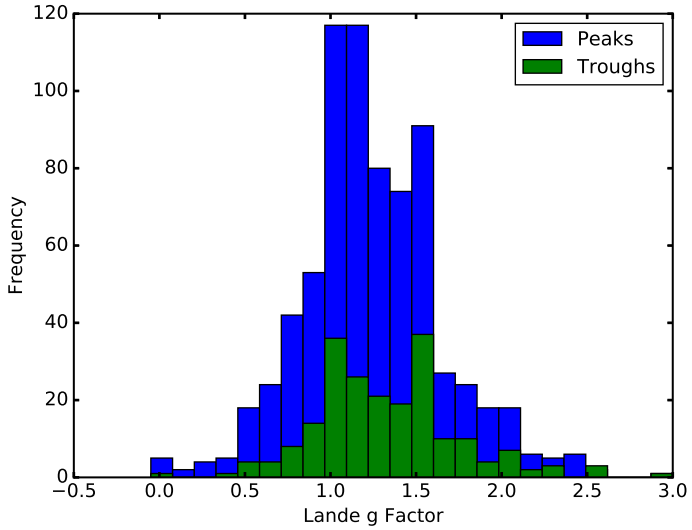


**Figure 3.23**: Both morphology types, features with a pseudo-absorption trough (called 'troughs' and shown in green) and features without (called 'peaks' and shown in blue) show the same underlying distribution in Landé g Factor. Feature morphology were identified by-eye.

regions like spots and plage. It would be expected that Landé g factor, being a measure of magnetic sensitivity, could be used as a proxy to gauge feature morphology with lines having a higher Landé g factor being more likely to show a pseudo-absorption trough.

Spectral lines form over a range heights in the stellar atmosphere, with the wings of a line forming deeper than the core. In a star, the magnetic field strength changes as a function of atmospheric height so any information gained from knowing the magnetic susceptibility of a line is lost as the line migrates up to the stellar surface. Additionally, lines begin to form at different heights (the Fe I lines, for example, are known to form in the photosphere of stars). This argument of line formation height makes it so that no clear correlation may be seen between the magnetic sensitivity of the line and the morphology produced in the relative spectra.

The situation for excitation potential is less clear and more difficult to interpret. The excitation potential takes a wider range of values so may suffer from low number statistics but may also be confused by different elements (see Figure 3.24). To explore this, individual excitation potential histograms for different elements were produced but due to low numbers only four have enough data to plot anything meaningful, these are: Cr, Fe, Ni, and Ti (see Figure 3.25). In the plot, Cr and Ti show a preference for lower excitation potential for morphologies showing the pseudo-absorption trough. A bimodal distribution can also be seen for most cases, most likely due to the existence of

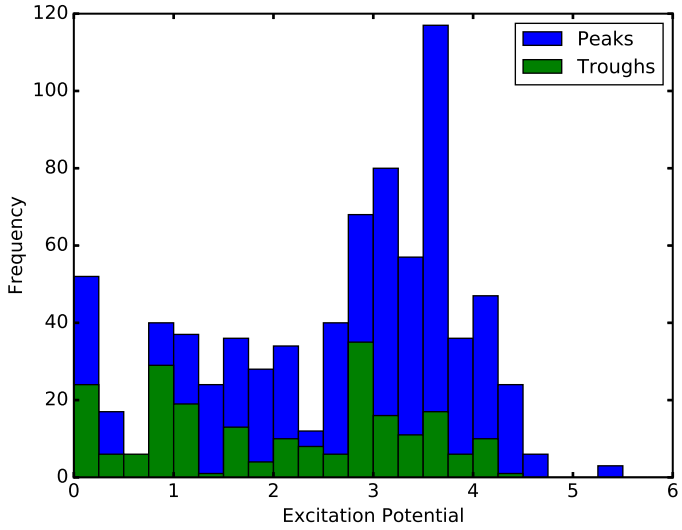


**Figure 3.24**: No conclusion can be drawn about the distribution of feature morphology with excitation potential, with the range of possible value of excitation potential resulting in low numbers and preventing any meaningful statistics being drawn. Features with a pseudo-absorption trough are called 'troughs' and shown in green, while features without are called 'peaks' and shown in blue.

neutral and ionised variants of the elements, most clearly seen in the case of Cr and Ni. This result is susceptible to low number statistics (even more so with the breakdown by element) and no real firm conclusions can be drawn from it. An equivalent breakdown per elemental species was carried out for the Landé g factor, all species show a similar result to the global fit seen in Figure 3.23.

The low numbers in some of the histograms means that no meaningful conclusion can be made about correlations of the properties of spectral lines with the feature morphology. Using a more robust method of identifying the features automatically may help better classify some of the unidentifiable features, giving a larger dataset to test again. In addition, the analysis of $\alpha$ Cen B could be extended to $>$ 5300Å to look for features, the larger likelihood of tellurics in this part of the spectrum would need to be considered as they may prove troublesome for the data processing.

## 3.8 Conclusions

With the push towards finding more Earth-like exoplanets, getting a better grasp on the impact that stellar activity has on the spectrum of its hosts is becoming a fundamental problem to solve. Techniques such as the FF' use photometry to predict the RV jitter activity could have. This method works well if the activity changes cause large contrast changes, like, for example, spots but fails for predicting jitter caused by plage. Variabil-

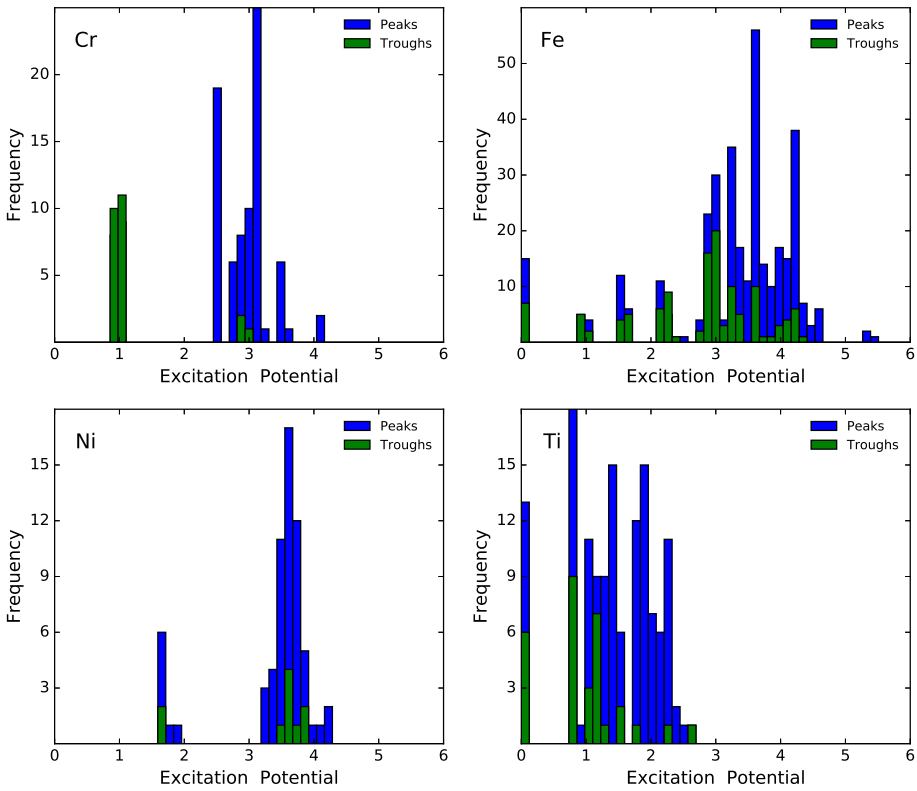


**Figure 3.25**: Histograms for the four elements Cr, Fe, Ni, Ti plots for other elements suffered from low numbers so no meaningful information can be gained. In all four cases no clear correlation can be seen with Cr and Ni showing indications that the features with pseudo-absorption troughs have lower excitation potentials but this is not conclusive due to low number statistics. All four show signs of bimodal distributions, most likely an effect of grouping neutral and ionised elements together.

ity of low-activity stars (i.e. the stars usually targeted for RV analysis) are known to be plage-dominated (Radick et al. 1990; Hall et al. 2009; Lockwood et al. 2007; Shapiro et al. 2016) causing a breakdown of the technique.

The results presented here show more directly the effects that activity can have on the spectrum of a star. The modelling demonstrates that the pseudo-emission features observed in the relative spectra may be able to track spot and, more importantly, plage. The relative spectra also highlight a number of other effects that need to be considered, most notably that of the difference between the immaculate photosphere during a high-activity phase compared to the lowest activity phase. As pointed out, the modelling approach used in this work is too simplistic to fully delve into the effects various activity types (from spots and plage to MBPs) could have on the shape of lines – both in the spectrum and in the relative spectrum, but does identify activity as the cause of the

features seen in the relative spectrum.

The modelling, however, does show that hotter regions (like plage) and broadening of the immaculate photosphere line contribution (through MBPs/plage) are needed to fit the features observed in the relative spectra. This indicates that the pseudo-emission features are influenced by changes in the plage filling factor. Plage being low contrast is not well traced by activity measures, making it difficult to property account for the RV variation it induces, with none of the techniques highlighted in Chapter 2 (directly) tracking changes in plages. If plage can be shown to be the cause of the features (as suggested here) it may provide a way to directly measure the level of plage and provide the basis of a technique to remove its activity contribution to RV measurement, which is the dominant RV jitter source of low activity stars.

The relative spectra also show the extent that activity can affect observations, with most strong lines showing some kind of feature. The strength of the feature in the relative spectrum does not necessary correlate with the strength of the line and may indicate the potential of mitigating the effects of activity by selectively avoiding lines with strong features in the relative spectra, these could then be used in more tailored CCF masks. In effect, this would give rise to two line lists, one that is sensitive to magnetic activity and one that is insensitive to magnetic activity. The lines of low activity sensitivity could be used to form the basis of improved CCF masks, these line would be less affected by changes in magnetic activity on the star and could improve RV precision. The second line list of highly sensitive lines could also be useful, providing a means to probe the surface of stars, with the potential of determining the coverage of active regions on the surface of these stars in a way that has not be achievable before.

The ability to measure the spot and plage filling factors could be an important stellar parameter gained from this analysis. This information would be vital in the push down towards unpicking the $\sim$ 10cm s$^{-1}$ RV signal of an Earth-analog, allowing for the RV jitter caused by activity to be more accurately mitigated. The spot and plage filling factors would also be useful to atmospheric studies of exoplanets, where the existence of haze in the atmosphere of exoplanets is determined based on the Raleigh scattering slope seen in the UV (Sing et al. 2016). Spots and plage are known to cause variations here, which would impact the measurements of the slope. Knowing the spot and plage filling factors could then be helpful in determining its contribution to the Raleigh scattering slope.

The first of the next generation of exoplanet detecting echelle spectrographs, ESPRESSO, has recently seen first light. With an expected RV precision of 10cm s$^{-1}$ strategies solutions for better mitigation of stellar jitter need to be developed. This work highlights one possible route to improved stellar jitter mitigation but

also shows the complexities of magnetic activity and its effect on the surface of stars.

*Chapter 4*

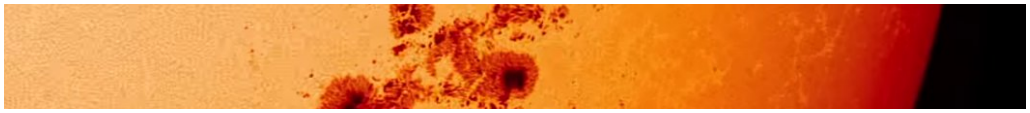

# Activity on the Sun

## 4.1 Introduction

In Thompson et al. (2017) – referred to as Paper 1 in this chapter – the activity on the surface of $\alpha$ Cen B was found to produce features in the 'relative spectra' that could add noise to RV measurements. The analysis of the relative spectra found morphological differences between some features that were closely separated in wavelength. I suggest that these differences may indicate the type of activity (either spots or faculae) responsible for the features. Although the pseudo-emission features were modelled to better gauge the effects that various types of activity has on the relative spectra, the modelling used was simplistic and full Magneto Hydro Dynamic (MHD) modelling of various spectral lines would probably be required to properly identify the source of the features. An alternative to full MHD simulations, which is both computationally expensive and dependant on the current (incomplete) understanding of the interaction of magnetic fields with the convection zones of stars, is to use the Sun as a benchmark to examine the effects of activity. The Sun is the only low mass main sequence star where the surface is resolvable, which enables the opportunity to directly relate observable features on the solar surface to spectroscopic variability.

The HARPS-N Solar Telescope is a project that takes full-integrated disk spectroscopic measurements of the Sun to better understand how surface inhomogeneities can affect precise RV measurements. A small 3-inch solar telescope takes light from the Sun and fiber feeds it to the HARPS-N instrument. Being the only setup to operate at the telescope during the day the survey is run continuously, using a 5 minute exposure time to reduce the effects of solar oscillations (Dumusque et al. 2015). This approach of observing the Sun as a star allows for any activity related features seen in spectra to be compared directly to images of the Sun taken using dedicated solar instruments (like the Solar Dynamics Observatory – SDO). Since seeing first light on 18$^{\text{th}}$ July 2015 the telescope has been continuously taking data, and currently there are over 48, 000 high resolution, high signal-to-noise measurements of the Sun spanning almost three years.

This dataset represents a unique opportunity to investigate the effects that activity has on the spectra of stars. The high precision HARPS instrument is currently the workhorse of RV planet surveys, and understanding how activity impacts the spectra (as well as the data-reduction pipeline products like the CCF or bisector span) may help in removing signals due to stellar jitter. In this chapter I continue the investigation of the effects of activity on stellar spectra by employing the unique 'Sun-as-a-star' observing capability afforded by the HARPS-N Solar Telescope. I follow the framework laid out in the previous chapter on $\alpha$ Cen B, producing relative spectra to highlight any changes in the strength of spectral lines and correlate these with either activity indicators like $\log R'_{HK}$ or by taking advantage of the network of solar imaging satellites

to better examine the various types of activity. This work was done in collaboration with a number of other people, notably J. Costes[1], and R. Haywood[2], and includes my supervision of the Masters Student N. Hartin[1], whose work was essential to this study. Their contributions are explicitly highlighted in the relevant sections.

## 4.2 Data and Data Reduction

For the analysis, two intervals within the data were selected based on the level of solar activity, and were processed in a similar way to Paper 1 to produce comparable results. The two time intervals selected were 16$^{th}$ June 2016 to 24$^{th}$ August 2016, and 24$^{th}$ June 2017 to 11$^{th}$ October 2016. The 2016 interval was selected as this shows a clear periodic modulation of the $\log R'_{HK}$ over two solar rotation periods (highlighted in light grey in Figure 4.1) and exhibited one of the largest changes in activity over a single solar rotation period. Within this range the low-activity template was also selected as 26$^{th}$ June 2016 (shown as the yellow plus in Figure 4.1), this day was compared to SDO/HMI images, which showed no spots on the surface and very little faculae, so represents a closer approximation of the Sun having a truly immaculate photosphere. The 2017 interval was identified using SDO-HMI images and shows a large spot group on the surface of the Sun lasting several rotation periods (dark grey region in Figure 4.1). The use of the two intervals also allowed for the investigation of any long term changes in activity in addition to rotationally modulated activity. As the data for the low activity template was chosen from within the 2016 interval, any long term activity effects (similar to those alluded to in Paper 1) would be limited for this period, isolating variations due to rotationally modulated activity. The 2017 interval, in addition to rotationally modulated activity, may be affected by longer term activity (e.g. from the 11-year solar cycle). Comparing the results of the two intervals could probe for the effects of any longer term activity trends.

As a note, the $\log R'_{HK}$ measurements shown in Figure 4.1 shows some rising trends and discontinuous 'jumps', these are systematics due to an effect known as cold-plate warm-up. This effect is caused ice building up on part of the cooling mechanism of HARPS known as the cold-plate. This ice acts as an insulator reducing the effectiveness of the cold-plate and causing the long term rising trend seen in Figure 4.1. To solve the icing issue, the instrument is occasionally allowed to warm up to breakdown the ice that has build up – this leads to the discontinuities. These ramping up and discontinuity events may have a widespread consequence for all data obtained by HARPS. The effect is most obvious here due to the high cadence of data measurements from the HARPS-

[1]Queen's University Belfast, Belfast, Northern Ireland
[2]Harvard University, Cambridge, Massachusetts

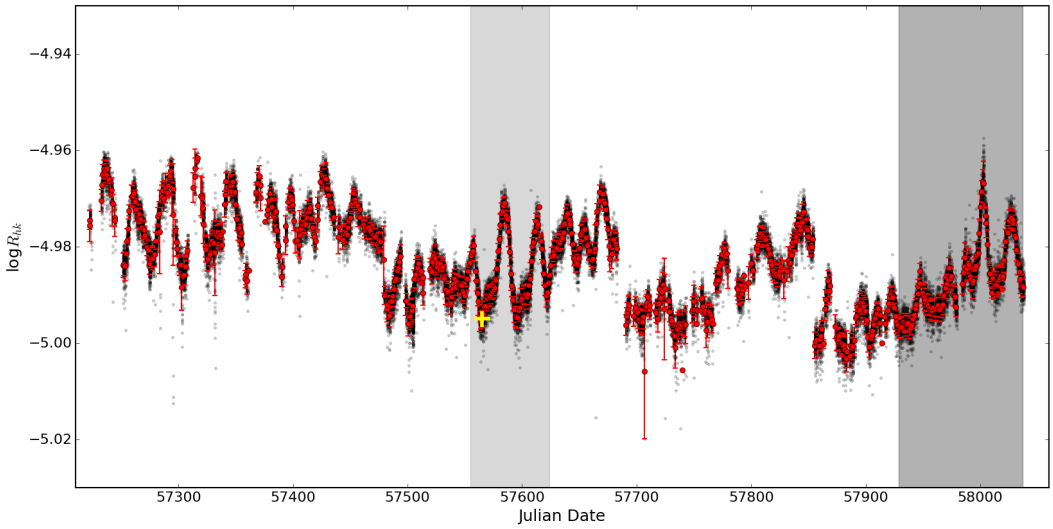


**Figure 4.1**: $\log R'_{HK}$ measurements of the Sun, the sinusoidal nature to the values is due to active regions rotating on and off the solar surface. Although a large amount of variation can be seen, all these values can be considered as being from a 'quiet' star. The two intervals selected for analysis are shows in light and dark grey. The light grey time interval was chosen from the $\log R'_{HK}$ values, while the dark grey was selected based on activity seen in SDO/HMI images. The yellow plus indicates the day selected for the low activity template.

N Solar Telescope but is also likely to be an effect on the $\log R'_{HK}$ measurements of other star (especially studies looking into long term stellar cycles). However, all of the $\log R'_{HK}$ values shown in Figure 4.1 would still be classed as being from a 'quiet' star and although the data suggests a large amount of variation it is, in reality, quite small. A change in $\log R'_{HK}$ of 0.03 looks large and significant on the scale shown here but would not be considered a large change in the activity levels of a star. The effect, though, is worth considering especially if it is able to improve the overall measurements of this activity indicator. This also shows an secondary benefit of the HARPS-N Solar Telescope project where we are able to dig more into the instrumental behaviour of HARPS-N and provide better systematic corrections to all HARPS data.

Initial analysis followed a similar approach to that of Paper 1, where the spectra for a single day were stacked after being continuum normalised and interpolated on to the wavelength grid of the low activity template spectrum. Although the $\log R'_{HK}$ for the Sun is much lower than that of $\alpha$ Cen B the large number of higher SNR spectra should allow greater sensitivity to spectral changes arising due to activity.

### 4.2.1 Data Processing

For the analysis the '2D spectra' were used, these are an earlier HARPS-N pipeline product and are stacks of extracted echelle orders, with each row containing the flux information of a single echelle order. This was done due to a strong ripple pattern seen when creating the relative spectra from the 1D spectra (discussed in more detail in Section 4.2.2). This ripple pattern was thought to be due, in part, to the re-interpolation to a constant wavelength grid done as part of the standard HARPS-N data reduction. At the blue end of the HARPS-N spectrograph the pixel-scale is $\sim 0.012$Å per pixel, while at the red end this goes up to $\sim 0.021$Å per pixel. When the echelle orders are stitched together they are reinterpolated to a constant wavelength grid of 0.01Å per pixel, which could be responsible for the pattern. It is shown later in Section 4.2.2 that this is not the case but is due to some other underlying systematic. Using the 2D spectra, however, provided a more optimal dataset for removing the ripple, and minimises the number of times the spectra are reinterpolated.

Using the 2D spectra adds additional steps in the data processing. The blaze effect (defined as the characteristic efficiency change along each order) was removed by dividing through by the blaze calibration file available per day, and if more that one blaze file was available these were averaged together. The blaze function was corrected on an order-by-order basis with individual blaze functions available per order. The 2D spectra were still on a pixel scale and must be converted to a wavelength scale, $\lambda$. This was done using:

$$\lambda = a_0 + \sum_{i=1}^{3} a_i n_{pix}^i \tag{4.1}$$

where $n_{pix}$ is the pixel number, and $a_i$ are calibration coefficients defined per echelle order and determined as part of the standard HARPS-N data reduction pipeline. After this point the data were processed in a similar way to Paper 1, a master template spectrum was created to act as a reference wavelength grid as well as being the low solar activity comparison for the data. For this low-activity master template, data from 26$^{\text{th}}$ June 2016 was used, and the spectra from this day were individually checked for any obvious issues. A total of 69 spectra from this day were selected. The header files contain the signal-to-noise ratio (SNR) per order, which were used to identify the highest SNR spectrum to use as the template to continuum normalise all the other spectra to. A mean of the SNR values for orders $40-50$ was used for the selection.

Each echelle order was then RV corrected but, rather than using the barycentric RV defined by the HARPS pipeline, the RVs were calculated using the JPL Hori-

zons system[3]. While the HARPS-N pipeline is able to accurately measure RVs to the m $s^{-1}$ level, the instrument is not calibrated for taking solar data. Effects from the Earth's orbit and rotation, the Moon and the Sun are accounted for when moving to the barycentre of the solar system, but the effects of the planets (most notably Jupiter) are not considered – as the solar system planets would have no effect on the RV measurements of other stars. When observing the Sun, this is no longer the case and the planets induce a measurable solar Doppler wobble. The RVs from the JPL Horizons systems does take into account these effects and so more precisely removes the Doppler wobble of the planets as well as other major bodies in the Solar System (JPL RV calculations provided by J. Costes, private communication). In this way, data from the HARPS-N Solar telescope is unique. Since the RV variations due to orbiting planets has been accounted for and removed, only the effects of stellar activity remain as an astrophysical source of RV jitter. The effects of activity on the spectrum of a star can more accurately be measured in this Sun-as-a-star approach, without the effects of (unknown) planets adding complexity, which would be the case for any other star.

These blaze and RV corrected spectra were next interpolated onto a common wavelength grid using a spline fit, with a spline knot defined at each point on the reference spectrum. Finally, all spectra were stacked per echelle order using a weighted mean with the weights being the same mean of the SNR in orders $40-50$ defined earlier.

For all high activity spectra, a similar process was followed but with a number of caveats. First, the low activity master templates created were used to define the wavelength grid and second, rather than a by-eye evaluation of the spectra, a cut of $> 100$ is set in the SNR to remove bad spectra. Again, the spectra were RV corrected using the JPL Horizons data and stacked per echelle order using a weighted mean. Finally, each stacked spectral echelle order was divided by the equivalent low-activity master template echelle order to produce relative spectra for each order. On producing the relative spectra, however, a significant sinusoidal variation could be seen across the entire range. Figure 4.3 shows a few examples of the ripple pattern seen in the relative spectra. This ripple pattern was persistent across all the relative spectra, becoming more obvious towards the redder wavelengths.

### 4.2.2 Investigation and Removal of the Ripple Pattern

Initial investigation of the ripple pattern was performed by eye and showed that the pattern is not at a constant frequency, but instead shows a decrease in frequency moving from the blue to the red end of the spectrum. The separation between peaks at

[3]JPL Horizons:https://ssd.jpl.nasa.gov/horizons.cgi

$\sim$ 4000Å is $\sim$ 0.2Å, which becomes $\sim$ 0.5Å at $\sim$ 5800Å. The ripple appears invariant to the activity of the Sun, with the variations of $\log R'_{HK}$ over the period ranges considered having no impact on the strength or frequencies of the ripple pattern. To allow for a more in depth analysis the investigation of the ripple pattern was limited to a reduced dataset. As the ripple pattern is only seen in the relative spectra, the data of two days was needed: the 26$^{\text{th}}$ June 2016 (as the low activity template) and 14$^{\text{th}}$ July 2016 (as a high activity comparison) were selected. As the purpose of this investigation was to identify the source of, and remove the ripple pattern (while maintaining any activity related pseudo-emission features), relative spectra showing larger pseudo-emission features aid in evaluating the effectiveness of the removal process. These days were chosen as they show a large difference in $\log R'_{HK}$, and were expected to show the strongest pseudo-emission features in the relative spectrum if present.

Prior to investigating the ripple pattern each spectrum from the sample were individually checked for obvious features that could lead to the pattern. Effects from echelle order mismatch, poor seeing/weather, RV offsets, etc. could be the source of the ripple but none of the spectra showed any effects of this nature. As production of the relative spectra involved continuum matching and interpolating the wavelength grid to that of the low-activity template, the choice of low activity template could also be the source of the ripple pattern or at least contributing to it. Spectra from 12$^{\text{th}}$ November 2016 were selected as an alternative low-activity template but, again, the ripple pattern still persisted.

Another source of error could come from the HARPS-N pipeline itself, where order edge effects could play a role in producing the ripple pattern. Instead of working with the full 1D spectra, the final pipeline product, the analysis considered the data products at the previous step. These include the 2D spectra and blaze functions (as outlined earlier). The two days of data were processed following the procedure outlined earlier (Section 4.2.1) to produce relative spectra per order. For each order a GLS periodogram (see Section 2.5.4) was performed, which shows a peak in frequency that decreases moving from the lower echelle orders to the higher orders (see Figure 4.2). The GLS also shows that, per order, the ripple pattern is well defined by a small range of frequencies.

Although the source of the ripple pattern is not understood, per echelle order, the pattern is evolving by only a small amount, making removal if it a more approachable task. The process of removing the ripple pattern involved fitting sinusoids to the relative spectra. As the pattern is not static but has an evolving periodicity, multiple sinusoids were fitted to approximate this evolving periodicity. Over a single echelle order the

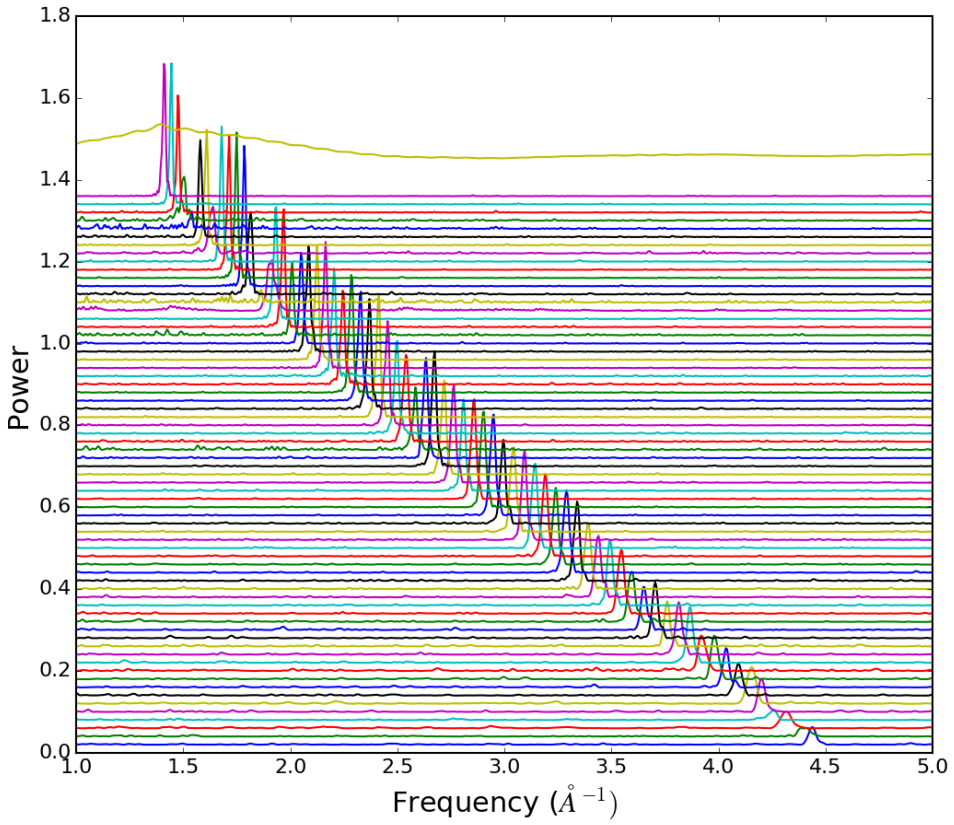


**Figure 4.2**: The GLS per echelle order, with internal order 1 at the bottom and internal order 69 at the top highlighting the period of the ripple pattern. Per order, the ripple is close to having a non-evolving static periodicity. The extended peak at order 69 is due to the large number of tellurics causing inverse P Cygni-like profiles that are being confused for periodicity.

ripple pattern was captured by applying a low number of sinusoidal fits, with the fit done on an order-by-order basis. To start, a GLS periodogram was performed on the relative spectra of a single echelle order, the highest peak was then identified and set as the frequency of the sine wave, and the amplitude of the sine fit was calculated following the derivation from Zechmeister & Kürster (2009) where the amplitude, $A$, is defined as:

$$A = \sqrt{a^2 + b^2} \tag{4.2}$$

and $a$ and $b$ are defined as the set of sums:

$$a = \frac{YC \cdot SS - YS \cdot CS}{D} \qquad \text{and} \qquad b = \frac{YS \cdot CC - YC \cdot CS}{D} \tag{4.3}$$

$Y$, $S$, $C$, and $D$ are summations defined in Section 2.5.4. Finally, the phase of the sine wave was determined using a Markov Chain Monte Carlo (MCMC) simulation. An MCMC evaluates goodness-of-fit of the current step to the previous step, it then accepts or rejects this new step based on the Metropolis-Hastings algorithm (Metropolis et al. 1953). This algorithm always accepts steps that produce a better fit than the previous step, however steps that produce a worse fit can also be accepted with some probability. This can formally be written as:

$$A(x'|x) = \min\left(1, \frac{P(x')}{P(x)} \frac{g(x|x')}{g(x'|x)}\right) \tag{4.4}$$

where $A(x'|x)$ is the acceptance probability between state $x$ and $x'$, $P(x)$ and $P(x')$ are the probability distributions of $x$ and $x'$, respectively, and $g(x|x')$ and $g(x'|x)$ are proposal distributions given a transition from state $x$ to $x'$ and vice versa. The MCMC algorithm is typically used when analysing models with multi-dimensional distributions helping prevent these models becoming stuck in local maxima. For this analysis, the MCMC was chosen to model the phase as it was found that more conventional $\chi^2$ minimisation techniques were not effective at determining a precise value for the phase due to the weak nature of the signal as well as the model only approximating the evolving periodicity of the pattern. The MCMC helps to better explore the parameter space around the best fit value. The MCMC was run with multiple burn in phases, after which a final MCMC was run to explore the local parameter space. A boundary condition was also put on the phase only allowing values between 0 and $2\pi$. A total of 10 burn-in phases each having 1000 steps were run, and at each step the $\chi^2$ value of the fit was calculated and compared to the previous fit for acceptance or rejection based on the Metropolis-Hastings algorithm. At the end of each burn-in run the step size was adjusted and taken as the standard deviation of the values. This allows for a larger step size when far from the best fit and a reduced step size as the model parameters approach good estimates. A final MCMC was run over 5000 steps and the values of this run were saved and used to estimate the phase. A histogram of these saved MCMC values was calculated and a Gaussian was fit to the histogram, with the peak of the fitted Gaussian defining the phase of the sine wave model.

This model sine wave was then removed from the relative spectrum and the process was rerun over the residuals to fit the next strongest periodic signal. It was found that by

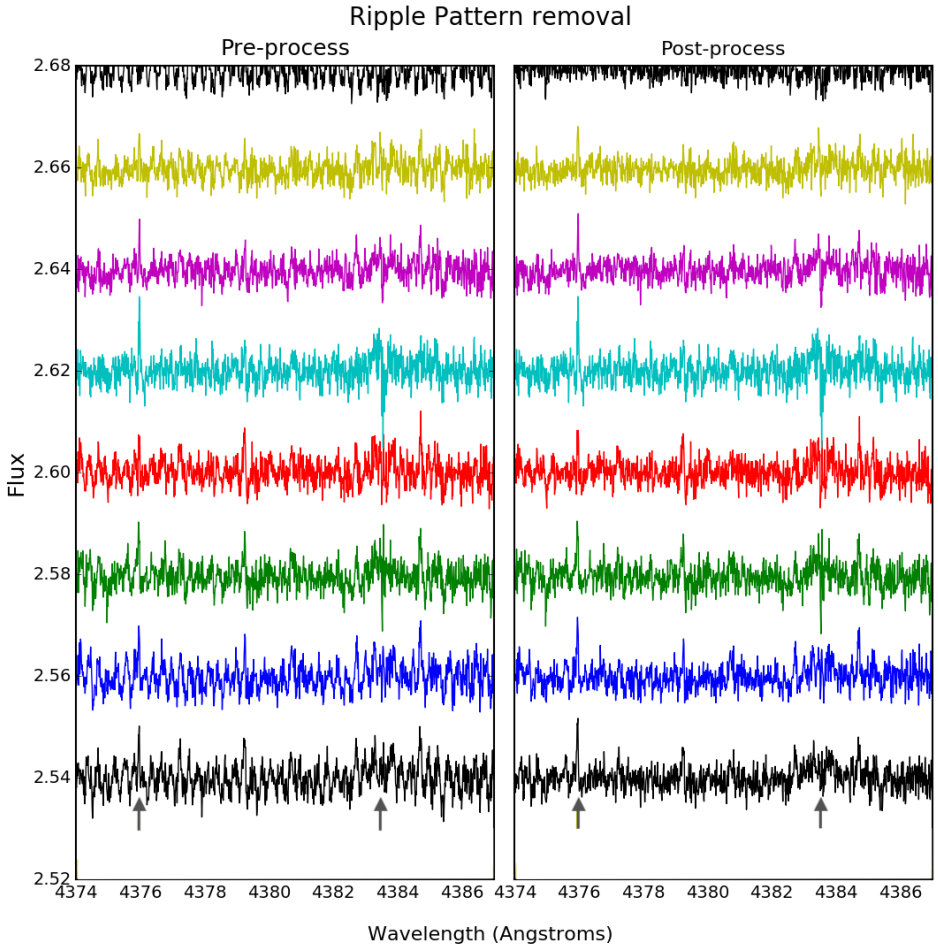


**Figure 4.3**: Pre- and post-processing of the daily stacked relative spectra to remove the ripple pattern. Each relative spectrum was from a different day and shows the variation in the strength of the pattern, demonstrating why a manual by-eye reduction was needed. The gray arrows indicate the position of known features in the relative spectrum. The relative spectrum in black shows a good example of the success of the ripple removal process, where the features cannot be clearly seen prior to the removal but are an obvious signal in the post-processed relative spectrum.

applying the ripple removal process 3 times the evolving periodicity was almost entirely removed. On some occasions it was found that only 1 or 2 sine waves were needed to remove the ripple pattern and by fitting additional sine waves sinusoidal variations were re-introduced into the relative spectra. The choice of the final model then required a by-eye approach to stop any overfitting. Examples of the ripple and the removal are shown in figure 4.3, where the pattern can be seen in some cases to completely obscure real activity driven features.

At this point the relative spectra were still affected by the ripple pattern, the process of removing this is time intensive, requiring a visual inspection of each model to

confirm its effectiveness. To speed up the analysis, a subset of the echelle orders that showed the most interesting features were identified. For this process the relative spectra from 14$^{th}$ July 2016, having the highest activity level (as measured by $\log R'_{HK}$), was selected as any activity based features would be strongest here. All 69 echelle orders for this one day were processed to removed the ripple pattern (the process for this is outlined in Section 4.2.2), with 8 out of the 69 orders selected for processing across the full dataset (orders 15, 18, 22, 24, 30, 36, and 37) covering a total of 188 days over the 2016 and 2017 intervals. Low orders were avoided as these were dominated by lower SNR so no features could be seen from these, with higher order also avoided due to the known tellurics in that region of the spectrum. All other orders showed little to no indications of activity based features (initial work on identification and selection of lines done by N. Hartin, supervised by myself).

## 4.3 Feature Search

The final 8 reduced echelle orders all showed some indications of features that could be due to activity on the Sun. The features highlighted in Paper 1 were 4375Å, 4383Å, and 4404Å, and these features are seen in the Sun as well but are far weaker due to the lower activity level of the Sun than $\alpha$ Cen B. Figure 4.4 shows a comparison between the Sun and $\alpha$ Cen B for the lines 4375Å, 4383Å. The 4404Å line is not shown as this line is in a different echelle order (order 19 rather than order 18) that has not been processed to remove the ripple pattern. However, manual processing of one of the daily stacked spectra shows that the feature at 4404Å is indeed present but is not shown here (this is a broad feature, which is difficult to measure and not used in this analysis). Visual inspection of the relative spectra was used to identify features that showed correlation with $\log R'_{HK}$. From this, 6 features were selected as showing variability that could be linked to activity (see Table 4.1), other features initially identified were either too weak to be seen in any of the other spectra or did not show variability consistent with activity (they may be weak telluric lines that are only seen here due to the very high signal-to-noise of the daily stacked spectra). A Gaussian was fit to each of the features identified, with the area of the fitted Gaussian taken as an estimate of the feature strength (a pseudo-equivalent width, similar to that used in Paper 1). The features seen in the relative spectra are weak and at times are lost in the noise, for these cases no Gaussian was fit and the feature in this particular relative spectrum was not considered. Additional constraints were put on the height and width of the fitted Gaussian before a final by-eye examination was performed to ensure that noise was not mistakenly being fit as a feature.

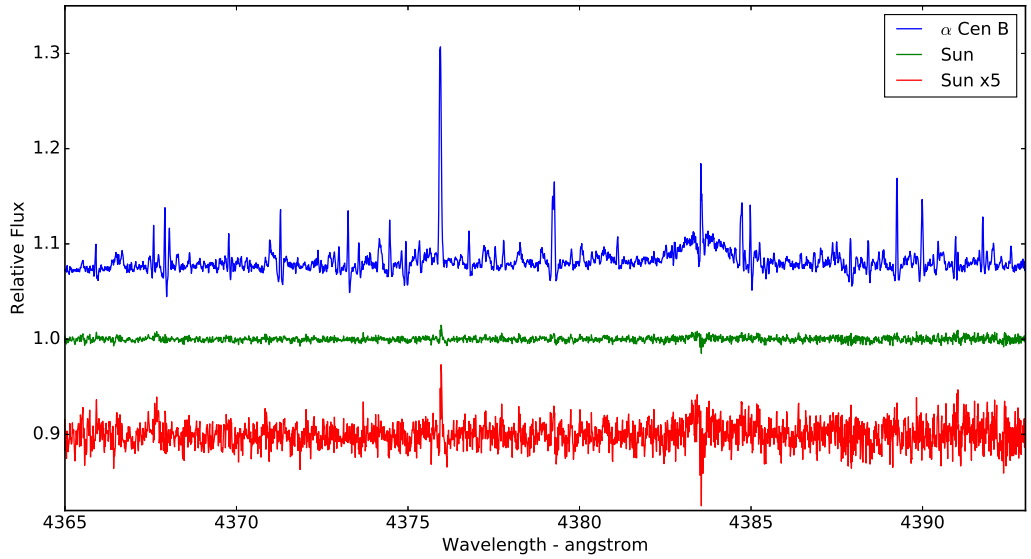


**Figure 4.4**: Comparison of the features on $\alpha$ Cen B, discussed in Paper 1, with features found on the Sun. The strongest narrow peak belongs to Fe I 4375Å lines, and the broader feature is due to Fe I 4383Å. The lower activity level of the Sun means that the features are a lot weaker. Both the red and green lines show relative spectra from the Sun but with the values increased by a factor of 5 for the red lines, allowing the features to be more easily observed.

| Line (wavelength Å) | Element/ Ion | Echelle Order | Pearson's r Spots | Pearson's r Faculae | log $R'_{HK}$ |
|---|---|---|---|---|---|
| 4375.95 | Fe I | 18 | 0.55 | 0.70 | 0.71 |
| 4501.35 | *unidentified* | 22 | 0.32 | 0.56 | 0.58 |
| 4783.43 | Mn I | 30 | 0.60 | 0.79 | 0.69 |
| 5007.26 | Ti I | 36 | 0.41 | 0.68 | 0.73 |
| 5012.12 | Fe I | 36 | 0.45 | 0.75 | 0.67 |
| 5014.26 | Ni I | 36 | 0.56 | 0.74 | 0.74 |

**Table 4.1**: Lines that show a feature in the relative spectra and the echelle order each line is in. The Pearson's r statistic is shown for each of the features with respect to spot and faculae filling factor. This is for the interval 16$^{\text{th}}$ June to 24$^{\text{th}}$ August 2016.

The strength of the pseudo-equivalent width was compared to $\log R'_{HK}$ as was done in Paper 1 to determine if they are activity related but, with the solar spectra, images of the surface of the Sun are also available. Changes in the relative spectra can be directly compared to inhomogeneities seen on the solar surface. Haywood et al. (2016) used images from the Helioseismic and Magnetic Imager (HMI) aboard the Solar Dynamics Observatory (SDO, Scherrer et al. 2012) to measure the filling factor of faculae and spots on the visible surface of the Sun. While $\log R'_{HK}$ is a good proxy for the level of activity on the surface of a star it traces chromospheric activity. Images of

the surface, however, enable the photospheric activity to be directly tracked and allow spot and plage contributions to be monitored separately. Haywood et al. (2016) used SDO/HMI flattened intensitygrams, line-of-sight Dopplergrams and unsigned magnetograms to determine the faculae and sunspot contributions. A threshold in the magnetic field strength of each pixel was used to separate quiet Sun from active regions, while a threshold in the flattened continuum intensity allows for spots and faculae to be differentiated.

The process was applied to the SDO/HMI images for the periods used in this analysis and produced faculae and spot filling factors as a percentage coverage of the visible face of the Sun (R. Haywood, private communication). The pseudo-equivalent width of the features in the relative spectra are compared to $\log R'_{HK}$ and the spot and facular filling factors as shown in Figure 4.5.

All 6 features show variations that appear to correlate with $\log R'_{HK}$, showing a peak in the pseudo-equivalent width measurements close to where the peak in $\log R'_{HK}$ can be seen. This is most clear for the lines at 4375Å and 4501Å in Figure 4.5, where the two peaks in $\log R'_{HK}$ at $\sim$ 30 days and $\sim$ 57 day have equivalent peaks in the pseudo-equivalent width of the two lines. This is a similar result to that seen in Paper 1 and adds further evidence to the features being caused by activity. Additionally, comparing the pseudo-equivalent widths with the spot and faculae filling factors shows an offset in the peak of the pseudo-equivalent widths compared to the peak in the spot filling factor. The Pearson's r correlation for pseudo-equivalent widths versus spot filling factor and faculae filling factor are shown in Table 4.1 and show a stronger correlation to changes in facular filling factor than changes in spots filling factor.

To further test this, the interval of $4^{\text{th}}$ to $27^{\text{th}}$ July 2016 was isolated in the dataset. This period shows an extended facular region that is not coincident with the spot group seen, this is confirmed by SDO/HMI images that show an extended facular region with few associated spots (see Figure 4.6). A large spot group is seen to appear on the surface of the Sun a few days later and is offset from the main faculae region (see Figure 4.6). The Pearson's r was measured for the features in this range and shows an overall increase in the correlation with the faculae but a decrease in correlation with the spots (see Table 4.2). This shows that the features seen in the relative spectra are tracing changes in the faculae coverage of the Sun.

The feature at 4501.35Å does not show much of a change in correlation strength between the full dataset and the reduced set. This feature, however, is the only one to show a pseudo-absorption dip rather than a pseudo-emission peak in the relative

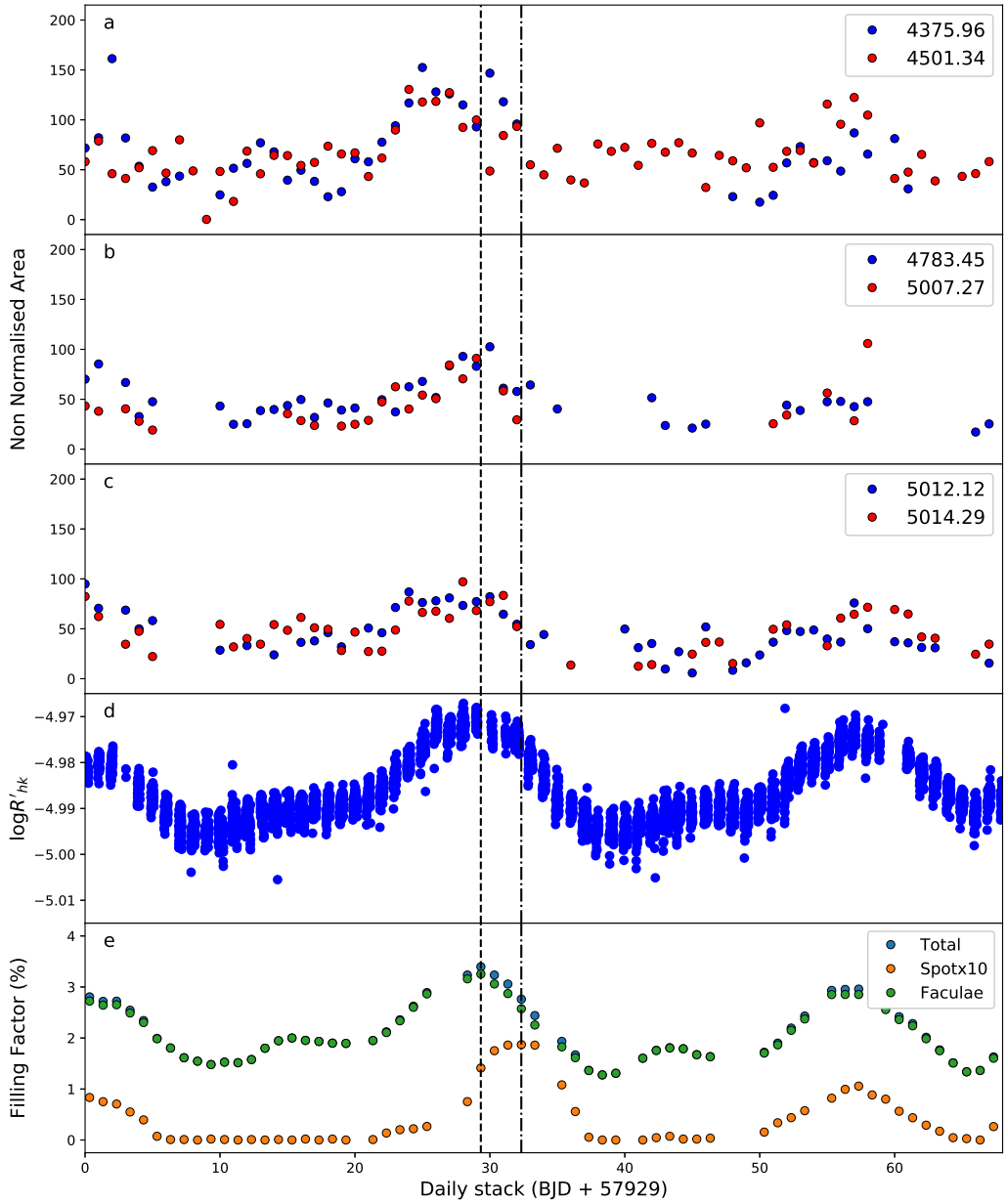


**Figure 4.5**: Pseudo-equivalent widths for all 6 features separated over 3 plots for ease of viewing. (a) features at 4375Å and 4501Å, (b) features at 4783Å and 5007Å, and (c) features at 5012Å and 5014Å. These are compared to $\log R'_{HK}$ (d) and spot and facular filling factors (e). The spot filling factor has been increased by a factor of 10 to allow ease of viewing. The dashed and dot-dashed lines show the peak in faculae and spot filling factors, respectively. Note the faculae have a phase offset in their peak filling factor, indicating unassociated faculae, and how the changing equivalent width of the pseudo-emission features appear to better trace the variation in faculae filling factor rather than spots filling factor.

| Line (wavelength Å) | Element/ Ion | Echelle Order | Pearson's r Spots | Pearson's r Faculae | log $R'_{HK}$ |
|---|---|---|---|---|---|
| 4375.95 | Fe I | 18 | 0.55 | 0.83 | 0.90 |
| 4501.35 | *unidentified* | 22 | 0.08 | 0.56 | 0.64 |
| 4783.43 | Mn I | 30 | 0.53 | 0.87 | 0.81 |
| 5007.26 | Ti I | 36 | 0.40 | 0.82 | 0.77 |
| 5012.12 | Fe I | 36 | 0.17 | 0.81 | 0.82 |
| 5014.26 | Ni I | 36 | 0.49 | 0.87 | 0.81 |

**Table 4.2**: The Pearson's r statistic measuring the correlation between the features and the spot and faculae filling factors for the range 4$^{th}$ to 27$^{th}$ July 2016, which has faculae that is unassociated with spots. The results indicate that the features better trace the changes in faculae coverage than spot coverage.

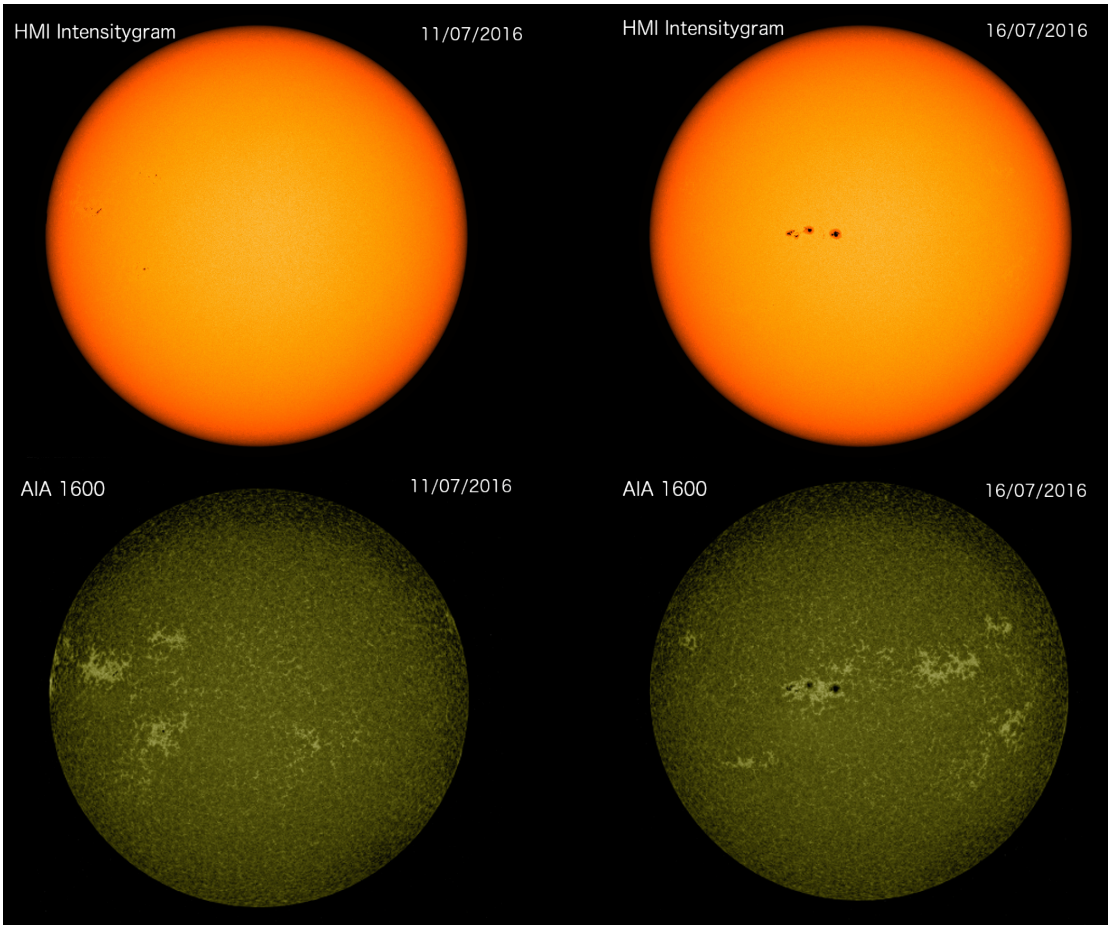


**Figure 4.6**: SDO/HMI images of the Sun from two different dates highlighting the extended unassociated facular regions. The images show two filters chosen to better view each type of activity, with the faculae most visible in the AIA 1600 and the spots clearly seen in the HMI Intensitygram. The left hand image clearly shows that faculae rotate into view before the spot group appears.

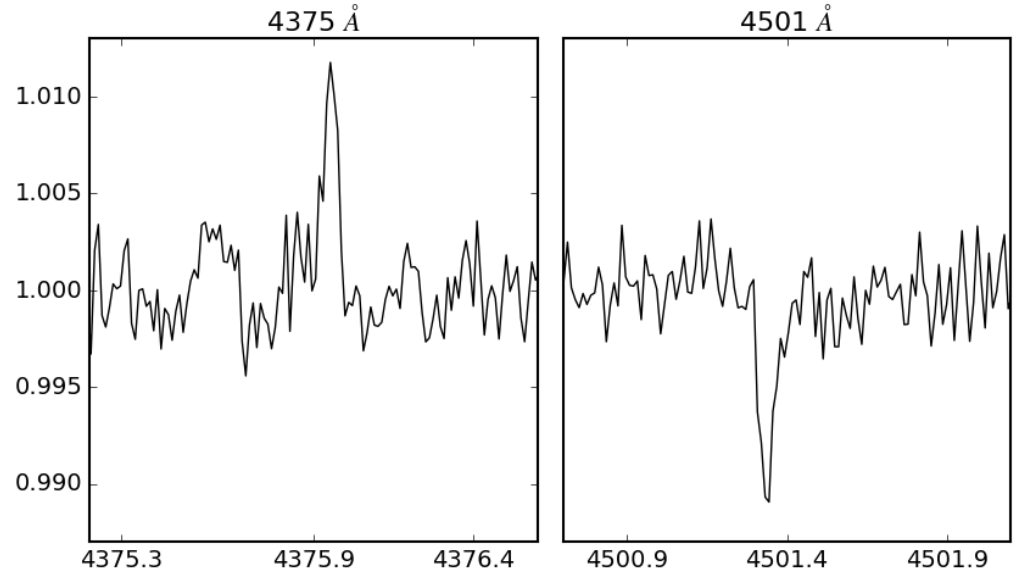


**Figure 4.7**: Example of the pseudo-absorption dip of the 4501Å feature as well as the 4375Å feature for comparison. This example is from the 14th July 2016 and is one of the highest activity days of the 2016 interval.

spectra (Figure 4.7 shows an example of this feature as well as the 4375 Å feature for comparison). This suggests that the line responsible for this feature is deeper when the Sun is in a higher activity state, as opposed to the rest of the lines, which show pseudo-emission peaks and are shallower in the high activity state. This pseudo-emission dip feature can also be seen in the simple models of $\alpha$ Cen B, Figure 3.11 panel *h*, for example, shows a dip feature that is the result of the line being deeper in the high activity state.

The second period of solar data analysed was 24th June 2017 to 11th October 2017, this 2017 interval was selected as it showed the largest spot coverage during the operational period of the HARPS-N Solar telescope. The same pseudo-equivalent width measurements were performed here but the results do not indicate as strong a correlation between the changes in activity as indicated by both $\log R'_{HK}$ or the spot and faculae filling factors. In fact, for most of the daily stacked spectra considered no strong features could be found. Figure 4.8 shows the same comparison plot of pseudo-equivalent width and the $\log R'_{HK}$ and spot and faculae filling factors as Figure 4.5. Pearson's r statistic for this range shows a moderate amount of correlation with the strength of some of the features to $\log R'_{HK}$ and spot and faculae filling factors (see Table 4.3). The lines with a † denote cases where, for a large number of days during the period, no feature could be measured. None of the features found are long-lived enough to determine if they are modulated on the rotation period of the Sun, which would be another check

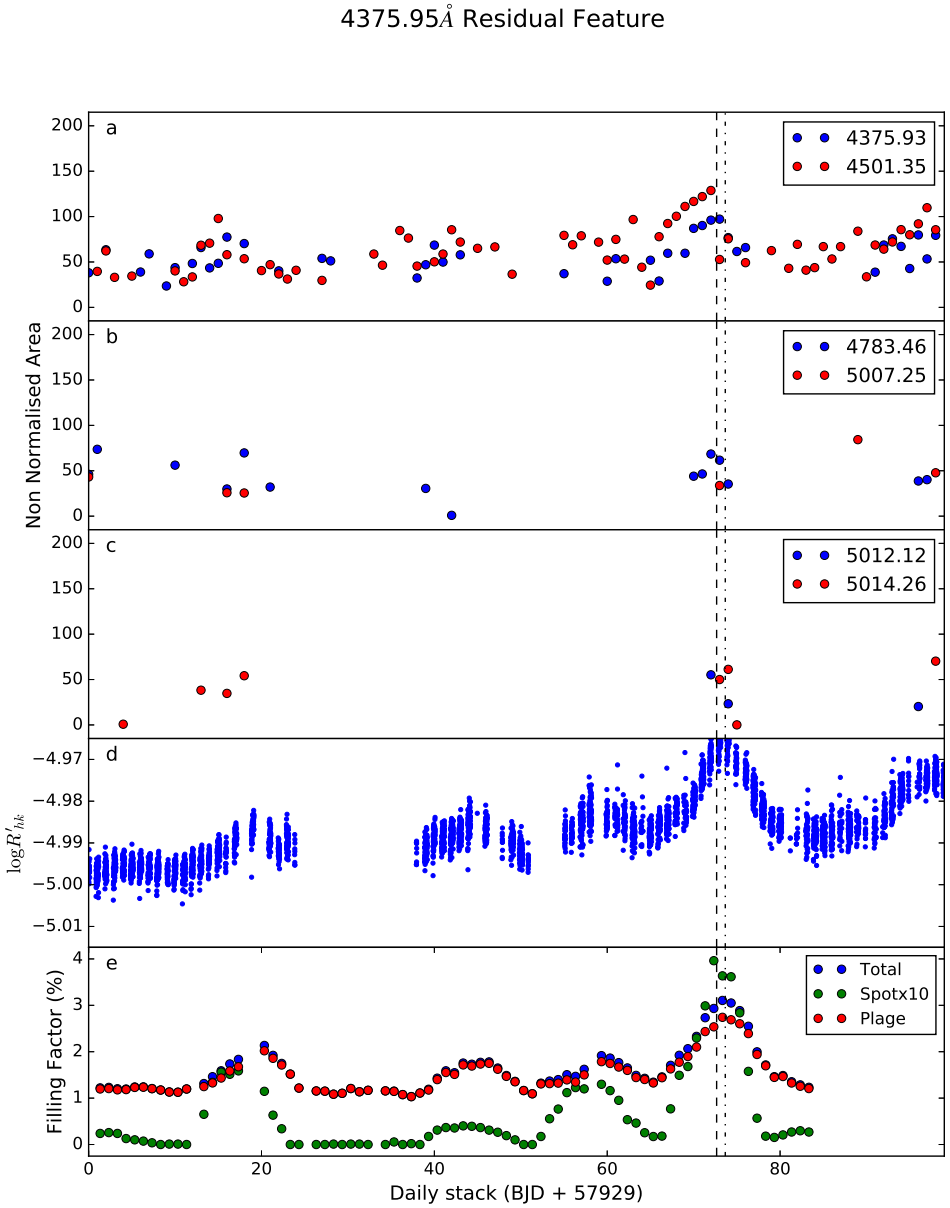


**Figure 4.8**: Same as Figure 4.5 but for the interval 24th June 2017 to 11th October 2017. In this case the large gaps in the pseudo-equivalent width measurements is due to no measurable feature being detected. This indicates that during this period, the correlation between the features and the changing levels of activity are not as strong.

of activity relation.

The correlation for the 4375.95Å line, however, is still relatively strong, while that of the 4501.35Å line has dropped significantly, even going as far as not correlating well with $\log R'_{HK}$. The other lines have no measurable feature for a large majority of the 2017 period. Examining the SDO/HMI images for this period shows that, while

| Line (wavelength Å) | Element/ Ion | Pearson's r (Spots) | Pearson's r (Faculae) | Pearson's r ($\log R'_{HK}$) |
|---|---|---|---|---|
| 4375.95 | Fe I | 0.542 | 0.618 | 0.621 |
| 4501.35 | *unidentified* | 0.043 | 0.112 | 0.306 |
| 4783.43† | Mn I | 0.399 | 0.310 | 0.247 |
| 5007.26† | Ti I | 0.059 | -0.010 | 0.161 |
| 5012.12† | Fe I | 0.039 | -0.035 | 0.216 |
| 5014.26 | Ni I | 0.421 | 0.360 | 0.449 |

**Table 4.3**: The Pearson's r statistic measuring the correlation of the features for the range 24$^{th}$ June 2017 to 11$^{th}$ October 2017. This range is noted as having no unassociated faculae on the surface of the Sun. The features during this period are weaker with some showing no measurable strength during a large portion of the period, these are highlighted with the †.

a large amount of activity (including a large and complex active region) exist during this time interval, it has a marked difference of the spectra from the 2016 interval. The 2017 interval shows very little unassociated faculae regions compared to the 2016 interval, with most faculae being associated with the large spot groups that form (this is discussed further in Section 4.4)

### 4.3.1 Trailed Spectra of Features

The weak features of the Sun make it difficult to see how well they correlate with rotation period or if they exhibit measurable RV variations. Viewing the spectra as an image, or as trailed spectra can help identify variations. The time period can be viewed as an image where the x-axis is the wavelength, the y-axis is each daily stacked relative spectrum and the pixel value is the relative flux of each spectrum. Figure 4.9 shows a trailed spectrum of the 4375Å line for the 2016 interval, this is one of the strongest features seen in the relative spectra and shows a clear signal in the trailed spectrum. The dashed and dot-dashed lines represent the Carrington rotation period (25.38 days, Carrington 1859) and half of that, respectively. As only one hemisphere of the Sun can be seen, the half rotation period can be useful in determining when an active region would migrate off the visible surface of the Sun. The position of the markers was chosen from the SDO/HMI images, where the zero-point was selected based on when a large feature is seen to rotate onto the visible surface of the Sun and is *not* chosen to intentionally line up with any features. In Figure 4.9 the feature at 4375Å is seen to be encapsulated within a half-rotation of the Sun i.e. as one would expect from an active region rotating on and off the solar surface. This can most easily be seen at $\sim 22-35$ days, where the feature can be easily picked out from the background noise. The feature can also be seen to have a directionality showing a positive slant;

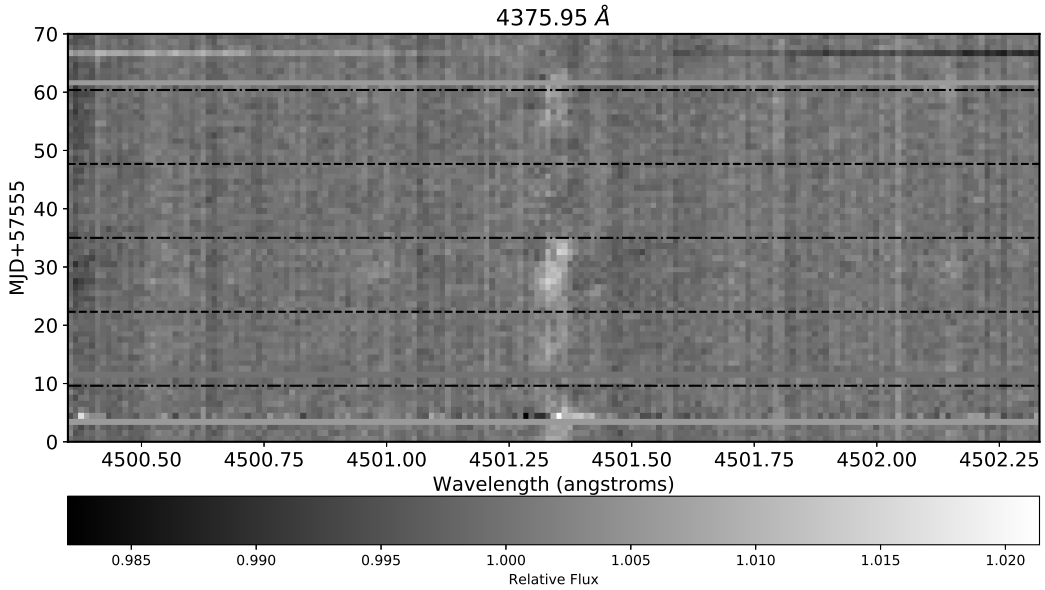


**Figure 4.9**: Trailed relative spectrum of the 4375Å line for the 2016 interval, the horizontal dashed and dot-dashed lines are the Carrington rotation period and the half period, respectively. The main feature from the 4375Å pseudo-emission peak can be seen to have a positive slant indicating that the feature has a radial velocity component appearing to move from blueshift to redshift as it traverse the solar disk. Note the spectrum at $\sim 5$ days has low signal-to-noise, explaining the offset feature.

this would indicate a radial velocity component of the feature moving from blue-shifted to red-shifted, which would be expected if the feature was a result of activity rotating across the solar surface. A number of daily spectra were not considered from the time range due to instrument or weather effects, the position of these spectra can be seen as solid horizontal lines in the trailed spectrum.

Figure 4.10 show the same trailed spectrum for the 4501Å, i.e. the dip feature. Again, the features are fully captured in a half rotation period indicating that the changes are due to the active regions on the surface. The rest of the features show a similar scenario, where the peaks in pseudo-equivalent width show a modulation on the solar rotation period but no indication of RV variation can be seen in these cases. However, applying the same methods to the 2017 interval does not yield as convincing a result. Figure 4.11 shows the same 4375Å and 4501Å features for the 2017 interval, and only around the $\sim 65$ day mark can a feature be identified and for the rest of the time no real periodic modulation of the features can be seen. The other features showed few cases where a pseudo-emission peak or pseudo-absorption dip could be identified and an equivalent width measured, the trailed spectra for these lines reflect this fact with no notable features seen.

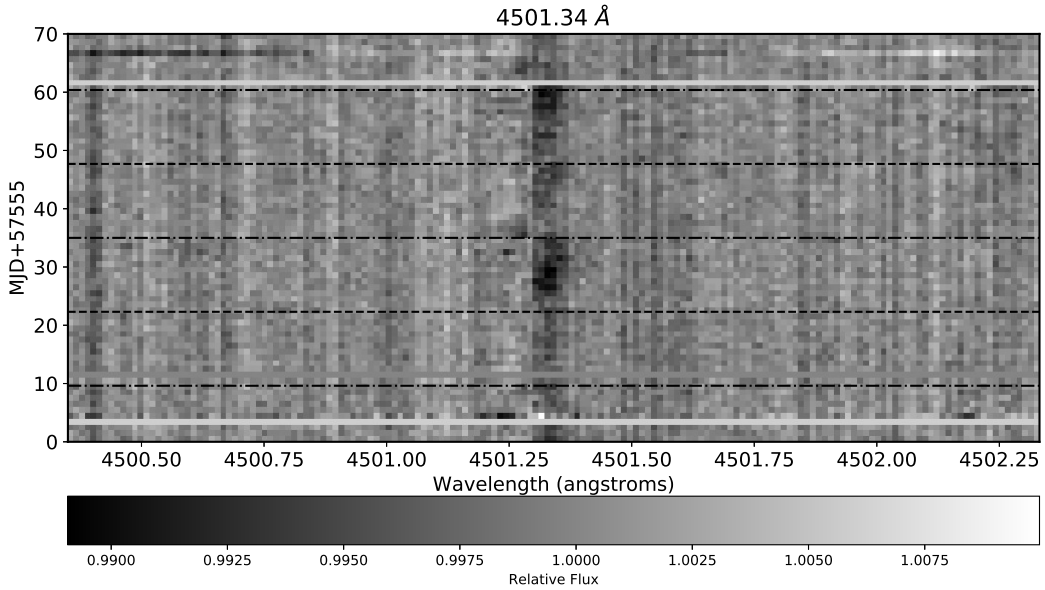


**Figure 4.10**: Trailed relative spectrum of the 4501Å line for the 2016 interval. The difference in colour with respect to Figure 4.9 is due to this line producing a pseudo-absorption dip. Again, the feature can be seen moving from blueshift to redshift.

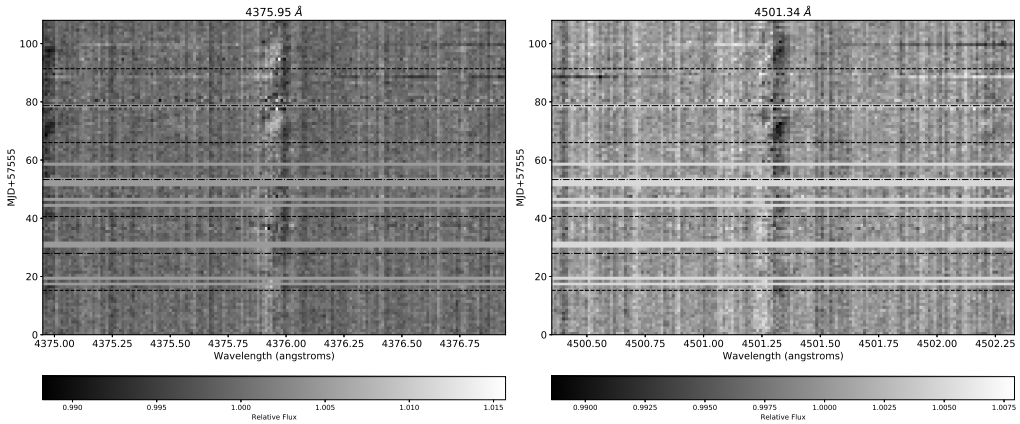


**Figure 4.11**: Trailed relative spectrum of the 4375Å (left) and 4501Å (right) lines for the 2017 interval. In contrast to the 2016 interval, the period modulation of the features is less clear, a small redshift can be seen at $\sim 65$ days. Again the dash and dot-dashed lines are for the Carrington rotation and half rotation periods.

## 4.4 Discussion

In many cases, the same 'pseudo-emission' features found in $\alpha$ Cen B are seen in the Sun. This is despite the Sun being in, or approaching, a relatively deep minimum in the solar activity cycle. This shows that we are sensitive to variations in individual lines in even quiet stars. With resolved images of the surface of the Sun, the features can be further characterised as being due to changes in the level of facular coverage, which is supported by the Pearson's r statistic showing a stronger correlation of the features

with faculae than spots. More notably, the 2017 interval, which shows a higher level of activity (as traced by $\log R'_{HK}$), shows fewer features in the relative spectra than that of the 2016 interval. Examination of the SDO/HMI images for these periods show that, besides the larger activity of the 2017 interval, the main difference between the two is the presence of faculae unassociated with spots. It may be that the presence of the spot group is reducing the convective blueshift suppression of the faculae.

The 2016 interval shows that the peak in pseudo-equivalent width of the relative features are offset from $\log R'_{HK}$ and spot filling factor activity indicators. By considering the SDO/HMI images, the peak can seen to better coincide with the appearance of the unassociated facular region and the migration of this region as it moves from the east to the west limb of the Sun. The second peak in the pseudo-equivalent width can be seen at $\sim 58$ days and corresponds to the same extended unassociated facular region returning. The dashed lines in the trailed spectrum of Figures 4.9 and 4.10 were set from SDO/HMI images, with the zero point taken from when a major active region can be seen to move onto the solar surface. For the 2016 interval this is the unassociated facular region and explains why the features line up in the trailed spectra.

One interesting feature that can be seen in the 2017 interval occurs at $\sim 66$ days (see Figure 4.8), where the pseudo-absorption dip of the 4501Å line becomes very well behaved and displays an increase in pseudo-equivalent width that shows very good correlation with the changes in activity during the 30$^{\text{th}}$ August to 5$^{\text{th}}$ September 2017. Figure 4.12 shows the relative spectra from this interval. The pseudo-absorption dip is obvious and the surrounding scatter is a similar level across the relative spectra, meaning that the pseudo-equivalent width measured is not a result of poor fitting. SDO images shows a large extended spot group appear on the surface at the same time as the pseudo-absorption feature of the 4501Å line becomes clearly distinguishable from the background scatter. The feature almost disappears when the active region moves past disk centre i.e. the 4501Å line shows a strong pseudo-absorption dip while the active region is on the blue-shifted hemisphere of the Sun but this almost disappears on the red-shifted hemisphere. The disappearance of this feature on the 6$^{\text{th}}$ September 2017 also coincides with a large X9-class flare. As this is the only occurrence of this situation during the time intervals analysed it is difficult to gauge if the flare could have changed the magnetic structure of the Sun, affecting the generation of the features in the relative spectrum.

Other work has shown that the RV jitter of low activity stars is dominated by the effects of plage/faculae (Radick et al. 1990; Hall et al. 2009; Lockwood et al. 2007; Shapiro et al. 2016), the results here for the Sun align with this paradigm. The results

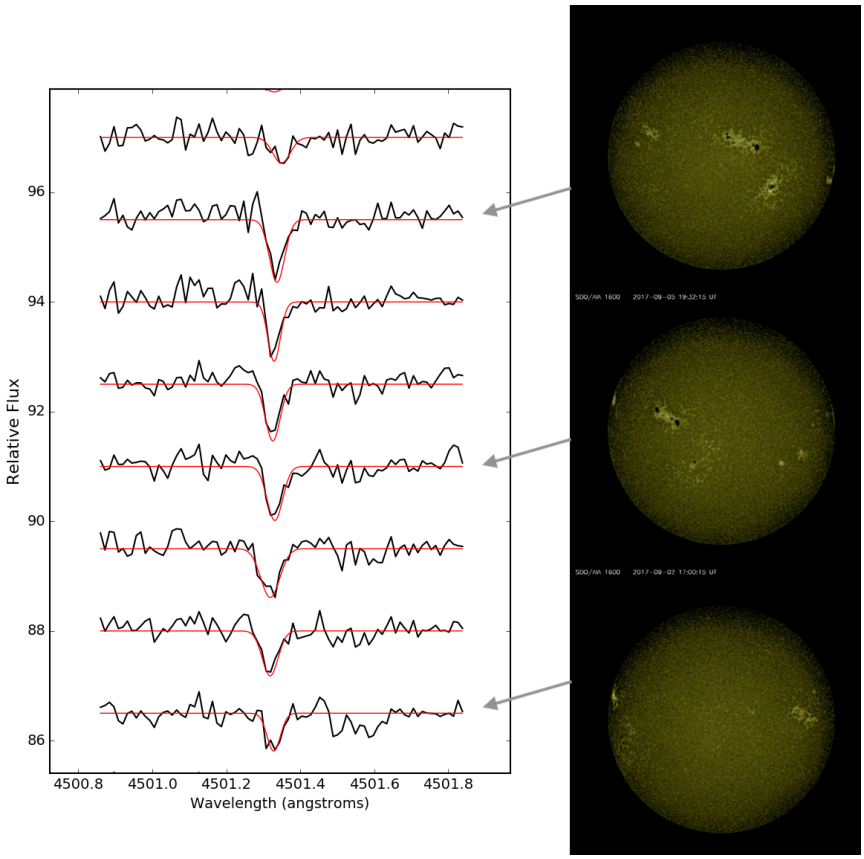


**Figure 4.12**: The relative spectra for the 30th August to 5th September 2017, with the fitted Gaussians over-plotted, this interval shows the only well correlated features during the 2017 interval and lines up with the appearance of a large spot group on the Sun.

also show, however, that the effects of activity are more complex than can be captured by the $\log R'_{HK}$ of a star. For the Sun at least, associated spots and faculae seem to show some form of competing mechanism that can almost cancel out any effects seen in the relative spectra, this may mean that certain active region configurations (i.e. spots and associated faculae) may show less stellar jitter than others for identical filling factors. This suggests that the RV jitter due to activity could vary even if the $\log R'_{HK}$ of the star does not change and could have a significant impact on the use of some stellar jitter reduction techniques.

The FF' method (Aigrain et al. 2012), for example, takes the activity variations seen in photometry to estimate the RV jitter. While the effects of faculae and plage can dominate the RV jitter of low activity stars, the low contrast of these active regions against the quiet star photosphere means they cause little photometric variability. The FF' method accounts for the effects of faculae and plage by assuming that it is related to the spots. The technique assumes that a spot is surrounded by an extended magnetised area that suppresses the convective blue-shift (e.g. plage/faculae) and the RV

jitter caused by this region can be estimated by tracking variability due to spots (see Section 2.5.5 for more detail). The results here show that, for low activity stars like the Sun and for certain configurations of activity, the unassociated faculae may generate a more significant impact on the relative spectrum than that of associated spots and faculae. The nature of the impact of this on the FF' method is two-fold. In one instance, if faculae/plage is not associated with spots then the FF' method will not be able to take these regions into account. Given that the results of this chapter imply that unassociated faculae/plage is the main driver behind the stellar jitter, this means the FF' method would fail to capture such variations. Additionally, as the unassociated faculae is offset from any spots the RV jitter correction applied by the FF' will have a phase shift from what could be a major contributor to the activity and, in turn, inject spurious signals into the RV measurements. The results for the Sun also show that the spots with associated faculae have little impact on the relative spectrum and that the correction applied by the FF' may overestimate the RV jitter of these regions. Recent work by Oshagh et al. (2017) found that the FF' method systematically under-predicted the amplitude of the RV jitter over the range of activity levels tested, which became significant at low-activity levels i.e. the level at which plage/faculae effects are expected to dominate. The work here further supports this result, giving a physical interpretation of how activity driven photometric variability may incorrectly account for the RV jitter of low activity stars.

## 4.5 Conclusion and Future Work

In this Chapter, spectra taken from the HARPS-N Solar telescope were examined in a similar way to $\alpha$ Cen B by Thompson et al. (2017). After processing the spectra to remove a strong ripple pattern, the relative spectra of the Sun showed features that correlate with changes in activity, strengthening the results found in Thompson et al. (2017). Images of the surface of the Sun were analysed to determine the spot and facular filling factors, and these were compared to pseudo-equivalent width measurements of the features in the relative spectra, which show that the features better trace changes in faculae filling factor than spot filling factor. This further strengthens the findings reported in Chapter 3 for $\alpha$ Cen B, namely that plage/MBPs are also required to explain the morphologies of the relative features. The analysis of the Sun looked at two time periods, a 2016 interval that showed unassociated faculae and a 2017 interval that showed higher levels of activity but no unassociated faculae (i.e. only faculae associated with spots was observed). For the 2017 interval very few features were observed in the relative spectra, further strengthening the hypothesis that the features seen are driven by changes in unassociated faculae.

The work has opened up a number of questions into the nature of the relative features and how they relate to changes in surface inhomogeneities of stars not explored here. Full relative spectra analysis of the entire HARPS-N Solar telescope time period may identify additional unassociated faculae regions that could help strengthen the results found. It may allow for a lower limit on the level of the facular filling factor that shows a feature in the relative spectra as well as an investigation into what defines 'unassociated' faculae/plage. Here the term is used qualitatively but a measure of the spatial association of spots and faculae (by making further use of SDO images) may show some interesting results, with the degree of association maybe affecting the point when the facular filling factor begins producing a feature in the relative spectrum. The well correlated relative spectra of the 2017 interval show some connection to the large extended spot group as well as the X-class flare that occurred during this time. By analysing the whole $\sim 3$ years of HARPS-N Solar data other strong flare events or extended spot groups will help better explore the appearance and disappearance of such features.

From a theoretical perspective, the individual lines that show a feature in the relative spectra could be modelled using a semi-empirical method to identify the height at which different parts of the lines form in the atmosphere of the Sun. This can give an indication of the activity mechanism responsible for the line changes and allow for a finer tuning of any correlations found between the features seen in the relative spectra and active regions seen on the surface of the Sun, gaining a deeper understanding of the source of the features. The models, for example, could look at how the structure of the stellar atmosphere could affect the thermal broadening, or the magnetic sensitivity (landé factor) of the lines. Being able to isolate these effects could better probe the nature of the relative features observed. An alternative is to make use of the SDO images as a template for creating a model spectrum (similar to that of the SOAP 2.0 models, Dumusque et al. 2014). Each pixel of the SDO can be assigned as either immaculate photosphere or flagged as a type of activity (i.e. spot umbra, spot penumbra, faculae, pore, flare, etc). Spectra from each type of activity can then be applied (per pixel) to build up a complete model of the surface of the Sun. This can be compared against measured HARPS-N spectra testing the goodness-of-fit of the models, and, if shown to be successful, could be used to predict the spot and plage filling factors. The model could also be used to generate active regions in any configuration desired, looking at larger, more extended active regions than has been seen on the Sun. This could then help inform on the spot and plage filling factors of other stars (of a similar spectral type to the Sun) that are more active.

The HARPS-N Solar Telescope provides a unique dataset for understanding the effects of activity on high precision RV measurements. The Solar system is the only

system where the RV effects of planets are entirely known and so can be removed. This leaves activity as the only source of the RV jitter and allows for a deeper investigation into its effects than was possible before. The RV component of the relative features has not been measured here, but measuring this could better inform on the impact that plage can have on the RV jitter of the Sun. Providing a way to track the spectral variations due to plage. This, combined with an estimate of the plage filling factor, could help in improving the accuracy of high precision RV measurements, or for exoplanet atmosphere studies. The slope in the UV part of the spectrum is indicative of haze and Rayleigh scattering (Sing et al. 2016) but is also perturbed by spots and plage. With an estimate of the filling factors for these active regions, the contribution for spots and plage could be removed and a more robust measure of haze in exoplanet atmospheres can be made.

*Chapter 5*

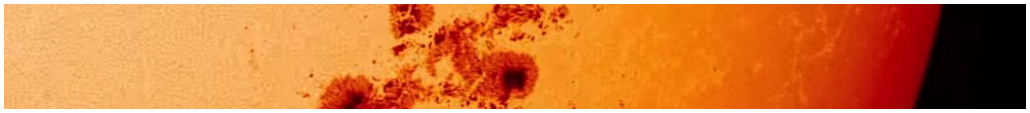

# Stellar Rotation with NGTS

SS

## 5.1 Introduction

The measurement of a rotation period from photometry, especially for FGK stars (i.e. the kind targeted by exoplanet photometric surveys), requires the presence of active regions on the surface of the star. This activity can act as a nuisance in the radial velocity follow-up of transiting planets, since plage and starspots can manifest themselves as apparent RV shifts that can mask or (in extreme cases) mimic orbiting planets (e.g. Queloz et al. 2001; Huélamo et al. 2008). However, the rotation period of a star revealed by the presence of activity can also provide a valuable additional constraint on the planetary system. For example, with a stellar rotation period the age of a star can be estimated using gyrochronology (Barnes 2007; Barnes et al. 2016), as well as permitting highly misaligned transiting planetary systems to be identified through determination of the inclination of the stellar spin axis without the need for Rossiter-McLaughlin (RM) observations (e.g. Watson et al. 2010; Simpson et al. 2010; Schlaufman 2010).

In this chapter I look at using a number of different techniques to search for the rotation period of exoplanet host stars. For this, I use photometry from the Next Generation Transit Survey (NGTS) to investigate the use of wavelet analysis, in conjunction with more conventional period searching techniques, to both independently validate any signals found and gain information on the location in the light-curves where these periods are most strongly seen. This work is done in collaboration with the NGTS consortium. As of writing, one planet has been publicised by the consortium, with other work to be released in three upcoming publications (highlighted in the relevant sections). These publications (which I am a co-author on) made use of the tool described in this chapter.

### 5.1.1 The Next Generation Transit Survey (NGTS)

The Next Generation Transit Survey (NGTS, Wheatley et al. 2018, see Figure 5.1) is a ground based exoplanet wide-field photometric survey designed to target planets in the Neptune size range around low mass stars bright enough for RV follow-up. The facility consists of twelve 8 inch telescopes, each on a separate mount allowing for independent field selection. With an on sky pixel size of $\sim 5$ acrsec, the $2048 \times 2048$ deep depletion, red sensitive CCDs cover 96 deg$^2$ simultaneously. The CCDs are red sensitive, in order to better match the peak emission from K and early M stars, which are the primary targets for the survey. The high photometric precision of NGTS allows it to aim at detecting planet transits at the 0.1% depth level, which would allow it to target Neptune-sized planets around Sun-like stars and super-Earths around early M-dwarfs (see Figure 5.2). While similar sized planets have already been detected by space based surveys like Kepler (Borucki et al. 2010) and CoRoT (Auvergne et al.

**Figure 5.1**: Image of the NGTS facility at Paranal, Chile. The facility contains 12 independent telescopes doing a wide field search for transiting exoplanets. Credit: ESO/ R. West.

2009), most of these are too faint for RV follow-up. NGTS will specifically aim for stars with $V < 15$, allowing for follow-up confirmation (using HARPS and ESPRESSO) and mass determination of these planets. Below I will outline the basic data processing and target vetting used by NGTS, full details can be found in Wheatley et al. (2018).

NGTS data reduction starts by first identifying all sources in the field and generating a catalogue of target stars using a stacked master image, with each image dithered to allow for sub-pixel sampling. The NGTS catalogue is then cross-matched against other catalogues (e.g. 2MASS, and Gaia), which allows for preliminary spectral classification and initial vetting of exoplanet candidates. The images are then bias-subtracted and flat-fielded using the standard approach, with bias and flat-field frames taken on a nightly basis. Aperture photometry is performed on each star identified in the catalogue using a 3 pixel aperture creating light-curves of each star. These light-curves are then detrended to remove systematic signals from the data, this is done using SysRem (Tamuz et al. 2005) – an algorithm that looks for signals common to multiple light-curves and removes them.

The data can then be analysed for potential planetary transits using the BLS (Box Least Squares) periodogram (Kovács et al. 2002, see Section 2.5.4) after which the proposed candidates are put through a manual first-pass vetting to remove obvious false positive detections. Candidates that pass this first check are given a more detailed false positive analysis, looking for secondary eclipses at 0.5 phase and comparing even and odd transit shapes, which would indicate an eclipsing stellar companion (a process

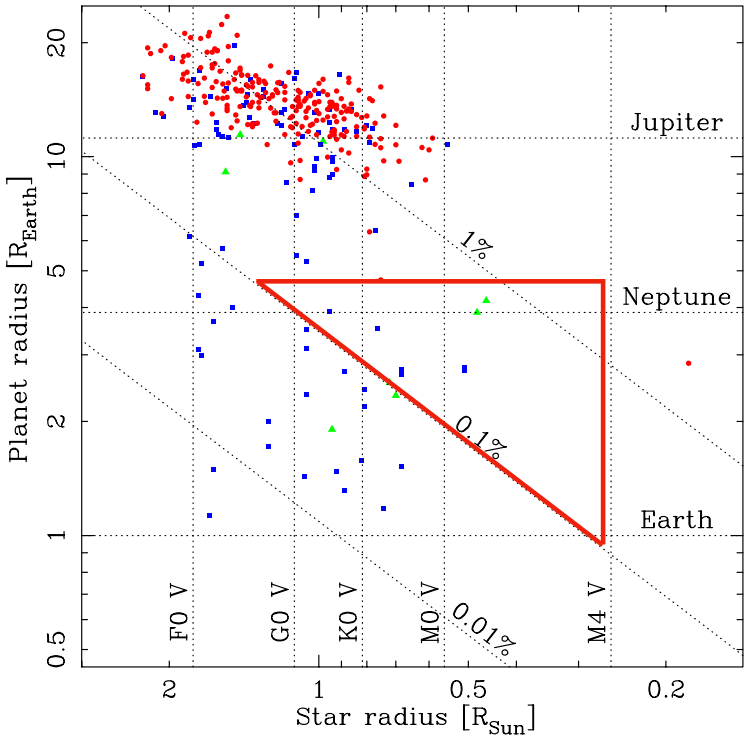


**Figure 5.2**: The planet and stellar radius of transiting exoplanets with masses determined to better than 20%. The diagonal dotted lines are lines of equal transit depth and the horizontal lines show the radius of the Solar System planets. NGTS is aiming for transit depths of 0.1% allowing for the detection of Neptune-sized planets around Sun-like stars and super-Earths around early M-dwarfs. Red circles are ground-based transit discoveries, while the blue squares are for those discovered from space. The green triangles are planets discovered by RV measurements. The red line highlights the approximate discovery space of NGTS. Figure modified from Wheatley et al. (2018).

referred to as eyeballing). Out-of-transit ellipsoidal variation is also looked at, which could indicate a short period binary or stellar activity and, finally, the pixel centroid is tested for signs of variation during transit/eclipse, indicating a blended binary. If the candidate passes these checks it is passed on for RV follow-up observations and, occasionally, higher precision photometry in the cases where the transit depths are close to NGTS's observing limit. Within the NGTS consortium I developed a package called UnEarth (a stellar rotation period search tool) that is used as part of the follow-up strategy.

## 5.2 Stellar Rotation Detection Techniques

To more robustly identify stellar rotation periods, I make use of a number of methods within the UnEarth package. Each of theses techniques are independent and so provide a useful validation of any periods found, with periods common to all techniques being more believable. This does not address the systematic effects of aliasing, window functions or harmonic effects as these are dependent on the data but provides a more detailed picture of the signals that exist in the light-curves. The techniques used are outlined below.

### 5.2.1 Generalised Lomb-Scargle Periodogram

Periodograms are essential tools for conducting searches for periodic signals in data, the most commonly used periodogram within exoplanet work is the Generalised Lomb-Scargle (GLS). The workings of a GLS periodogram have been discussed previously in Section 2.5.4, so details will not be given here. For this work I use the GLS as the main period detecting tool, with the other methods employed to back-up what was seen in the GLS or to better understand the nature and origin of the signals.

The use of GLS periodograms for rotation period searches in photometry is not new, but by tying it to variations seen in other periodic signal detecting algorithms the validity and origin of any signals can be checked.

### 5.2.2 Discrete Correlation Function

In a general sense, if two signals are seen to vary in time, knowing if this variation is correlated can be useful in determining a relationship between the two. The process of cross-correlating takes a signal and compares it with a delayed version of the second signal. The level of correlation can be plotted as a function of delay or 'lag' and is known as the Cross-Correlation Function (CCF). A peak in the CCF indicates the lag at which the two signals are the most correlated. One example already discussed in previous chapters is the use of CCFs to measure the RV variations of spectra to high precision. In this case, the spectrum of a star is correlated against a model spectrum or line mask over a number of lags to produce the CCF. The peak of the CCF then defines the RV shift of the star.

An auto-correlation takes this general case and, instead of comparing one dataset to another, the dataset is compared to a delayed version of itself. This is a useful tool for searching for repeating patterns, such as those of periodicity. The issue with applying these techniques to real data is that real data tends to not have a set cadence of obser-

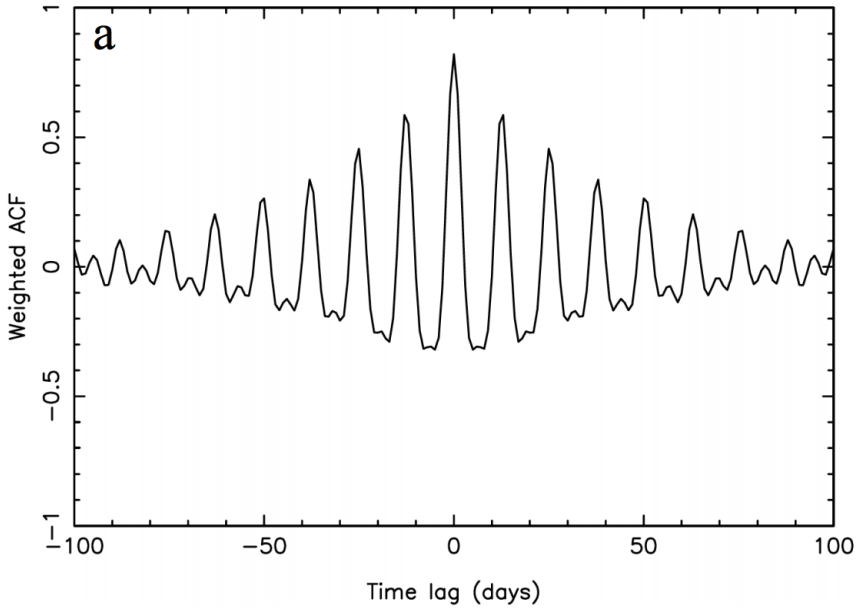


**Figure 5.3**: The Auto Correlation Function (ACF) of Kepler 78. The peaks are spaced 12.6 days apart, capturing the rotation period of the star. The strength of the peaks decrease over time due to the evolution of active regions on the stellar surface. Image credit: Pepe et al. (2013).

vations, and instead shows variations in the sample timing, or gaps in the time series. Additionally, for the cross-correlation case one of the datasets needs to be interpolated, which can add uncertainties to any measured correlations.

Edelson & Krolik (1988) introduced a new correlation technique, the Discrete Correlation Function (DCF), that instead of measuring the correlation of the entire dataset using a number of lags, measures a set of discrete correlations between two points $(a_i, b_j)$ , where each pair has its own pairwise lag defined. These pairs are then binned in time to produce the DCF. Edelson & Krolik (1988) points out that binning does mean a small amount of interpolation but this is acceptable in the case of a smoothly varying function (as one would expect from stellar rotation). The DCF is therefore a useful tool for measuring variability. Pepe et al. (2013) used the technique to measure the 12.6 day rotation period of Kepler 78, comparing the light-curve to a delayed version of itself using the Auto-Correlation Function– ACF (see Figure 5.3). In addition, the ACF of Kepler 78 showed a reduction in the strength of each successive correlation peak, which the authors attributed to the evolution of active regions on the stellar surface.

### 5.2.3 Wavelet Analysis

One of the main issues with measuring the rotation period of a star from photometry is its dependence on surface inhomogeneities to cause measurable variability in flux. Active regions likes spots exist on the surface of stars and show a photometric variability that can be used to measure rotation period. These active regions are non-stationary and can exhibit evolution or migration that can change the strength of the measured signal. Additionally, multiple active regions can appear on the surface at the same time, which can affect the measured periodicity, introducing dominant harmonic effects (i.e. $P_{rot}/2$, or $P_{rot}/3$ being significant additional peaks in the periodogram). Where algorithms like the GLS periodogram can pick up on periodicity, they are not well designed for signals that grow and decay over time (like stellar activity).

Wavelet analysis is a tool used for analysing localised variations in a dataset. Where other methods, like the GLS periodogram, search for periodicity that exist throughout the whole dataset, wavelet analysis decomposes the data into time-frequency space, allowing it to determine localised periodicity. In other words, the wavelet analysis can not only find the strongest periods that exist in the dataset (the same as the GLS algorithm) but is able to determine what part of the data contributes to this period. In this thesis I make use of the wavelet analysis as outlined by Torrence & Compo (1998). I also make use of codes available[1] and adapt theses for use with NGTS data within the UnEarth package. Here I will only outline the main aspects of the method of the wavelet, with a full methodology available in Torrence & Compo (1998), and an extended guide available at http://paos.colorado.edu/research/wavelets/.

As mentioned above, active regions are not static on the stellar surface, they migrate and evolve making measuring rotation periods using activity more difficult. If, during the observation of a star, an active region forms, grows, and decays away the GLS will measure a rotation period from its light-curve. Phase-folding the data, which contains both active and inactive phases, onto the stellar rotation period may not produce a clear periodic signal as the inactive phase could mask the rotation period. In addition, active regions can form at any longitude on the stellar surface so multiple, independent, high activity time ranges may not be coherent when phase-folded, with the variation seen in the two time ranges interacting destructively and hindering the positive detection of a rotation period. By utilising the wavelet analysis the higher activity periods can be isolated and the stellar rotation period better determined by selectively phase-folding only the time ranges where the period is significant.

Wavelet analysis is an adaption of the more conventional windowed Fourier Trans-

[1] codes available at https://github.com/chris-torrence/wavelets

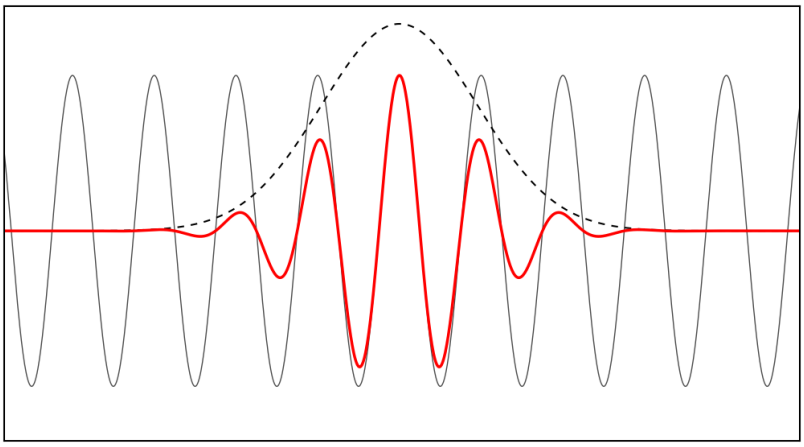

**Figure 5.4**: Example of the Morlet wavelet, with a wavenumber, $\omega_0 = 6$, is shown in red, which is simply a sine wave (solid grey line) multiplied by a Gaussian envelope (dashed grey line). This is used as the window function for the wavelet analysis. It is one of the simplest wavelets and also perfectly suits the periodic nature arising from rotational modulation, plus the growth and decay of active regions.

form (FT). It revolves around the definition of a window function that better represents the data than the box-car shaped window used by the windowed FT. This 'better' window function takes the form of a wavelet. The most commonly used is the Morlet wavelet, which is simply a sine wave multiplied by a Gaussian envelope, and is given by

$$\psi_0(\eta) = \pi^{-1/4}\, e^{i\omega_0\eta}\, e^{-\eta^2/2} \tag{5.1}$$

where $i$ is the imaginary number, $\eta$ is a non-dimensional 'time' parameter, and $\omega_0$ is the wavenumber. The choice of wavelet is important as it should represent the data and the nature of the pattern being fit. The Morlet wavelet is also used in this analysis, as it is has a simple waveform and exhibits wave-like behaviour of a similar form seen in the periodic signals associated with stellar rotation. The Morlet wavelet is also a common choice of wavelet when searching for smoothly varying periodicity. For the wavelet to be used it has to satisfy the conditions of having a mean of zero and be localised in time and space, a so-called 'admissible' wavelet. Setting the wavenumber $\omega_0 = 6$ satisfies these conditions for the Morlet wavelet (an example of this wavelet is shown in Figure 5.4).

The wavelet function can then be scaled and translated across the data set

$$\psi\left[\frac{(n-n')\delta t}{s}\right] = \left(\frac{\delta t}{s}\right)^{\frac{1}{2}} \psi_0\left[\frac{(n-n')\delta t}{s}\right] \tag{5.2}$$

where $s$ is the scaling (or dilation) parameter and $n$ is the translation parameter. The $s^{-1/2}$ is a normalisation constant. Thus, for a dataset with $y_n$ points separated by $\delta t$, the wavelet transform is just the convolution of the wavelet function with the data

$$W_n(s) = \sum_{n'=0}^{N} y_{n'} \psi^*\left[\frac{(n-n')\delta t}{s}\right] \tag{5.3}$$

where $^*$ denotes the complex conjugate and $N$ is the number of data points in the data set. However, rather than using this equation it is both faster and simpler to do the calculation in Fourier space where all $N$ convolutions can be done simultaneously, and thus the wavelet transform becomes:

$$W_n(s) = \sum_{k=0}^{N} \hat{y}_{k'} \hat{\psi}^*(s\omega_k) e^{i\omega_k n \delta t} \tag{5.4}$$

where $k$ are the frequencies being considered, and the angular frequency, $\omega_k$, is defined as

$$\omega_k = \begin{cases} \frac{2\pi k}{N\delta t}, & k \leq \frac{N}{2} \\ \frac{-2\pi k}{N\delta t}, & k > \frac{N}{2} \end{cases} \tag{5.5}$$

The wavelet analysis can be described as taking a FT of the wavelet and the time-series and applying the wavelet transform (Equation 5.4) at each scale (or frequency, Equation 5.5). The final result can be captured as a contour map, called the 'wavelet power spectrum' and taken as $|W_n(s)|^2$ defined at each datapoint, $n$, and scale, $s$. This power spectrum contains both frequency and temporal information (an example can be seen in panel *e* of Figure 5.5). Summing the contour map along the time direction gives the global wavelet spectrum, a measure of periodicity very similar to that of the GLS (though at lower frequency resolution).

## 5.3 Combined Approach to Period Searching

Instead of looking at individual techniques for detecting periodicity, I combine the three methods outlined above into a single package called UnEarth. By using multiple techniques, any signals detected in one can be verified by looking for analogous

detections in the other methods. This analysis concentrated on providing a useful tool for analysing NGTS light-curves, I have applied it to a number of recently discovered NGTS planetary systems (one of which, NGTS-1b, has been published – Bayliss et al. 2018), a rare M-dwarf binary found by NGTS and an active flare star. Prior to any period search I go through a process of 'cleaning' the data for use with UnEarth, this is a useful step to remove known (false) periodic signals from the data. Transits are removed from the light-curve, followed by a pre-whitening procedure (see Section 2.5.6) to remove known systematics resulting from moon contamination (giving a $\sim 28$ day period) and a 1-day alias resulting from the 1-day windowing of the data. This pre-whitening was done using the code Period04[2] (Lenz & Breger 2005). This performs a Discrete Fourier Transform (DFT) on the data. The strongest period in the DFT spectrum is identified and fitted out by removing a sine wave of the identified period from the data. The amplitude and phase of the wave are determined using the least-squares fitting algorithm built into Period04. The DFT is then run again on the residuals and the next strongest period identified and fitted out in an identical way. This process is repeated until the noise floor is reached, which is defined as the point when no strong peaks are seen in the DFT spectrum. The transit-clipped, pre-whitened data was then run through the UnEarth code, a multiple period search algorithm package, which I developed within the IDL programming language.

To speed up calculations of the various periodogram searches the data is binned into 0.01 days (14.4 min). This is because NGTS operates on a 10s exposure time and the stellar rotation period is of the order of days, thus binning substantially reduces the run time without causing a noticeable effect on the period regime aimed at by UnEarth. In addition, for the wavelet analysis, a constant time step is required so rebinning is necessary. The bins where no data exist are set to zero. To test the significance of this zero approximation on the wavelet analysis, a sine wave with random noise was generated. This sine wave model was then sampled in a uniform way as is expected for the wavelet and then more randomly, with gaps in the sampling filled by zeros. These two datasets were run through the wavelet analysis, with no qualitative change in the wavelet power spectrum seen. Thus, for the purposes that the wavelet analysis will be used, this zero approximation assumption is valid.

For the GLS periodogram, false alarm probabilities (FAPs) were also calculated by performing a boot-strapping of the data. This involves randomly rearranging the flux values of the data while keeping the time values the same. The periodogram is then rerun after each randomisation and the boot-stapped FAP are calculated based on the spread of values seen at each frequency. Any strong periods found in this boot-

[2] Available at: https://www.univie.ac.at/tops/Period04/

strapping process are not real but a result of data sampling. 90%, 95%, and 99% FAPs are calculated from these bootstrapped periodograms. For the wavelet analysis, 90% confidence intervals were calculated for the 2D contour plot using the codes provided by Torrence & Compo (1998).

As a test of the UnEarth code, a star showing obvious stellar rotation was analysed a flare star known as NG0612-2518.000463 within the NGTS consortium), the results of which can be seen in Figure 5.5. A clear period of $\sim 3.88$ days was found by all methods. Panel *e* of Figure 5.5 shows the wavelet power spectrum and highlights the ability of wavelet analysis to produce localised frequency information. The time axis of the wavelet power spectrum corresponds to that of the light-curve, making it easy to directly compare the two. The green and blue areas correspond to high power, showing most of the power for the $\sim 3.88$ day period comes from the middle potion of the data, where the longest continuous observations occur. Areas in white correspond to times of zero power, which correlate with times where no data is available and the zero approximation (described above) is used – qualitatively, this does not affect the ability to detect the rotation period of the star. The cross-hatched regions at the edges of the power spectrum are known as the 'cone of influence', power inside these regions are not to be believed as they are strongly affected by aliases and windowing of the data (Nyquist frequency) effects.

The Global Wavelet Spectrum (GWS), which is the power spectrum summed along the time direction, shows a broader peak than the GLS periodogram. The wavelet has sacrificed frequency resolution for time information, and this is one of the disadvantages of the technique. This is why it is useful (for the purposes of measuring stellar rotation periods) to pair it with the GLS, with the GLS providing high resolution frequency information and the wavelet providing time information. Phase folding the light-curve onto this period shows a clear modulation of the flux (i.e. the rotation period of the star), with the large spikes being seen due to flares from the stars (see Figure 5.6).

Looking at the wavelet power spectrum more closely, there is an increased amount of power at $\sim 110$ days, with additional power at shorter periods. The light-curve for this time range shows two flares occurring in quick succession, which is being picked up as short period variability. At the same time, enhanced power is seen in the wavelet power spectrum at $\sim 3.88$ days suggesting the presence of enhanced activity. The light-curve of this time range also shows activity modulated variations that are more pronounced. This shows the power of wavelet analysis over just applying the GLS. Wavelet analysis is able to not only determine where periods are seen in the light-curve but is also able to determine the strength of the signal. For the flare stars,

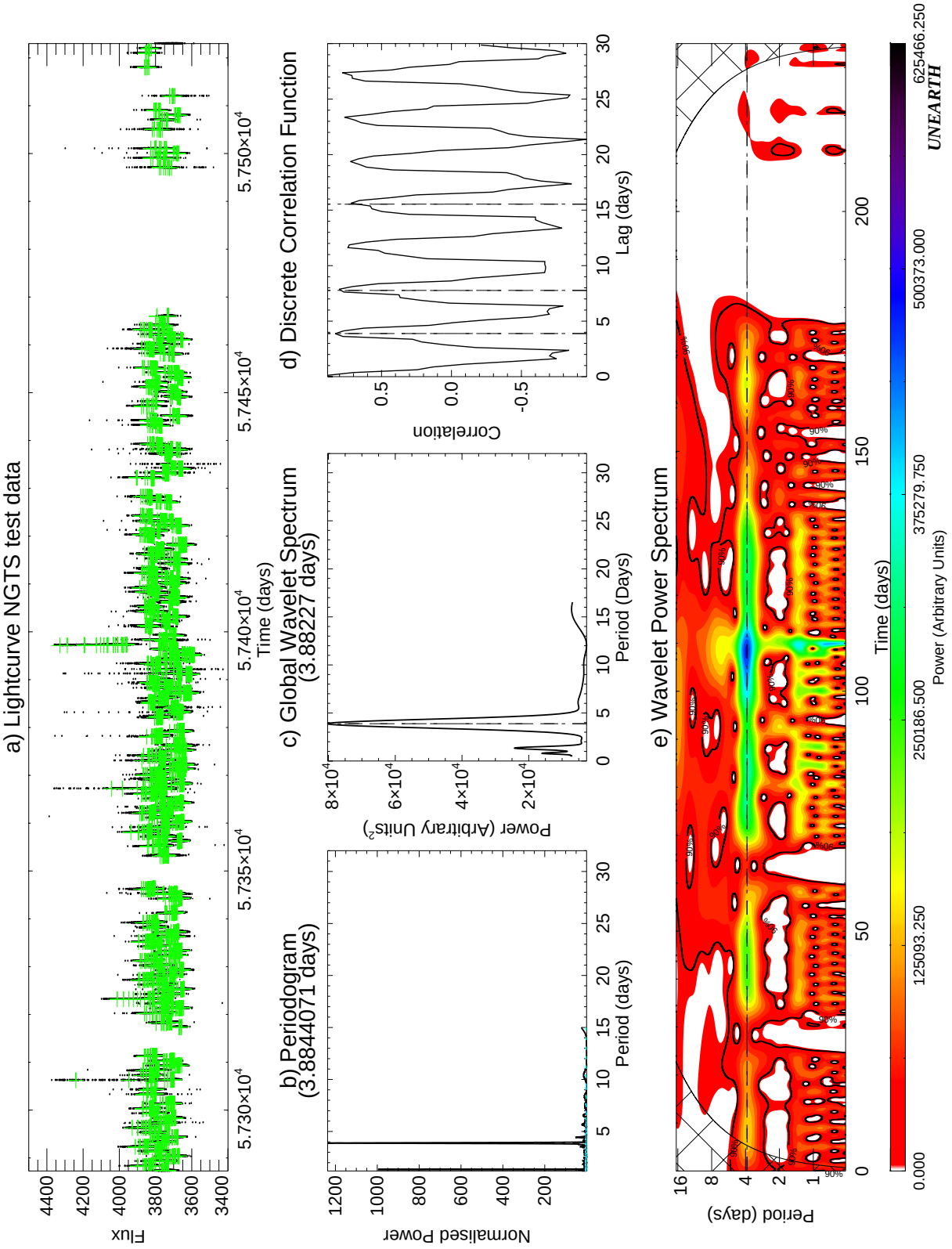


**Figure 5.5**: Output from UnEarth. *a)* full light-cuve, the green plus symbols are the binned data points. *b)* shows the GLS periodogram, and *c)* shows the global wavelet spectrum (GWS – which is the wavelet power spectrum but compressed along the time direction). *d)* Discrete correlation function, the vertical lines show the expected correlation peak for the GLS and GWS. *e)* the wavelet power spectrum, blue indicating high power and red indicating low power. The solid black contour lines show the 90% confidence limit and the horizontal dash line shows the peak period of the GLS. A clear periodicity of $\sim 3.88$ days is found across all techniques. The very high power at $\sim 110$ days is from two close by flare events being mistaken for periodicity. Note, the hashed region at the edge of panel *e)* is the cone-of-influence, power inside this region cannot be trusted due to alias effects.

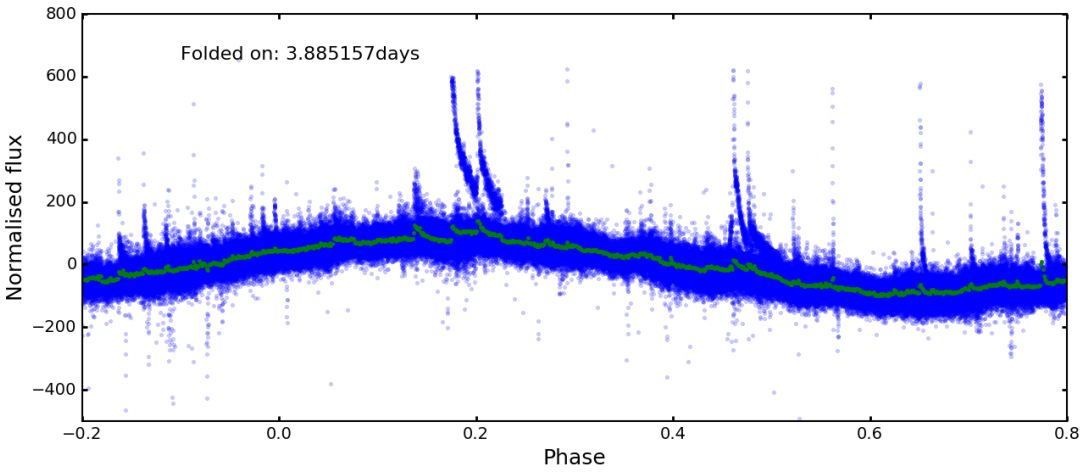


**Figure 5.6**: NGTS data of NG0612-2518.000463 phase folded on the period found from UNEARTH. The spikes in flux are due to flares from the star.

this could provide a useful measure of activity and may allow for correlations between increased activity (as traced by power in the wavelet power spectrum) with probability of a flare. For RV follow-up it is easy to imagine how knowing the strength of the activity as seen in photometry can aid in performing high precision RV measurements, allowing time ranges when the RVs are least affected by stellar activity to be identified.

### 5.3.1 NGTS-1b – A hot Jupiter around an M-dwarf

NGTS-1b is a hot Jupiter (with a mass of $0.812 M_J$) transiting an early M-dwarf and is the first exoplanet discovered by the NGTS survey (Bayliss et al. 2018). This planetary system adds to the growing number found around M-dwarfs e.g. TRAPPIST-1 (Gillon et al. 2017) and Proxima Centauri (Anglada-Escudé et al. 2016). The low intrinsic luminosity of these stars means that the habitable zone lies close in to the host star. Although the lower star-planet mass ratio of M-dwarf systems should make finding planets (especially hot Jupiters) easier, their low intrinsic luminosity makes performing high precision photometry more difficult. In addition, NGTS is designed to target exoplanet candidate systems bright enough for RV follow-up, but the spectra of M-dwarfs are dominated by molecular lines making RV measurements more difficult. However, M-dwarfs are the most numerous type of star in the galaxy (making up close to 75% of nearby stars, Henry et al. 2006), and understanding the planet frequency around these stars better explores the planet population of the galaxy, making these planetary systems valuable targets.

As part of the investigation into NGTS-1 the light-curve was analysed for any periodicity that could indicate a stellar rotation period. NGTS observations for this star span 100 nights between $10^{th}$ August to $7^{th}$ December 2016. The data were reduced using the standard pipeline described in Section 5.1.1, which identified the star as having

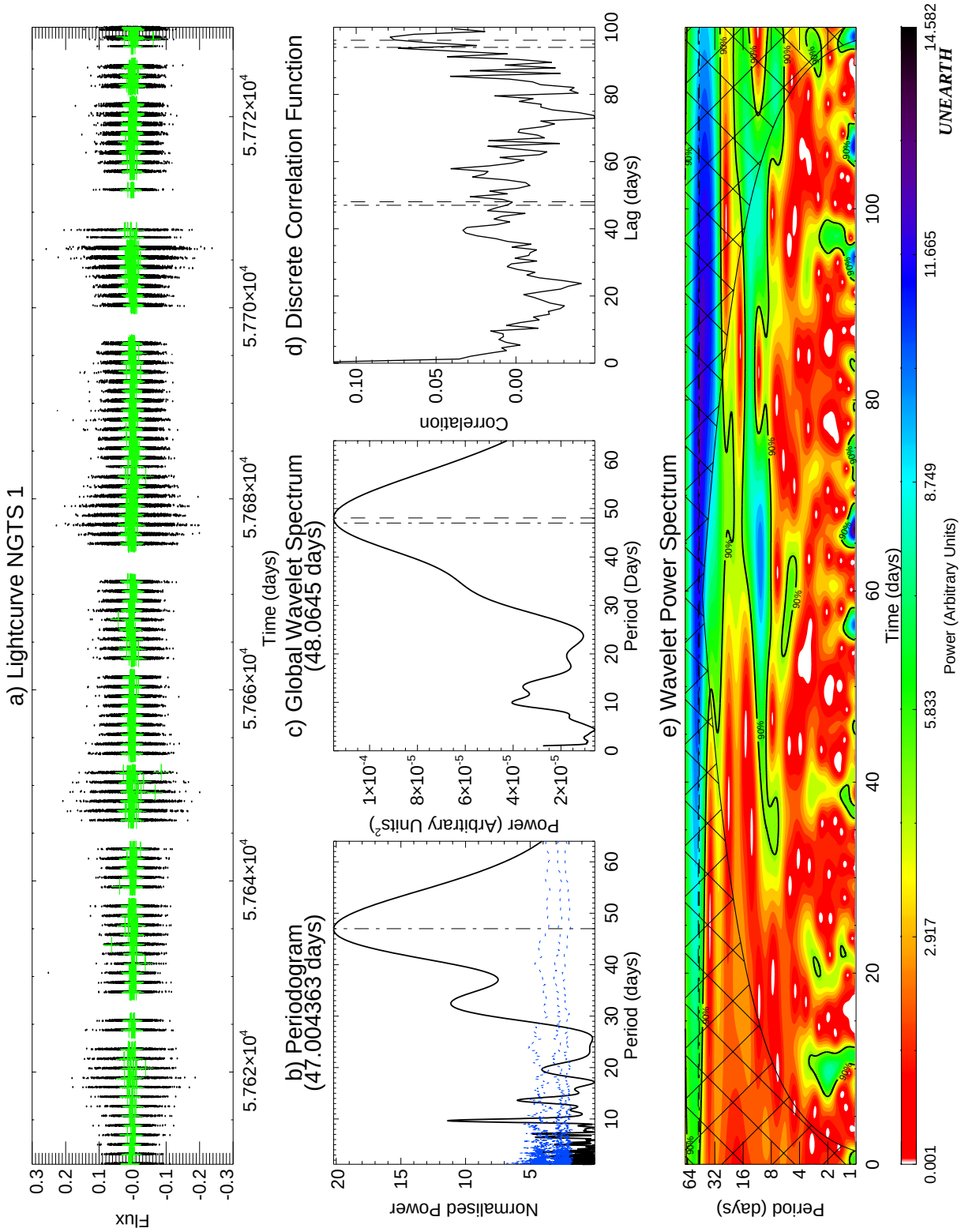


**Figure 5.7**: NGTS-1 period search, all figures are the same as that described in Figure 5.5. The 90%, 95%, and 99% FAP limits can be seen as the dotted blue lines in panel *b*. The dashed lines in panel *c* and *d* are the peak period of the GWS, while the dot-dashed line is the peak period seen in the GLS. Note the strongest period found is inside the cone of influence in the wavelet power spectrum, the power here cannot be trusted due to aliasing and Nyquist frequency effects.

a 2.5% depth transit on a ~ 2.65 day period (more details on the system can be found in Bayliss et al. 2018). To search for a stellar rotation period the light-curve was further processed. As a first step the transits were removed from the light-curve as these variations are known to be due to a planet and could be picked up by UnEarth, adding further complexity to the GLS and GWS power spectra. The data was pre-whitened (using Period04) run over a range of $0-1.2$ days$^{-1}$. The analysis identified two strong periods at ~ 35.81 days and ~ 1.02 days. The ~ 1 day period is due to windowing of the data, while the source of the ~ 35.81 day period is unknown. As the ~ 35.81 day is an unknown signal it should not be removed and only known signals should be removed, the pre-whitening was repeated with only the ~ 1 day signal being fitted out. The pre-whitened data is then fed into the UnEarth code, where it was binned on 0.01 of a day (14.4 min) prior to a period search. UnEarth was run over a period range of 0 to 64 days, the usual period search of UnEarth is $0-32$ days but as Period04 identified a period at ~ 36 days this was extended to 64 days (chosen due to the wavelet scaling working in power-of-two multiples).

Figure 5.7 shows the UnEarth output for NGTS-1. A large broad feature is seen at ~ 47 days in the GLS but the wavelet power spectrum (panel *e*) shows that this power comes from within the cone of influence and so is influenced by aliasing effects. This period is most likely due to systematics, which was confirmed by the lack of a clearly modulating signal in the phase folded light-curve. The power spectrum also shows that the ~ 35.81 day period identified by the DFT analysis of Period04 also partially resides inside the cone of influence and is also a systematic. A third strong peak is seen in the GLS at 9.676533 days but again no clear signal that can be ascribed to stellar modulation is seen when the light-curve of NGTS-1 is phase-folded on this period. This is in keeping with the results of (Bayliss et al. 2018). The authors used the clean algorithm (Roberts et al. 1987) to search for periodicity, this algorithm performs a nonlinear deconvolution in the frequency domain. The authors identified similar periods to those shown here and concluded that the amplitude of the signal was at the level expected for systematic noise. HARPS spectra are also available for this object but with a $v \sin i < 1$ km s$^{-1}$ the rotation period cannot be further constrained.

### 5.3.2 NGTS-2b – An inflated hot Jupiter Orbiting an F-Star

NGTS-2b is a hot Jupiter planet orbiting a bright F6V star, with an orbital period of close to 4.5 days. This puts the 0.53 $M_J$ planet close to its host star resulting in an effective temperature of the planet of 1312 K (Raynard et al, *submitted*)[3]. Analysis shows that the planet is inflated with a bulk density of 0.203g cm$^{-3}$, making it one

[3]the results from UnEarth are used as part of this publication

of the lowest density exoplanets discovered to date. The bright (V = 10.69) host star makes the system a good candidate for exoplanet atmospheric studies. Discovering more of these planets is necessary in order to expand atmosphere studies and provide a more holistic picture of the formation and evolution of such planets including their atmospheres.

As with NGTS-1, the light-curve of NGTS-2 was analysed for periodicity. A total of 138 nights of photometric data are available from NGTS for this system, from $16^{th}$ June to $20^{th}$ August 2017. Again, the transits were removed and the data were pre-whitened using Period04. Two periods were found ~ 1.0 day (the 1-day window) and ~ 158.5 days, both periods were removed in the pre-whitening. The ~ 158.5 day period most likely relates to the Nyquist frequency and should not have a major effect on the period range aimed at here but was also removed as it showed a strong signal in the DFT spectrum. I applied the UnEarth code to the data, with a binning of 0.01 days and covering a period range of 0 – 32 days (see Figure 5.8).

A number of strong periods are seen in the GLS periodogram (in the GWS the lower frequency resolution means all the peaks have blended together – see panel *e* of Figure 5.8), the strongest of which is seen at 7.255 days. The wavelet power spectrum shows two distinct timespans where these signals are strongest (from ~70 – 120 days, and again from ~150 – 200 days – see panel *e* of Figure 5.8). The light-curve was phase-folded on the strongest periods seen for the entire dataspan, as well as only for times when the wavelet analysis indicated high power at those periods. However, on phase-folding, no clear evidence of a rotationally modulated signal is seen in any of these results.

A median periodogram was produced for the ~11,000 other stars within the same NGTS field as NGTS-2, observed in the same season and with the same camera (Figure 5.9 – Chaushev and Raynard, private communication). This shows significant periodicity around ~4 days, as well as a forest of power at shorter periods, indicating that these periods arise due to systematics. While there is also a very broad, minor peak covering periods between ~6 and ~8 days across the field, the ~ 7.25 day signal seen for NGTS-2 in the GLS and wavelet analysis is much tighter and stronger.

HARPS spectra of the star show a $v \sin i$ = 15.2 km s$^{-1}$, which is combined with the stellar radius (1.702R$_\odot$) determined using species (Soto & Jenkins 2018) to obtain $P_{rot} = 5.66 \pm 0.34$. This period is not found in any of the techniques used in UnEarth. Phase-folding on the 5.66 day period found from spectroscopic measurements does not show any clear modulation. If this spectroscopic periodic is to be believed, the period seen in the photometry would be a systematic. Assuming $\sin i = 1$, the rotation period

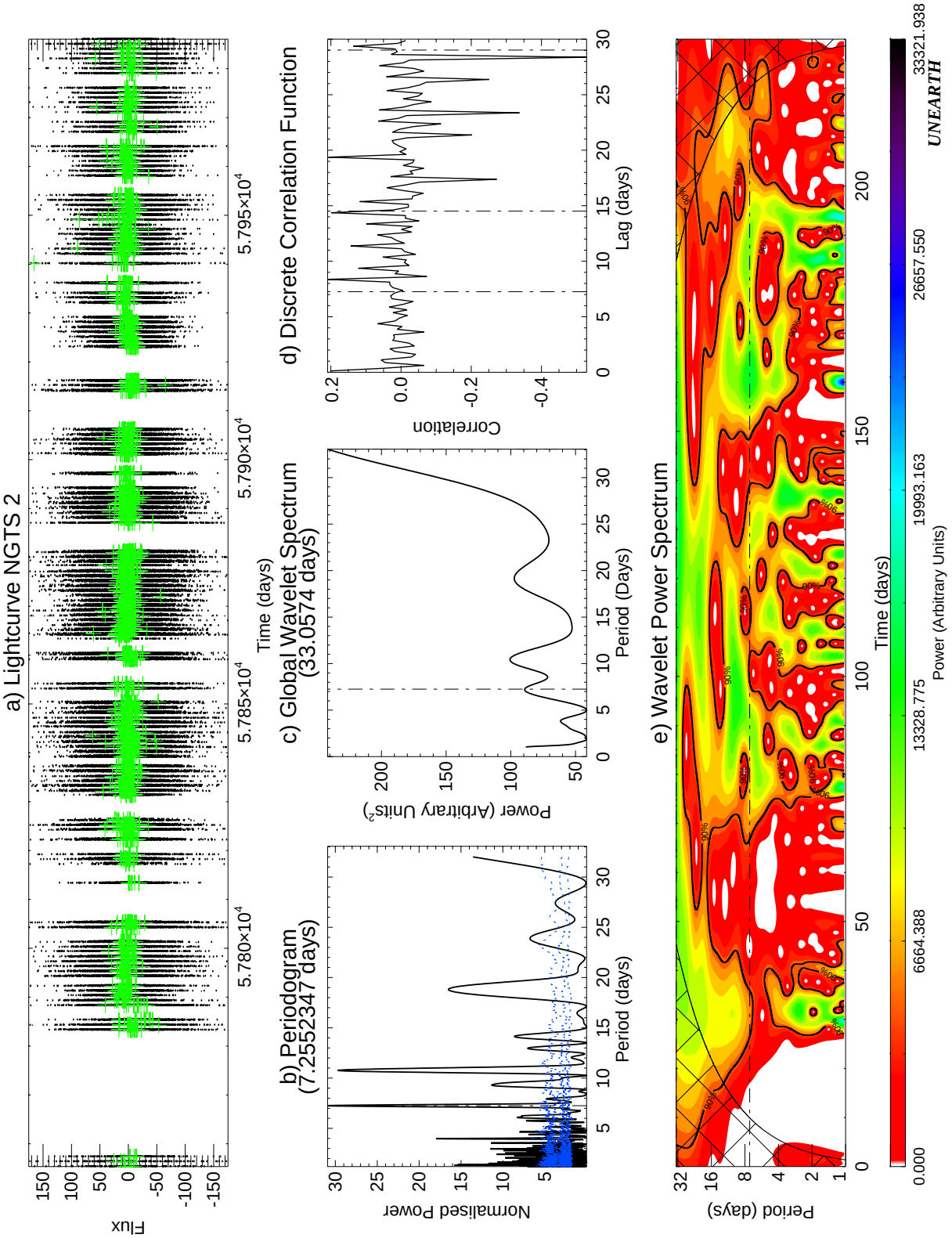


**Figure 5.8**: NGTS-2 period search, all figures are the same as that described in Figure 5.5. A number of strong periods can be seen in the GLS, none of which appear to be isolated in the cone of influence. Each period was checked by phase-folding but none showed any periodicity.

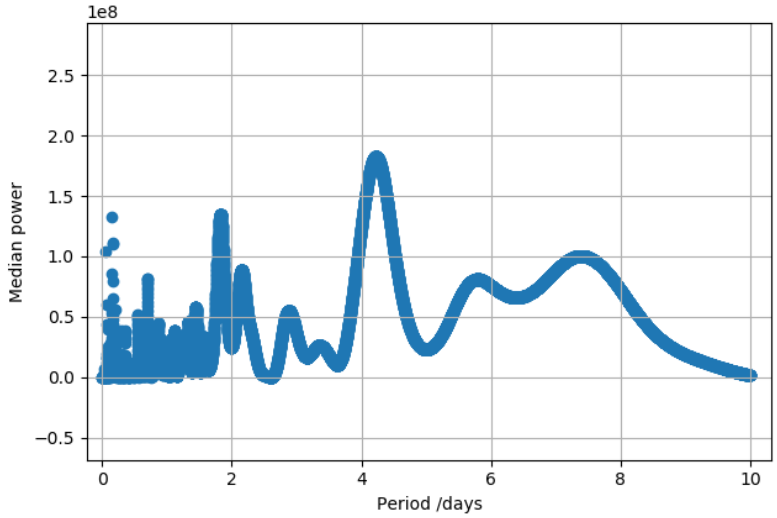


**Figure 5.9**: Median GLS periodogram of the NGTS field of NGTS-2. None of the strong periods seen in the NGTS-2 are seen here, reducing the likelihood that the peaks being seen are due to aliases. Credit: Chaushev and Raynard, private communication.

of the star, $P_{rot}$, can be calculated by,

$$P_{rot} = \frac{2\pi R_\star}{v \sin i} \sin i \tag{5.6}$$

where $R_\star$ is the radius of the star. A $P_{rot} \approx 7.25$ days would lead to a $\sin i \approx 1.2$ (which is unphysical) or, assuming the $\sim 7.25$ day period is the stellar rotation period, a $v \sin i = 11.9$km s$^{-1}$– implying an overestimate of the $v \sin i$ of the star. Watson et al. (2010) showed that for a number of planets an unphysical $\sin i > 1$ was calculated based on the $P_{rot}$, $v \sin i$ and $R_\star$ measured for the systems. The authors suggest that incorrect treatment of instrumental and intrinsic line broadening can cause an overestimate of the $v \sin i$. The effect becomes more pronounced for slowly rotating stars or, in this case, hotter stars.

The measurement of $P_{rot}$ (from photometry) and $v \sin i$ and $R_\star$ from spectroscopy can enable measurements of the inclination of the system without the need for Rossiter-McLaughlin analysis (Rossiter 1924; McLaughlin 1925, or see Section 1.4). The results of NGTS-2 suggest that further photometric observations are required. These may help better constrain the stellar rotation (depending on the activity level of the star). The system also highlights the use of the UnEarth code in providing an in-depth investigation of the photometric variability of stars.

### 5.3.3 NGTS-4b – An Ultra-short Period hot Jupiter

An interesting subset of transiting exoplanets are the ultra-short period planets, these are characterised as having an orbital period of $< 1$ day and are ideal candidates for studying the effects of star-planet interactions such as tidal forces (Penev et al. 2018), or migration theory (Section 1.3.3). Ultra-short period exoplanets are some of the best studied hot Jupiters in the field (e.g. WASP-18b, Hellier et al. 2009; WASP-19b, Hebb et al. 2009; and WASP-43, Hellier et al. 2011).

NGTS-4b is a newly discovered ultra-short period planet found by the NGTS facility, with an orbital period of 0.767 days around a K3 V star (V= 14.43). Detailed stellar and planetary parameters are still being determined for this system (McCormac et al, *in prep.*) so an in-depth analysis of the system is not possible at this stage. As part of this analysis I searched for the rotation period of the star using NGTS photometry.

NGTS-4 was observed over 237 nights between 21$^{st}$ September 2015 and 14$^{th}$ May 2016. The UnEarth code was used to search for periodicity in the data, with pre-processing of the data (similar to NGTS-1 and NGTS-2) conducted before the search. The transits were removed from the data and the light-curve was fed into Period04 for pre-whitening. A number of strong signals were seen at $\sim 17.64$ days, $\sim 26.74$ days, $\sim 14.53$ days, and $\sim 0.98$ days. Only the periods at $\sim 26.74$, and $\sim 0.98$ days (corresponding to moon contamination and the 1-day alias, respectively) were fitted out. The pre-whitened light-curve was then binned to 0.01 days (i.e. 14.4 mins) and then run through the UnEarth code over a period range of $0-32$ days (see Figure 5.10).

A number of strong peaks can be seen in the GLS, the strongest being at 17.4149 days, close to the $\sim 17.64$ day period found in Period04. Phase folding the light-curve on this period produces an observable variation and suggests that this is the rotation period of the star (see top panel of Figure 5.11). The modulation of the flux is, however, quite weak.

Here the power of the wavelet analysis can be seen where, rather than the entire dataset contributing to the $\sim 17.41$ day signal, it is seen to be isolated to two time periods: $30-60$ days and $100-150$ days (see panel *e* of Figure 5.10). Figure 5.11 shows the effects of isolating ranges within the dataset and phase-folding the data within those ranges on the period seen in the GLS periodogram. Besides the full dataset (top panel) the ranges of $30-60$ days, $60-100$ days, and $100-150$ days were isolated and the data phase-folded on the $\sim 17.41$ day period. As expected, the range of $60-100$ days shows little to no variation when phase-folded on the detected stellar rotation period. The other two time ranges of $30-60$ days and $100-150$ days both show

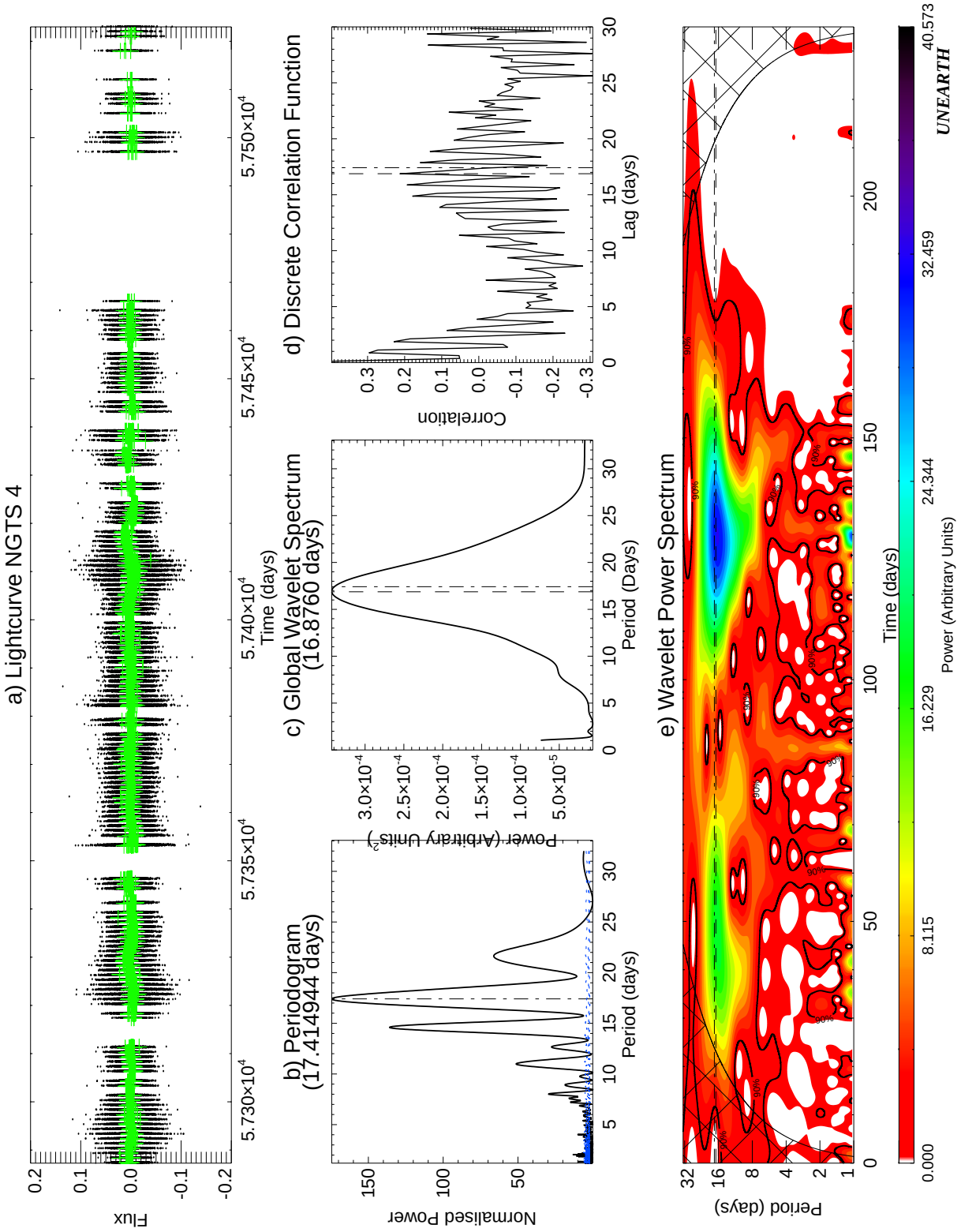


**Figure 5.10**: NGTS-4 period search, all figures are the same as that described in Figure 5.5. A number of strong periods can be seen in the GLS, the strongest at ~ 17.64 days. The wavelet power spectrum shows that the period is localised to two regions within the data – 30 – 70 days and 100 – 150 days.

variations when phase-folded on to the ~ 17.41 day period. The size of the variation seen in each range correlates the strength of the power in the wavelet power spectrum, with the 30 – 60 day range only weakly modulating on the rotation period and the 100 – 150 day range showing a more obvious variation (mimicking the large power seen in this range in the wavelet power spectrum). Comparing these two time ranges also highlights an offset in the position of the peak in flux, with the peak seen at close to a phase of 0.5 in the 30 – 60 day range and a phase of 0.6 in the 100 – 150 day range, which may indicate that two different spot groups are responsible for these signals and that they formed at different longitudes. The phase offset of these two signals may therefore reduce the strength of the signal in the full phase-folded light-curve.

In the case of NGTS-4 the stellar rotation period is still weakly seen in the full phase-folded light-curve, but this shows the power of the wavelet. Wavelet analysis is able to identify time ranges within the light-curve that show lower levels of rotationally modulated variability. This could be used to help improve transit measurements as activity may have less of an impact on this range. The algorithm shows the ability also help isolate time ranges where the rotation period is stronger allowing for more a robust measurement. NGTS-4 highlights a case where simultaneous photometry could be used to inform RV follow-up of periods when the star was active or inactive. RV measurements taken during inactive periods would thus improve the precision of the planet parameters. Determination of the rotation period from photometry could also be used to estimate spin-orbit mis-alignment, aiding in selecting candidates for RM observations (as outlined in Section 1.4).

Having such a short orbital period, NGTS-4b most likely did not form in situ but rather moved in by some migration mechanism (See Section 1.3.3). The ultimate fate of such a short period planet is to spiral into its host star. This is due to tidal interactions, where angular momentum is transferred between the planet and the host star, causing the planet to move in and the star to spin up. Penev et al. (2018) looked at 75 systems to calculate an empirical tida dissipation relation, this is usually quoted as the tidal quality factor, $Q'_\star$, calculated as,

$$Q'_\star(P_{tide}) = \max\left[\frac{10^6}{(\mathrm{P_{tide}/days})^{3.1}}\ ,\ 10^5\right] \tag{5.7}$$

$P_{tide}$ is the tidal forcing period and given by,

$$P_{tide} \equiv \frac{1}{2(P_{orb}^{-1} - P_{spin}^{-1})} \tag{5.8}$$

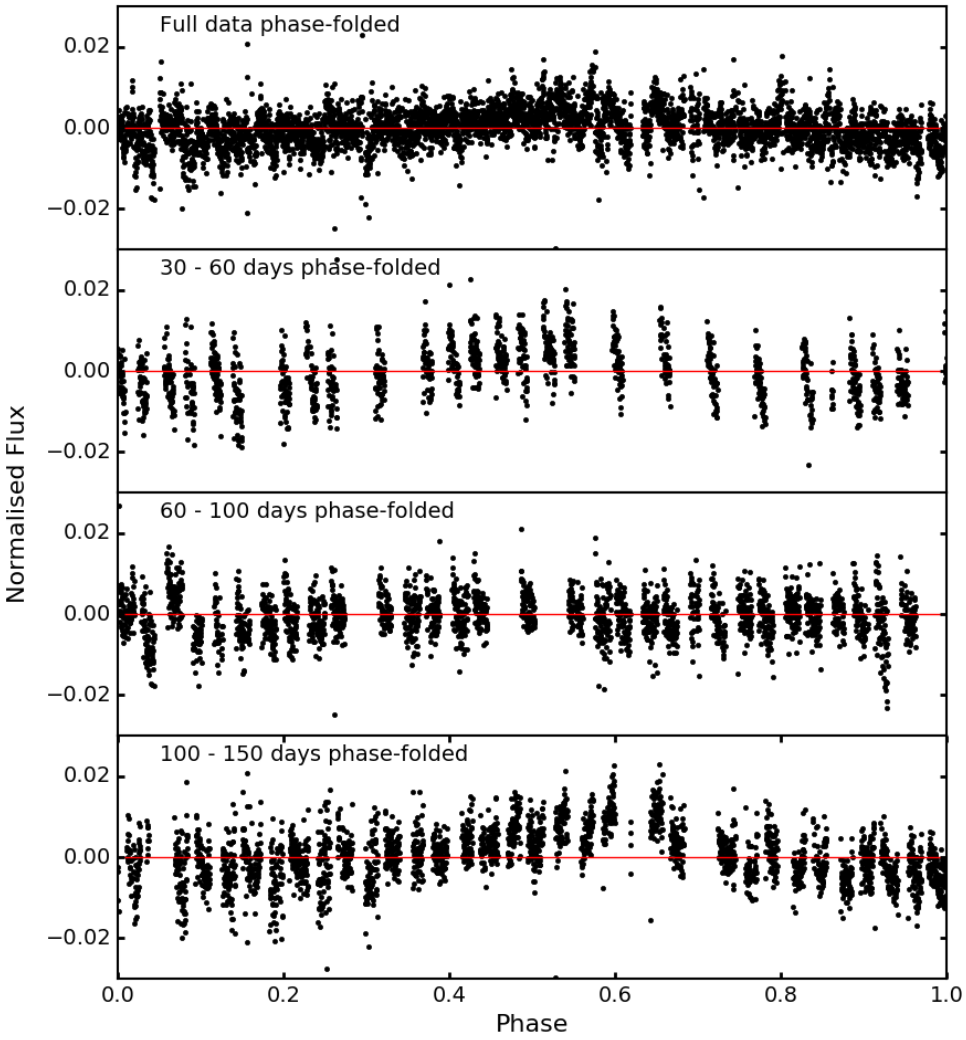


**Figure 5.11**: Phase-folded light-curve of NGTS-4 folded on the ∼ 17.41 day period seen in the GLS periodogram. From top to bottom the plots show the light-curve phase-folded on: the full dataset, 30 – 60 days, 60 – 100 days, and 100 – 150 days. The lack of clear signal in the 60 – 100 day range confirms the results seen in the wavelet power spectrum. The red line is set to zero to help guide the eye.

where $P_{orb}$ is the orbital period of the planet and $P_{spin}$ is the rotational period of the star. Using the values calculated for NGTS-4b leads to $Q'_\star \sim 10^7$. This is in line with the expected tidal quality factor calculated for hot Jupiters by Penev et al. (2018) and indicates a planet that is long lived but will eventually spiral into the host star. This is only a preliminary result, with a more refined value of $Q'_\star$ being estimated with full system parameters in (McCormac et al, *in prep.*).

### 5.3.4 A Rare Equal-mass eclipsing M-dwarf Binary

For exoplanet detections, low mass M-dwarfs lie in an under-represented part of parameter space. They are the most abundant type of star (accounting for roughly 75% of all stars in the Galaxy) and their small size makes them ideal candidates for finding Earth-sized planets as the spectroscopic and photometric perturbations caused by Earth-sized planets are greater around these low mass stars. However, for isolated M-dwarfs, the mass and radius can only be estimated based on evolutionary models (e.g. BCAH15, Baraffe et al. 2015), combined with luminosity measurements, and the mass-luminosity relation (e.g. Delfosse et al. 2000).

In a review of the fundamental properties of lower main sequence stars Torres (2013) highlights the discrepancy between models and measured masses and radii of M-dwarfs (determined from eclipsing binaries with an M-dwarf component). M-dwarfs in binaries are $5-10\%$ larger than predicted by models, while their effective temperature can be cooler by around $2-5\%$. This discrepancy would affect the precise measurement of some essential exoplanet properties (e.g. bulk density), as these rely on accurate stellar parameters. The addition of magnetic activity, such as spots, to M-dwarf models could be helpful in explaining the discrepancy, where spots can reduce the effective radiating surface, puffing the star up and reducing the temperature (Chabrier et al. 2007). Although this can help bring the model values into line with some of the observed masses and radii it still is not able to explain all the M-dwarfs measured. Another solution instead looks at improving empirical mass-radius relations. These are based on actual measurements of M-dwarfs (using, for example, eclipsing binaries) and can complement the values obtained from theoretical models. Low mass eclipsing binaries are rare, making them highly sought after targets for precise measurements of M-dwarf masses.

A by-product of any wide field survey like NGTS is the transient discovery of other interesting targets. Although not the main pursuit of the NGTS mission, one such object is the binary M-dwarf system NGTS J052218.2-250710.4. This is the third discovered late eclipsing M-dwarf binary pair (the other two being CM Dra and KOI26 Morales et al. 2009; Carter et al. 2011, respectively) with both components having similar masses (see Table 5.1), making it an interesting system to follow-up. This system represents the addition of two new well defined M-dwarfs, which is vital in building an empirical mass-radius relation for these low mass stars and achieving more accurate planet parameters around M-dwarfs. I perform a search for the stellar rotation period using NGTS data and the UnEarth code (presented in this section). The results presented were used as part of the analysis in Casewell et al, (*submitted*).

NGTS observations of NGTS J052218.2-250710.4 occurred between 21$^{st}$ Septem-

ber 2015 and $3^{rd}$ May 2016 spanning a total of 226 days, with 156 nights of data available. The UnEarth code was, again, used to search for periodicity. Similar to the other objects, the eclipse events (both primary and secondary eclipses) were removed and the data were pre-whitened using Period04. The DFT of Period04 identified three strong periods: ∼1.75 days, the orbital period of the binary system; ∼29.3 days, the period of the moon; and ∼1.1 days, the 1-day windowing of the data. The periods belonging to lunar variation and the 1-day window were fitted out of the light-curve prior to the analysis. As with the previous objects, the light-curve was then binned at the 0.01 day level and the UnEarth code was run for a range of $0-32$ days (see Figure 5.12).

A number of strong peaks are seen in the GLS periodogram with the strongest being *sim*1.75 days, which is close to the orbital period of the system. The light-curve was phase-folded onto this period and an obvious periodicity was observed (see panel a of Figure 5.13). This periodicity does not arise from ellipsoidal modulations due to distortion of the component stars, as this would present 2 'peaks' and 'troughs' in the phase-folded light-curve. In addition, the binary components lie well within their Roche lobes, and thus ellipsoidal modulation is not expected in this system. The out-of-eclipse light-curve modulation on the orbital period can be attributed to activity on the surface of one (or both) of the stars. Casewell et al (*submitted*) measured H$\alpha$ emission for the spectra, which confirms that there is magnetic activity in the system. They were also able to identify a flare (on $31^{\text{st}}$ December 2015) in the photometry, further confirming that the system is active. This would imply that one (or both) of the stars has its rotation period close to the orbital period, and hence be (or be close to) tidally locked.

A second strong period is seen at *sim*2.33 days, phase-folding the light-curve on this period also shows variability (though less sinusoidal) and could represent a situation where one of the stars is not tidally locked (see panel b of Figure 5.13). This period, however, is $\frac{4}{3}P_{rot}$ and could be the effect of a close harmonic. The UnEarth code was re-run but with the ∼1.75 day period identified by Period04 also removed in the pre-whitening. Periods close to the 2.33 day period were found but on phase-folding no signal could be seen, indicating that a harmonic effect is most likely the source of the signal.

Panel *a* of Figure 5.13, shows an approximate peak-to-peak variation in the light-curve of the order of ∼2%. Assuming completely dark spots, this would also imply a minimum (inhomogeneous) spot coverage of ∼2% relative to the total observed surface area of the binary, or ∼4% if the active region is constrained to just one of the stellar components. In reality, the spot coverage must be higher than this due to the

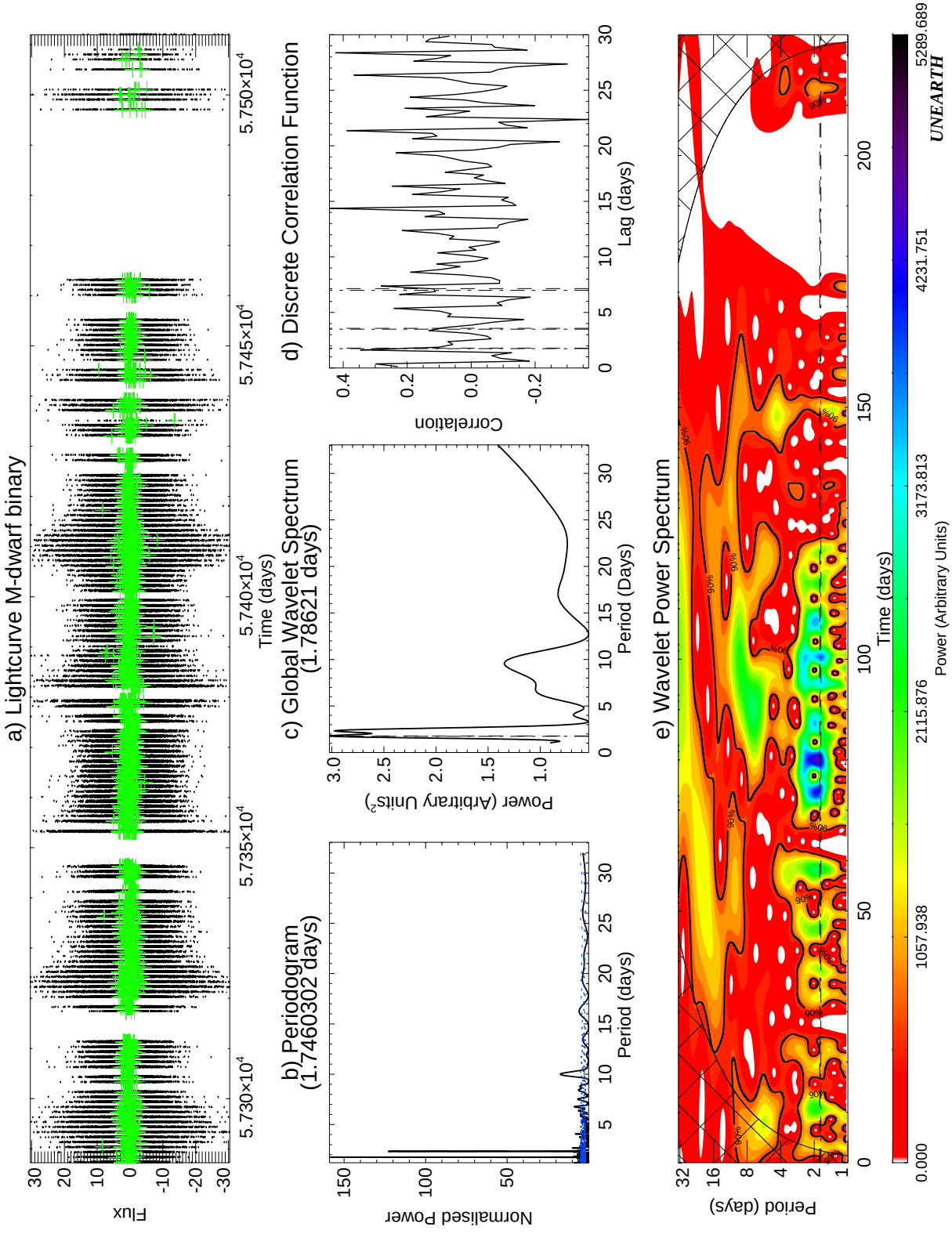


**Figure 5.12**: M-dwarf binary period search, all figures are the same as that described in Figure 5.5. Two strong periods are found in both the GLS and wavelet at 1.74 days and 2.33 days. The DCF also shows a correlation at 1.74 days.

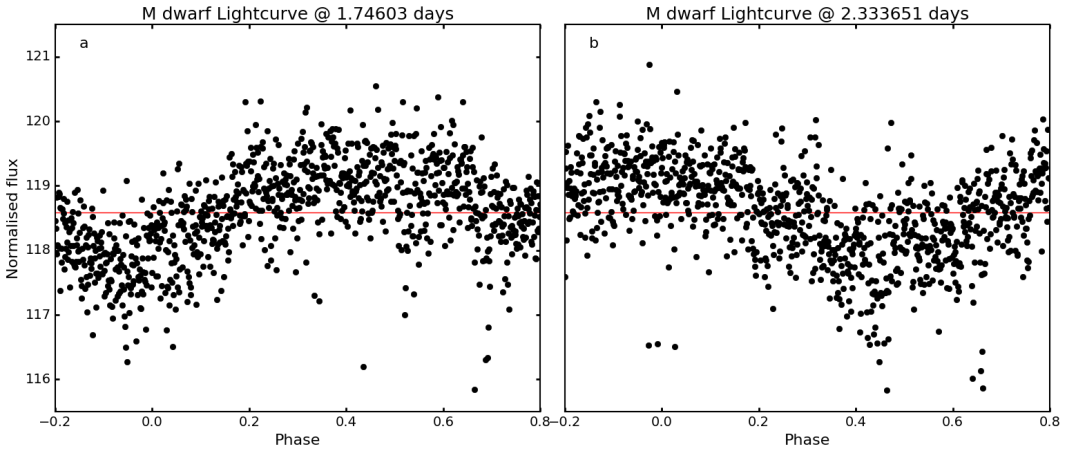


**Figure 5.13**: Phase-folded light-curve of the M-dwarf binary with the folding period shown on the title of the plot. *a)* this is close to the orbital period of the binary so implies near synchronous rotation period of one (or both) of the stars with the orbital period. *b)* another strong period found, at approximately $1.33 \times 1.75$ days, which could represent the rotation of one of the stars, but is more likely a harmonic effect.

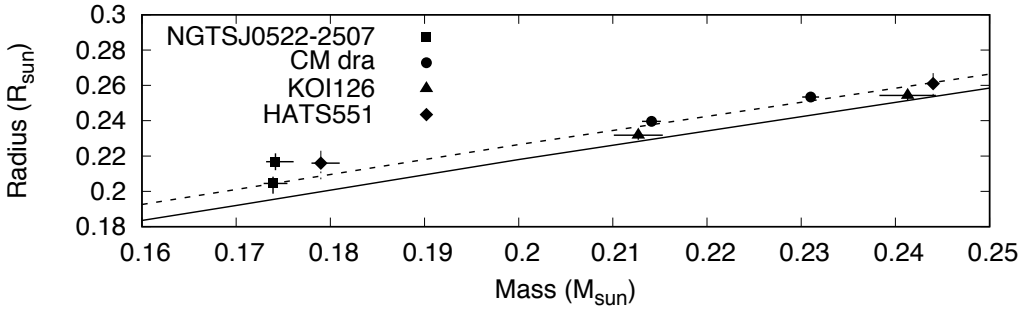


**Figure 5.14**: Mass-radius relations for the four known eclipsing low mass binaries. NGTS J052218.2-250710.4 is plotted with squares, CM Dra with circles, HATS551-027 with diamonds and KOI126 with triangles. The isochrones from Baraffe et al. (2015) (solid line) and the Marigo et al. (2017) (dotted line) are also plotted with ages 5 Gyr. Figure credit: Casewell et al (*submitted*).

much lower spot-to-immaculate photosphere contrast of M-dwarfs as a result of the M-dwarf's lower effective temperature, coupled to NGTS observations being red-sensitive (i.e. the spots will not appear entirely dark). In addition, the light-curve variations only track the inhomogeneous spot coverage - the absolute spot coverage may be higher.

Given that the binary displays significant evidence of activity, determining whether the masses and radii of the components matched theoretical expectations was explored. This is important, as the models of Spada et al. (2013) suggest that both binary and

| Parameter | Description | Unit | Value | $1\sigma$ Error |
|---|---|---|---|---|
| $R_{\rm pri}$ | radius of primary | $R_\odot$ | 0.2045 | $^{+0.0038}_{-0.0058}$ |
| $R_{\rm sec}$ | radius of secondary | $R_\odot$ | 0.2168 | $^{+0.0047}_{-0.0048}$ |
| $m_{\rm pri}$ | mass of primary | $M_\odot$ | 0.17391 | $^{+0.00153}_{-0.00099}$ |
| $m_{\rm sec}$ | mass of secondary | $M_\odot$ | 0.17418 | $^{+0.00193}_{-0.00059}$ |

**Table 5.1**: Derived mass and radius parameters of the two components of NGTS J052218.2-250710.4. Table adapted from Casewell et al (*submitted*).

single M dwarfs suffer from a radius discrepancy, and that this discrepancy is largest in binaries with short periods (typically < 1.5 days) and in lone, low mass (M<0.4 $M_\odot$), low metallicity objects. This inflation for objects in short period binaries is also seen by Boyajian et al. (2012) and Kraus et al. (2011) who suggest the inflation is due to the presence of the companion star, probably because they are tidally locked into very high rotation speeds that may enhance activity and inhibit convection. NGTS J052218.2-250710.4 matches a number of these criteria, having a short ~1.7 day orbital period, low stellar masses (see Table 5.1), and evidence of tidal locking. Indeed, Table 5.1 (taken from Casewell et al, *submitted*) shows that, despite both M-dwarf components having almost identical masses, they have radii that disagree at the ~6 per cent level (though only at the $2\sigma$ confidence level) – and that one of these components appears to lie above the theoretical isochrones of (Marigo et al. 2017, see figure 5.14). The work presented here suggests that at least one component displays rotationally modulated activity and flares – though it is not possible to determine whether the activity levels or rotational properties of the other component is different.

NGTS J052218.2-250710.4 is a highly interesting system that can help better constrain the masses and radii of low-mass stars. Follow-up observations of the system to better measure the eclipses could verify (or otherwise) the radius discrepancy between the 2 components. Further monitoring of the system may find eclipse events with spot occultations within the eclipse phase. If spot occultations occur more regularly (or exclusively) on either the primary or secondary eclipse, this may indicate a disparity in activity levels between the stars, providing an explanation for the suspected inflation of one of the components.

## 5.4 Conclusions

Searching for stellar periodicity (from the perspective of exoplanet characterisation) is essential in gaining a deeper understanding of the system. At times, the lack of any measurable periodicity is preferable over finding a strong signal, with a strong signal being due to high levels of activity, which can reduce the accuracy, bias the estima-

tion of the planet properties, or make RV follow-up more difficult. Knowing the stellar period is also a benefit, it allows an estimate of the age of the star (via gyrochronology, Barnes 2007; Barnes et al. 2016) or to determine the expected activity level and optimise RV follow-up by targeting candidates that are more slowly rotating. By determining the rotation period, the spin-orbit alignment of the system can also be estimated, providing targets for follow-up Rossiter-McLaughlin observations. The rotation period also feeds into determining the tidal quality factor $Q'_\star$, giving an indication of stability of an orbit and predicting the future fate of ultra-short period planets.

Here I introduce the software package UnEarth, which I developed. This package brings together wavelet analysis and more conventional period searching techniques (the GLS and DCF) to probe periodicity more deeply. The temporal localisation of wavelet analysis allows for an understanding not just of what periods exist in the data, but the time ranges where these periods are seen most strongly. The NGTS planets considered show a range of possible outcomes from this search for periodicity. NGTS-1 shows no measurable periodicity in the photometry, which is confirmed by the $v \sin i < 1 \mathrm{km\ s^{-1}}$ indicating a slow rotator, and most likely, inactive star. NGTS-2 shows a strong periodic signal that does not correlate with estimated rotation periods from $v \sin i$ measurements and cannot be seen in the photometry, this points towards either the period seen in the photometry being a result of some unaccounted for systematic or an overestimate of the $v \sin i$ resulting in a shorter period being calculated. NGTS-4, however, shows a clear rotational period, with the period well localised to two time ranges within the data. This period localisation property of wavelet analysis could be a useful tool for optimising RV follow-up, an essential part of the NGTS mission. Highly prized planet candidates (e.g. super-Earths around a M-dwarf, or Neptune-sized worlds around a K-star) can be monitored by one of the NGTS telescopes during the RV-follow-up campaigns, where searching for rotationally modulated variation in the photometry could inform on the activity. This could allow for better target selection optimisation, where periods of lower (photometric) activity could be selected as a window for higher precision RV follow-up.

In addition to finding planets, NGTS has also discovered a range of other interesting object. A rare eclipsing M-dwarf binary found was also analysed using the UnEarth code. Results of a period search using the light-curve of the M-dwarf binary showed that one or both of the stars are tidally locked to the orbital period of the binary. One of the components also show indications that it could be inflated, the evidence of tidal locking (together with the short orbital period, and low mass) would add validity to the case of an inflated stellar component. In addition, Jackman et al. (2018) reported the detection of two superflare events of a G8 star with NGTS data. These flaring stars are known to be active so rotation periods should be readily measured from them, the

UnEarth code could provide a quick and efficient tool for analysing periodicity within this subsample of stars. This has been considered already with the test-case data of Figure 5.5 being from a flare star, which showed hints of a correlation between activity level (as tracked by power in the wavelet power spectrum) and the likelihood of a flare event. Both these cases demonstrate the use of the UnEarth code across a broader range of NGTS targets.

The use of wavelet analysis, or the UnEarth code, is not restricted to NGTS data but could be applied to any transiting planet survey. The only requirements from the data is that a long enough baseline of well sampled measurements is available to effectively search for periodicity. NGTS operates in a 'stare mode' looking at the same field for $\sim 3$ months, allowing for an effective search of periods up to $\sim 30$ days (longer periods being highly influenced by moon contamination). Surveys like K2, TESS and PLATO would also have light-curve with a long baseline of measurements making the data from them well suited to the use of the wavelet analysis in the context used here.

This work could also be combined with my spectroscopic work, probing whether the features seen in the relative spectra can be linked to photometric variability. This could indicate if changes in starspots, which are the main contributor to photometric variability (due to their high contrast with the immaculate photosphere), could be linked to changes in the depth of spectral lines. The simultaneous spectroscopic and photometric measurements of CoRoT-7 (Haywood et al. 2014) would be well suited to such an investigation.

*Chapter 6*

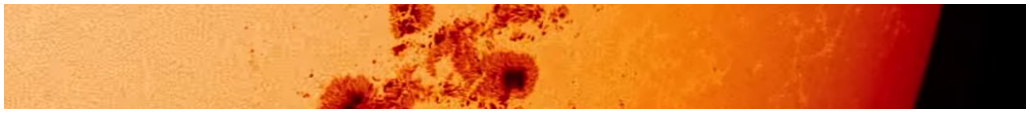

# Conclusions and Future Work

## 6.1 Conclusions

As we strive towards finding Earth-analogs, instrumental precision no longer presents the limiting factor for confirming such planets via the Doppler wobble effect. The activity of the host star has been shown to produce apparent RV variations that can mask, or in extreme cases, mimic the effects of a planet. To find low-mass planets, the effects of activity on spectroscopic measurements needs to be better understood. Throughout this thesis, I have investigated the effects of stellar activity on the spectra of stars by considering the well observed $\alpha$ Cen B, as well as the unique dataset of the HARPS-N Solar Telescope. This 'Sun-as-a-star' observing capability allowed for a deeper understanding of the manifestation of different active regions on the solar surface. Finally, I developed a software package (called UnEarth) that pulls together the GLS periodogram, the Discrete Correlation Function, and wavelet analysis to search for rotation periods in the light-curves of NGTS. The results and conclusions for each of these investigations are summarised below.

### 6.1.1 Relative Spectra of $\alpha$ Cen B

The extensive HARPS data of $\alpha$ Cen B has allowed for an in-depth look at the effects of activity on a stellar spectrum. The data spanned $\sim 4$ years of observations, over which the star showed a ramping up in its activity level. In addition, during a particularly well observed time range, the activity of the star (as traced by $\log R'_{HK}$) shows a clear periodicity that is modulated on its stellar rotation period.

Chapter 3 follows my investigation of this system, where the HARPS $\alpha$ Cen B dataset was used to create 'relative spectra' by dividing nightly stacked spectra by a low-activity template spectrum (defined as the night showing the lowest $\log R'_{HK}$ value), the creation of which highlights the effect of activity on a stellar spectrum. A forest of pseudo-emission features were seen in the relative spectrum, which are loosely classified as either being narrow or broad. Some of the features were seen to come from Fe I lines, which are known to be photospheric in origin and indicative of surface inhomogeneities (e.g. spots or faculae) being responsible for the features. In addition, some of the lines that produce a broad pseudo-emission feature have been used for stellar classification due to their temperature sensitivity (e.g. 4383Å Fe I line, Giridhar 2010) – and hence may indicate an effective spectral type variation.

The strength of the pseudo-emission features were traced over two stellar rotation cycles, which showed that the strength of the features were modulated on the stellar rotation period. The strength of the pseudo-emission features also show a strong correlation with $\log R'_{HK}$ (showing a Pearson's r correlation of $> 0.9$). Finally, the positions

of the features were measured, which showed a peak-to-peak RV shift of $\sim 300$ m s$^{-1}$ of the line centre over the two stellar rotation periods considered. These three pieces of evidence indicate that the pseudo-emission features are caused by active regions rotating on and off the stellar surface.

A more in-depth look at the narrow pseudo-emission features revealed two distinct morphologies, with some features showing pseudo-absorption troughs either side of the main peak. To investigate this a simple model was constructed that generated two line profile shapes, one without any activity and the other with an active region placed at disk centre. A model relative line profile was then created from these and compared to the pseudo-emission feature morphologies seen. The model indicated that a broadening of the line profile in the 'immaculate' photosphere (possibly through MBPs, Cegla et al. 2013) in the high activity case was needed to explain the pseudo-absorption troughs. Further iterations of the model used line strengths from VALD, which showed that a hotter region (i.e. due to faculae/plage) was needed to produce the pseudo-emission features. This result aligns with the current understanding that the stellar jitter of low activity stars (like $\alpha$ Cen B) is dominated by plage (Radick et al. 1990; Hall et al. 2009; Lockwood et al. 2007; Shapiro et al. 2016)

A final analysis of the features looked at possible correlations with various line parameters (as found in VALD). All narrow pseudo-emission features were categorised, by eye, based on morphology. The 950 features positively identified were compared to values of Landé factor and excitation potential, searching for potential correlations with the feature morphology. No correlation was detected for Landé factor, while the large range of classifications for excitation potential (both by element and by ionisation state) resulted in low numbers and stopped any possible correlations from being robustly determined.

The results of my work also demonstrate the potential information that is overlooked by current astrophysical noise mitigation techniques. Most work on activity only considers the analysis of data products such as the CCF (and correlations with the CCF bisector span) or $\log R'_{HK}$. The results show that the changes in activity affects each line differently with the effect depending on the fundamental properties of the line (e.g. its depth change inside and outside an active region, or the magnetic susceptibility of the line). The number and variety of pseudo-emission features detected in the relative spectra provide a platform to better constrain the extent and effects of active regions on spectral lines.

### 6.1.2 Sun-as-a-star Analysis with the HARPS-N Solar Telescope

The HARPS-N Solar Telescope provides a unique dataset that allows for observations of the Sun as if it were any other star in the sky. This Sun-as-a-star approach provides valuable insight into the effects of activity on spectroscopic measurements. The RV motions of the planets orbiting the Sun can be removed, allowing for the RV variations due to activity alone to be isolated and studied.

In Chapter 4, I used a similar approach to that of $\alpha$ Cen B (Chapter 3) to analyse the effects of activity on the relative spectra of the Sun. The initial results were confused due to the presence of a strong evolving ripple pattern seen in the relative spectra. This led to the use of '2D spectra' – a data product from an earlier stage in the HARPS data reduction pipeline – and a removal of the ripple pattern on an order-by-order basis.

As with $\alpha$ Cen B, relative spectra were generated by dividing each daily stacked spectra by a low-activity template spectrum. The relative spectra, again, show pseudo-emission features but in the case of the Sun these were weaker (due to the lower activity levels of the Sun) and less abundant. A number of the features (across several echelle orders) were selected and a pseudo-equivalent width for each feature was measured. These were shown to correlate with $\log R'_{HK}$, indicating that the features are activity driven and further strengthening the conclusions found for $\alpha$ Cen B.

With the Sun, resolved images of the surface are also available (e.g. via SDO) so activity can be directly viewed rather than inferred from activity measures like $\log R'_{HK}$. Using these images the spot and faculae filling factors were determined directly (making use of the method outlined in Haywood et al. 2016) and compared to the changing strength of the pseudo-emission features of the relative spectra. The results show that the pseudo-emission features better trace changes in faculae filling factor than spot filling factor. More notably, it is the faculae that is unassociated with spot regions that are responsible for the features, with faculae associated with spot regions showing no discernible features in the relative spectrum.

This result could have a large impact on RV jitter removal for low activity stars. Methods like the FF' use spot induced photometric variability to infer the RV jitter, where the estimate of the convective blueshift suppression of plage assumes the plage is associated with the spots. For high activity stars (where spots dominate the RV jitter) this may still be a valid assumption but in low-activity stars (where plage dominates the RV jitter) the results here suggest it is the unassociated plage regions that are responsible for creating variations in the spectra, which the FF' method is not able to account for.

### 6.1.3 Periodicity in NGTS Light-curves

Finally, in Chapter 5, I bring together wavelet analysis, GLS and DCF in a tool for period analysis. Wavelet analysis is a similar process to a windowed Fourier Transform but with the window function being defined by a more complex wavelet. Due to the sinusoidal nature of the stellar rotation signal, the Morlet wavelet was used as it is both simple and shows, like stellar rotation, sinusoidal properties. By using the wavelet analysis together with the Generalised Lomb-Scargle periodogram (GLS) and the Discrete Correlation Function (DCF), periodicity searches were performed using three independent techniques, adding validity to any suspected stellar rotation periods found. The main advantage of wavelet analysis is its ability not only to show what periods exist in the data, but also identify the time ranges within the data where these periods are most strongly connected. The ability to temporally localise the signal allows for a more in-depth period analysis of light-curves, potentially allowing for more robust rotation period analysis. These period searching algorithms were incorporated into a software package I developed called UnEarth, which was a tool specifically designed to be used with NGTS data to search for stellar periodicities. This was then applied to NGTS light-curves of five specific objects as outlined below.

**Flare star:** As a test of the UnEarth code, a flare star with a clear periodic variability in its light-curve was analysed. All three techniques were able to identify a strong period at $\sim 3.88$ days, the light-curve was phase-folded on this period and showed an obvious detection of the stellar rotation period, validating the effectiveness of the UnEarth code. Additionally, the wavelet analysis was able to identify greater power around 110 days, which coincides with a greater modulation of the light-curve and two flares occurring in quick succession. This could indicate a potential correlation between the signal strength seen in the wavelet power spectrum (indicating the presence of a significant, localised active region on the star) and the likelihood of observing a flare event. More flare stars would need to be considered to confirm this (see Section 6.2.6 for potential future work in this area).

**NGTS-1:** The first published planet of the NGTS facility is a hot Jupiter of mass $0.812 M_J$ transiting an early M-dwarf. Analysis of the light-curve using UnEarth showed a number of strong peaks but, on phase-folding, no variation could be seen, indicating that the periods found were systematics. The star has a measured projected equatorial rotation velocity of $v \sin i < 1$ km s$^{-1}$ so no period could be estimated from the spectroscopic measurements. Estimates of the strength of the signal in photometry using the clean algorithm also indicate that the peaks found are most likely systematic

effects.

**NGTS-2:** Period analysis of the light-curve of NGTS-2 using UnEarth revealed a strong signal at $\sim 7.25$ days. However, phase-folding on this period did not show any obvious variations. HARPS spectra of the star allowed an upper estimate of the rotation period of $P_{rot} = 5.66 \pm 0.34$ to be determined, potentially indicating that the signal seen in the light-curve is a systemic. To complicate matters, a median GLS periodogram of all stars in the NGTS-2 field was produced and showed a signal at ~8 days. This was broader and smaller than the peak seen in NGTS-2, and may indicate that some of the power could be due to systematics, but is not able to account for all of it. If the period found from photometry is to be believed it would indicate the $v \sin i$ has been overestimated, follow-up photometric observations may provide additional insights into the period detected by UnEarth.

**NGTS-4:** This system is part of an ongoing analysis so detailed system parameters are not available at this time. The planet detected, however, is known to be a hot Jupiter and part of a subclass of ultra-short period exoplanets, having an orbital period of 0.767 days. Period analysis of the light-curve revealed a strong signal at 17.4149 days. Phase-folding on this period shows an obvious variation in the flux indicating that this represents the rotation period of the star. The power of the wavelet analysis can be seen here, where most of the power responsible for the periodicity is localised to two time ranges within the data. Phase-folding each of these time ranges independently on the stellar rotation period shows a phase offset, which, when phase-folding on the entire dataset, interacts destructively to reduce the signal seen. Coupling the detected stellar period with the orbital period of the planet give a tidal Quality factor $Q'_\star \sim 10^7$, which implies the planet is long lived but will eventually spiral into its host star.

**An equal mass eclipising M-dwarf Binary:** NGTS J052218.2-250710.4 is an M-dwarf binary found within the NGTS fields. Period analysis of this system shows a strong signal at ~1.75 days, which is also the orbital period of the system. Phase-folding on this period shows a clear periodic signal and indicates that the system is tidally locked. A second period was found at $\sim 2.33$ days and on phase-folding also shows a signal. This period, however, is close to $\frac{4}{3}P_{rot}$ and is most likely the result of a harmonic effect. One of the component stars shows evidence that it is inflated (though only at the $2\sigma$ confidence level), which is supported by its low mass, short orbital period, and tidally locked stellar rotation period (found by UnEarth) as seen in other similar objects.

As more planet candidates (or other interesting objects) are found with NGTS the UnEarth tool should become an essential component of the vetting, validation and follow-up strategies of NGTS. It can provide insight into the stellar stellar rotation period, which can be used to help better constrain planet-star spin-orbit alignment, or be useful in optimising RV follow-up by identifying (and avoiding) time ranges with higher levels of rotationally modulated activity.

## 6.2 Future Work

The work discussed in this thesis has had the effect of raising more questions than it answers. The exploration of stellar activity with a goal of removing its effect on exoplanet detectability is a relatively new area of research and bridges the divide between the exoplanet community, stellar astrophysics and the deep understanding of the manifestation of magnetic fields on the Sun (solar physics). Below I highlight the main areas of future work that could help in answering some of these open questions.

### 6.2.1 Extended Analysis of $\alpha$ Cen B

The morphology of narrow pseudo-emission features of $\alpha$ Cen B was investigated by simple modelling and comparison to line properties as found within VALD (the Vienna Atomic Line-list Database). The analysis of Chapter 3 used a by-eye approach to identify the morphology of the residuals, a more robust method of determination could better determine the morphology, especially for the more marginal cases where the presence of a pseudo-absorption trough could not be positively identified.

Accurate measurement of the pseudo-absorption troughs and correlating this with $\log R'_{HK}$ or rotation period could provide additional information on the cause of the features. This could also be compared to the pseudo-emission peaks, which may indicate if these features are both caused by the same underlying physics or if different active regions are responsible for the different pseudo-emission feature morphologies.

An extension of the wavelength range (i.e. $> 5300$Å) may show other features in the relative spectra, this range was excluded due to the gap in the detector and the tellurics known to exist on the red-ward half of the HARPS instrument, which could have affected the data processing. Additional features could be found in this wavelength range that may aid in searching for correlations with line parameters like Landé factor and excitation potential, as well as exploring whether there is a wavelength dependence of the strengths of the relative features. This latter aspect may arise if, for example, spots generated some component of the features that we see. As one moves to redder wavelengths, the spot contrast will be reduced, and hence one may expect the contributions

of spots to any of the feature morphologies to similarly reduce. The opposite may be true for brighter/hotter plage regions.

In the current sample, the low number of positively identified features in the relative spectra made it difficult for any definitive statement to be made about the effects line excitation potential has on the morphology of the narrow pseudo-emission features. This was due to the range of elements and ionisation states present, which meant that categorising by element and ionisation state led to low-number statistics. An increase in the total number of features identified may help improve the ability to say something more definitive of the effects of excitation potential on the pseudo-emission feature morphologies.

Broad pseudo-emission features were also seen in the relative spectra, most of the broad features appear to belong to Fe I but this has not been fully explored. A similar comparison to line parameters like Landé factor and excitation potential, or simple modelling (similar to that performed on the narrow features) could reveal further insight into these broad features.

### 6.2.2 Atlas of Tailored CCF masks

The relative spectra of $\alpha$ Cen B highlight the effects that activity can have on various spectral lines. The results of the analysis show that the spectral lines of $\alpha$ Cen B can be broken down into two subsets – lines that show high-sensitivity to the presence of magnetically active regions, and those that are insensitive to the presence of active regions. Current CCF masks for instruments like HARPS take as many strong lines as possible to help increase the precision of the RV measurements. The results of Chapter 3 indicate that this may not be the best approach.

One possible route for future work would be to look at generating CCF masks that properly account for the effects of stellar activity. By generating two line-masks to be used in the cross-correlation process used to derive RV measurements, one containing the magnetically sensitive lines and the other the insensitive lines, the impact of stellar activity may be disentangled from planetary variations. The orbital motions of planets would be seen in the RV variations of both CCF masks but the magnetically sensitive lines would also show effects from due to stellar activity. Subtracting one from the other would remove the planetary RV shifts (including as yet unseen/unknown planets in the system) from each set of RVs, thereby isolating the RV jitter due to activity. The difference between the two cross-correlation analyses would then track the activity related jitter, which could then be used to 'clean' the full RV dataset (see Figure 6.1 for a schematic outlining this process). This would mark a significant advance in the

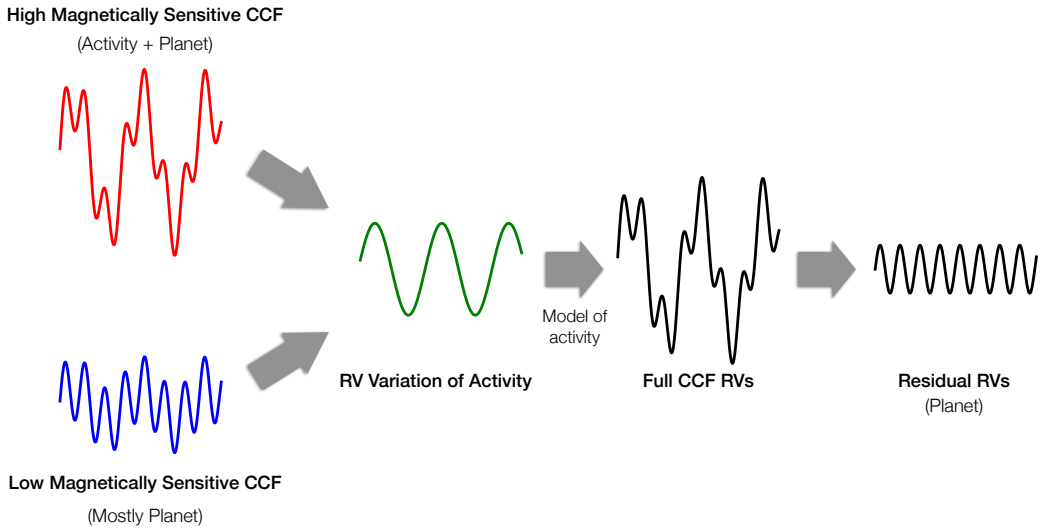


**Figure 6.1**: Schematic of the different RV variations seen in the CCF of the high magnetically sensitive lines (red plot) and the low magnetically sensitive lines (blue plot). Subtracting one from the other would isolated the effects of activity (green plot), which could form the basis of a model to 'clean' the full RV dataset and identify the RVs of a planet.

development of astrophysical noise mitigation techniques, since none of the current methods provide a means of precisely isolating stellar jitter from the RV variations caused by known and unknown planets.

There is no reason to believe that the choice of lines in each of the CCF masks would be constant across all spectral types, with changing spectral types affecting the strength and formation height of lines, which would, then, affect the strength of features in the relative spectrum. Applying the analysis of $\alpha$ Cen B to a range of stars from mid F to late K and possibly down to M-dwarfs (but the low intrinsic luminosity and prevalence of molecular lines in M-dwarfs may complicate the analysis) would provide a dataset of pseudo-emission features as a function of spectral type. The mask used in the CCF could then be modified to better represent the low- or non-activity sensitive lines of that spectral type. These tailored CCF masks would produce an atlas that could be used to more precisely measure the RV motion of a planet.

This analysis may also be useful in understanding more about the surface of stars, potentially revealing the coverage of active regions like spots and plage. Being able to determine the spot coverage of a star would be a useful constraint for measuring exoplanet atmospheres using transmission spectroscopy. The presence of haze in the atmospheres of exoplanets is indicated by measuring the Rayleigh scattering slope (Sing

et al. 2016), unocculted spots are known to cause variations in this slope, thereby mimicking the effect of Rayleigh scattering. With better determination of the presence and level of various active regions on the surface of the host star, a more conclusive detection of molecules (e.g. water) and haze can be achieved.

### 6.2.3 Line Formation Models

A major restriction of the work up to this point is a lack of a physical understanding of line formation as a function of height in the convective layer and the influence of magnetic fields. The Landé factor can indicate the magnetic susceptibility of a line that, at first glance, could be thought to indicate whether a line would produce a feature in the relative spectra. In reality, lines form over a range of heights so any information about the perturbations of the line due to magnetic activity is lost due to the changing levels of magnetic activity as a function of formation height.

To better probe this, Magneto-Hydrodynamic (MHD) codes could be used to model the outer layers of low-mass stars. With careful control over the parameters of the model (e.g. magnetic field strength, temperature, and metallicity) a deeper understanding of the mechanism that creates the pseudo-emission features could be probed. Lines that create strong features, both from the Sun and $\alpha$ Cen B, can be used as inputs to the model and the effect of various spots and plage configurations (and various limb angles) on these lines can be measured.

Codes like MURaM (Vögler et al. 2005) can be used for this in-depth simulation. An alternative approach could be to use models like PHOENIX (Hauschildt & Baron 1999) where individual pseudo-emission features (possibly from a range of narrow feature morphologies) could be modelled by selecting a range of temperatures to represent the expected change of the line in different active regions like spots and plage.

One of the downsides to a full MHD is information about the atmospheres of stars other than the Sun is more limit. An alternative to this would be to apply Radiative Transfer modelling to this problem. In this case, deeper understanding of the mechanisms at play could be obtained by constructing an atmospheric model and studying the formation of the spectral line over a height range in the atmosphere. This would give information about what layers in the star various parts of a line form, which can help better interpret the range of relative feature morphologies observed. In effect, this would take a more realistic approach to modelling relative features that that presented for $\alpha$ Cen B in Section 3.4.

### 6.2.4 The HARPS-N Solar Telescope and Semi-empirical Model

The results of Chapter 4 highlighted the rich dataset of the HARPS-N Solar telescope. However, the work only analysed a small section of the total data available, with the methods used expandable over the whole dataset. The expansion to the whole dataset would have multiple benefits. First, it could highlight other interesting activity intervals, the 2017 interval highlighted a potential interaction between the pseudo-emission features and flares. Further investigation of this by identifying other flare events and generating relative spectra for these time ranges could reveal more about whether this is a real interaction. Second, the $\sim$ 2.5 years of HARPS-N Solar Telescope data will allow a look at the effects of long term solar activity from the Sun-as-a-star perspective. This dataset is unique, the Sun is the only star where all the planets are known and can be removed, meaning the effects of solar activity on precise RV measurements can be isolated, which may reveal interesting long term activity behaviours.

The Sun also presents a case for building a semi-empirical model of the effects of activity. SDO images allow for active regions to be located on the stellar disk as well as categorised into the different types of magnetic activity. This could form the basis of a model, with each pixel being assigned a state (e.g. quite Sun, plage region, spot umbra, spot penumbra, etc.). In addition, high resolution spectra from solar instruments could provide spectra for a range of active regions. These could be combined together to produce a disk-integrated spectrum of the solar surface and compared to the HARPS-N Solar Telescope spectrum.

Initial testing would look at recreating the HARPS-N based on SDO images, this could then evolve to a predictive approach where specific lines (with large pseudo-emission features) could act as activity 'pathfinders' to inform on the expected spot and faculae filling factor. 'Fake' SDO images could also be constructed to generate spectra for active regions far larger or at latitudes not seen in the Sun, producing relative spectra of these could explore a range of stellar activity arrangements not possible on the Sun. It may also be possible to expand this to other stars and have a semi-empirical model that can be used to estimate spot and plage coverage.

### 6.2.5 Data from Solar Telescopes

An under-utilised dataset that could prove useful for mitigating astrophysical noise in RV exoplanet detections would come from dedicated solar telescopes (e.g. the Dunn Solar Telescope – DST). These provide high-resolution images and spectra of various solar features, which could help provide a deeper understanding of the effects of activity. I have started some initial work on this front. Figure 6.2 shows the results of

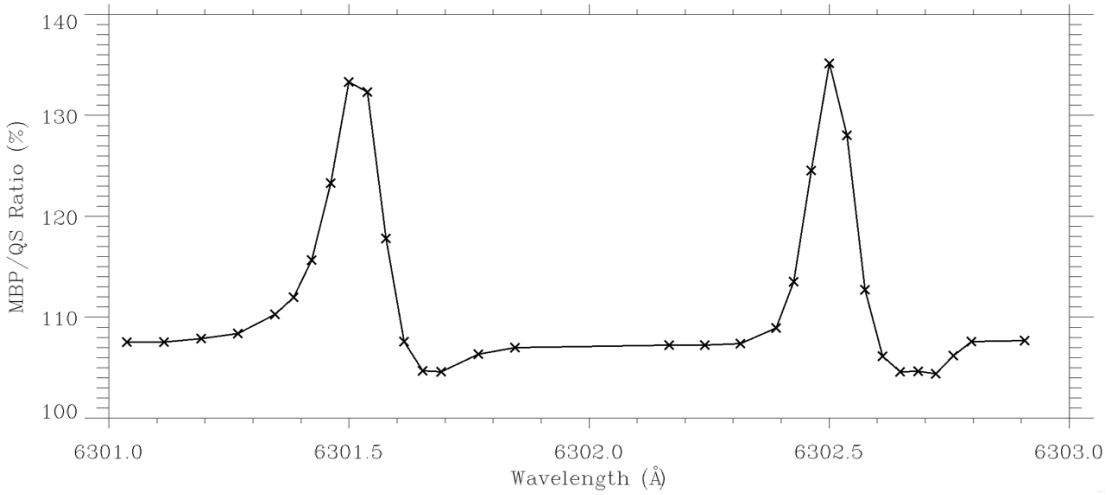


**Figure 6.2**: Relative spectra generated using data from the Dunn Solar Telecscope. Spectra from MBPs were divided by spectra of quiet Sun regions to produce the relative spectra. The two lines are shown are Fe I 6301Å and 6302Å. A clear pseudo-emission peak and pseudo-absorption trough can be seen.

dividing 51,118 individual magnetic bright point (BMP) spectra, by over 66,500,330 individual quiet Sun (QS) spectra representing high- and low-activity states, respectively – with data taken from the DST (Jess, D and Mathioudakis, M, private communication). Here the Fe I lines 6301Å and 6302Å were looked at, and again pseudo-emission peaks are clearly seen (see Figure 6.2. This demonstrates that the method of producing relative spectra would also work here. The features also show a pseudo-absorption trough but only on the red wing of the feature. This is different from the results of $\alpha$ Cen B, which found pseudo-absorption troughs flanking both sides of the relative features. However, this is in keeping with the expected contribution of MBPs on G stars (Beeck et al. 2015; Cegla et al. 2013 and Section 3.4). This result directly confirms the interpretation of $\alpha$ Cen B where MBPs can be seen to produce a pseudo-emission features similar to that report including the pseudo-absorption trough.

Solar telescope data, provides yet another avenue of exploration of the effects of activity. Spectra from a range of activity features and limb angles would provide an interesting dataset for a deeper exploration of activity and may help to better understand the physical processes responsible for the morphologies of the relative features. As an example, generating the same plot as Figure 6.2 but with different active regions like a spot instead of an MBP could indicate the effects that spots have on the ionFeI 6301Å and 6302Å lines. Additionally, any feature seeen could also be tracked over the solar surface to consider the effects of limb angle. Other DST spectra, similar to the result presented here are also available. In addition to the Fe I lines it also covers the wavelength range of some of the features seen on $\alpha$ Cen B (see Chapter 3).

### 6.2.6 UnEarth Code Distribution

Further testing of the UnEarth code on other NGTS targets would be useful to properly test the validity of the results. Targets tested so far have either had an obvious rotational modulation of the light-curve or showed no variability. Confirming more marginal cases, like NGTS-2, would help to better validate the approach. The addition of robust error estimates could resolve the discrepancies between the photometric and spectroscopic stellar rotation periods.

The discovery of a flare star by Jackman et al. (2018) and an M-dwarf binary by Casewell et al (*submitted*) in the NGTS data may provide an additional source of targets for period searches. These two targets demonstrate some of the potential transient science from NGTS. Finding more M-dwarf binaries can help improve estimates of their radii and masses, which feeds directly into characterisation of planets around these stars. The superflare events reported in Jackman et al. (2018) pose a potential risk. Flares seen on the Sun are much weaker, understand why this is, or finding a way to predict flare events may be beneficial to space weather predictions. The one flare star analysed as part of this thesis showed an increase in power of the wavelet power spectrum around the time of two large flares. This would indicate a correlation between more concentrated active regions on the stellar surface and flare events, which may provide a way of predicting the likelihood of a flare. The flare stars also provide a good test of the UnEarth code, flare events mean that these stars must be active, with possibly easy to measure rotation periods. The Next Generation Flare Survey (NGFS) is part of the NGTS consortium, but with a dedicated pipeline optimised to find flare stars. The UnEarth code could be useful as an analysis and prediction tool for the $> 350$ candidates found as part of this survey.

The ability of the wavelet analysis to provide temporal information can be a useful addition to the follow-up strategy of NGTS. For high value planet candidates (e.g. Neptune-sized planets around a K-stars) the ability to limit the impact of activity would help improve RV precision. With simultaneous monitoring of targets by one of the NGTS telescopes during the RV-follow-up campaigns, the wavelet analysis could help inform on the current activity level (by looking for the stellar rotation period), allowing for target optimisation.

The ultimate goal of the UnEarth code is to produce a tool for measuring and localising periodicity in data, with the hope of distributing this code to the community. Generalising the code for use with any data will provide a useful tool for more in-depth period measurements, easily applicable to light-curves from K2 (Howell et al. 2014), the recently launched TESS (Ricker et al. 2014), or the near future space mission PLATO (Rauer et al. 2014).

# Appendix

## A.1 Morphology line list

**Table A.1**: All features with a VALD strength > 0.5 the continuum normalised line depth for the spectral range 4300 – 5300Å of $\alpha$ Cen B. The relative feature of spectral line was classified by-eye: p, pseudo-emission peak only; t, pseudo-absorption trough around main peak; n, no feature seen; u, unidentifiable due to noise

| Element | Wavelength (air – Å) | Excitation potential (eV) | Landé factor | Line Depth | Feature Type |
|---|---|---|---|---|---|
| Ti 2 | 4300.0424 | 1.1801 | 1.210 | 0.932 | p |
| Fe 1 | 4300.2035 | 3.8816 | 1.060 | 0.622 | n |
| Cr 1 | 4300.5020 | 3.4348 | 0.990 | 0.518 | n |
| Ti 1 | 4300.5538 | 0.8259 | 1.000 | 0.931 | p |
| Fe 1 | 4300.8239 | 3.9841 | 0.680 | 0.748 | n |
| CH 1 | 4300.9990 | 0.3121 | 99.000 | 0.508 | n |
| Ti 1 | 4301.0787 | 0.8360 | 1.140 | 0.936 | p |
| CH 1 | 4301.1270 | 0.3122 | 99.000 | 0.520 | u |
| Cr 1 | 4301.1740 | 3.4488 | 1.100 | 0.680 | p |
| Fe 1 | 4301.4965 | 4.1034 | 1.580 | 0.561 | p |
| Ti 2 | 4301.9225 | 1.1610 | 0.840 | 0.877 | p |
| Fe 1 | 4302.1855 | 3.0469 | 1.030 | 0.832 | p |
| CH 1 | 4302.2470 | 0.3129 | 99.000 | 0.508 | u |
| CH 1 | 4302.2960 | 0.3130 | 99.000 | 0.520 | u |
| Ca 1 | 4302.5280 | 1.8989 | 1.500 | 0.946 | t |
| CH 1 | 4302.7480 | 0.2680 | 99.000 | 0.514 | n |
| CH 1 | 4302.9050 | 0.2681 | 99.000 | 0.527 | n |
| Fe 2 | 4303.1700 | 2.7043 | 1.440 | 0.744 | u |
| Nd 2 | 4303.5700 | 0.0000 | 1.370 | 0.712 | u |
| CH 1 | 4303.8310 | 0.2687 | 99.000 | 0.513 | u |
| CH 1 | 4303.9140 | 0.2688 | 99.000 | 0.527 | u |
| CH 1 | 4304.3860 | 0.2270 | 99.000 | 0.517 | u |
| Fe 1 | 4304.5402 | 2.9488 | 1.130 | 0.809 | u |
| CH 1 | 4304.5770 | 0.2271 | 99.000 | 0.531 | u |
| Fe 1 | 4304.8684 | 3.3014 | 0.880 | 0.682 | u |
| Fe 1 | 4305.1335 | 2.7275 | 0.600 | 0.554 | u |
| Fe 1 | 4305.2060 | 3.5465 | 0.570 | 0.662 | u |
| CH 1 | 4305.3140 | 0.2276 | 99.000 | 0.516 | u |
| CH 1 | 4305.4370 | 0.2277 | 99.000 | 0.531 | t |
| Cr 1 | 4305.4380 | 2.8895 | 2.160 | 0.546 | t |
| Fe 1 | 4305.4500 | 3.0173 | 1.280 | 0.876 | t |
| Sc 2 | 4305.7140 | 0.5955 | 0.910 | 0.742 | t |
| Ti 1 | 4305.9074 | 0.8484 | 1.250 | 0.946 | t |
| CH 1 | 4305.9080 | 0.1893 | 99.000 | 0.516 | t |
| CH 1 | 4306.1370 | 0.1894 | 99.000 | 0.533 | u |
| V 1 | 4306.2149 | 0.0170 | 1.480 | 0.653 | u |
| Fe 1 | 4306.5796 | 3.4302 | 0.830 | 0.641 | u |
| CH 1 | 4306.6910 | 0.1898 | 99.000 | 0.516 | u |

| Element | Wavelength (air – Å) | Excitation potential (eV) | Landé factor | Line Depth | Feature Type |
|---|---|---|---|---|---|
| CH 1 | 4306.8570 | 0.1899 | 99.000 | 0.532 | n |
| V 1 | 4307.1723 | 0.0000 | 1.420 | 0.574 | t |
| CH 1 | 4307.3060 | 0.1548 | 99.000 | 0.512 | n |
| CH 1 | 4307.5790 | 0.1550 | 99.000 | 0.531 | n |
| Ca 1 | 4307.7438 | 1.8858 | 1.500 | 0.926 | t |
| Ti 2 | 4307.8656 | 1.1649 | 1.470 | 0.888 | u |
| Fe 1 | 4307.9016 | 1.5574 | 1.120 | 0.973 | p |
| CH 1 | 4307.9530 | 0.1553 | 99.000 | 0.512 | u |
| CH 1 | 4308.1690 | 0.1554 | 99.000 | 0.530 | u |
| Fe 1 | 4308.4928 | 2.4534 | 1.540 | 0.526 | n |
| Ti 1 | 4308.4995 | 1.0666 | 1.490 | 0.686 | n |
| CH 1 | 4308.5720 | 0.1237 | 99.000 | 0.503 | n |
| CH 1 | 4308.8990 | 0.1239 | 99.000 | 0.525 | u |
| Fe 1 | 4309.0302 | 3.6343 | 1.020 | 0.811 | u |
| CH 1 | 4309.0950 | 0.1241 | 99.000 | 0.503 | u |
| CH 1 | 4309.3710 | 0.1242 | 99.000 | 0.525 | t |
| Fe 1 | 4309.3740 | 2.9488 | 1.200 | 0.895 | t |
| Fe 1 | 4309.4537 | 3.1110 | 2.210 | 0.862 | u |
| Y 2 | 4309.6215 | 0.1797 | 1.170 | 0.823 | u |
| Fe 1 | 4309.7131 | 4.5844 | 1.040 | 0.657 | u |
| V 1 | 4309.7942 | 0.0401 | 1.440 | 0.576 | u |
| CH 1 | 4310.0910 | 0.0962 | 99.000 | 0.515 | u |
| Fe 1 | 4310.3716 | 3.9286 | 1.310 | 0.698 | u |
| CH 1 | 4310.4570 | 0.0964 | 99.000 | 0.515 | u |
| Mn 1 | 4312.5431 | 2.9408 | 1.890 | 0.638 | u |
| Ti 2 | 4312.8600 | 1.1801 | 1.490 | 0.882 | t |
| Sc 2 | 4314.0830 | 0.6184 | 1.140 | 0.908 | t |
| Ti 1 | 4314.3434 | 0.8360 | 2.250 | 0.672 | p |
| Ti 1 | 4314.7290 | 0.8181 | 1.080 | 0.685 | u |
| Ti 1 | 4314.7998 | 0.8360 | 1.370 | 0.892 | u |
| Ti 2 | 4314.9708 | 1.1610 | 1.320 | 0.881 | u |
| Fe 1 | 4315.0843 | 2.1979 | 1.900 | 0.955 | n |
| Fe 1 | 4315.9517 | 2.4327 | 2.100 | 0.562 | u |
| Ti 2 | 4316.7942 | 2.0477 | 0.670 | 0.562 | p |
| Fe 1 | 4317.0475 | 3.5465 | 0.960 | 0.627 | p |
| Ti 1 | 4318.6316 | 2.2556 | 1.120 | 0.748 | t |
| Ca 1 | 4318.6516 | 1.8989 | 1.500 | 0.929 | t |
| Fe 1 | 4320.4860 | 3.4170 | 1.310 | 0.578 | p |
| Sc 2 | 4320.7320 | 0.6055 | 1.000 | 0.897 | t |
| Ti 2 | 4320.9500 | 1.1649 | 2.180 | 0.782 | t |
| Cr 1 | 4321.4508 | 2.9826 | 0.850 | 0.531 | u |
| Ti 1 | 4321.6522 | 2.2363 | 0.900 | 0.692 | p |
| Fe 1 | 4321.7859 | 3.4149 | 0.930 | 0.789 | p |
| Ti 1 | 4323.4337 | 1.0666 | 1.500 | 0.514 | u |
| Fe 1 | 4324.7280 | 4.2204 | 1.340 | 0.562 | u |
| Fe 1 | 4324.9478 | 2.1979 | 0.690 | 0.705 | u |

| Element | Wavelength (air – Å) | Excitation potential (eV) | Landé factor | Line Depth | Feature Type |
|---|---|---|---|---|---|
| Sc 2 | 4324.9960 | 0.5955 | 0.740 | 0.880 | t |
| Cr 1 | 4325.0610 | 2.9674 | 0.830 | 0.720 | u |
| Ti 1 | 4325.1256 | 2.2492 | 1.000 | 0.730 | u |
| Fe 1 | 4325.1753 | 3.0176 | 1.420 | 0.512 | u |
| Ni 1 | 4325.5998 | 3.3061 | 1.360 | 0.710 | n |
| Fe 1 | 4325.6131 | 4.1034 | 1.460 | 0.689 | n |
| Fe 1 | 4325.7389 | 0.0000 | 1.480 | 0.882 | t |
| Fe 1 | 4325.7615 | 1.6079 | 0.910 | 0.973 | t |
| Fe 1 | 4325.9400 | 3.2671 | 1.100 | 0.780 | n |
| Ti 1 | 4326.3511 | 0.8259 | 1.340 | 0.774 | t |
| Fe 1 | 4326.7528 | 2.9488 | 0.910 | 0.819 | t |
| Fe 1 | 4327.0954 | 3.5465 | 1.030 | 0.858 | p |
| Fe 1 | 4327.9033 | 3.3014 | 0.870 | 0.786 | t |
| V 1 | 4330.0229 | 0.0000 | 0.390 | 0.781 | p |
| Ti 2 | 4330.2378 | 2.0477 | 1.350 | 0.553 | u |
| Ti 2 | 4330.6980 | 1.1801 | 1.900 | 0.734 | p |
| Fe 1 | 4330.8019 | 3.0173 | 1.310 | 0.744 | p |
| Fe 1 | 4330.9516 | 3.2671 | 1.520 | 0.700 | p |
| Fe 1 | 4331.4256 | 3.3965 | 2.090 | 0.598 | p |
| Ni 1 | 4331.6421 | 1.6764 | 1.080 | 0.832 | t |
| V 1 | 4332.8186 | 0.0170 | 1.000 | 0.804 | t |
| Fe 1 | 4332.9119 | 4.5800 | 1.220 | 0.517 | p |
| La 2 | 4333.7500 | 0.1729 | 0.930 | 0.660 | p |
| Fe 1 | 4334.0764 | 4.1777 | 1.400 | 0.590 | u |
| Fe 1 | 4336.8596 | 3.4170 | 2.370 | 0.523 | u |
| Fe 1 | 4337.0453 | 1.5574 | 0.990 | 0.958 | t |
| Fe 1 | 4337.2384 | 4.5931 | 1.220 | 0.664 | p |
| Fe 1 | 4337.5167 | 2.5881 | 1.280 | 0.616 | u |
| Cr 1 | 4337.5570 | 0.9684 | 0.750 | 0.933 | p |
| Ti 2 | 4337.9142 | 1.0800 | 0.860 | 0.905 | t |
| Fe 1 | 4338.2478 | 2.1759 | 0.820 | 0.834 | t |
| Cr 1 | 4339.3990 | 0.9829 | 0.990 | 0.942 | u |
| Cr 1 | 4339.7100 | 0.9610 | 0.000 | 0.918 | t |
| Cr 1 | 4340.1270 | 2.7079 | 1.370 | 0.579 | p |
| H 1 | 4340.4620 | 10.1988 | 99.000 | 0.517 | u |
| V 1 | 4341.0098 | 0.0401 | 1.230 | 0.828 | p |
| Fe 1 | 4341.2349 | 3.3965 | 1.910 | 0.556 | u |
| Cr 1 | 4341.3178 | 3.0004 | 0.910 | 0.660 | u |
| Ti 2 | 4341.3559 | 1.1156 | 0.500 | 0.784 | p |
| Fe 1 | 4343.2152 | 4.1034 | 1.170 | 0.779 | u |
| Fe 1 | 4343.2707 | 3.2515 | 1.720 | 0.799 | u |
| Fe 1 | 4343.6970 | 3.0469 | 1.070 | 0.818 | t |
| Ti 2 | 4344.2806 | 1.0842 | 1.420 | 0.792 | u |
| Fe 1 | 4344.4989 | 3.6025 | 1.510 | 0.790 | t |
| Cr 1 | 4344.5010 | 1.0037 | 1.110 | 0.950 | t |
| Fe 1 | 4344.8860 | 4.1544 | 1.210 | 0.724 | p |

| Element | Wavelength (air – Å) | Excitation potential (eV) | Landé factor | Line Depth | Feature Type |
|---|---|---|---|---|---|
| Fe 1 | 4346.5522 | 3.3014 | 0.860 | 0.788 | t |
| Cr 1 | 4346.8190 | 2.9826 | 0.940 | 0.639 | p |
| Fe 1 | 4347.2328 | 0.0000 | 1.500 | 0.849 | t |
| Fe 1 | 4347.8326 | 3.6025 | 1.740 | 0.739 | p |
| Fe 1 | 4348.9365 | 2.9904 | 0.960 | 0.781 | t |
| Ti 2 | 4350.8378 | 2.0613 | 1.270 | 0.519 | u |
| Cr 1 | 4351.0490 | 0.9684 | 0.750 | 0.915 | t |
| Fe 1 | 4351.5436 | 2.9904 | 0.880 | 0.834 | p |
| Fe 2 | 4351.7618 | 2.7043 | 1.070 | 0.812 | t |
| Cr 1 | 4351.7620 | 1.0300 | 1.190 | 0.951 | t |
| Fe 1 | 4351.8378 | 4.1544 | 1.470 | 0.576 | u |
| Mg 1 | 4351.9056 | 4.3458 | 99.000 | 0.882 | p |
| Fe 1 | 4352.7344 | 2.2227 | 1.730 | 0.943 | t |
| V 1 | 4352.8654 | 0.0686 | 1.320 | 0.851 | p |
| Mg 1 | 4354.5280 | 4.3458 | 99.000 | 0.616 | u |
| Sc 2 | 4354.5980 | 0.6055 | 1.460 | 0.640 | u |
| Fe 1 | 4354.8899 | 4.2305 | 0.320 | 0.516 | u |
| Ca 1 | 4355.0789 | 2.7090 | 0.990 | 0.810 | p |
| Ni 1 | 4355.8998 | 3.6353 | 1.100 | 0.515 | u |
| Fe 1 | 4358.4991 | 2.9488 | 0.920 | 0.844 | p |
| Y 2 | 4358.7241 | 0.1042 | 0.990 | 0.703 | u |
| Fe 1 | 4358.9022 | 4.2176 | 1.090 | 0.614 | u |
| Ni 1 | 4359.5772 | 3.3990 | 1.220 | 0.701 | u |
| Cr 1 | 4359.6240 | 0.9829 | 1.250 | 0.923 | p |
| Fe 1 | 4360.7636 | 4.1909 | 1.110 | 0.679 | u |
| Fe 1 | 4360.8032 | 3.6416 | 1.500 | 0.682 | u |
| Cr 1 | 4363.1280 | 2.9674 | 0.880 | 0.688 | u |
| Fe 1 | 4365.8962 | 2.9904 | 0.600 | 0.762 | t |
| Fe 1 | 4367.5780 | 2.9904 | 1.080 | 0.876 | p |
| Ti 2 | 4367.6522 | 2.5903 | 1.050 | 0.611 | u |
| Fe 1 | 4367.9032 | 1.6079 | 0.500 | 0.899 | t |
| V 1 | 4368.0407 | 0.0401 | 1.560 | 0.531 | p |
| Ti 1 | 4369.6828 | 2.5783 | 1.130 | 0.598 | u |
| Fe 1 | 4369.7716 | 3.0469 | 1.010 | 0.908 | t |
| Cr 1 | 4371.2268 | 1.0037 | 1.370 | 0.929 | u |
| Cr 1 | 4371.2750 | 1.0037 | 1.370 | 0.917 | t |
| Fe 1 | 4372.9817 | 3.0173 | 1.110 | 0.669 | p |
| Cr 1 | 4373.2550 | 0.9829 | 2.250 | 0.809 | t |
| Fe 1 | 4373.5604 | 3.0176 | 0.780 | 0.816 | t |
| Fe 1 | 4374.1356 | 4.1777 | 1.360 | 0.575 | u |
| Cr 1 | 4374.1540 | 3.0004 | 0.990 | 0.679 | u |
| Sc 2 | 4374.4570 | 0.6184 | 1.240 | 0.876 | t |
| Fe 1 | 4374.4888 | 3.3009 | 0.830 | 0.610 | u |
| Fe 1 | 4374.5000 | 3.3010 | 99.000 | 0.709 | u |
| Ti 2 | 4374.8165 | 2.0613 | 0.910 | 0.569 | u |
| Y 2 | 4374.9329 | 0.4087 | 0.960 | 0.894 | t |

| Element | Wavelength (air – Å) | Excitation potential (eV) | Landé factor | Line Depth | Feature Type |
|---|---|---|---|---|---|
| Cr 1 | 4375.3310 | 2.9826 | 0.990 | 0.601 | t |
| Fe 1 | 4375.4767 | 3.5732 | 0.870 | 0.507 | n |
| Fe 1 | 4375.9293 | 0.0000 | 1.490 | 0.969 | p |
| Fe 1 | 4375.9860 | 3.0469 | 1.910 | 0.784 | u |
| Fe 1 | 4376.7724 | 3.0173 | 1.520 | 0.740 | p |
| Fe 1 | 4376.7820 | 3.6416 | 1.320 | 0.583 | p |
| Fe 1 | 4377.2805 | 4.6076 | 0.810 | 0.637 | u |
| Fe 1 | 4377.7906 | 3.2740 | 1.070 | 0.676 | p |
| Fe 1 | 4378.9705 | 4.1544 | 1.470 | 0.591 | n |
| V 1 | 4379.2304 | 0.3006 | 1.080 | 0.937 | t |
| Cr 1 | 4381.1100 | 2.7088 | 1.540 | 0.595 | p |
| Fe 1 | 4382.7676 | 3.5732 | 1.030 | 0.802 | t |
| Fe 1 | 4383.5444 | 1.4849 | 1.150 | 0.971 | p |
| Ni 1 | 4384.5352 | 3.4646 | 0.840 | 0.659 | n |
| Fe 1 | 4384.6718 | 3.0173 | 1.350 | 0.770 | u |
| V 1 | 4384.7130 | 0.2866 | 1.100 | 0.929 | t |
| Sc 2 | 4384.8140 | 0.5955 | 1.510 | 0.631 | u |
| Cr 1 | 4384.9750 | 1.0300 | 1.420 | 0.903 | p |
| Fe 2 | 4385.3769 | 2.7785 | 1.330 | 0.693 | u |
| Ti 2 | 4386.8465 | 2.5977 | 0.930 | 0.571 | t |
| Fe 1 | 4387.8907 | 3.0713 | 1.680 | 0.842 | t |
| Fe 1 | 4388.4066 | 3.6025 | 1.660 | 0.857 | t |
| Fe 1 | 4389.2441 | 0.0516 | 1.500 | 0.930 | p |
| V 1 | 4389.9793 | 0.2753 | 1.010 | 0.918 | u |
| Fe 1 | 4390.4477 | 2.9904 | 1.200 | 0.711 | p |
| Fe 1 | 4390.9503 | 3.0176 | 1.060 | 0.850 | t |
| Ti 2 | 4391.0258 | 1.2313 | 1.110 | 0.647 | p |
| Cr 1 | 4391.7510 | 1.0037 | 2.010 | 0.798 | t |
| Fe 1 | 4392.5794 | 3.8816 | 1.170 | 0.535 | p |
| Fe 1 | 4392.8529 | 3.2671 | 0.730 | 0.523 | u |
| Fe 1 | 4393.2687 | 4.5844 | 1.190 | 0.583 | u |
| Ti 1 | 4393.9226 | 2.2674 | 1.050 | 0.662 | p |
| Ti 2 | 4394.0586 | 1.2214 | 1.340 | 0.782 | p |
| Ti 2 | 4395.0312 | 1.0842 | 1.070 | 0.930 | t |
| V 1 | 4395.2233 | 0.2670 | 0.750 | 0.896 | p |
| Fe 1 | 4395.2739 | 3.6537 | 2.030 | 0.684 | u |
| Fe 1 | 4395.4982 | 3.8835 | 1.630 | 0.564 | p |
| Ti 2 | 4395.8394 | 1.2429 | 1.210 | 0.746 | p |
| Y 2 | 4398.0103 | 0.1296 | 1.000 | 0.778 | p |
| Ni 1 | 4399.5988 | 3.8474 | 1.000 | 0.507 | p |
| Ti 2 | 4399.7652 | 1.2369 | 1.400 | 0.859 | p |
| Sc 2 | 4400.3890 | 0.6055 | 1.080 | 0.863 | t |
| V 1 | 4400.5717 | 0.2619 | 0.440 | 0.862 | t |
| Ni 1 | 4400.8591 | 3.6552 | 1.220 | 0.611 | p |
| Fe 1 | 4401.2896 | 3.6025 | 1.570 | 0.832 | t |
| Fe 1 | 4401.4425 | 2.8316 | 1.970 | 0.803 | p |

| Element | Wavelength (air – Å) | Excitation potential (eV) | Landé factor | Line Depth | Feature Type |
|---|---|---|---|---|---|
| Ni 1 | 4401.5408 | 3.1930 | 1.180 | 0.865 | p |
| Fe 1 | 4403.9660 | 4.1544 | 1.340 | 0.555 | p |
| Ti 1 | 4404.2696 | 2.2497 | 1.150 | 0.661 | p |
| Ti 1 | 4404.3895 | 1.0529 | 1.000 | 0.633 | p |
| Fe 1 | 4404.7498 | 1.5574 | 1.130 | 0.970 | p |
| Ti 1 | 4404.8964 | 1.8792 | 1.150 | 0.530 | u |
| Fe 1 | 4405.0184 | 0.0516 | 1.510 | 0.872 | p |
| V 1 | 4406.6382 | 0.3006 | 1.480 | 0.871 | t |
| V 1 | 4407.6338 | 0.2866 | 1.480 | 0.891 | p |
| Fe 1 | 4407.6566 | 3.0173 | 1.210 | 0.753 | u |
| Ti 2 | 4407.6727 | 1.2214 | 0.330 | 0.520 | u |
| Fe 1 | 4407.7085 | 2.1759 | 1.830 | 0.906 | p |
| V 1 | 4408.1958 | 0.2753 | 1.440 | 0.894 | p |
| Fe 1 | 4408.4131 | 2.1979 | 1.980 | 0.918 | p |
| V 1 | 4408.4931 | 0.2619 | 1.380 | 0.868 | p |
| V 1 | 4408.5162 | 0.2670 | 1.440 | 0.885 | p |
| Fe 1 | 4409.1189 | 3.3009 | 1.490 | 0.685 | t |
| Ti 2 | 4409.5176 | 1.2313 | 1.460 | 0.552 | p |
| Ni 1 | 4410.5183 | 3.3061 | 0.820 | 0.687 | p |
| Cr 1 | 4411.0880 | 3.0133 | 1.260 | 0.586 | p |
| Ti 2 | 4411.9297 | 1.2241 | 1.300 | 0.514 | u |
| Fe 1 | 4411.9371 | 3.8816 | 1.460 | 0.588 | u |
| Cr 1 | 4412.2510 | 1.0300 | 1.890 | 0.709 | p |
| Fe 1 | 4412.4253 | 2.1759 | 1.790 | 0.763 | p |
| Fe 1 | 4413.3953 | 4.0758 | 0.530 | 0.629 | u |
| Fe 1 | 4414.2257 | 3.0713 | 0.970 | 0.682 | p |
| Fe 1 | 4414.4608 | 4.1777 | 1.140 | 0.632 | n |
| Mn 1 | 4414.8764 | 2.8884 | 1.500 | 0.805 | p |
| Fe 1 | 4414.9314 | 3.8835 | 1.220 | 0.598 | u |
| Fe 1 | 4415.1221 | 1.6079 | 1.100 | 0.968 | t |
| Sc 2 | 4415.5570 | 0.5955 | 0.670 | 0.847 | p |
| V 1 | 4416.4662 | 0.2670 | 2.480 | 0.788 | p |
| Fe 2 | 4416.8186 | 2.7785 | 0.770 | 0.740 | u |
| Ti 1 | 4417.2734 | 1.8871 | 1.150 | 0.737 | p |
| Ti 2 | 4417.7136 | 1.1649 | 0.790 | 0.869 | t |
| Ti 2 | 4418.3309 | 1.2369 | 1.270 | 0.731 | p |
| Fe 1 | 4419.7912 | 3.3009 | 1.150 | 0.533 | p |
| V 1 | 4421.5674 | 0.2753 | 2.140 | 0.790 | p |
| Ti 1 | 4421.7518 | 2.2393 | 1.020 | 0.563 | p |
| Ti 2 | 4421.9378 | 2.0613 | 1.270 | 0.536 | u |
| Fe 1 | 4422.5677 | 2.8450 | 1.020 | 0.902 | t |
| Y 2 | 4422.5845 | 0.1042 | 0.500 | 0.713 | t |
| Cr 1 | 4422.7730 | 2.5443 | 99.000 | 0.793 | u |
| Ti 1 | 4422.8198 | 1.0666 | 1.190 | 0.732 | p |
| Fe 1 | 4423.1406 | 2.9904 | 1.190 | 0.704 | p |
| Fe 1 | 4423.8408 | 3.6537 | 1.820 | 0.728 | p |

| Element | Wavelength (air – Å) | Excitation potential (eV) | Landé factor | Line Depth | Feature Type |
|---|---|---|---|---|---|
| Fe 1 | 4424.0673 | 3.6416 | 1.320 | 0.509 | p |
| Fe 1 | 4424.1873 | 3.5465 | 0.920 | 0.695 | p |
| Cr 1 | 4424.2780 | 3.0106 | 1.260 | 0.552 | p |
| Ca 1 | 4425.4370 | 1.8793 | 0.500 | 0.911 | p |
| V 1 | 4425.9974 | 0.2866 | 2.040 | 0.758 | p |
| Ti 1 | 4426.0513 | 1.8792 | 1.030 | 0.684 | u |
| Ti 1 | 4427.0976 | 1.5025 | 1.100 | 0.859 | p |
| Fe 1 | 4427.2981 | 3.6537 | 1.700 | 0.815 | p |
| Fe 1 | 4427.3094 | 0.0516 | 1.480 | 0.968 | p |
| V 1 | 4428.5100 | 0.2670 | 1.850 | 0.699 | p |
| V 1 | 4429.7894 | 0.3006 | 1.880 | 0.617 | p |
| Fe 1 | 4430.1886 | 3.0173 | 1.430 | 0.820 | t |
| Ti 1 | 4430.3635 | 1.4432 | 1.450 | 0.687 | p |
| Fe 1 | 4430.6135 | 2.2227 | 2.500 | 0.922 | t |
| Cr 1 | 4432.1670 | 2.8719 | 1.500 | 0.616 | p |
| Fe 1 | 4432.5674 | 3.5732 | 1.070 | 0.745 | p |
| Fe 1 | 4433.2182 | 3.6537 | 1.540 | 0.845 | p |
| Fe 1 | 4433.7817 | 3.6025 | 1.470 | 0.788 | p |
| Ti 1 | 4433.9654 | 1.4298 | 1.530 | 0.662 | p |
| Ti 1 | 4434.0177 | 1.8732 | 0.830 | 0.729 | p |
| Ca 1 | 4434.9570 | 1.8858 | 1.000 | 0.929 | p |
| Fe 1 | 4435.1484 | 0.0873 | 1.480 | 0.936 | p |
| Ca 1 | 4435.6790 | 1.8858 | 1.000 | 0.900 | p |
| V 1 | 4436.1323 | 0.2619 | 2.090 | 0.765 | p |
| Mn 1 | 4436.3474 | 2.9197 | 1.490 | 0.798 | p |
| Fe 1 | 4436.9204 | 3.0469 | 0.940 | 0.763 | p |
| Ni 1 | 4436.9745 | 3.4980 | 0.200 | 0.681 | p |
| V 1 | 4437.8304 | 0.2866 | 1.630 | 0.805 | p |
| Fe 1 | 4438.3424 | 3.6864 | 2.490 | 0.715 | p |
| Fe 1 | 4439.6340 | 3.0469 | 0.760 | 0.568 | p |
| Fe 1 | 4439.8808 | 2.2786 | 1.750 | 0.774 | t |
| Ti 1 | 4440.3426 | 1.8732 | 0.840 | 0.657 | p |
| Fe 1 | 4440.4788 | 3.6025 | 1.790 | 0.624 | p |
| Fe 1 | 4440.8239 | 3.9597 | 0.990 | 0.644 | p |
| Fe 1 | 4441.0026 | 4.2204 | 1.240 | 0.606 | p |
| Fe 1 | 4441.0862 | 4.5485 | 1.200 | 0.557 | p |
| Fe 1 | 4441.5379 | 4.2833 | 1.040 | 0.523 | u |
| V 1 | 4441.6800 | 0.2753 | 1.760 | 0.823 | t |
| Ti 2 | 4441.7288 | 1.1801 | 1.400 | 0.651 | u |
| Fe 1 | 4442.3386 | 2.1979 | 1.660 | 0.941 | t |
| Fe 1 | 4442.8310 | 2.1759 | 0.990 | 0.824 | t |
| Fe 1 | 4443.1937 | 2.8581 | 0.560 | 0.904 | t |
| Fe 1 | 4443.1953 | 3.0713 | 1.120 | 0.788 | t |
| Ti 2 | 4443.8008 | 1.0800 | 0.920 | 0.917 | t |
| V 1 | 4444.2059 | 0.2670 | 2.100 | 0.800 | p |
| Ti 2 | 4444.5541 | 1.1156 | 1.020 | 0.713 | p |

| Element | Wavelength (air – Å) | Excitation potential (eV) | Landé factor | Line Depth | Feature Type |
|---|---|---|---|---|---|
| Fe 1 | 4445.4706 | 0.0873 | 1.500 | 0.832 | t |
| Fe 1 | 4446.8319 | 3.6864 | 1.960 | 0.765 | p |
| Fe 1 | 4446.8956 | 3.3014 | 1.000 | 0.591 | u |
| Fe 1 | 4447.1298 | 2.1979 | 2.000 | 0.827 | t |
| Fe 1 | 4447.2461 | 4.2562 | 1.180 | 0.513 | u |
| Fe 1 | 4447.7168 | 2.2227 | 2.000 | 0.936 | t |
| Fe 1 | 4447.8027 | 4.2204 | 1.360 | 0.660 | u |
| Ti 1 | 4449.1425 | 1.8871 | 1.210 | 0.824 | p |
| Ti 1 | 4449.9665 | 1.8792 | 1.240 | 0.511 | n |
| Fe 1 | 4450.3155 | 3.1110 | 1.880 | 0.771 | p |
| Ti 2 | 4450.4821 | 1.0842 | 1.040 | 0.840 | p |
| Ti 1 | 4450.8939 | 1.8792 | 1.060 | 0.806 | p |
| Mn 1 | 4451.5806 | 2.8884 | 1.430 | 0.866 | t |
| V 1 | 4452.0051 | 1.8676 | 1.050 | 0.648 | p |
| Fe 1 | 4452.6095 | 3.9433 | 1.410 | 0.529 | p |
| Mn 1 | 4452.9992 | 2.9408 | 1.500 | 0.763 | t |
| Ti 1 | 4453.3128 | 1.4298 | 0.650 | 0.836 | p |
| Fe 1 | 4453.3189 | 3.9597 | 0.630 | 0.664 | p |
| Ti 1 | 4453.6987 | 1.8732 | 0.750 | 0.773 | p |
| Fe 1 | 4454.3807 | 2.8316 | 1.350 | 0.888 | t |
| Ca 1 | 4454.7790 | 1.8989 | 1.160 | 0.937 | t |
| Mn 1 | 4455.0038 | 3.0722 | 1.970 | 0.747 | p |
| Fe 1 | 4455.0268 | 3.8816 | 1.240 | 0.763 | p |
| Mn 1 | 4455.3058 | 3.0722 | 2.060 | 0.771 | p |
| Ti 1 | 4455.3168 | 1.4432 | 1.090 | 0.851 | p |
| Mn 1 | 4455.8096 | 3.0722 | 1.090 | 0.732 | p |
| Ca 1 | 4455.8870 | 1.8989 | 1.340 | 0.897 | p |
| Fe 1 | 4456.3254 | 3.0469 | 1.180 | 0.754 | p |
| Ca 1 | 4456.6160 | 1.8989 | 2.000 | 0.777 | p |
| Fe 1 | 4456.6280 | 3.8816 | 1.240 | 0.645 | p |
| Mn 1 | 4457.0345 | 3.0733 | 1.960 | 0.723 | p |
| Ti 1 | 4457.4268 | 1.4601 | 1.250 | 0.865 | u |
| V 1 | 4457.4696 | 0.2753 | 1.150 | 0.756 | p |
| Mn 1 | 4457.5387 | 3.0733 | 1.750 | 0.793 | p |
| Fe 1 | 4458.0800 | 3.8835 | 1.290 | 0.764 | p |
| Mn 1 | 4458.2476 | 3.0733 | 1.210 | 0.813 | p |
| Cr 1 | 4458.5070 | 3.5505 | 1.130 | 0.600 | p |
| Cr 1 | 4458.5430 | 3.0106 | 1.090 | 0.681 | p |
| Ni 1 | 4459.0329 | 3.3061 | 1.080 | 0.821 | p |
| Fe 1 | 4459.1170 | 2.1759 | 1.590 | 0.940 | p |
| Fe 1 | 4459.3521 | 4.1777 | 1.400 | 0.751 | p |
| Cr 1 | 4459.3750 | 2.7079 | 1.640 | 0.636 | p |
| Cr 1 | 4459.7340 | 3.0133 | 1.120 | 0.609 | p |
| V 1 | 4459.7536 | 0.2866 | 1.250 | 0.838 | p |
| V 1 | 4460.2914 | 0.3006 | 1.360 | 0.871 | p |

| Element | Wavelength (air – Å) | Excitation potential (eV) | Landé factor | Line Depth | Feature Type |
|---|---|---|---|---|---|
| Mn 1 | 4460.3680 | 3.0751 | 1.810 | 0.575 | p |
| Mn 1 | 4461.0778 | 3.0751 | 1.650 | 0.754 | p |
| Fe 1 | 4461.1954 | 3.0173 | 1.310 | 0.806 | p |
| Fe 1 | 4461.3718 | 3.4149 | 0.820 | 0.605 | p |
| Fe 1 | 4461.6523 | 0.0873 | 1.530 | 0.964 | p |
| Fe 1 | 4461.9682 | 3.6025 | 0.900 | 0.793 | u |
| Fe 1 | 4461.9941 | 3.0713 | 1.440 | 0.745 | u |
| Mn 1 | 4462.0148 | 3.0751 | 1.270 | 0.844 | u |
| Fe 1 | 4462.1976 | 3.6025 | 1.450 | 0.505 | u |
| V 1 | 4462.3574 | 1.8599 | 1.030 | 0.622 | p |
| Ni 1 | 4462.4548 | 3.4646 | 0.680 | 0.746 | p |
| Ti 1 | 4463.3807 | 1.8792 | 1.500 | 0.545 | p |
| Fe 1 | 4463.4037 | 4.2562 | 1.270 | 0.616 | p |
| Ti 1 | 4463.5311 | 1.8871 | 1.530 | 0.575 | p |
| Ti 2 | 4464.4485 | 1.1610 | 0.490 | 0.780 | t |
| Mn 1 | 4464.6725 | 2.9197 | 1.370 | 0.818 | p |
| Fe 1 | 4464.6902 | 3.2410 | 1.300 | 0.598 | p |
| Fe 1 | 4464.7656 | 3.0173 | 1.460 | 0.784 | p |
| Ti 1 | 4465.8054 | 1.7393 | 1.500 | 0.761 | p |
| Fe 1 | 4466.5510 | 2.8316 | 1.210 | 0.930 | p |
| Fe 1 | 4466.5721 | 0.1101 | 1.500 | 0.926 | p |
| Co 1 | 4466.8799 | 3.0160 | 1.420 | 0.505 | p |
| Fe 1 | 4466.9373 | 3.9286 | 1.090 | 0.710 | p |
| Ti 2 | 4468.4926 | 1.1305 | 1.050 | 0.916 | t |
| Ti 2 | 4469.1512 | 1.0842 | 1.280 | 0.607 | p |
| Fe 1 | 4469.3753 | 3.6537 | 1.490 | 0.864 | t |
| Co 1 | 4469.5478 | 2.9577 | 1.460 | 0.622 | p |
| V 1 | 4469.7033 | 1.8535 | 1.000 | 0.545 | p |
| Mn 1 | 4470.1319 | 2.9408 | 1.200 | 0.769 | p |
| Ni 1 | 4470.4772 | 3.3990 | 0.970 | 0.791 | p |
| Ti 2 | 4470.8532 | 1.1649 | 1.330 | 0.738 | p |
| Ti 1 | 4471.2372 | 1.7335 | 1.470 | 0.758 | p |
| Fe 1 | 4471.6759 | 0.1101 | 1.520 | 0.658 | p |
| Fe 1 | 4472.7049 | 3.6398 | 1.090 | 0.630 | p |
| Mn 1 | 4472.7875 | 2.9532 | 0.000 | 0.743 | p |
| Cr 1 | 4473.8270 | 2.7079 | 1.410 | 0.602 | u |
| Ti 1 | 4474.8513 | 1.4432 | 1.530 | 0.643 | p |
| Fe 1 | 4476.0184 | 2.8450 | 1.060 | 0.918 | u |
| Fe 1 | 4476.0753 | 3.6864 | 1.460 | 0.885 | p |
| Fe 1 | 4478.0173 | 2.1979 | 2.080 | 0.606 | p |
| Fe 1 | 4479.5979 | 3.6343 | 0.900 | 0.681 | p |
| Fe 1 | 4479.6145 | 3.6864 | 1.110 | 0.686 | p |
| Ti 1 | 4479.7015 | 1.7335 | 2.490 | 0.621 | p |
| Fe 1 | 4479.9620 | 3.9841 | 0.290 | 0.654 | p |
| Fe 1 | 4480.1365 | 3.0469 | 1.170 | 0.787 | p |
| Fe 1 | 4480.2702 | 3.6025 | 2.360 | 0.595 | p |

| Element | Wavelength (air – Å) | Excitation potential (eV) | Landé factor | Line Depth | Feature Type |
|---|---|---|---|---|---|
| Fe 1 | 4480.8174 | 4.5931 | 1.190 | 0.624 | p |
| Ti 1 | 4481.2592 | 1.7489 | 1.660 | 0.805 | p |
| Fe 1 | 4481.6089 | 3.6864 | 1.640 | 0.746 | p |
| Fe 1 | 4482.1691 | 0.1101 | 1.510 | 0.959 | p |
| Fe 1 | 4482.2523 | 2.2227 | 1.000 | 0.928 | p |
| Ti 1 | 4482.6865 | 1.4601 | 1.500 | 0.643 | p |
| Fe 1 | 4482.7389 | 3.6537 | 1.150 | 0.763 | p |
| Fe 1 | 4484.2198 | 3.6025 | 1.230 | 0.830 | p |
| Fe 1 | 4485.6755 | 3.6864 | 2.460 | 0.800 | p |
| Fe 1 | 4487.3560 | 3.6025 | 0.860 | 0.633 | p |
| Cr 1 | 4487.4990 | 2.7088 | 1.400 | 0.541 | u |
| Cr 1 | 4488.0480 | 2.9872 | 1.290 | 0.604 | p |
| Fe 1 | 4488.1331 | 3.6025 | 1.470 | 0.710 | p |
| Ti 2 | 4488.3239 | 3.1235 | 1.070 | 0.513 | u |
| Fe 1 | 4488.9057 | 3.6537 | 1.480 | 0.672 | p |
| Ti 1 | 4489.0881 | 1.7393 | 1.500 | 0.755 | p |
| Fe 2 | 4489.1758 | 2.8281 | 1.390 | 0.590 | u |
| Cr 1 | 4489.4630 | 3.5561 | 1.000 | 0.559 | n |
| Fe 1 | 4489.7387 | 0.1213 | 1.550 | 0.948 | t |
| Mn 1 | 4490.0732 | 2.9532 | 1.500 | 0.752 | p |
| Fe 1 | 4490.0839 | 3.0173 | 1.280 | 0.834 | p |
| Fe 1 | 4490.7596 | 3.9433 | 1.160 | 0.753 | p |
| Fe 1 | 4490.8110 | 3.9433 | 1.110 | 0.600 | p |
| Fe 2 | 4491.3971 | 2.8555 | 0.420 | 0.654 | u |
| Cr 1 | 4492.3060 | 3.3752 | 1.240 | 0.545 | u |
| Fe 1 | 4492.6782 | 3.9841 | 0.640 | 0.613 | u |
| Ti 2 | 4493.5220 | 1.0800 | 1.200 | 0.506 | u |
| Fe 1 | 4494.0520 | 3.9841 | 1.000 | 0.555 | u |
| Fe 1 | 4494.4644 | 2.9488 | 0.640 | 0.537 | u |
| Fe 1 | 4494.5628 | 2.1979 | 1.190 | 0.942 | u |
| Fe 1 | 4495.5671 | 3.6025 | 1.500 | 0.600 | u |
| Fe 1 | 4495.9524 | 3.6537 | 1.400 | 0.697 | u |
| Ti 1 | 4496.1448 | 1.7489 | 1.510 | 0.754 | p |
| Ti 1 | 4496.2323 | 0.0211 | 1.040 | 0.608 | p |
| Cr 1 | 4496.8520 | 0.9414 | 1.330 | 0.924 | t |
| Zr 2 | 4496.9620 | 0.7133 | 0.770 | 0.523 | u |
| Cr 1 | 4498.7240 | 2.9151 | 1.200 | 0.537 | p |
| Mn 1 | 4498.8915 | 2.9408 | 1.500 | 0.780 | p |
| Fe 1 | 4499.1352 | 4.5485 | 1.200 | 0.528 | p |
| Cr 1 | 4500.2780 | 3.0790 | 0.820 | 0.676 | p |
| Cr 1 | 4501.1000 | 2.9151 | 1.500 | 0.520 | p |
| Ti 2 | 4501.2697 | 1.1156 | 0.910 | 0.905 | t |
| Mn 1 | 4502.2128 | 2.9197 | 1.500 | 0.783 | p |
| Fe 1 | 4502.5906 | 3.5732 | 1.560 | 0.519 | p |
| Fe 1 | 4504.8304 | 3.2657 | 0.710 | 0.674 | p |
| Cr 1 | 4505.3304 | 3.1044 | 1.230 | 0.626 | n |

| Element | Wavelength (air – Å) | Excitation potential (eV) | Landé factor | Line Depth | Feature Type |
|---|---|---|---|---|---|
| Fe 2 | 4508.2803 | 2.8555 | 0.500 | 0.740 | p |
| Fe 1 | 4509.7346 | 4.2204 | 1.390 | 0.655 | p |
| Cr 1 | 4511.8910 | 3.0869 | 1.090 | 0.674 | p |
| Ca 1 | 4512.2680 | 2.5257 | 1.160 | 0.505 | p |
| Ti 1 | 4512.7339 | 0.8360 | 1.500 | 0.878 | t |
| Fe 1 | 4514.1839 | 3.0469 | 1.170 | 0.766 | t |
| Fe 1 | 4514.4148 | 4.5485 | 1.110 | 0.602 | u |
| Cr 1 | 4514.4729 | 2.9135 | 1.300 | 0.531 | u |
| Fe 1 | 4514.5025 | 3.9286 | 1.300 | 0.526 | u |
| Fe 2 | 4515.3330 | 2.8441 | 1.040 | 0.707 | p |
| Fe 1 | 4516.4493 | 3.6537 | 0.730 | 0.501 | n |
| Fe 1 | 4517.5238 | 3.0713 | 1.530 | 0.789 | t |
| Ti 1 | 4518.0220 | 0.8259 | 1.480 | 0.892 | p |
| Ti 2 | 4518.3317 | 1.0800 | 0.610 | 0.599 | p |
| Ti 1 | 4518.6890 | 1.4298 | 0.670 | 0.588 | p |
| Ni 1 | 4519.9829 | 1.6764 | 0.880 | 0.641 | p |
| Fe 2 | 4520.2182 | 2.8067 | 1.340 | 0.686 | p |
| La 2 | 4522.3700 | 0.0000 | 0.940 | 0.666 | n |
| Fe 2 | 4522.6276 | 2.8441 | 0.920 | 0.771 | p |
| Ti 1 | 4522.7970 | 0.8181 | 1.490 | 0.891 | p |
| Fe 1 | 4523.3986 | 3.6537 | 2.010 | 0.621 | p |
| Fe 1 | 4525.1364 | 3.6025 | 1.360 | 0.884 | p |
| Fe 1 | 4526.3981 | 3.8816 | 1.100 | 0.752 | u |
| Cr 1 | 4526.4540 | 2.5441 | 1.330 | 0.815 | u |
| Fe 1 | 4526.5606 | 3.1110 | 1.410 | 0.745 | u |
| Ca 1 | 4526.9280 | 2.7090 | 1.010 | 0.783 | p |
| Ti 1 | 4527.3041 | 0.8129 | 1.510 | 0.875 | p |
| Cr 1 | 4527.3450 | 2.5446 | 1.500 | 0.643 | p |
| Cr 1 | 4527.4560 | 2.9872 | 1.160 | 0.520 | p |
| Fe 1 | 4528.6136 | 2.1759 | 1.220 | 0.950 | p |
| Fe 1 | 4528.7565 | 3.3014 | 0.940 | 0.723 | u |
| Fe 1 | 4528.8203 | 3.0173 | 1.010 | 0.690 | u |
| Ti 2 | 4529.4799 | 1.5718 | 1.010 | 0.679 | p |
| Fe 1 | 4529.5498 | 3.8835 | 1.340 | 0.748 | p |
| Fe 1 | 4529.6715 | 3.5465 | 1.020 | 0.750 | p |
| Cr 1 | 4529.8450 | 2.5441 | 1.580 | 0.526 | p |
| Cr 1 | 4530.6830 | 2.5446 | 1.430 | 0.671 | u |
| Cr 1 | 4530.7380 | 2.5446 | 1.240 | 0.800 | u |
| Co 1 | 4530.9493 | 2.9275 | 1.470 | 0.743 | u |
| Fe 1 | 4531.1477 | 1.4849 | 1.300 | 0.941 | p |
| Fe 1 | 4531.6254 | 3.2112 | 1.400 | 0.680 | p |
| Fe 1 | 4531.6355 | 3.6343 | 0.700 | 0.594 | u |
| Fe 1 | 4533.1261 | 3.2740 | 0.730 | 0.737 | u |
| Ti 1 | 4533.2394 | 0.8484 | 1.410 | 0.937 | t |
| Ti 2 | 4533.9599 | 1.2369 | 1.100 | 0.909 | t |
| Ti 1 | 4534.7761 | 0.8360 | 1.350 | 0.930 | t |

| Element | Wavelength (air – Å) | Excitation potential (eV) | Landé factor | Line Depth | Feature Type |
|---|---|---|---|---|---|
| Cr 1 | 4535.1360 | 2.5443 | 1.360 | 0.658 | p |
| Ti 1 | 4535.5686 | 0.8259 | 1.250 | 0.920 | p |
| Fe 1 | 4535.6272 | 4.6076 | 1.700 | 0.626 | u |
| Cr 1 | 4535.6960 | 2.5446 | 1.120 | 0.763 | u |
| Cr 1 | 4535.7520 | 2.5446 | 1.550 | 0.587 | u |
| Ti 1 | 4535.8433 | 1.4432 | 1.090 | 0.544 | u |
| Ti 1 | 4535.9176 | 0.8181 | 1.000 | 0.907 | u |
| Ti 1 | 4536.0403 | 0.8129 | 0.000 | 0.900 | u |
| Fe 1 | 4538.7479 | 2.2786 | 1.510 | 0.519 | p |
| Fe 1 | 4538.8361 | 3.9433 | 0.750 | 0.611 | p |
| Cr 1 | 4539.7810 | 2.5438 | 1.390 | 0.597 | p |
| Cr 1 | 4540.4980 | 2.5443 | 0.900 | 0.759 | p |
| Cr 1 | 4540.7040 | 3.1044 | 1.220 | 0.741 | p |
| Cr 1 | 4541.0610 | 2.5446 | 1.510 | 0.612 | p |
| Fe 2 | 4541.5156 | 2.8555 | 0.770 | 0.625 | p |
| Fe 1 | 4542.4116 | 3.6398 | 1.030 | 0.604 | p |
| Fe 1 | 4542.4515 | 4.2562 | 1.340 | 0.529 | u |
| Co 1 | 4543.8120 | 2.7177 | 1.210 | 0.544 | p |
| Fe 1 | 4543.8597 | 4.6520 | 1.560 | 0.561 | u |
| Ti 2 | 4544.0162 | 1.2429 | 1.400 | 0.509 | p |
| Cr 1 | 4544.6120 | 2.5438 | 0.360 | 0.752 | p |
| Ti 1 | 4544.6871 | 0.8181 | 1.490 | 0.873 | p |
| Ti 2 | 4545.1327 | 1.1305 | 0.890 | 0.616 | p |
| Cr 1 | 4545.3310 | 2.5443 | 1.510 | 0.548 | p |
| Fe 1 | 4545.7540 | 3.2367 | 1.090 | 0.524 | n |
| Cr 1 | 4545.9530 | 0.9414 | 1.920 | 0.906 | t |
| Ni 1 | 4546.9267 | 4.1646 | 1.030 | 0.656 | p |
| Fe 1 | 4547.0169 | 1.5574 | 1.170 | 0.792 | p |
| Ni 1 | 4547.2239 | 3.6353 | 1.080 | 0.547 | p |
| Fe 1 | 4547.8467 | 3.5465 | 1.010 | 0.815 | p |
| Ti 1 | 4548.7635 | 0.8259 | 1.490 | 0.887 | p |
| Fe 1 | 4549.4654 | 3.8816 | 1.160 | 0.689 | p |
| Fe 2 | 4549.4662 | 2.8281 | 1.030 | 0.772 | p |
| Ti 2 | 4549.6217 | 1.5839 | 1.040 | 0.895 | p |
| Co 1 | 4549.6584 | 3.0665 | 1.470 | 0.565 | p |
| Ti 2 | 4549.8129 | 1.1801 | 0.580 | 0.642 | p |
| Fe 1 | 4552.1463 | 4.3714 | 0.970 | 0.559 | u |
| Ti 1 | 4552.4533 | 0.8360 | 1.520 | 0.888 | p |
| Ba 2 | 4554.0311 | 0.0000 | 99.000 | 0.871 | t |
| Ba 2 | 4554.0316 | 0.0000 | 99.000 | 0.894 | t |
| Ba 2 | 4554.0319 | 0.0000 | 99.000 | 0.809 | t |
| Ba 2 | 4554.0323 | 0.0000 | 99.000 | 0.878 | t |
| Ba 2 | 4554.0336 | 0.0000 | 99.000 | 0.944 | t |
| Fe 1 | 4554.4510 | 2.8654 | 1.510 | 0.552 | p |
| Cr 1 | 4555.0820 | 3.1044 | 1.200 | 0.663 | u |
| Ti 1 | 4555.4829 | 0.8484 | 1.550 | 0.873 | p |

| Element | Wavelength (air – Å) | Excitation potential (eV) | Landé factor | Line Depth | Feature Type |
|---|---|---|---|---|---|
| Fe 2 | 4555.8868 | 2.8281 | 1.250 | 0.753 | p |
| Fe 1 | 4556.0864 | 2.9488 | 1.230 | 0.653 | u |
| Fe 1 | 4556.1258 | 3.6025 | 1.470 | 0.831 | p |
| Fe 1 | 4556.9241 | 3.2515 | 0.930 | 0.510 | p |
| Fe 1 | 4558.1053 | 3.6416 | 0.820 | 0.584 | p |
| Cr 2 | 4558.6500 | 4.0734 | 1.160 | 0.645 | p |
| Fe 1 | 4560.0881 | 3.6025 | 0.610 | 0.656 | p |
| Fe 1 | 4561.1980 | 4.3201 | 1.200 | 0.591 | u |
| Fe 1 | 4561.4132 | 4.4153 | 0.890 | 0.575 | p |
| Fe 1 | 4561.4300 | 2.7586 | 1.050 | 0.591 | p |
| Ti 1 | 4562.6277 | 0.0211 | 1.170 | 0.583 | p |
| Ti 2 | 4563.7574 | 1.2214 | 0.990 | 0.896 | t |
| Fe 1 | 4565.3102 | 3.2740 | 1.530 | 0.584 | u |
| Fe 1 | 4565.4106 | 4.4456 | 0.500 | 0.520 | u |
| Cr 1 | 4565.5040 | 0.9829 | 1.840 | 0.834 | p |
| Co 1 | 4565.5789 | 3.0160 | 1.460 | 0.624 | u |
| Fe 1 | 4565.6615 | 3.2410 | 2.010 | 0.679 | p |
| Fe 1 | 4566.5145 | 3.3009 | 0.990 | 0.621 | p |
| Fe 1 | 4566.8649 | 4.3125 | 1.140 | 0.686 | p |
| Fe 1 | 4566.9885 | 3.4149 | 0.610 | 0.670 | p |
| Fe 1 | 4568.7633 | 3.2657 | 2.250 | 0.633 | p |
| Cr 1 | 4569.6150 | 3.1216 | 1.140 | 0.551 | p |
| Mg 1 | 4571.0956 | 0.0000 | 99.000 | 0.929 | p |
| Cr 1 | 4571.6710 | 2.5441 | 1.150 | 0.716 | p |
| Ti 2 | 4571.9713 | 1.5718 | 0.940 | 0.888 | t |
| Fe 1 | 4574.2153 | 3.2112 | 1.900 | 0.614 | p |
| Fe 1 | 4574.7172 | 2.2786 | 1.500 | 0.764 | t |
| Fe 2 | 4576.3329 | 2.8441 | 1.180 | 0.588 | n |
| V 1 | 4577.1740 | 0.0000 | 0.660 | 0.791 | p |
| Ca 1 | 4578.5510 | 2.5213 | 0.760 | 0.788 | u |
| Fe 1 | 4579.3301 | 2.8325 | 1.490 | 0.605 | u |
| Fe 1 | 4579.8200 | 3.0713 | 1.680 | 0.545 | p |
| Cr 1 | 4580.0480 | 0.9414 | 1.750 | 0.878 | p |
| V 1 | 4580.3967 | 0.0170 | 0.880 | 0.815 | p |
| Fe 1 | 4580.4600 | 2.8316 | 1.440 | 0.632 | u |
| Fe 1 | 4580.5767 | 3.6537 | 0.860 | 0.579 | u |
| Ca 1 | 4581.3949 | 2.5230 | 1.010 | 0.809 | t |
| Ca 1 | 4581.4672 | 2.5230 | 0.910 | 0.671 | t |
| Fe 1 | 4581.5077 | 3.2410 | 0.970 | 0.756 | t |
| Co 1 | 4581.5955 | 2.9577 | 1.460 | 0.665 | t |
| Fe 2 | 4582.8296 | 2.8441 | 1.630 | 0.537 | t |
| Fe 1 | 4582.9424 | 2.8450 | 1.440 | 0.627 | t |
| Fe 1 | 4583.7193 | 3.1110 | 1.600 | 0.704 | p |
| Fe 2 | 4583.8292 | 2.8067 | 1.140 | 0.791 | p |
| Fe 1 | 4584.5967 | 4.5485 | 1.120 | 0.738 | u |
| Fe 1 | 4584.7159 | 3.6025 | 1.510 | 0.689 | p |

| Element | Wavelength (air – Å) | Excitation potential (eV) | Landé factor | Line Depth | Feature Type |
|---|---|---|---|---|---|
| Fe 1 | 4584.8187 | 3.6025 | 1.640 | 0.743 | p |
| Ca 1 | 4585.8654 | 2.5257 | 1.140 | 0.827 | p |
| Ca 1 | 4585.9639 | 2.5257 | 1.210 | 0.669 | p |
| V 1 | 4586.3660 | 0.0401 | 1.020 | 0.832 | p |
| Fe 1 | 4587.1273 | 3.5732 | 1.040 | 0.702 | p |
| Cr 2 | 4588.1990 | 4.0712 | 1.060 | 0.596 | u |
| Ti 2 | 4589.9580 | 1.2369 | 1.120 | 0.783 | p |
| Fe 1 | 4590.7884 | 4.3865 | 1.070 | 0.639 | p |
| Cr 1 | 4591.3910 | 0.9684 | 2.000 | 0.866 | t |
| Fe 1 | 4591.5116 | 4.6520 | 1.210 | 0.523 | u |
| Ni 1 | 4592.5262 | 3.5432 | 0.940 | 0.746 | u |
| Fe 1 | 4592.6509 | 1.5574 | 1.170 | 0.921 | p |
| V 1 | 4594.1158 | 0.0686 | 1.030 | 0.844 | p |
| Fe 1 | 4594.9385 | 3.2740 | 2.240 | 0.545 | u |
| Fe 1 | 4595.3581 | 3.3014 | 1.430 | 0.754 | p |
| Fe 1 | 4596.0598 | 3.6025 | 1.450 | 0.756 | t |
| Fe 1 | 4597.7472 | 4.6076 | 1.250 | 0.524 | p |
| Fe 1 | 4597.8715 | 4.4346 | 0.950 | 0.627 | p |
| Fe 1 | 4598.1166 | 3.2830 | 0.750 | 0.783 | p |
| Fe 1 | 4598.3237 | 0.9582 | 0.660 | 0.723 | u |
| Fe 1 | 4599.8401 | 4.3125 | 0.890 | 0.614 | p |
| Cr 1 | 4600.0958 | 2.5441 | 1.310 | 0.594 | p |
| Ni 1 | 4600.3589 | 3.5972 | 0.450 | 0.691 | p |
| Cr 1 | 4600.7490 | 1.0037 | 1.590 | 0.905 | t |
| Fe 1 | 4600.9314 | 3.2367 | 1.070 | 0.576 | p |
| Cr 1 | 4601.0170 | 2.5446 | 1.360 | 0.582 | p |
| Fe 1 | 4602.0005 | 1.6079 | 1.010 | 0.857 | t |
| Fe 1 | 4602.9405 | 1.4849 | 1.740 | 0.935 | p |
| Fe 1 | 4603.3424 | 2.8450 | 1.320 | 0.516 | p |
| Fe 1 | 4603.9482 | 2.9904 | 1.100 | 0.577 | p |
| Fe 1 | 4604.5562 | 4.4733 | 0.790 | 0.610 | p |
| Ni 1 | 4604.9875 | 3.4800 | 1.080 | 0.771 | p |
| Fe 1 | 4605.0952 | 2.8581 | 1.390 | 0.561 | u |
| Fe 1 | 4605.5871 | 4.3201 | 1.390 | 0.634 | p |
| Ni 1 | 4606.2210 | 3.5972 | 0.320 | 0.590 | p |
| Sr 1 | 4607.3310 | 0.0000 | 99.000 | 0.837 | p |
| Fe 1 | 4607.6462 | 3.2657 | 1.250 | 0.799 | p |
| Fe 1 | 4611.1837 | 2.8512 | 1.500 | 0.670 | u |
| Fe 1 | 4611.2786 | 3.6537 | 1.890 | 0.856 | u |
| Fe 1 | 4611.2918 | 3.6537 | 1.160 | 0.518 | u |
| Fe 1 | 4611.3479 | 0.9146 | 0.890 | 0.796 | u |
| Fe 1 | 4613.2024 | 3.2918 | 0.010 | 0.767 | p |
| Cr 1 | 4613.3570 | 0.9610 | 2.510 | 0.885 | t |
| Fe 1 | 4614.2051 | 3.3009 | 0.660 | 0.520 | p |
| Cr 1 | 4616.1240 | 0.9829 | 1.670 | 0.911 | t |
| Ti 1 | 4617.2689 | 1.7489 | 1.160 | 0.829 | t |

| Element | Wavelength (air – Å) | Excitation potential (eV) | Landé factor | Line Depth | Feature Type |
|---|---|---|---|---|---|
| Fe 1 | 4618.7572 | 2.9488 | 1.490 | 0.714 | p |
| Cr 2 | 4618.8030 | 4.0735 | 0.910 | 0.529 | p |
| Fe 1 | 4619.2880 | 3.6025 | 1.700 | 0.787 | p |
| Cr 1 | 4619.5330 | 2.9872 | 1.400 | 0.623 | p |
| Cr 1 | 4621.9410 | 2.5446 | 1.210 | 0.505 | p |
| Cr 1 | 4621.9603 | 2.5446 | 1.200 | 0.765 | p |
| Cr 1 | 4622.4490 | 3.5505 | 1.330 | 0.638 | p |
| Ti 1 | 4623.0972 | 1.7393 | 1.100 | 0.791 | p |
| Fe 1 | 4625.0448 | 3.2410 | 1.370 | 0.816 | p |
| Cr 1 | 4626.1740 | 0.9684 | 2.010 | 0.901 | t |
| Ti 2 | 4629.2924 | 1.1801 | 0.780 | 0.659 | u |
| Fe 2 | 4629.3310 | 2.8067 | 1.310 | 0.722 | p |
| Ti 1 | 4629.3379 | 1.7335 | 1.050 | 0.716 | p |
| Co 1 | 4629.3617 | 3.0535 | 1.510 | 0.611 | p |
| Fe 1 | 4630.1196 | 2.2786 | 1.500 | 0.815 | t |
| Fe 1 | 4632.8197 | 3.6537 | 1.850 | 0.712 | p |
| Fe 1 | 4632.9112 | 1.6079 | 0.830 | 0.878 | p |
| Fe 1 | 4635.8461 | 2.8450 | 2.090 | 0.744 | t |
| Cr 1 | 4637.1730 | 2.5443 | 0.980 | 0.548 | p |
| Fe 1 | 4637.5029 | 3.2830 | 0.740 | 0.802 | p |
| Cr 1 | 4637.7600 | 2.5446 | 1.040 | 0.722 | p |
| Fe 1 | 4638.0095 | 3.6025 | 1.670 | 0.785 | p |
| Ti 1 | 4639.3628 | 1.7393 | 1.680 | 0.756 | u |
| Ti 1 | 4639.6608 | 1.7489 | 1.560 | 0.738 | p |
| Ti 1 | 4639.9388 | 1.7335 | 2.010 | 0.738 | p |
| Fe 1 | 4641.2080 | 5.3303 | 1.350 | 0.567 | u |
| Fe 1 | 4643.4633 | 3.6537 | 1.840 | 0.773 | t |
| Ti 1 | 4645.1884 | 1.7335 | 2.500 | 0.649 | p |
| Cr 1 | 4646.1620 | 1.0300 | 1.250 | 0.929 | t |
| Fe 1 | 4647.4339 | 2.9488 | 1.200 | 0.856 | t |
| Ni 1 | 4648.6520 | 3.4195 | 1.170 | 0.795 | p |
| Cr 1 | 4648.8680 | 2.5443 | 0.730 | 0.641 | p |
| Cr 1 | 4649.4320 | 3.5561 | 1.160 | 0.503 | p |
| Fe 1 | 4649.8163 | 3.2367 | 0.790 | 0.518 | p |
| Ti 1 | 4650.0097 | 1.7393 | 1.980 | 0.597 | p |
| Cr 1 | 4651.2840 | 0.9829 | 1.000 | 0.886 | t |
| Cr 1 | 4652.1570 | 1.0037 | 1.170 | 0.922 | t |
| Fe 1 | 4653.4886 | 0.9901 | 1.420 | 0.651 | p |
| Fe 1 | 4654.4976 | 1.5574 | 1.730 | 0.894 | t |
| Fe 1 | 4654.6050 | 3.6025 | 1.640 | 0.788 | p |
| Fe 1 | 4654.6311 | 3.2112 | 1.420 | 0.791 | p |
| Ti 1 | 4656.4680 | 0.0000 | 0.830 | 0.891 | t |
| Ti 2 | 4657.2006 | 1.2429 | 0.590 | 0.615 | p |
| Fe 1 | 4657.5848 | 2.8450 | 1.400 | 0.611 | p |
| Fe 1 | 4661.9702 | 2.9904 | 1.470 | 0.678 | p |
| Cr 1 | 4663.3120 | 3.1009 | 2.260 | 0.582 | p |

| Element | Wavelength (air – Å) | Excitation potential (eV) | Landé factor | Line Depth | Feature Type |
|---|---|---|---|---|---|
| Co 1 | 4663.4033 | 3.1330 | 1.470 | 0.552 | p |
| Cr 1 | 4663.8160 | 3.1107 | 1.750 | 0.636 | p |
| Cr 1 | 4664.7810 | 3.1251 | 1.630 | 0.654 | p |
| Fe 1 | 4665.2544 | 4.3865 | 1.310 | 0.540 | n |
| Cr 1 | 4666.1980 | 2.9674 | 0.810 | 0.512 | u |
| Cr 1 | 4666.4780 | 3.1442 | 1.570 | 0.639 | p |
| Fe 1 | 4666.6038 | 5.3448 | 0.890 | 0.569 | n |
| Ni 1 | 4666.9859 | 3.7963 | 0.710 | 0.507 | u |
| Fe 1 | 4667.4531 | 3.6025 | 1.480 | 0.825 | p |
| Ti 1 | 4667.5850 | 0.0211 | 1.000 | 0.901 | p |
| Ni 1 | 4667.7590 | 3.7057 | 1.120 | 0.590 | u |
| Fe 1 | 4668.0613 | 3.6864 | 1.680 | 0.727 | p |
| Fe 1 | 4668.1339 | 3.2657 | 0.970 | 0.824 | p |
| Na 1 | 4668.5595 | 2.1044 | 99.000 | 0.569 | p |
| Fe 1 | 4669.1492 | 3.6864 | 2.490 | 0.680 | p |
| Fe 1 | 4669.1711 | 3.6537 | 1.920 | 0.761 | p |
| Cr 1 | 4669.3170 | 3.1676 | 1.560 | 0.587 | p |
| Sc 2 | 4670.4070 | 1.3570 | 1.000 | 0.651 | p |
| Fe 1 | 4672.3211 | 5.3194 | 1.190 | 0.627 | p |
| Fe 1 | 4672.8300 | 1.6079 | 0.260 | 0.642 | p |
| Fe 1 | 4673.1635 | 3.6537 | 1.820 | 0.796 | p |
| Fe 1 | 4673.1636 | 3.6537 | 99.000 | 0.781 | p |
| Fe 1 | 4673.2700 | 3.6537 | 99.000 | 0.756 | p |
| Fe 1 | 4673.2703 | 3.6537 | 1.420 | 0.685 | p |
| Fe 1 | 4674.0810 | 5.3204 | 1.250 | 0.585 | p |
| Fe 1 | 4675.0934 | 4.1034 | 1.500 | 0.638 | p |
| Ti 1 | 4675.1167 | 1.0666 | 1.490 | 0.645 | p |
| Fe 1 | 4678.8455 | 3.6025 | 1.300 | 0.815 | p |
| Fe 1 | 4679.2200 | 3.3683 | 1.730 | 0.655 | p |
| Fe 1 | 4679.2247 | 3.2515 | 0.860 | 0.614 | p |
| Fe 1 | 4680.2945 | 1.6079 | 1.820 | 0.760 | p |
| Fe 1 | 4680.4672 | 2.8581 | 1.320 | 0.658 | p |
| Ti 1 | 4681.9090 | 0.0480 | 1.130 | 0.907 | p |
| Fe 1 | 4683.5597 | 2.8316 | 1.520 | 0.747 | p |
| Ca 1 | 4685.2680 | 2.9325 | 1.000 | 0.670 | p |
| Ni 1 | 4686.2131 | 3.5972 | 0.660 | 0.685 | t |
| Fe 1 | 4687.3022 | 0.9582 | 1.450 | 0.710 | p |
| Fe 1 | 4687.3860 | 2.8316 | 1.200 | 0.656 | p |
| Zr 1 | 4687.8000 | 0.7301 | 1.200 | 0.530 | p |
| Cr 1 | 4689.3560 | 3.1251 | 0.990 | 0.625 | p |
| Fe 1 | 4690.1375 | 3.6864 | 2.140 | 0.681 | p |
| Ti 1 | 4691.3325 | 1.0666 | 1.190 | 0.764 | p |
| Fe 1 | 4691.4114 | 2.9904 | 1.050 | 0.827 | p |
| Ti 1 | 4693.6647 | 0.0211 | 0.920 | 0.544 | p |
| Cr 1 | 4693.9380 | 2.9826 | 1.040 | 0.536 | p |
| Cr 1 | 4697.0500 | 2.7079 | 1.270 | 0.557 | p |

| Element | Wavelength (air – Å) | Excitation potential (eV) | Landé factor | Line Depth | Feature Type |
|---|---|---|---|---|---|
| Cr 1 | 4698.4600 | 3.1442 | 1.120 | 0.689 | p |
| Cr 1 | 4698.6060 | 2.7088 | 1.890 | 0.516 | p |
| Ti 1 | 4698.7609 | 1.0529 | 0.990 | 0.728 | p |
| Fe 1 | 4700.1576 | 4.3201 | 1.190 | 0.652 | p |
| Fe 1 | 4700.1903 | 3.6946 | 1.160 | 0.671 | u |
| Fe 1 | 4701.0447 | 3.6864 | 1.520 | 0.629 | p |
| Ni 1 | 4701.3517 | 3.4800 | 1.200 | 0.549 | p |
| Ni 1 | 4701.5297 | 4.0882 | 1.250 | 0.594 | p |
| Mg 1 | 4702.9909 | 4.3458 | 99.000 | 0.866 | p |
| Ni 1 | 4703.8068 | 3.6576 | 1.070 | 0.682 | p |
| Fe 1 | 4704.9476 | 3.6864 | 2.490 | 0.694 | p |
| Fe 1 | 4705.4567 | 3.5465 | 0.500 | 0.526 | p |
| Fe 1 | 4707.2738 | 3.2410 | 1.080 | 0.839 | p |
| Fe 1 | 4707.4875 | 2.8450 | 1.560 | 0.743 | p |
| Cr 1 | 4708.0130 | 3.1676 | 1.270 | 0.716 | p |
| Ti 2 | 4708.6627 | 1.2369 | 0.530 | 0.590 | p |
| Fe 1 | 4708.9682 | 3.6398 | 0.880 | 0.591 | p |
| Fe 1 | 4709.0876 | 3.6537 | 1.720 | 0.779 | p |
| Mn 1 | 4709.7100 | 2.8884 | 1.330 | 0.745 | p |
| Ti 1 | 4710.1834 | 2.1747 | 1.330 | 0.627 | p |
| Ti 1 | 4710.1892 | 1.0460 | 0.510 | 0.720 | p |
| Fe 1 | 4710.2833 | 3.0176 | 0.760 | 0.810 | p |
| Ni 1 | 4712.0561 | 3.6576 | 0.940 | 0.511 | u |
| Ni 1 | 4714.4173 | 3.3799 | 1.120 | 0.833 | p |
| Ti 1 | 4715.3016 | 0.0480 | 1.150 | 0.542 | p |
| Ni 1 | 4715.7617 | 3.5432 | 1.090 | 0.736 | p |
| Cr 1 | 4718.4190 | 3.1952 | 1.330 | 0.737 | p |
| Fe 1 | 4721.0003 | 2.9904 | 1.520 | 0.580 | p |
| Zn 1 | 4722.1530 | 4.0297 | 1.750 | 0.621 | u |
| Ti 1 | 4722.6059 | 1.0529 | 1.010 | 0.569 | p |
| Cr 1 | 4723.0980 | 3.0790 | 0.980 | 0.547 | p |
| Ti 1 | 4723.1631 | 1.0666 | 1.330 | 0.557 | p |
| Cr 1 | 4724.4120 | 3.0869 | 1.180 | 0.548 | p |
| Cr 1 | 4727.1490 | 3.0004 | 1.170 | 0.584 | p |
| Fe 1 | 4727.3946 | 3.6864 | 2.070 | 0.756 | u |
| Mn 1 | 4727.4600 | 2.9197 | 1.200 | 0.744 | u |
| Co 1 | 4727.9360 | 0.4318 | 1.450 | 0.509 | p |
| Fe 1 | 4728.5456 | 3.6537 | 1.540 | 0.760 | t |
| Fe 1 | 4729.0192 | 4.0758 | 1.540 | 0.562 | p |
| Fe 1 | 4729.6766 | 3.3965 | 1.180 | 0.527 | u |
| Mg 1 | 4730.0286 | 4.3458 | 99.000 | 0.592 | p |
| Cr 1 | 4730.7100 | 3.0790 | 0.870 | 0.685 | p |
| Fe 2 | 4731.4476 | 2.8910 | 0.660 | 0.529 | u |
| Fe 1 | 4731.4901 | 3.6864 | 1.460 | 0.717 | p |
| Ni 1 | 4731.7978 | 3.8327 | 0.730 | 0.536 | u |
| Ni 1 | 4732.4566 | 4.1054 | 1.390 | 0.533 | u |

| Element | Wavelength (air – Å) | Excitation potential (eV) | Landé factor | Line Depth | Feature Type |
|---|---|---|---|---|---|
| Fe 1 | 4733.5911 | 1.4849 | 1.380 | 0.879 | t |
| Fe 1 | 4735.8428 | 4.0758 | 1.170 | 0.645 | p |
| Fe 1 | 4736.7726 | 3.2112 | 1.260 | 0.870 | t |
| Cr 1 | 4737.3480 | 3.0869 | 1.130 | 0.700 | p |
| Fe 1 | 4737.6346 | 3.2671 | 1.050 | 0.652 | p |
| Mn 1 | 4739.0900 | 2.9408 | 0.800 | 0.711 | p |
| Fe 1 | 4740.3398 | 3.0176 | 1.490 | 0.625 | p |
| Fe 1 | 4741.0693 | 3.3320 | 1.620 | 0.538 | p |
| Fe 1 | 4741.5292 | 2.8316 | 1.460 | 0.819 | p |
| Ti 1 | 4742.7892 | 2.2363 | 0.840 | 0.675 | p |
| Fe 1 | 4744.3838 | 5.3884 | 1.390 | 0.561 | p |
| Fe 1 | 4745.7996 | 3.6537 | 1.400 | 0.745 | p |
| Co 1 | 4749.6730 | 3.0535 | 1.260 | 0.563 | u |
| Ni 1 | 4752.4198 | 3.6576 | 1.480 | 0.638 | p |
| Mn 1 | 4754.0400 | 2.2816 | 1.640 | 0.882 | t |
| Ni 1 | 4754.7624 | 3.6353 | 1.220 | 0.565 | p |
| Cr 1 | 4756.1117 | 3.1044 | 1.100 | 0.727 | p |
| Ni 1 | 4756.5153 | 3.4800 | 1.250 | 0.751 | p |
| Fe 1 | 4757.5780 | 3.2740 | 1.340 | 0.693 | p |
| Ti 1 | 4758.1178 | 2.2492 | 1.020 | 0.731 | p |
| Ti 1 | 4759.2697 | 2.2556 | 1.180 | 0.743 | p |
| Mn 1 | 4761.5100 | 2.9532 | 0.500 | 0.760 | p |
| Mn 1 | 4762.3700 | 2.8884 | 1.120 | 0.843 | p |
| Ni 1 | 4762.6267 | 1.9354 | 1.180 | 0.674 | p |
| Ti 2 | 4763.8832 | 1.2214 | 0.350 | 0.572 | u |
| Ni 1 | 4763.9441 | 3.6552 | 1.280 | 0.627 | p |
| Cr 1 | 4764.2930 | 3.5505 | 1.070 | 0.513 | p |
| Fe 1 | 4765.2448 | 5.3711 | 1.200 | 0.577 | n |
| Fe 1 | 4765.4799 | 1.6079 | 1.080 | 0.702 | p |
| Mn 1 | 4765.8500 | 2.9408 | 0.900 | 0.787 | p |
| Mn 1 | 4766.4200 | 2.9197 | 1.080 | 0.815 | t |
| Fe 1 | 4766.8654 | 3.4170 | 1.210 | 0.576 | u |
| Fe 1 | 4768.3201 | 3.6864 | 1.180 | 0.754 | p |
| Fe 1 | 4768.3960 | 2.9398 | 1.620 | 0.726 | p |
| Fe 1 | 4771.6960 | 2.1979 | 1.490 | 0.714 | p |
| Fe 1 | 4772.8030 | 1.5574 | 1.290 | 0.876 | p |
| Fe 1 | 4772.8303 | 3.0173 | 1.340 | 0.721 | p |
| Fe 1 | 4779.4389 | 3.4149 | 0.820 | 0.660 | p |
| Ti 2 | 4779.9850 | 2.0477 | 1.380 | 0.631 | p |
| Fe 1 | 4781.7419 | 3.5732 | 1.140 | 0.554 | p |
| Mn 1 | 4783.4300 | 2.2976 | 1.970 | 0.889 | p |
| Ni 1 | 4786.2812 | 1.6764 | 1.460 | 0.590 | p |
| Ni 1 | 4786.5354 | 3.4195 | 1.340 | 0.770 | p |
| Fe 1 | 4786.8067 | 3.0173 | 1.220 | 0.804 | p |
| Fe 1 | 4787.8264 | 2.9980 | 1.710 | 0.655 | p |
| Fe 1 | 4788.7564 | 3.2367 | 1.180 | 0.745 | p |

| Element | Wavelength (air – Å) | Excitation potential (eV) | Landé factor | Line Depth | Feature Type |
|---|---|---|---|---|---|
| Cr 1 | 4789.3350 | 2.5441 | 1.150 | 0.765 | p |
| Fe 1 | 4789.6500 | 3.5466 | 99.000 | 0.805 | p |
| Fe 1 | 4789.6507 | 3.5465 | 0.980 | 0.799 | p |
| Fe 1 | 4791.2462 | 3.2740 | 0.750 | 0.587 | u |
| Ti 1 | 4792.4823 | 2.3341 | 0.980 | 0.505 | p |
| Cr 1 | 4792.5094 | 3.1128 | 1.080 | 0.632 | p |
| Co 1 | 4792.8543 | 3.2524 | 0.960 | 0.562 | p |
| Fe 1 | 4798.2646 | 4.1864 | 1.170 | 0.643 | p |
| Ti 2 | 4798.5313 | 1.0800 | 0.410 | 0.529 | u |
| Fe 1 | 4798.7312 | 1.6079 | 1.080 | 0.626 | p |
| Fe 1 | 4799.4058 | 3.6398 | 1.310 | 0.507 | p |
| Ti 1 | 4799.7946 | 2.2674 | 0.950 | 0.588 | p |
| Fe 1 | 4800.1275 | 3.0385 | 1.920 | 0.573 | p |
| Fe 1 | 4800.6485 | 4.1426 | 1.360 | 0.682 | p |
| Cr 1 | 4801.0247 | 3.1216 | 1.340 | 0.679 | p |
| Fe 1 | 4802.8744 | 3.6946 | 0.980 | 0.561 | t |
| Fe 1 | 4802.8797 | 3.6416 | 1.180 | 0.703 | t |
| Ti 2 | 4805.0850 | 2.0613 | 1.140 | 0.695 | u |
| Ti 1 | 4805.4144 | 2.3447 | 1.080 | 0.588 | p |
| Ni 1 | 4806.9872 | 3.6785 | 1.360 | 0.640 | p |
| Fe 1 | 4807.7080 | 3.3683 | 1.320 | 0.625 | p |
| Zn 1 | 4810.5280 | 4.0779 | 1.260 | 0.643 | u |
| Cr 1 | 4810.7300 | 3.0790 | 0.910 | 0.544 | u |
| Co 1 | 4813.4764 | 3.2158 | 1.080 | 0.613 | p |
| Fe 1 | 4817.7781 | 2.2227 | 0.480 | 0.625 | p |
| Ti 1 | 4820.4094 | 1.5025 | 0.960 | 0.731 | p |
| Mn 1 | 4823.5200 | 2.3192 | 1.390 | 0.891 | p |
| Cr 2 | 4824.1270 | 3.8707 | 1.340 | 0.534 | u |
| Fe 1 | 4824.1644 | 3.6352 | 0.950 | 0.502 | p |
| V 1 | 4827.4529 | 0.0401 | 1.340 | 0.638 | p |
| Ni 1 | 4829.0231 | 3.5421 | 1.160 | 0.724 | p |
| Cr 1 | 4829.3720 | 2.5446 | 1.030 | 0.733 | u |
| Ni 1 | 4831.1757 | 3.6060 | 1.380 | 0.713 | p |
| V 1 | 4831.6462 | 0.0170 | 1.190 | 0.683 | p |
| V 1 | 4832.4237 | 0.0000 | 0.800 | 0.645 | p |
| Ni 1 | 4832.6911 | 3.7963 | 1.420 | 0.505 | u |
| Fe 1 | 4832.7273 | 3.6398 | 1.040 | 0.658 | p |
| Fe 1 | 4834.5061 | 2.4242 | 1.500 | 0.581 | p |
| Fe 1 | 4835.8671 | 4.1034 | 1.360 | 0.577 | p |
| Cr 1 | 4836.8520 | 3.1044 | 1.240 | 0.548 | p |
| Fe 1 | 4838.5112 | 3.4170 | 1.500 | 0.668 | p |
| Ni 1 | 4838.6431 | 4.1646 | 1.130 | 0.587 | p |
| Fe 1 | 4839.5442 | 3.2671 | 1.050 | 0.725 | p |
| Co 1 | 4840.2521 | 3.1701 | 1.150 | 0.649 | u |
| Fe 1 | 4840.3210 | 4.1544 | 1.320 | 0.592 | p |
| Ti 1 | 4840.8737 | 0.8995 | 1.000 | 0.842 | p |

| Element | Wavelength (air – Å) | Excitation potential (eV) | Landé factor | Line Depth | Feature Type |
|---|---|---|---|---|---|
| Fe 1 | 4842.7874 | 4.1034 | 0.750 | 0.557 | u |
| Fe 1 | 4843.1428 | 3.3965 | 1.510 | 0.694 | p |
| Ni 1 | 4843.1582 | 1.6764 | 1.170 | 0.534 | p |
| Fe 1 | 4844.0132 | 3.5465 | 1.300 | 0.605 | p |
| Fe 1 | 4845.6462 | 3.6352 | 0.500 | 0.562 | p |
| Fe 1 | 4848.8821 | 2.2786 | 2.010 | 0.705 | p |
| V 1 | 4851.4901 | 0.0000 | 0.510 | 0.754 | p |
| Ni 1 | 4852.5542 | 3.5421 | 1.730 | 0.559 | p |
| Y 2 | 4854.8611 | 0.9923 | 0.700 | 0.613 | p |
| Ni 1 | 4855.4109 | 3.5421 | 1.460 | 0.766 | p |
| Fe 1 | 4855.6727 | 3.3683 | 1.530 | 0.711 | p |
| Ti 1 | 4856.0103 | 2.2556 | 1.090 | 0.722 | p |
| Ni 1 | 4857.3924 | 3.7398 | 1.380 | 0.629 | p |
| Fe 1 | 4859.7414 | 2.8755 | 0.750 | 0.896 | p |
| Fe 1 | 4860.9774 | 3.3965 | 1.350 | 0.531 | p |
| H 1 | 4861.3230 | 10.1988 | 99.000 | 0.519 | u |
| Cr 1 | 4861.8410 | 2.5446 | 0.960 | 0.693 | p |
| Fe 1 | 4862.5980 | 4.1544 | 0.500 | 0.557 | p |
| Fe 1 | 4863.6434 | 3.4302 | -0.000 | 0.716 | p |
| V 1 | 4864.7298 | 0.0170 | 0.890 | 0.785 | p |
| Ni 1 | 4866.2711 | 3.5388 | 1.470 | 0.737 | p |
| Co 1 | 4867.8695 | 3.1168 | 1.190 | 0.679 | p |
| Ti 1 | 4868.2588 | 2.2363 | 0.830 | 0.710 | p |
| Ti 1 | 4870.1246 | 2.2492 | 1.020 | 0.707 | p |
| Cr 1 | 4870.7970 | 3.0790 | 0.750 | 0.703 | p |
| Ni 1 | 4870.8309 | 3.7434 | 0.450 | 0.635 | p |
| Fe 1 | 4871.3177 | 2.8654 | 1.020 | 0.917 | t |
| Fe 1 | 4871.9278 | 3.2515 | 1.370 | 0.664 | p |
| Fe 1 | 4872.1372 | 2.8820 | 2.280 | 0.906 | t |
| Ni 1 | 4873.4422 | 3.6988 | 1.650 | 0.680 | p |
| V 1 | 4875.4859 | 0.0401 | 1.100 | 0.809 | p |
| Fe 1 | 4875.8768 | 3.3320 | 1.530 | 0.671 | p |
| Ca 1 | 4878.1260 | 2.7090 | 0.990 | 0.794 | p |
| Fe 1 | 4878.2106 | 2.8852 | 3.000 | 0.886 | p |
| V 1 | 4881.5569 | 0.0686 | 1.130 | 0.824 | p |
| Fe 1 | 4881.7173 | 3.3014 | 0.850 | 0.720 | p |
| Fe 1 | 4882.1429 | 3.4170 | 1.000 | 0.720 | p |
| Y 2 | 4883.6821 | 1.0840 | 1.140 | 0.704 | p |
| Ti 1 | 4885.0794 | 1.8871 | 1.070 | 0.776 | p |
| Fe 1 | 4885.4301 | 3.8816 | 0.890 | 0.725 | p |
| Fe 1 | 4886.3310 | 4.1544 | 1.300 | 0.732 | p |
| Ni 1 | 4886.9837 | 3.6353 | 1.160 | 0.502 | u |
| Cr 1 | 4887.0120 | 3.0869 | 0.920 | 0.715 | p |
| Fe 1 | 4887.1931 | 4.1909 | 1.130 | 0.693 | p |
| Zr 1 | 4887.7500 | 0.7301 | 1.850 | 0.692 | u |
| Fe 1 | 4888.6361 | 4.1034 | 1.380 | 0.734 | p |

| Element | Wavelength (air – Å) | Excitation potential (eV) | Landé factor | Line Depth | Feature Type |
|---|---|---|---|---|---|
| Fe 1 | 4889.0007 | 2.1979 | 0.830 | 0.824 | p |
| Fe 1 | 4889.1018 | 3.8835 | 1.410 | 0.693 | p |
| Fe 1 | 4890.7548 | 2.8755 | 1.760 | 0.914 | t |
| Fe 1 | 4891.1463 | 4.1426 | 1.360 | 0.581 | n |
| Fe 1 | 4891.4919 | 2.8512 | 1.100 | 0.926 | t |
| Fe 1 | 4892.8586 | 4.2176 | 1.480 | 0.594 | u |
| Ti 1 | 4899.9088 | 1.8792 | 1.000 | 0.761 | p |
| Y 2 | 4900.1189 | 1.0325 | 1.010 | 0.680 | p |
| Fe 1 | 4902.2322 | 4.5585 | 1.630 | 0.541 | u |
| Cr 1 | 4903.2340 | 2.5438 | 0.550 | 0.598 | p |
| Fe 1 | 4903.3096 | 2.8820 | 2.240 | 0.881 | p |
| Ni 1 | 4904.4118 | 3.5421 | 1.270 | 0.739 | p |
| Fe 1 | 4907.3200 | 4.1426 | 1.080 | 0.526 | n |
| Fe 1 | 4907.7315 | 3.4302 | 1.490 | 0.679 | p |
| Fe 1 | 4909.3831 | 3.9286 | 1.370 | 0.667 | p |
| Fe 1 | 4910.0163 | 3.3965 | 1.240 | 0.755 | p |
| Fe 1 | 4910.3248 | 4.1909 | 0.790 | 0.747 | p |
| Fe 1 | 4910.5643 | 4.2176 | 1.120 | 0.746 | p |
| Fe 1 | 4911.7786 | 3.9286 | 1.350 | 0.539 | p |
| Ni 1 | 4912.0180 | 3.7681 | 0.100 | 0.557 | p |
| Ti 1 | 4913.6134 | 1.8732 | 0.870 | 0.746 | p |
| Ni 1 | 4913.9730 | 3.7434 | 1.540 | 0.612 | p |
| Fe 1 | 4917.2294 | 4.1909 | 1.470 | 0.627 | p |
| Fe 1 | 4918.0120 | 4.2305 | 1.470 | 0.566 | p |
| Ni 1 | 4918.3640 | 3.8410 | 1.010 | 0.670 | p |
| Fe 1 | 4918.9538 | 4.1544 | 1.560 | 0.732 | u |
| Fe 1 | 4918.9935 | 2.8654 | 1.630 | 0.915 | t |
| Ti 1 | 4919.8607 | 2.1603 | 0.990 | 0.585 | p |
| Fe 1 | 4920.5021 | 2.8325 | 1.180 | 0.931 | t |
| Ti 1 | 4921.7638 | 2.1747 | 1.090 | 0.631 | u |
| Cr 1 | 4922.2650 | 3.1044 | 1.100 | 0.753 | p |
| Fe 2 | 4923.9212 | 2.8910 | 1.690 | 0.808 | t |
| Fe 1 | 4924.7692 | 2.2786 | 1.330 | 0.834 | t |
| Fe 1 | 4925.2838 | 4.1034 | 1.710 | 0.537 | p |
| Ni 1 | 4925.5634 | 3.6552 | 1.370 | 0.599 | p |
| Fe 1 | 4926.8162 | 3.6343 | 0.860 | 0.518 | n |
| Fe 1 | 4927.4177 | 3.5732 | 0.640 | 0.579 | p |
| Fe 1 | 4927.8634 | 4.2176 | 1.490 | 0.698 | p |
| Ti 1 | 4928.3361 | 2.1535 | 0.730 | 0.640 | p |
| Fe 1 | 4930.3148 | 3.9597 | 0.980 | 0.677 | p |
| Fe 1 | 4933.2923 | 3.3009 | 1.220 | 0.636 | u |
| Fe 1 | 4933.3407 | 4.2305 | 0.760 | 0.686 | p |
| Fe 1 | 4934.0047 | 4.1544 | 0.820 | 0.735 | u |
| Ba 2 | 4934.0744 | 0.0000 | 99.000 | 0.798 | p |
| Ba 2 | 4934.0751 | 0.0000 | 99.000 | 0.832 | p |
| Ba 2 | 4934.0755 | 0.0000 | 99.000 | 0.704 | p |

| Element | Wavelength (air – Å) | Excitation potential (eV) | Landé factor | Line Depth | Feature Type |
|---|---|---|---|---|---|
| Ba 2 | 4934.0758 | 0.0000 | 99.000 | 0.811 | p |
| Ba 2 | 4934.0773 | 0.0000 | 99.000 | 0.911 | p |
| Fe 1 | 4934.0834 | 3.3014 | 1.080 | 0.548 | p |
| Ni 1 | 4935.8305 | 3.9410 | 0.850 | 0.622 | p |
| Cr 1 | 4936.3350 | 3.1128 | 0.600 | 0.641 | p |
| Ni 1 | 4937.3478 | 3.6060 | 1.260 | 0.691 | p |
| Fe 1 | 4938.1733 | 3.9433 | 0.600 | 0.715 | p |
| Fe 1 | 4938.8137 | 2.8755 | 2.010 | 0.867 | p |
| Fe 1 | 4939.2354 | 4.2176 | 0.400 | 0.611 | p |
| Fe 1 | 4939.2407 | 4.1544 | 1.380 | 0.698 | p |
| Fe 1 | 4939.6861 | 0.8590 | 1.490 | 0.907 | t |
| Fe 1 | 4942.4584 | 4.2204 | 0.640 | 0.552 | p |
| Cr 1 | 4942.4950 | 0.9414 | 1.850 | 0.765 | p |
| Ni 1 | 4945.4445 | 3.7963 | 0.750 | 0.537 | p |
| Fe 1 | 4945.6356 | 4.2089 | 0.790 | 0.523 | p |
| Fe 1 | 4946.3871 | 3.3683 | 1.340 | 0.788 | t |
| Fe 1 | 4950.1052 | 3.4170 | 1.470 | 0.708 | t |
| Ni 1 | 4953.2081 | 3.7398 | 0.970 | 0.621 | u |
| Cr 1 | 4954.8060 | 3.1216 | 0.750 | 0.655 | p |
| Fe 1 | 4957.2978 | 2.8512 | 1.570 | 0.911 | t |
| Fe 1 | 4957.5960 | 2.8083 | 1.280 | 0.935 | t |
| Fe 1 | 4957.6818 | 4.1909 | 0.720 | 0.671 | u |
| Fe 1 | 4962.5711 | 4.1777 | 0.750 | 0.625 | p |
| Cr 1 | 4964.9270 | 0.9414 | 2.170 | 0.717 | p |
| Fe 1 | 4966.0881 | 3.3320 | 1.410 | 0.828 | t |
| Fe 1 | 4967.8966 | 4.1909 | 1.880 | 0.737 | p |
| Fe 1 | 4968.3916 | 4.2204 | 1.650 | 0.536 | p |
| Fe 1 | 4968.6900 | 3.6398 | 99.000 | 0.633 | p |
| Fe 1 | 4968.6978 | 3.6398 | 0.850 | 0.633 | p |
| Fe 1 | 4969.9168 | 4.2176 | 1.520 | 0.701 | p |
| Fe 1 | 4970.4958 | 3.6352 | 0.760 | 0.643 | p |
| Ni 1 | 4971.3445 | 3.6576 | 1.430 | 0.646 | p |
| Ni 1 | 4971.5905 | 3.6785 | 1.220 | 0.594 | n |
| Fe 1 | 4973.1014 | 3.9597 | 0.660 | 0.713 | p |
| Ti 1 | 4975.3431 | 2.5057 | 1.090 | 0.531 | p |
| Ni 1 | 4976.3255 | 1.6764 | 1.060 | 0.621 | p |
| Ti 1 | 4978.1875 | 1.9685 | 0.590 | 0.594 | p |
| Na 1 | 4978.5414 | 2.1023 | 99.000 | 0.567 | p |
| Fe 1 | 4978.6027 | 3.9841 | 0.300 | 0.719 | p |
| Fe 1 | 4978.6912 | 4.0758 | 1.240 | 0.681 | u |
| Ni 1 | 4980.1727 | 3.6060 | 1.020 | 0.753 | p |
| Fe 1 | 4980.2823 | 4.1777 | 1.800 | 0.519 | p |
| Ti 1 | 4981.7305 | 0.8484 | 1.160 | 0.916 | t |
| Fe 1 | 4982.4989 | 4.1034 | 1.350 | 0.826 | p |
| Na 1 | 4982.8134 | 2.1044 | 99.000 | 0.630 | p |
| Fe 1 | 4983.2499 | 4.1544 | 1.580 | 0.787 | t |

| Element | Wavelength (air – Å) | Excitation potential (eV) | Landé factor | Line Depth | Feature Type |
|---|---|---|---|---|---|
| Fe 1 | 4983.8521 | 4.1034 | 1.470 | 0.809 | t |
| Ni 1 | 4984.1163 | 3.7963 | 0.800 | 0.753 | t |
| Fe 1 | 4985.2526 | 3.9286 | 1.150 | 0.769 | t |
| Fe 1 | 4985.5465 | 2.8654 | 1.870 | 0.843 | t |
| Fe 1 | 4986.2221 | 4.2176 | 0.770 | 0.554 | p |
| Fe 1 | 4988.9493 | 4.1544 | 0.900 | 0.736 | t |
| Fe 1 | 4988.9501 | 4.1544 | 99.000 | 0.684 | t |
| Ti 1 | 4989.1300 | 1.9807 | 0.830 | 0.633 | p |
| Ti 1 | 4991.0660 | 0.8360 | 1.050 | 0.911 | p |
| Fe 1 | 4991.2675 | 4.1909 | 1.460 | 0.750 | p |
| Fe 1 | 4991.2683 | 4.1909 | 99.000 | 0.710 | p |
| Fe 1 | 4993.6805 | 4.2089 | 99.000 | 0.532 | u |
| Fe 1 | 4993.7505 | 4.1864 | 1.500 | 0.510 | n |
| Fe 1 | 4994.1290 | 0.9146 | 1.500 | 0.914 | t |
| Ni 1 | 4996.8444 | 3.6353 | 1.170 | 0.539 | p |
| Ti 1 | 4997.0967 | 0.0000 | 0.910 | 0.758 | p |
| Ni 1 | 4998.2242 | 3.6060 | 1.310 | 0.625 | u |
| Ti 1 | 4999.5030 | 0.8259 | 1.000 | 0.905 | p |
| Fe 1 | 5000.2109 | 4.6382 | 1.090 | 0.510 | u |
| Ni 1 | 5000.3427 | 3.6353 | 1.040 | 0.671 | t |
| Ti 1 | 5000.9900 | 1.9969 | 1.020 | 0.662 | p |
| Fe 1 | 5001.8630 | 3.8816 | 1.110 | 0.839 | t |
| Fe 1 | 5002.5829 | 4.1864 | 0.700 | 0.629 | u |
| Fe 1 | 5002.7919 | 3.3965 | 1.450 | 0.721 | p |
| Ni 1 | 5003.7407 | 1.6764 | 1.250 | 0.595 | p |
| Fe 1 | 5004.0432 | 4.2089 | 1.880 | 0.553 | u |
| Fe 1 | 5005.7120 | 3.8835 | 1.330 | 0.841 | p |
| Fe 1 | 5006.1183 | 2.8325 | 1.540 | 0.899 | p |
| Ti 1 | 5007.2093 | 0.8181 | 0.830 | 0.897 | p |
| Fe 1 | 5007.2740 | 4.1034 | 1.120 | 0.783 | u |
| Ti 1 | 5009.6447 | 0.0211 | 1.210 | 0.721 | p |
| Ni 1 | 5010.9381 | 3.6353 | 1.200 | 0.571 | p |
| Fe 1 | 5012.0676 | 0.8590 | 1.400 | 0.932 | p |
| Fe 1 | 5012.1566 | 4.1909 | 1.020 | 0.658 | u |
| Fe 1 | 5012.4405 | 4.1426 | 1.060 | 0.639 | u |
| Ni 1 | 5012.4426 | 3.6988 | 1.270 | 0.636 | u |
| Ti 1 | 5013.2800 | 2.0169 | 1.070 | 0.686 | p |
| Cr 1 | 5013.3130 | 2.7079 | 1.350 | 0.622 | p |
| Ti 1 | 5014.1861 | 0.0000 | 0.750 | 0.876 | p |
| Ti 1 | 5014.2762 | 0.8129 | 0.510 | 0.888 | p |
| Fe 1 | 5014.9422 | 3.9433 | 1.050 | 0.796 | t |
| Ti 1 | 5016.1609 | 0.8484 | 1.330 | 0.831 | t |
| Fe 1 | 5016.8808 | 4.2204 | 1.700 | 0.625 | p |
| Ni 1 | 5017.5760 | 3.5388 | 1.390 | 0.748 | t |
| Ni 1 | 5018.2815 | 3.8327 | 0.850 | 0.654 | u |
| Fe 2 | 5018.4356 | 2.8910 | 1.930 | 0.812 | t |

| Element | Wavelength (air – Å) | Excitation potential (eV) | Landé factor | Line Depth | Feature Type |
|---|---|---|---|---|---|
| Ti 1 | 5020.0263 | 0.8360 | 1.250 | 0.849 | t |
| Fe 1 | 5021.5894 | 4.2562 | 0.380 | 0.651 | u |
| Fe 1 | 5021.6812 | 4.2176 | 1.110 | 0.534 | u |
| Cr 1 | 5021.9010 | 0.9414 | 1.510 | 0.608 | u |
| Fe 1 | 5021.9398 | 3.2740 | 2.370 | 0.646 | u |
| Fe 1 | 5022.2352 | 3.9841 | 0.620 | 0.761 | p |
| Fe 1 | 5022.7891 | 2.9904 | 1.250 | 0.701 | u |
| Ti 1 | 5022.8679 | 0.8259 | 1.080 | 0.850 | t |
| Ti 1 | 5024.8444 | 0.8181 | 0.670 | 0.829 | p |
| Ti 1 | 5025.5700 | 2.0406 | 1.100 | 0.704 | p |
| Fe 1 | 5027.1222 | 4.1544 | 1.420 | 0.763 | u |
| Fe 1 | 5027.2254 | 3.6398 | 1.170 | 0.601 | u |
| Fe 1 | 5027.7567 | 4.2089 | 99.000 | 0.594 | u |
| Fe 1 | 5028.1258 | 3.5732 | 0.870 | 0.752 | p |
| Fe 1 | 5029.6175 | 3.4149 | 1.300 | 0.626 | t |
| Sc 2 | 5031.0210 | 1.3570 | 1.000 | 0.661 | p |
| Fe 1 | 5034.4594 | 4.2833 | 2.140 | 0.630 | u |
| Ni 1 | 5035.3622 | 3.6353 | 1.000 | 0.771 | p |
| Ti 1 | 5035.9030 | 1.4601 | 1.050 | 0.816 | p |
| Ni 1 | 5035.9719 | 3.6552 | 1.260 | 0.711 | u |
| Fe 1 | 5036.2682 | 4.1777 | 1.740 | 0.631 | u |
| Ti 1 | 5036.4639 | 1.4432 | 1.010 | 0.808 | p |
| Ti 1 | 5038.3979 | 1.4298 | 0.830 | 0.794 | p |
| Ni 1 | 5038.5908 | 3.8327 | 1.510 | 0.619 | u |
| Fe 1 | 5039.2511 | 3.3683 | 1.550 | 0.724 | t |
| Ti 1 | 5039.9574 | 0.0211 | 1.010 | 0.885 | t |
| Ti 1 | 5040.6136 | 0.8259 | 2.160 | 0.573 | p |
| Fe 1 | 5040.8517 | 4.2562 | 1.190 | 0.702 | p |
| Fe 1 | 5040.9061 | 4.2833 | 0.690 | 0.721 | p |
| Fe 1 | 5041.0713 | 0.9582 | 1.500 | 0.908 | p |
| Ca 1 | 5041.6180 | 2.7090 | 1.010 | 0.740 | p |
| Fe 1 | 5041.7554 | 1.4849 | 1.510 | 0.914 | p |
| Fe 1 | 5041.8485 | 4.2833 | 1.120 | 0.657 | n |
| Ni 1 | 5042.1865 | 3.6576 | 0.790 | 0.633 | p |
| Ti 1 | 5043.5838 | 0.8360 | 2.010 | 0.600 | p |
| Fe 1 | 5044.2106 | 2.8512 | 1.770 | 0.751 | p |
| Ni 1 | 5048.0572 | 3.8327 | 0.500 | 0.548 | n |
| Fe 1 | 5048.4355 | 3.9597 | 1.430 | 0.693 | p |
| Cr 1 | 5048.7480 | 0.9829 | 1.920 | 0.622 | p |
| Ni 1 | 5048.8470 | 3.8474 | 1.070 | 0.627 | p |
| Fe 1 | 5049.8192 | 2.2786 | 1.140 | 0.900 | t |
| Ni 1 | 5051.5079 | 3.6552 | 1.240 | 0.593 | u |
| Fe 1 | 5051.6342 | 0.9146 | 1.350 | 0.923 | t |
| Cr 1 | 5051.8970 | 0.9414 | 2.000 | 0.703 | p |
| Ti 1 | 5052.8685 | 2.1747 | 1.200 | 0.506 | u |
| Fe 1 | 5054.6423 | 3.6398 | 1.260 | 0.589 | p |

| Element | Wavelength (air – Å) | Excitation potential (eV) | Landé factor | Line Depth | Feature Type |
|---|---|---|---|---|---|
| Fe 1 | 5060.0354 | 4.3013 | 0.730 | 0.589 | t |
| Fe 1 | 5060.0782 | 0.0000 | 1.130 | 0.798 | t |
| Ti 1 | 5064.6526 | 0.0480 | 1.120 | 0.891 | p |
| Fe 1 | 5064.9519 | 4.2562 | 1.480 | 0.574 | u |
| Fe 1 | 5065.0174 | 4.2562 | 0.870 | 0.780 | u |
| Fe 1 | 5065.1924 | 3.6416 | 0.960 | 0.676 | p |
| Ti 1 | 5065.9851 | 1.4432 | 0.920 | 0.564 | p |
| Fe 1 | 5067.1490 | 4.2204 | 1.280 | 0.647 | p |
| Cr 1 | 5067.7130 | 2.7088 | 1.160 | 0.517 | u |
| Cr 1 | 5068.2920 | 1.0037 | 1.720 | 0.604 | p |
| Fe 1 | 5068.7655 | 2.9398 | 1.740 | 0.854 | t |
| Ti 1 | 5071.4673 | 1.4601 | 1.160 | 0.546 | p |
| Fe 1 | 5072.0778 | 4.2833 | 0.880 | 0.684 | p |
| Fe 1 | 5072.6715 | 4.2204 | 1.470 | 0.671 | u |
| Cr 1 | 5072.9260 | 0.9414 | 1.500 | 0.741 | p |
| Fe 1 | 5074.7475 | 4.2204 | 1.060 | 0.759 | t |
| Fe 1 | 5076.2637 | 4.3013 | 0.370 | 0.658 | u |
| Fe 1 | 5078.9740 | 4.3013 | 1.870 | 0.735 | p |
| Fe 1 | 5079.2222 | 2.1979 | 1.480 | 0.852 | p |
| Fe 1 | 5079.7394 | 0.9901 | 1.510 | 0.896 | t |
| Ni 1 | 5079.9584 | 1.8261 | 0.510 | 0.626 | p |
| Ni 1 | 5080.5325 | 3.6552 | 1.030 | 0.768 | u |
| Ni 1 | 5081.1103 | 3.8474 | 0.980 | 0.734 | t |
| Ni 1 | 5082.3441 | 3.6576 | 1.210 | 0.637 | t |
| Fe 1 | 5083.3380 | 0.9582 | 1.250 | 0.912 | t |
| Ni 1 | 5084.0957 | 3.6785 | 1.250 | 0.726 | p |
| Ti 1 | 5087.0582 | 1.4298 | 0.750 | 0.602 | p |
| Y 2 | 5087.4190 | 1.0840 | 1.260 | 0.624 | u |
| Fe 1 | 5090.7726 | 4.2562 | 1.180 | 0.724 | p |
| Fe 1 | 5090.7740 | 4.2562 | 99.000 | 0.727 | p |
| Cr 1 | 5091.8830 | 1.0037 | 0.660 | 0.655 | p |
| Ni 1 | 5096.8629 | 3.7398 | 1.480 | 0.520 | p |
| Fe 1 | 5096.9972 | 4.2833 | 1.290 | 0.739 | p |
| Fe 1 | 5097.4821 | 4.3013 | -0.020 | 0.593 | p |
| Fe 1 | 5098.5722 | 3.9286 | 1.520 | 0.731 | t |
| Fe 1 | 5098.6981 | 2.1759 | 1.500 | 0.857 | t |
| Fe 1 | 5099.0767 | 3.9841 | 0.900 | 0.642 | p |
| Ni 1 | 5099.3202 | 3.6552 | 1.310 | 0.653 | u |
| Ni 1 | 5099.9304 | 3.6785 | 1.260 | 0.706 | p |
| Ni 1 | 5102.9659 | 1.6764 | 1.240 | 0.645 | t |
| Fe 1 | 5104.0301 | 3.0173 | 1.480 | 0.504 | p |
| Cu 1 | 5105.5370 | 1.3889 | 1.150 | 0.791 | p |
| Fe 1 | 5107.4471 | 0.9901 | 1.000 | 0.902 | p |
| Fe 1 | 5107.6405 | 1.5574 | 1.490 | 0.894 | u |
| Fe 1 | 5109.6514 | 4.3013 | 1.150 | 0.622 | u |
| Fe 1 | 5110.3580 | 3.5732 | 1.010 | 0.709 | u |

| Element | Wavelength (air – Å) | Excitation potential (eV) | Landé factor | Line Depth | Feature Type |
|---|---|---|---|---|---|
| Fe 1 | 5110.4128 | 0.0000 | 1.570 | 0.932 | p |
| Ti 1 | 5113.4401 | 1.4432 | 0.990 | 0.648 | p |
| Ni 1 | 5115.3922 | 3.8339 | 1.100 | 0.673 | u |
| Ti 1 | 5120.4152 | 2.5783 | 1.080 | 0.602 | p |
| Fe 1 | 5121.6386 | 4.2833 | 1.000 | 0.657 | u |
| Cr 1 | 5123.4600 | 1.0300 | 0.860 | 0.526 | p |
| Fe 1 | 5123.7196 | 1.0111 | -0.010 | 0.901 | p |
| Fe 1 | 5125.1163 | 4.2204 | 1.300 | 0.780 | p |
| Fe 1 | 5125.1171 | 4.2204 | 99.000 | 0.763 | p |
| Ni 1 | 5125.2319 | 3.6785 | 0.810 | 0.603 | p |
| Fe 1 | 5126.1922 | 4.2562 | 1.070 | 0.658 | u |
| Fe 1 | 5126.1930 | 4.2562 | 99.000 | 0.610 | u |
| Ni 1 | 5126.8255 | 3.6988 | 1.110 | 0.682 | n |
| Fe 1 | 5127.3587 | 0.9146 | 1.500 | 0.894 | p |
| Fe 1 | 5127.6796 | 0.0516 | 0.990 | 0.579 | p |
| Ti 2 | 5129.1562 | 1.8917 | 1.110 | 0.622 | p |
| Ni 1 | 5129.3710 | 3.6785 | 0.990 | 0.608 | p |
| Fe 1 | 5131.4678 | 2.2227 | 2.500 | 0.794 | p |
| Ni 1 | 5131.7676 | 3.6988 | 1.150 | 0.573 | u |
| Fe 1 | 5133.6876 | 4.1777 | 1.090 | 0.802 | t |
| Ni 1 | 5137.0738 | 1.6764 | 1.210 | 0.808 | p |
| Fe 1 | 5137.3813 | 4.1777 | 1.380 | 0.735 | t |
| Fe 1 | 5139.2503 | 2.9980 | 1.810 | 0.869 | t |
| Ni 1 | 5139.2580 | 3.6576 | 1.670 | 0.531 | t |
| Fe 1 | 5139.4620 | 2.9398 | 1.700 | 0.890 | t |
| Fe 1 | 5141.7384 | 2.4242 | 1.000 | 0.827 | t |
| Fe 1 | 5142.4935 | 4.3013 | 0.770 | 0.663 | u |
| Fe 1 | 5142.5401 | 4.2562 | 1.200 | 0.733 | u |
| Ni 1 | 5142.7763 | 3.7057 | 1.020 | 0.694 | u |
| Ni 1 | 5142.9279 | 3.6988 | 1.310 | 0.635 | t |
| Fe 1 | 5142.9282 | 0.9582 | 1.510 | 0.903 | t |
| Fe 1 | 5143.7226 | 2.1979 | 0.350 | 0.506 | u |
| Fe 1 | 5145.0937 | 2.1979 | 1.830 | 0.742 | t |
| Ti 1 | 5145.4602 | 1.4601 | 1.140 | 0.678 | p |
| Ni 1 | 5146.4820 | 3.7057 | 0.960 | 0.719 | p |
| Ti 1 | 5147.4777 | 0.0000 | 1.470 | 0.773 | p |
| Fe 1 | 5148.0419 | 4.2833 | 1.220 | 0.728 | p |
| Fe 1 | 5148.2283 | 4.2562 | 1.250 | 0.742 | p |
| Fe 1 | 5150.8389 | 0.9901 | 1.500 | 0.904 | p |
| Fe 1 | 5151.9105 | 1.0111 | 1.510 | 0.883 | t |
| Ti 1 | 5152.1835 | 0.0211 | 1.530 | 0.765 | p |
| Cu 1 | 5153.2307 | 3.7859 | 0.860 | 0.526 | p |
| Ti 2 | 5154.0680 | 1.5658 | 1.500 | 0.615 | p |
| Fe 1 | 5154.1002 | 3.8816 | 1.580 | 0.558 | u |
| Ni 1 | 5155.1259 | 3.8983 | 0.910 | 0.532 | u |
| Ni 1 | 5155.7639 | 3.8983 | 1.140 | 0.685 | p |

| Element | Wavelength (air – Å) | Excitation potential (eV) | Landé factor | Line Depth | Feature Type |
|---|---|---|---|---|---|
| Fe 1 | 5159.0570 | 4.2833 | 1.130 | 0.651 | p |
| Fe 1 | 5162.2720 | 4.1777 | 1.390 | 0.786 | t |
| Fe 1 | 5165.4098 | 4.2204 | 1.330 | 0.728 | t |
| Fe 1 | 5166.2816 | 0.0000 | 1.790 | 0.915 | p |
| Mg 1 | 5167.3216 | 2.7091 | 99.000 | 0.927 | p |
| Fe 1 | 5167.4879 | 1.4849 | 1.150 | 0.937 | p |
| Ni 1 | 5168.6589 | 3.6988 | 0.680 | 0.640 | u |
| Fe 1 | 5168.8972 | 0.0516 | 1.620 | 0.921 | p |
| Fe 2 | 5169.0282 | 2.8910 | 1.330 | 0.797 | p |
| Fe 1 | 5171.5960 | 1.4849 | 1.250 | 0.923 | p |
| Fe 1 | 5171.6717 | 3.6416 | 0.670 | 0.573 | u |
| Mg 1 | 5172.6843 | 2.7116 | 99.000 | 0.936 | t |
| Ti 1 | 5173.7431 | 0.0000 | 0.670 | 0.881 | t |
| Ni 1 | 5176.5603 | 3.8983 | 1.120 | 0.587 | u |
| Mg 1 | 5183.6042 | 2.7166 | 99.000 | 0.938 | t |
| Fe 1 | 5184.2657 | 4.2833 | 1.210 | 0.668 | u |
| Fe 1 | 5184.2661 | 4.2833 | 99.000 | 0.615 | n |
| Ni 1 | 5184.5588 | 3.7057 | 1.070 | 0.575 | u |
| Fe 1 | 5185.7246 | 3.5732 | 1.040 | 0.508 | u |
| Ti 2 | 5185.9020 | 1.8927 | 0.890 | 0.598 | p |
| Fe 1 | 5187.9141 | 4.1426 | 0.990 | 0.566 | u |
| Ti 2 | 5188.6871 | 1.5818 | 1.200 | 0.749 | t |
| Ca 1 | 5188.8440 | 2.9325 | 1.000 | 0.741 | p |
| Fe 1 | 5191.4541 | 3.0385 | 2.000 | 0.876 | t |
| Fe 1 | 5192.3433 | 2.9980 | 1.830 | 0.888 | t |
| Ti 1 | 5192.9686 | 0.0211 | 1.080 | 0.886 | t |
| Fe 1 | 5194.9411 | 1.5574 | 1.090 | 0.907 | t |
| Fe 1 | 5195.4714 | 4.2204 | 0.970 | 0.763 | p |
| Fe 1 | 5196.0585 | 4.2562 | 1.090 | 0.704 | p |
| Mn 1 | 5196.5900 | 3.1350 | 1.060 | 0.503 | u |
| Fe 2 | 5197.5675 | 3.2305 | 0.670 | 0.609 | u |
| Fe 1 | 5198.7105 | 2.2227 | 1.500 | 0.834 | t |
| Y 2 | 5200.4097 | 0.9923 | 0.720 | 0.510 | n |
| Fe 1 | 5202.2553 | 4.2562 | 1.270 | 0.706 | u |
| Fe 1 | 5202.3354 | 2.1759 | 1.660 | 0.868 | p |
| Cr 1 | 5204.4980 | 0.9414 | 1.750 | 0.925 | u |
| Fe 1 | 5204.5825 | 0.0873 | 1.750 | 0.900 | p |
| Y 2 | 5205.7224 | 1.0325 | 1.080 | 0.579 | u |
| Cr 1 | 5206.0230 | 0.9414 | 1.920 | 0.929 | t |
| Cr 1 | 5208.4090 | 0.9414 | 1.330 | 0.932 | t |
| Fe 1 | 5208.5936 | 3.2410 | 1.500 | 0.820 | p |
| Ti 1 | 5210.3843 | 0.0480 | 1.260 | 0.891 | t |
| Fe 1 | 5215.1800 | 3.2657 | 1.500 | 0.818 | t |
| Fe 1 | 5216.2737 | 1.6079 | 0.680 | 0.899 | t |
| Fe 1 | 5217.3890 | 3.2112 | 1.490 | 0.805 | t |
| Fe 1 | 5217.9189 | 3.6398 | 0.970 | 0.621 | p |

| Element | Wavelength (air – Å) | Excitation potential (eV) | Landé factor | Line Depth | Feature Type |
|---|---|---|---|---|---|
| Cu 1 | 5218.1975 | 3.8167 | 1.090 | 0.579 | p |
| Ti 1 | 5219.7015 | 0.0211 | 1.500 | 0.698 | p |
| Fe 1 | 5223.1824 | 3.6352 | 0.500 | 0.608 | p |
| Ti 1 | 5224.3000 | 2.1344 | 1.420 | 0.637 | p |
| Ti 1 | 5224.5400 | 2.1029 | 1.250 | 0.522 | p |
| Cr 1 | 5224.9250 | 3.4499 | 1.610 | 0.593 | p |
| Ti 1 | 5224.9300 | 2.1171 | 1.340 | 0.590 | p |
| Fe 1 | 5225.5260 | 0.1101 | 2.250 | 0.857 | t |
| Ti 2 | 5226.5384 | 1.5658 | 0.860 | 0.714 | p |
| Fe 1 | 5226.8612 | 3.0385 | 2.170 | 0.873 | p |
| Fe 1 | 5227.1495 | 2.4242 | 0.980 | 0.878 | u |
| Fe 1 | 5227.1889 | 1.5574 | 1.000 | 0.931 | p |
| Fe 1 | 5228.3753 | 4.2204 | 0.970 | 0.559 | u |
| Fe 1 | 5229.8446 | 3.2830 | 1.500 | 0.805 | t |
| Fe 1 | 5229.8654 | 4.2204 | 1.390 | 0.732 | t |
| Fe 1 | 5232.9397 | 2.9398 | 1.260 | 0.907 | t |
| Fe 2 | 5234.6226 | 3.2213 | 0.870 | 0.579 | u |
| Fe 1 | 5235.3867 | 4.0758 | 1.200 | 0.680 | u |
| Fe 1 | 5236.2016 | 4.1864 | 0.390 | 0.508 | n |
| Fe 1 | 5242.4905 | 3.6343 | 1.000 | 0.743 | t |
| Fe 1 | 5243.7757 | 4.2562 | 1.300 | 0.644 | u |
| Fe 1 | 5243.7769 | 4.2562 | 99.000 | 0.582 | u |
| Fe 1 | 5245.6253 | 4.3125 | 1.240 | 0.679 | n |
| Fe 1 | 5247.0498 | 0.0873 | 1.990 | 0.840 | p |
| Cr 1 | 5247.5650 | 0.9610 | 2.510 | 0.837 | t |
| Fe 1 | 5250.2088 | 0.1213 | 3.000 | 0.835 | t |
| Fe 1 | 5250.6453 | 2.1979 | 1.500 | 0.829 | p |
| Ti 1 | 5252.0997 | 0.0480 | 1.520 | 0.644 | t |
| Fe 1 | 5253.4617 | 3.2830 | 1.510 | 0.720 | p |
| Fe 1 | 5254.9551 | 0.1101 | 2.260 | 0.858 | u |
| Cr 1 | 5255.1140 | 3.4635 | 1.310 | 0.538 | p |
| Mn 1 | 5255.3300 | 3.1326 | 1.160 | 0.542 | u |
| Fe 1 | 5259.0937 | 4.3714 | 1.120 | 0.643 | n |
| Ca 1 | 5260.3870 | 2.5213 | 2.000 | 0.509 | u |
| Ca 1 | 5261.7040 | 2.5213 | 1.000 | 0.738 | u |
| Ca 1 | 5262.2410 | 2.5213 | 0.500 | 0.753 | p |
| Fe 1 | 5263.3059 | 3.2657 | 1.500 | 0.814 | t |
| Fe 1 | 5263.8643 | 3.5732 | 0.880 | 0.527 | u |
| Cr 1 | 5264.1530 | 0.9684 | 2.010 | 0.876 | p |
| Ca 1 | 5264.2370 | 2.5230 | 1.330 | 0.739 | p |
| Ca 1 | 5265.5560 | 2.5230 | 0.990 | 0.799 | p |
| Cr 1 | 5265.7140 | 0.9684 | 1.990 | 0.821 | p |
| Ti 1 | 5265.9639 | 1.8871 | 1.170 | 0.566 | p |
| Co 1 | 5266.4970 | 2.0418 | 1.050 | 0.571 | u |
| Fe 1 | 5266.5542 | 2.9980 | 1.280 | 0.885 | t |
| Fe 1 | 5269.5365 | 0.8590 | 1.200 | 0.939 | p |

| Element | Wavelength (air – Å) | Excitation potential (eV) | Landé factor | Line Depth | Feature Type |
|---|---|---|---|---|---|
| Ca 1 | 5270.2700 | 2.5257 | 1.160 | 0.826 | p |
| Fe 1 | 5270.3560 | 1.6079 | 0.750 | 0.926 | p |
| Fe 1 | 5273.1632 | 3.2918 | 1.520 | 0.797 | p |
| Fe 1 | 5273.3727 | 2.4844 | 0.490 | 0.785 | p |
| Fe 1 | 5273.6239 | 4.3125 | 1.230 | 0.544 | n |
| Cr 1 | 5275.2768 | 2.8895 | 1.170 | 0.663 | t |
| Cr 1 | 5275.7470 | 2.8895 | 2.170 | 0.700 | p |
| Fe 2 | 5275.9968 | 3.1995 | 0.910 | 0.639 | p |
| Cr 1 | 5276.0670 | 2.8895 | 2.000 | 0.692 | p |
| Fe 1 | 5277.3052 | 4.4153 | 0.850 | 0.559 | u |
| Fe 1 | 5280.3608 | 3.6416 | 1.390 | 0.592 | p |
| Fe 1 | 5281.7894 | 3.0385 | 1.180 | 0.846 | t |
| Ti 1 | 5283.4381 | 1.8792 | 1.000 | 0.532 | p |
| Fe 1 | 5283.6207 | 3.2410 | 1.500 | 0.858 | t |
| Fe 1 | 5288.5247 | 3.6946 | 1.020 | 0.643 | p |
| Cr 1 | 5296.6910 | 0.9829 | 1.000 | 0.856 | t |
| Cr 1 | 5297.3760 | 2.8995 | 1.250 | 0.725 | p |
| Cr 1 | 5298.0140 | 2.8995 | 1.840 | 0.690 | p |
| Cr 1 | 5298.2710 | 0.9829 | 1.670 | 0.875 | p |
| Cr 1 | 5298.4900 | 2.8995 | 1.830 | 0.644 | p |
| Fe 1 | 5298.7755 | 3.6416 | 1.390 | 0.536 | n |

# Bibliography


Aigrain, S., Pont, F., & Zucker, S. 2012, MNRAS, 419, 3147

Albrecht, S., Winn, J. N., Johnson, J. A., et al. 2012, ApJ, 757, 18

Alibert, Y., Mousis, O., Mordasini, C., & Benz, W. 2005, ApJL, 626, L57

Anglada-Escudé, G., Amado, P. J., Barnes, J., et al. 2016, Nature, 536, 437

Applegate, J. H. 1992, ApJ, 385, 621

Auvergne, M., Bodin, P., Boisnard, L., et al. 2009, A&A, 506, 411

Babcock, H. W. 1961, ApJ, 133, 572

Baraffe, I., Homeier, D., Allard, F., & Chabrier, G. 2015, A&A, 577, A42

Baranne, A., Queloz, D., Mayor, M., et al. 1996, A&AS, 119, 373

Barnes, S. A. 2007, ApJ, 669, 1167

Barnes, S. A., Weingrill, J., Fritzewski, D., Strassmeier, K. G., & Platais, I. 2016, ApJ, 823, 16

Basri, G., Wilcots, E., & Stout, N. 1989, PASP, 101, 528

Bayliss, D., Gillen, E., Eigmüller, P., et al. 2018, MNRAS, 475, 4467

Beaulieu, J.-P., Bennett, D. P., Fouqué, P., et al. 2006, Nature, 439, 437

Beeck, B., Schüssler, M., Cameron, R. H., & Reiners, A. 2015, A&A, 581, A43

Bennett, D. P. & Rhie, S. H. 2002, The Astrophysical Journal, 574, 985

Beuermann, K., Hessman, F. V., Dreizler, S., et al. 2010, A&A, 521, L60

Boisse, I., Bonfils, X., & Santos, N. C. 2012, A&A, 545, A109

Boisse, I., Bouchy, F., Hébrard, G., et al. 2011, A&A, 528, A4

Boisse, I., Moutou, C., Vidal-Madjar, A., et al. 2009, A&A, 495, 959

Borucki, W. J., Koch, D., Basri, G., et al. 2010, Science, 327, 977

Borucki, W. J., Koch, D. G., Batalha, N., et al. 2012, ApJ, 745, 120

Boss, A. P. 1997, Science, 276, 1836

Boyajian, T. S., von Braun, K., van Belle, G., et al. 2012, ApJ, 757, 112

Bozza, V., Mancini, L., & Sozzetti, A., eds. 2016, Astrophysics and Space Science Library, Vol. 428, Methods of Detecting Exoplanets

Bradshaw, S. J. & Hartigan, P. 2014, ApJ, 795, 79

Broomhall, A.-M., Chaplin, W. J., Davies, G. R., et al. 2009, MNRAS, 396, L100

Carrington, R. C. 1859, MNRAS, 19, 81

Carter, J. A., Fabrycky, D. C., Ragozzine, D., et al. 2011, Science, 331, 562

Cassan, A., Kubas, D., Beaulieu, J.-P., et al. 2012, Nature, 481, 167

Cegla, H. M., Shelyag, S., Watson, C. A., & Mathioudakis, M. 2013, ApJ, 763, 95

Chabrier, G., Gallardo, J., & Baraffe, I. 2007, A&A, 472, L17

Chabrier, G., Johansen, A., Janson, M., & Rafikov, R. 2014, Protostars and Planets VI, 619

Chambers, J. E. & Wetherill, G. W. 1998, Icarus, 136, 304

Charbonneau, D., Brown, T. M., Latham, D. W., & Mayor, M. 2000, ApJL, 529, L45

Chauvin, G., Lagrange, A.-M., Dumas, C., et al. 2004, A&A, 425, L29

Choudhuri, A. R. 2007, in American Institute of Physics Conference Series, Vol. 919, Kodai School on Solar Physics, ed. S. S. Hasan & D. Banerjee, 49–73

Claret, A. 2000, A&A, 363, 1081

Collier Cameron, A. & Donati, J.-F. 2002, MNRAS, 329, L23

Cosentino, R., Lovis, C., Pepe, F., et al. 2012, in Proceedings of the SPIE, Vol. 8446, Ground-based and Airborne Instrumentation for Astronomy IV, 84461V

Dai, F., Winn, J. N., Gandolfi, D., et al. 2017, AJ, 154, 226

Dall, T. H., Santos, N. C., Arentoft, T., Bedding, T. R., & Kjeldsen, H. 2006, A&A, 454, 341

Delfosse, X., Forveille, T., Ségransan, D., et al. 2000, A&A, 364, 217

Delrez, L., Santerne, A., Almenara, J.-M., et al. 2016, MNRAS, 458, 4025

Desidera, S., Gratton, R. G., Endl, M., et al. 2004, A&A, 420, L27

Desort, M., Lagrange, A.-M., Galland, F., Udry, S., & Mayor, M. 2007, A&A, 473, 983

Díaz, R. F., Almenara, J. M., Santerne, A., et al. 2014, MNRAS, 441, 983

Dodson-Robinson, S. E., Veras, D., Ford, E. B., & Beichman, C. A. 2009, ApJ, 707, 79

Dravins, D. 1990, A&A, 228, 218

Dumusque, X., Boisse, I., & Santos, N. C. 2014, ApJ, 796, 132

Dumusque, X., Glenday, A., Phillips, D. F., et al. 2015, ApJL, 814, L21

Dumusque, X., Lovis, C., Ségransan, D., et al. 2011a, A&A, 535, A55

Dumusque, X., Pepe, F., Lovis, C., et al. 2012, Nature, 491, 207

Dumusque, X., Santos, N. C., Udry, S., Lovis, C., & Bonfils, X. 2011b, A&A, 527, A82

Dumusque, X., Udry, S., Lovis, C., Santos, N. C., & Monteiro, M. J. P. F. G. 2011c, A&A, 525, A140

Duncan, D. K., Vaughan, A. H., Wilson, O. C., et al. 1991, ApJS, 76, 383

Edelson, R. A. & Krolik, J. H. 1988, ApJ, 333, 646

Efron, B. 1992, in Breakthroughs in statistics (Springer), 569–593

Egeland, R., Soon, W., Baliunas, S., et al. 2017, ApJ, 835, 25

Figueira, P., Marmier, M., Bonfils, X., et al. 2010, A&A, 513, L8

Fischer, D. A. & Valenti, J. 2005, ApJ, 622, 1102

Gaudi, B. S. 2010, ArXiv e-prints

Gaudi, B. S. 2012, Annu. Rev. Astron. Astrophys., 50, 411

Gaudi, B. S., Bennett, D. P., Udalski, A., et al. 2008, Science, 319, 927

Gibson, N. P. 2014, MNRAS, 445, 3401

Gillon, M., Triaud, A. H. M. J., Demory, B.-O., et al. 2017, Nature, 542, 456

Giridhar, S. 2010, Bulletin of the Astronomical Society of India, 38, 1

Gray, D. F. 2008, The Observation and Analysis of Stellar Photospheres

Hall, J. C., Henry, G. W., Lockwood, G. W., Skiff, B. A., & Saar, S. H. 2009, AJ, 138, 312

Han, C., Udalski, A., Choi, J.-Y., et al. 2013, ApJL, 762, L28

Hatzes, A. P. 2002, Astronomische Nachrichten, 323, 392

Hatzes, A. P. 2012, Nature, 491, 200

Hatzes, A. P. 2013, ApJ, 770, 133

Hatzes, A. P., Dvorak, R., Wuchterl, G., et al. 2010, A&A, 520, A93

Hatzes, A. P., Fridlund, M., Nachmani, G., et al. 2011, ApJ, 743, 75

Hatzes, A. P. & Rauer, H. 2015, ApJL, 810, L25

Hauschildt, P. H. & Baron, E. 1999, Journal of Computational and Applied Mathematics, 109, 41

Haywood, R. D., Collier Cameron, A., Queloz, D., et al. 2014, MNRAS, 443, 2517

Haywood, R. D., Collier Cameron, A., Unruh, Y. C., et al. 2016, MNRAS, 457, 3637

Hebb, L., Collier-Cameron, A., Loeillet, B., et al. 2009, ApJ, 693, 1920

Hébrard, G., Bouchy, F., Pont, F., et al. 2008, A&A, 488, 763

Hellier, C., Anderson, D. R., Collier Cameron, A., et al. 2009, Nature, 460, 1098

Hellier, C., Anderson, D. R., Collier Cameron, A., et al. 2011, A&A, 535, L7

Henry, T. J., Jao, W.-C., Subasavage, J. P., et al. 2006, AJ, 132, 2360

Hirano, T., Narita, N., Sato, B., et al. 2011, PASJ, 63, L57

Howell, S. B., Sobeck, C., Haas, M., et al. 2014, PASP, 126, 398

Huélamo, N., Figueira, P., Bonfils, X., et al. 2008, A&A, 489, L9

Innes, R. T. A. 1915, Circular of the Union Observatory Johannesburg, 30, 235

Jackman, J. A. G., Wheatley, P. J., Pugh, C. E., et al. 2018, MNRAS, 477, 4655

Kane, S. R., Ciardi, D. R., Gelino, D. M., & von Braun, K. 2012, MNRAS, 425, 757

Kipping, D. M. 2009, MNRAS, 392, 181

Kopal, Z. 1950, Harvard College Observatory Circular, 454, 1

Kostik, R. & Khomenko, E. V. 2012, A&A, 545, A22

Kovács, G., Zucker, S., & Mazeh, T. 2002, A&A, 391, 369

Kozai, Y. 1962, AJ, 67, 591

Kraus, A. L., Tucker, R. A., Thompson, M. I., Craine, E. R., & Hillenbrand, L. A. 2011, ApJ, 728, 48

Lanza, A. F., Boisse, I., Bouchy, F., Bonomo, A. S., & Moutou, C. 2011, A&A, 533, A44

Leighton, R. B. 1969, ApJ, 156, 1

Lenz, P. & Breger, M. 2005, Communications in Asteroseismology, 146, 53

Lidov, M. L. 1962, *Planet. Space Sci.*, 9, 719

Lo Curto, G., Pasquini, L., Manescau, A., et al. 2012, The Messenger, 149, 2

Lockwood, G. W., Skiff, B. A., Henry, G. W., et al. 2007, ApJS, 171, 260

Lovis, C., Dumusque, X., Santos, N. C., et al. 2011, ArXiv e-prints

Lovis, C., Pepe, F., Bouchy, F., et al. 2006, in Proceedings of the SPIE, Vol. 6269, Society of Photo-Optical Instrumentation Engineers (SPIE) Conference Series, 62690P

Maldonado, J., Martínez-Arnáiz, R. M., Eiroa, C., Montes, D., & Montesinos, B. 2010, A&A, 521, A12

Marigo, P., Girardi, L., Bressan, A., et al. 2017, ApJ, 835, 77

Marois, C., Lafrenière, D., Doyon, R., Macintosh, B., & Nadeau, D. 2006, ApJ, 641, 556

Marois, C., Macintosh, B., Barman, T., et al. 2008, Science, 322, 1348

Marois, C., Nadeau, D., Doyon, R., Racine, R., & Walker, G. A. H. 2003, in IAU Symposium, Vol. 211, Brown Dwarfs, ed. E. Martín, 275

Marois, C., Zuckerman, B., Konopacky, Q. M., Macintosh, B., & Barman, T. 2010, Nature, 468, 1080

Martínez González, M. J., Collados, M., & Ruiz Cobo, B. 2006, A&A, 456, 1159

Mayor, M., Pepe, F., Queloz, D., et al. 2003, The Messenger, 114, 20

Mayor, M. & Queloz, D. 1995, Nature, 378, 355

McLaughlin, D. B. 1925, Popular Astronomy, 33, 295

Melo, C., Santos, N. C., Gieren, W., et al. 2007, A&A, 467, 721

Metropolis, N., Rosenbluth, A. W., Rosenbluth, M. N., Teller, A. H., & Teller, E. 1953, Journal of Chemical Physics, 21, 1087

Meunier, N., Desort, M., & Lagrange, A.-M. 2010, A&A, 512, A39

Meunier, N. & Lagrange, A.-M. 2013, A&A, 551, A101

Mihalas, D. 1978, Stellar atmospheres /2nd edition/

Morales, J. C., Ribas, I., Jordi, C., et al. 2009, ApJ, 691, 1400

Morton, T. D., Bryson, S. T., Coughlin, J. L., et al. 2016, ApJ, 822, 86

Muterspaugh, M. W., Lane, B. F., Kulkarni, S. R., et al. 2010, AJ, 140, 1657

Neff, J. E., O'Neal, D., & Saar, S. H. 1995, ApJ, 452, 879

Nelson, R. P. & Papaloizou, J. C. B. 2004, in Astronomical Society of the Pacific Conference Series, Vol. 321, Extrasolar Planets: Today and Tomorrow, ed. J. Beaulieu, A. Lecavelier Des Etangs, & C. Terquem, 367

Nesvorný, D., Kipping, D. M., Buchhave, L. A., et al. 2012, Science, 336, 1133

Noyes, R. W., Hartmann, L. W., Baliunas, S. L., Duncan, D. K., & Vaughan, A. H. 1984, ApJ, 279, 763

O'Neal, D. & Neff, J. E. 1997, AJ, 113, 1129

Oppenheimer, B. R., Baranec, C., Beichman, C., et al. 2013, ApJ, 768, 24

Oshagh, M., Santos, N. C., Figueira, P., et al. 2017, A&A, 606, A107

Parker, E. N. 1993, ApJ, 408, 707

Penev, K., Bouma, L. G., Winn, J. N., & Hartman, J. D. 2018, AJ, 155, 165

Pepe, F., Cameron, A. C., Latham, D. W., et al. 2013, Nature, 503, 377

Pepe, F., Molaro, P., Cristiani, S., et al. 2014, Astronomische Nachrichten, 335, 8

Perryman, M. 2011, The Exoplanet Handbook

Perryman, M., Hartman, J., Bakos, G. Á., & Lindegren, L. 2014, ApJ, 797, 14

Petigura, E. A., Howard, A. W., & Marcy, G. W. 2013, Proceedings of the National Academy of Science, 110, 19273

Piso, A.-M. A., Youdin, A. N., & Murray-Clay, R. A. 2015, ApJ, 800, 82

Queloz, D., Bouchy, F., Moutou, C., et al. 2009, A&A, 506, 303

Queloz, D., Henry, G. W., Sivan, J. P., et al. 2001, A&A, 379, 279

Radick, R. R., Lockwood, G. W., & Baliunas, S. L. 1990, Science, 247, 39

Rafikov, R. R. 2006, ApJ, 648, 666

Rajpaul, V., Aigrain, S., Osborne, M. A., Reece, S., & Roberts, S. 2015, MNRAS, 452, 2269

Rajpaul, V., Aigrain, S., & Roberts, S. 2016a, MNRAS, 456, L6

Rajpaul, V., Aigrain, S., & Roberts, S. 2016b, MNRAS, 456, L6

Rauer, H., Catala, C., Aerts, C., et al. 2014, Experimental Astronomy, 38, 249

Raymond, S. N., O'Brien, D. P., Morbidelli, A., & Kaib, N. A. 2009, Icarus, 203, 644

Ricker, G. R., Winn, J. N., Vanderspek, R., et al. 2014, in Proceedings of the SPIE, Vol. 9143, Space Telescopes and Instrumentation 2014: Optical, Infrared, and Millimeter Wave, 914320

Roberts, D. H., Lehar, J., & Dreher, J. W. 1987, AJ, 93, 968

Rossiter, R. A. 1924, ApJ, 60

Ryabchikova, T., Piskunov, N., Kurucz, R. L., et al. 2015, Physica Scripta, 90, 054005

Sanchez, S., Fournier, A., Pinheiro, K., & Aubert, J. 2013, ArXiv e-prints

Scargle, J. D. 1982, ApJ, 263, 835

Scherrer, P. H., Schou, J., Bush, R. I., et al. 2012, *Solar Phys.*, 275, 207

Schlaufman, K. C. 2010, ApJ, 719, 602

Schneider, J., Dedieu, C., Le Sidaner, P., Savalle, R., & Zolotukhin, I. 2011, A&A, 532, A79

Schrijver, C. J. & Zwaan, C. 2000, Solar and Stellar Magnetic Activity

Shapiro, A. I., Solanki, S. K., Krivova, N. A., Yeo, K. L., & Schmutz, W. K. 2016, A&A, 589, A46

Simpson, E. K., Pollacco, D., Hébrard, G., et al. 2010, MNRAS, 405, 1867

Sing, D. K., Fortney, J. J., Nikolov, N., et al. 2016, Nature, 529, 59

Skumanich, A. 1972, ApJ, 171, 565

Soter, S. 2006, AJ, 132, 2513

Soto, M. G. & Jenkins, J. S. 2018, ArXiv e-prints

Spada, F., Demarque, P., Kim, Y.-C., & Sills, A. 2013, ApJ, 776, 87

Tamuz, O., Mazeh, T., & Zucker, S. 2005, MNRAS, 356, 1466

Tanaka, H., Takeuchi, T., & Ward, W. R. 2002, ApJ, 565, 1257

Thompson, A. P. G., Watson, C. A., de Mooij, E. J. W., & Jess, D. B. 2017, MNRAS, 468, L16

Thompson, S. J., Queloz, D., Baraffe, I., et al. 2016, in Proceedings of the SPIE, Vol. 9908, Ground-based and Airborne Instrumentation for Astronomy VI, 99086F

Torrence, C. & Compo, G. P. 1998, Bulletin of the American Meteorological Society, 79, 61

Torres, G. 2013, Astronomische Nachrichten, 334, 4

Torres, G., Andersen, J., & Giménez, A. 2010, A&ARv, 18, 67

Udry, S. 2010, in In the Spirit of Lyot 2010

Uribe, A. L., Klahr, H., Flock, M., & Henning, T. 2011, ApJ, 736, 85

Vögler, A., Shelyag, S., Schüssler, M., et al. 2005, A&A, 429, 335

Vogt, S. S. & Penrod, G. D. 1983, PASP, 95, 565

Watson, C. A., Dhillon, V. S., & Shahbaz, T. 2006, MNRAS, 368, 637

Watson, C. A., Littlefair, S. P., Collier Cameron, A., Dhillon, V. S., & Simpson, E. K. 2010, MNRAS, 408, 1606

Watson, C. A., Steeghs, D., Shahbaz, T., & Dhillon, V. S. 2007, MNRAS, 382, 1105

Wheatley, P. J., Pollacco, D. L., Queloz, D., et al. 2013, in European Physical Journal Web of Conferences, Vol. 47, European Physical Journal Web of Conferences, 13002

Wheatley, P. J., West, R. G., Goad, M. R., et al. 2018, MNRAS, 475, 4476

Wilson, O. C. 1968, ApJ, 153, 221

Winn, J. N., Fabrycky, D., Albrecht, S., & Johnson, J. A. 2010, ApJL, 718, L145

Wolszczan, A. & Frail, D. A. 1992, Nature, 355, 145

Wright, J. T., Marcy, G. W., Butler, R. P., & Vogt, S. S. 2004, ApJS, 152, 261

Xie, J.-W., Dong, S., Zhu, Z., et al. 2016, Proceedings of the National Academy of Science, 113, 11431

Zechmeister, M. & Kürster, M. 2009, A&A, 496, 577

Zhao, L., Fischer, D. A., Brewer, J., Giguere, M., & Rojas-Ayala, B. 2018, AJ, 155, 24